INFORMATION TO USERS

This manuscript has been reproduced from the microfilm master. UMI films the text directly from the original or copy submitted. Thus, some thesis and dissertation copies are in typewriter face, while others may be from any type of computer printer.

The quality of this reproduction is dependent upon the quality of the copy submitted. Broken or indistinct print, colored or poor quality illustrations and photographs, print bleedthrough, substandard margins, and improper alignment can adversely affect reproduction.

In the unlikely event that the author did not send UMI a complete manuscript and there are missing pages, these will be noted. Also, if unauthorized copyright material had to be removed, a note will indicate the deletion.

Oversize materials (e.g., maps, drawings, charts) are reproduced by sectioning the original, beginning at the upper left-hand corner and continuing from left to right in equal sections with small overlaps. Each original is also photographed in one exposure and is included in reduced form at the back of the book.

Photographs included in the original manuscript have been reproduced xerographically in this copy. Higher quality 6" x 9" black and white photographic prints are available for any photographs or illustrations appearing in this copy for an additional charge. Contact UMI directly to order.

UMI

A Bell & Howell Information Company
300 North Zeeb Road, Ann Arbor MI 48106-1346 USA
313/761-4700 800/521-0600

IGNITION AND COMBUSTION OF BORON PARTICLES IN HYDROGEN/OXYGEN COMBUSTION PRODUCTS AT 30 TO 150 ATMOSPHERES

BY

ROBERT OLIVER FOELSCHE

B.S., Cornell University, 1990
M.S., University of Illinois, 1993

THESIS

Submitted in partial fulfillment of the requirements
for the degree of Doctor of Philosophy in Aeronautical and Astronautical Engineering in the Graduate College of the
University of Illinois at Urbana-Champaign, 1998

Urbana, Illinois

UNIVERSITY OF ILLINOIS AT URBANA-CHAMPAIGN

THE GRADUATE COLLEGE

NOVEMBER 4, 1997
(date)

WE HEREBY RECOMMEND THAT THE THESIS BY

ROBERT OLIVER FOELSCHE

ENTITLED IGNITION AND COMBUSTION OF BORON PARTICLES IN HYDROGEN/OXYGEN COMBUSTION PRODUCTS AT 30 TO 150 ATMOSPHERES

BE ACCEPTED IN PARTIAL FULFILLMENT OF THE REQUIREMENTS FOR

THE DEGREE OF DOCTOR OF PHILOSOPHY

Rodney L. Burton
Director of Thesis Research

W. P. Solomon
Head of Department

Committee on Final Examination†

Rodney L. Burton
Chairperson

Lee H. Sentman

Robert P. Lucht

Herman Krier

W. P. Solomon

† Required for doctor's degree but not for master's.

O-517

Abstract

The ignition and combustion of crystalline boron particles is studied at high pressures and temperatures in the combustion products of nitrogen diluted premixed hydrogen/oxygen mixtures in a high pressure, constant volume combustion chamber. A novel approach is used to inject particles after sufficient delay for gas phase combustion transients to equilibrate, permitting the particles to ignite and burn at high ambient temperature and nearly constant pressure conditions. Particle ignition and combustion are monitored optically by measuring combusting particle emissions. Using this injection technique, aluminum particle ignition delays and combustion times are measured at high pressure and compared to independent determinations showing excellent agreement. The methodology is used to measure the ignition and combustion times of ~24 micron boron particles over a range of pressures (30 - 150 atm), temperatures (2440, 2630, 2830 K), excess O_2 concentrations (5, 11, 20%), and with two proposed ignition enhancers (CO_2, HF). Several particles sizes are investigated at one condition (~12, ~24, ~48 μm) to determine particle scaling laws.

Although boron has been observed previously to exhibit a two-stage ignition process at lower pressures and temperatures, only a single continuously increasing luminous stage is observed here. Boron particle ignition delays for ~24 μm are of the order of 1-2 milliseconds, and are reduced with increased pressure, decreased particle size, and increased temperature but increase with increasing ambient oxygen concentrations. Ignition delays for ~12 μm particles are less than 0.3 msec. The measured ignition delays are shortened by convective heating resulting from the finite injection velocities into the dense gases by a factor of ~2 compared to statically heated particles. Although convective heating rates are functions of pressure, convective heating alone does not account for the measured pressure dependence. Combustion times for ~24 μm particles are between 1-5 msec, but drop significantly between 2440 K and 2600 K, decreasing by a factor of at least two, and are reduced with increased pressure. Both ignition delays and combustion times obey a d^1-scaling law (linear) as particle diameter increases, suggesting processes are kinetics-controlled. The two tested ignition-enhancing agents show no signs of accelerated ignition and 5% HF was found to increase ignition delays.

Measured ignition delays are compared to predictions from two ignition models showing generally good agreement in the average sense when convective heating is handled appropriately; however, current models fail to predict two important measured trends. The models under-predict the measured decrease in boron particle ignition delays with increasing pressure and do not predict the sharp decrease in ignition and combustion times as temperature is increased between 2440 K and 2600 K.

The results of this study demonstrate that boron particle lifetimes at elevated pressures are sufficiently short to make these particles suitable for additives to propellants and that smaller 1-10 μm sized particles, which have still shorter lifetimes, may be appropriate for addition to explosives.

Dedication

This thesis is dedicated to my mother Agnes Foelsche and father Horst W. J. Foelsche without whose encouragement and continual support this study would not have come to fruition. My father's untimely death at the hands of cancer during my research was a severe personal blow which placed severe strains on my perseverance, strains which could not have been overcome except for the steadfast support of the rest of my family and close friends. My father was the type of person who took great pleasure in the success and work of his children, and I would have liked to have debated the findings and merits of this thesis with him at length, as we did for my Master's Thesis.

Acknowledgments

The author would like to acknowledge the continued support and assistance of his thesis advisor, Prof. Rodney L. Burton of the Department of Aeronautical and Astronautical Engineering, whose keen engineering and practical insight kept this project a tenable adventure. The author is likewise indebted to the support of Prof. Herman Krier of the Department of Mechanical and Industrial Engineering. Both provided the opportunity for me to pursue this research which resulted in a thesis. I also acknowledge the continual assistance and working companionship of past and present fellow experimentalists S. R. Pirman, M. J. Spalding, and T. Rood and extend warm gratitude to T. A. Roberts for spurring my interest in metal particle ignition problems. Special thanks are due to undergraduates R. McMullen, C. Holtz, and M. Abogado, and graduate student D. Schneider for their valuable assistance in execution of the experiments.

The author would like to thank the contributions John Black during design of the combustion chamber. I am especially indebted to P. Hetman for his expert fabrication and machining of the combustion chamber and special insights into the main seal design. Likewise acknowledgment is due D. Roberts, R. Hendricks and R. Coverdill of the Mechanical Engineering Shop for their expert work during fabrication of related assemblies and C. Reiner and for design and fabrication of specialized electronics. Acknowledgment is due to W. Zhou and Dr. R. A. Yetter for several important discussions on the chemistry of boron combustion and for executing the Princeton/Aerodyne Model for the conditions of this study.

I am very grateful to the assistance and funding of our sponsors at the Office of Naval Research. This work was conducted under ONR Grant No. N00014-93-1-0654. Dr. R. S. Miller is the Project Director. The author is similarly indebted to the Department of Aeronautical and Astronautical Engineering at the University of Illinois for its support and facilities. Scanning electron microscopy was carried out in the Center for Microanalysis of Materials, University of Illinois, which is supported by the U.S. Department of Energy under grant DEFG02-91-ER45439.

I would especially like to thank my mother and father for all the support which they have given me throughout my education and especially that which has lead me to pursue further graduate study.

Table of Contents

List of Tables

List of Figures

Nomenclature

a_g	speed of sound in the gas mixture, m/sec
A_s	surface area, m^2
B_xO_y	boron oxide
B	Spalding transfer number, for evaporation processes
Bi	the particle Biot Number, defined as $\overline{h}_c L_c / k_p$
C_D	particle coefficient of drag
c_i	stoichiometric coefficient for a reaction or process
$c_{p,i}$	specific heat at constant pressure of i^{th} species, J/kg K
$c_{v,i}$	specific heat at constant volume of i^{th} species, J/kg K
Δ_x	uncertainty in the variable "x"
Da	Damköhler number; ratio of O_2-diffusion timescale to O_2-surface reaction timescale during particle combustion stage
d_p	particle diameter, μm
D_i	diffusion coefficient for i^{th} species in rest of mixture, m^2/sec
E_a	activation energy required for a chemical process, kcal
F_D	particle viscous drag force, N
F_g	particle gravity force, N
$H_{fus,i}$	heat of fusion, kJ/mol
$H_{vap,i}$	heat of vaporization, kJ/mol
$\Delta H^0_{f,298}$	heat of formation, standard state, kJ/mol
$\overline{h}_c$	surface-averaged convective heat transfer coefficient, W/m^2 K
k_B	Boltzmann's constant, 1.381e-23 J/K
k_i	thermal conductivity of i^{th} species, W/m K
k_{fi}	Forward rate constant of i^{th} reaction
k_{ri}	Reverse rate constant of i^{th} reaction
L_c	characteristic dimension, for sphere it is the ratio of volume to surface area
$\dot{m}$	surface burning rate, kg/sec
m_p	particle mass, gm
M_p	particle Mach number, defined as v_p/a_g
n_1	number density of $B_2O_3(l)$
n_i, n_c	diameter-scaling exponent for ignition or combustion times, e.g., $t_{ign} \sim d_p^{n_i}$
Nu_p	particle surface-averaged Nusselt number
$\overline{Nu}_p$	time-averaged particle Nu_p

p_1	initial chamber gas fill pressure, atm
p_2	calculated equilibrium peak combustion pressure, atm
p_c	pressure during particle ignition, atm
p_{e1}	equilibrium vapor pressure of $B_2O_3(l)$, atm
p_i	partial pressure of i^{th} species, atm
p_{vap}	vapor pressure of liquid, atm
Pr	Prandtl number, defined as $c_{p,g}\,\mu_g/k_g$
$\dot{q}_{con}$	heat transfer rate by convection, W (J/sec)
$\dot{q}_{rad}$	heat transfer rate by radiation, W
$\dot{q}_{rxn}$	heat production rate by chemical reactions, W
Q_i	heat of reaction of i^{th} process, kcal/mol
Re_p	particle Reynolds number, defined as $\rho_g \mid v_p - v_g \mid d_p/\mu_g$
r_a	absorption rate
r_p	particle radius, μm
R_C	Rockwell Hardness C, for metal hardening by heat treatment
R_u	Universal gas constant, 8.314 J/g-mol K
s_0	probability of a molecule sticking to a surface during collision
S_p	particle frontal area, πr_p^2, m^2
T_1	initial chamber gas fill temperature, K
T_2	calculated equilibrium peak combustion temperature, K
T_c	gas temperature during particle ignition, K
T_{cut}	temperature above which oxide layer removal occurs by chemical reactions, in the Li and Williams model, K
$T_{mp,i}$	melting point temperature of i^{th} species, K
$T_{bp,i}$	boiling point temperature of i^{th} species, K
T_{ign}	ignition temperature of material, K
T^*	the geometric mean temperature between the ambient gas and particle, K
t_1	Macek's first stage combustion time, equivalent to the oxide layer removal time, msec
t_{comb}	particle combustion time, msec
$t_{c:i}$	particle combustion time defined up to the instant where i% of the area under the net particle emission signal is reached, msec
$t_{heat\text{-}up}$	particle heating time, the time to heat to the temperature where chemical reactions begin to remove oxide layer, msec
$t_{hh}^{(i)}$	times corresponding to half peak-amplitude of net particle photodiode signal, i=1,2, msec

t_{ign}	particle ignition delay time, the sum of heat-up and oxide layer removal, msec
t^*_{ign}	ignition delay time for boron particles in a non-convective environment
t_{inj}	the injection delay time (particle injector), msec
Δt_{inj}	the time to inject the entire particle sample, msec
$t_{ox\text{-}rem}$	particle oxide layer removal time, msec
t_{pr}	pressure rise time in the combustion chamber, msec
t_{ps}	pressure stay time in the combustion chamber, msec
v_g	bulk chamber gas velocity, ~0, m/sec
v_p	particle velocity as a result of injection, m/sec
V_{hh}	half peak-amplitude of net particle signal as measured with photodiode, Arb.
V_{peak}	peak-amplitude of net particle signal as measured with photodiode, Arb.
$\bar{W}$	mixture molecular weight, gm/gm-mole
W_i	molecular weight of i^{th} species, gm/gm-mole
x_p	particle position or penetration depth into the ambient gas, m
X_i	mole fraction of i^{th} species
X_l	equilibrium mole fraction of BO(d) at the surface
X_{adtv}	mole fraction of ignition-enhancing additive
$Y_{g,ox,i}$	mass fraction of i^{th} oxidizing species in the gas phase

Greek Symbols:

α	coefficient of thermal expansion, m/m K
α_i	evaporation coefficient or reaction probability of i^{th} process
ε	gray body emissivity
γ	ratio of specific heats, $c_{p,i}/c_{v,i}$
μ_g	the gas mixture viscosity, kg/m sec
ν_i	Hertz-Knudsen factor i^{th} process
θ	oxide layer thickness, μm
Θ	fraction of surface covered by absorbed species
ρ	mass density, kg/m^3
σ	Stefan-Boltzmann constant, 5.67e-8 $W/m^2 K^4$
ω_i	rate of i^{th} process, mol/cm^2-sec

Subscripts, Superscripts:

0	initial
1	initial chamber conditions, before gas-phase combustion
2	peak chamber conditions, after gas-phase combustion

∞	the ambient mixture gas properties in the far field
*	analogous parameters in a non-convection environment
a	absorption process
B	boron property
c	chamber gas property during the particle ignition stage
g	gas phase mixture property
l	liquid phase mixture property
p	particle property

1. INTRODUCTION

1.1 Research Motivation

The high potential energy release of boron makes it a prime candidate for high enthalpy fuels, as a fuel additive to solid propellant formulations, and as an additive for tailoring energy release within explosive grains. As such boron combustion has received much research interest in the past 30 years (see for example Ref. 1). Theoretically, the high enthalpy of combustion, high combustion temperature, and low molecular weight products suggest a promising application in rocket propellants. Such applications require rapid energy release to make boron utilization efficient in practice, and this turns out to be a difficult task. Therefore a thorough understanding of the ignition and combustion behavior of boron particles is of prime interest to the propulsion designer.

The use of boron as a fuel additive is promising based on the fact that boron has the potential for great energy release both on a volumetric and gravimetric basis. King[1] has calculated the energy potential of common fuels, see Table 1.1, where the numbers assume the products formed are the stable product species in the phase listed. Boron possesses better fuel thermodynamic potential than many hydrocarbons including JP5 jet fuel, propane, and coal and also possesses more favorable energetics than such commonly used propellant additives as aluminum and magnesium (beryllium is discounted because of its high toxicity).

For many years a concentrated effort has been placed into the study of metal particle combustion due to the high energy density of metallized solid propellants. Currently aluminum and magnesium are the metal additives of choice;[2] however, if it is desired to obtain the highest possible energy release then boron is the leading material candidate. Theoretical performance calculations in Fig. 1.1 by Besser, et al.[3] indicate that the specific impulse[†] of boron particle laden propellants and boron-fuel slurries show significant advantages over baseline formulations. It is in the application to rocket propellant additives for missiles or rocket-ramjets where the ideal potential of boron has received the most interest and subsequent study.

Boron has also been considered a prime candidate to enhance the energy release in explosive grains, where the delayed energy release from boron particles can be used to control non-ideal detonations. The high energy output of boron coupled with delayed reaction could be used to tailor an expanded pressure-volume process which would result in significantly more useful work output than achieved by present formulations.

[†] The specific impulse is defined as the thrust generated divided by the weight flow of propellant. The volume specific impulse as the thrust generated divided by the volume flow of propellant.

Table 1.1: Calculated maximum energetics of various fuels and metallized propellant additives, from Refs. (1,3). Calculations assume products remain undissociated and in the phase listed.

Fuel/Additive	Gravimetric Heating Value [cal/gm]	Volumetric Heating Value [cal/cm^3]	Products
JP5, jet fuel	10,150	8,230	$CO_2(g)$, $H_2O(g)$
Kerosene	9,860	1,000	$CO_2(g)$, $H_2O(g)$
Propane	12,230	24,000	$CO_2(g)$, $H_2O(g)$
Coal, C(*s*)	7,830	17,700	$CO_2(g)$, $H_2O(g)$
$(CH_2)_n$	10,400	9,600	$CO_2(g)$, $H_2O(g)$
Aluminum	7,420	2,000	$Al_2O_3(l)$
Magnesium	5,910	10,300	$MgO(l)$
Beryllium	15,890	29,400	$BeO(l)$
Boron	**13,800**	**32,200**	**$B_2O_3(l)$**

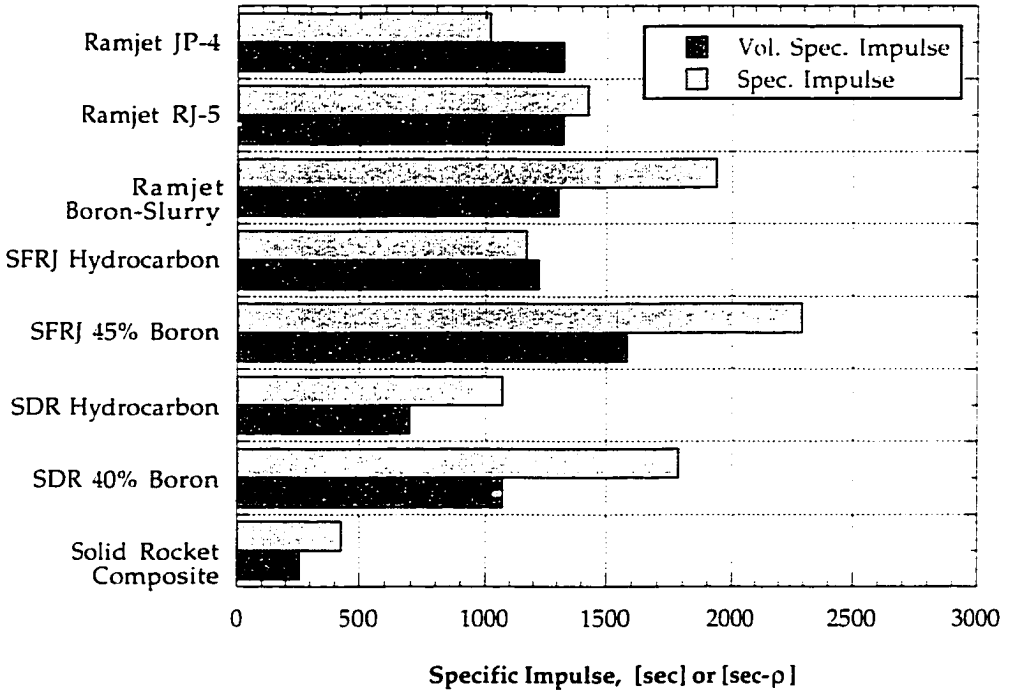

Fig. 1.1: Calculated increases in ramjet, solid-fueled ramjet (SFRJ), and solid ducted rocket (SDR) specific impulses for various boron-fuel combinations for Mach 2 conditions at sea level, from Ref. (3). Boron shows significant potential in these *air-breathing* systems.

The development of newer fluorinated oxidizers and propellants, such as difluoroamino/nitramino based oxidizers and new difluoroamino/azido oxetane binders (where $-NF_2$ groups substitute for $-NO_2$ groups in typical oxidizers), has rekindled investigation of boron-fluorine chemistry based on the potential for even greater energetics and reduced ignition delays.

In practice, the energy potential of boron has been difficult to harness due to several factors which inherently make boron particle oxidation a slow process compared to aluminum and other metallized-propellant additives. Boron ignition is hindered by a regenerating protective oxide coating which liquefies at relatively low temperatures (723 K at 1 atm) and slows oxidizer attack on the underlying nascent material. This oxide layer has a very low volatility and high temperatures are required to expel the layer (2316 K at 1 atm). In addition boron combustion is made difficult by the high vaporization temperature of boron (~4000 K at 1 atm) which generally precludes vapor phase burning and limits oxidation to slower heterogeneous surface reactions. At typical combustion temperatures, condensation of product species (B_2O_3) is a slow process which may favor product dissociation. In the presence of hydrogenated species, the products change in favor of gas phase species (HBO_2), resulting in significantly lower net energy release than suggested in Table 1.1.

These difficulties (slow ignition and combustion, incomplete energy release) generally precluded the use of boron from energetic fuels applications especially at pressures below 35 atm. Boron particles of the size range 10 to 50 μm diameter have long lifetimes at atmospheric pressures which lead to inefficient use in high speed combustion applications. In addition to these practical problems, very little is known for design purposes about the ignition and combustion behavior of boron particles at elevated pressures.

Key to understanding whether boron (or any other fuel enhancer) has a significant chance for application are several factors. These factors include: 1.) understanding the ignition and combustion behavior of the particles under a range of operating conditions applicable to the considered application; 2.) understanding the competing physical and chemical processes which may limit the full utilization of energy potential; and 3.) understanding the mitigating processes which can be used to overcoming shortfalls in performance.

1.2 Ignition and Combustion Behavior of Boron Particles

1.2.1 General Considerations for Metal Particle Combustion

In order for a material to be a candidate for a fuel or fuel additive, it must be able to ignite and burn to completion in the residence times afforded by the application. Typically in high speed propulsion applications, residence times on the order of 10 msec are available before product gases are exhausted to develop thrust. When explosive grains are considered, energy must be released to assist in the production of useful expansion or "*p-dv*" work, and available times can range from tens of microseconds to several milliseconds.

According to Price,[2] metal additives (including boron) are typically used to provide high energy density, high heat of reaction, and under some circumstances increased motor specific impulse. Some additives, such as randomly mixed 10 - 40 μm aluminum particles, also help to suppress propellant combustion instabilities. Magnesium is found to effectively neutralize the HCl in product gases of current hydroxyl-terminated polybutadiene (HTPB) solid propellants mixed with ammonium perchlorate oxidizer. In addition to these advantages, numerous problems can arise with metal additives used in propellant formulations. During propellant burn, metal particles typically melt and coalesce into small puddles on the propellant surface, not vaporizing individually due to insufficient flame temperatures, and subsequently burn more slowly as large agglomerates in the propellant products gases which typically have low excess oxidizer concentrations. This coalescence into larger droplets, which may not burn to completion, can lead to significant thermochemical and two-phase flow losses and slag formation which can clog nozzles and injector parts.

Many metallized propellant additives start with or form protective oxide coatings during ignition which further inhibit combustion. These oxide coatings may liquefy, as is the case for boron, and inhibit oxidizer attack on the underlying nascent metal. Or, the coatings may crack apart, due to different coefficients of thermal expansion between the underlying metal and oxide coating during particle heating, and become permeable to oxide attack. This later scenario is indicative of aluminum. Volatility of the metal surface and formation of a product cloud influence burning as well. Aluminum droplets vaporize and burn in a vapor cloud whereas boron is typically limited to surface burning and subsequent longer combustion times, due to its very high vaporization temperature (see Table 1.2 below).

An additional consideration is condensation of products, the lack of which can greatly reduce the energy potential if the combustion products become trapped in the gas phase. Aluminum oxide, Al_2O_3, condenses out in the product stream at typical combustion temperatures but boron oxide, B_2O_3, at temperatures greater than 2600 K may dissociate at lower pressures tying up energy in the gas phase. Condensation of products can lead to two-phase flow losses and accumulation of slag on machinery components of in nozzles. The thermochemically optimum condition for metal additive combustion may not coincide with the optimum from the standpoint of combustion efficiency and flow losses.

1.2.2 Low Pressure Boron Ignition and Combustion

Boron particle ignition and combustion is different from several more commonly known metal additives such as aluminum. The precise nature of the ignition and combustion processes is dictated by the nature of the oxidizing environment, but several general statements can be made for ignition in high temperature ambient gases. Under low temperature conditions, particles could oxidize very slowly

with little temperature rise where timescales are on the order of hours. This possibility is not of interest in this study where application to explosives and high speed combustors is considered. Of interest here is the onset of rapid particle oxidation and subsequent thermal-runaway energy release in high temperature, high pressure environments such as those produced in rocket motors, where the energetic processes lead to particle luminosity in the experiments. This is often characterized as a transition from "slow" heterogeneous reactions of the pre-ignition heating stage to "fast" heterogeneous or possibly detached gas-phase reactions marked by substantial increase in particle luminosity.

At atmospheric pressure and temperatures below 2600 K, boron particles have been generally observed to exhibit a two-stage ignition process in oxidizing environments.[4-10] The first stage is considered to consist of oxide layer removal and the second stage the re-ignition and combustion of the clean oxide-free particle. The first stage is observed to be a very luminous phase dominated by the consumption of the oxide layer coating; during this phase very little particle size change is observed[8,9] as generally the oxide layer is very thin, thought to be on the order of tens to hundreds of angstroms. Under low oxygen concentrations and at increased pressure, Macek observed this first stage often becomes indistinguishable from the second stage.[6] Other work has reported an obscuring of the separate luminous stages at increased flame temperatures.[8] The second stage directly follows the consumption of the oxide layer and consists of "clean" boron-surface oxidation in the absence of an oxide layer. It will be shown in later chapters that in the experiments conducted here, at higher pressures and lower ambient O_2 fraction, only single stage ignition is observed. Single-stage ignition (based on luminosity) was also observed by Rood[11,12] performing tests on boron behind reflected shocks at 8.5 atm in pure oxygen.

The full-fledged combustion phase follows ignition when either the particle is hot enough to purge itself of an oxide layer or when gasification by chemical reaction is fast enough to consume the layer. The combustion phase is characterized by "clean" surface oxidation where the particle temperature rises above the boron oxide boiling point, $T_{bp,B2O3}$ = 2316 K (1 atm), and the particle melting point, $T_{mp,B}$ = 2350±50 K (1 atm), and is accompanied by a second increase in luminosity generally observed as a bright green flame. The burn phase at high ambient temperatures or in pure oxygen is expected to be very hot, for example at stoichiometric proportions and 300 K initial temperature the adiabatic flame temperature calculated with an equilibrium code is ~4100 K at 10 atm pressure in pure oxygen, and then a detached gas-phase vapor burn stage can ensue.

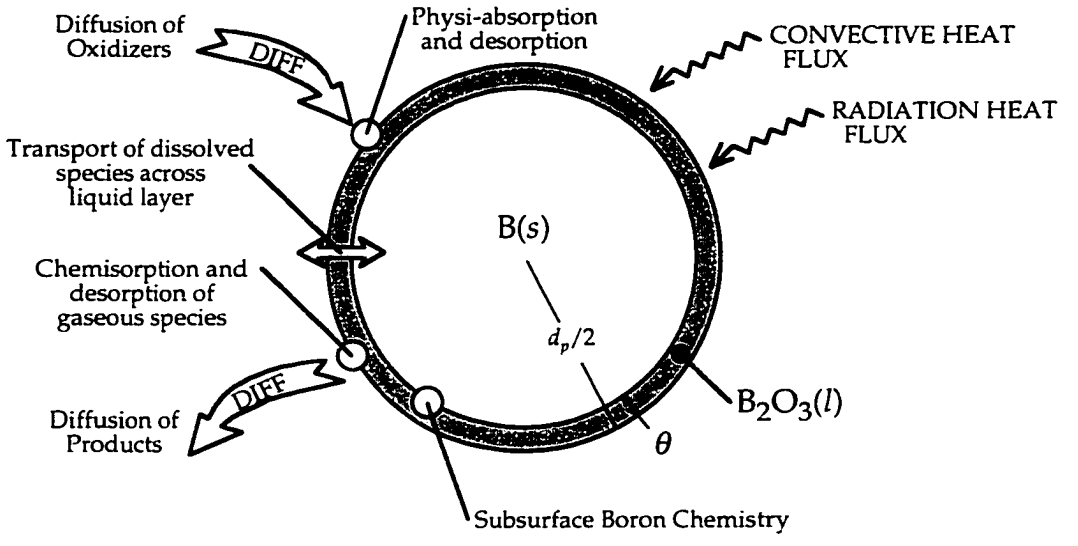

Fig. 1.2: Schematic of an idealized boron particle in a hot combustion environment.

1.2.3 Why it is so Difficult to Ignite Boron

A boron particle introduced into a hot combustion region of a rocket chamber will first be heated by convective and radiative means, as shown schematically in Fig. 1.2. At a fairly low particle temperature of 723 K at 1 atm, the oxide layer liquefies over the particle thereby hindering the attack of oxidizer on the subsurface boron. Boron particle ignition, as defined by transition to fast combustion, requires that the protective oxide coating be stripped to expose the underlying boron to the oxidizer. The main factor to particle ignition is heat-up to a high enough temperature where oxide layer vaporization and gasification by surface chemistry can occur. This temperature is generally fairly high for boron, estimated by Li[9] to be ~1650 K depending on oxidizer and other conditions and increasing as the partial pressure of oxygen increases. Once particle temperatures are high enough, gasification of the oxide layer can proceed by evaporation and/or by chemical reactions in the presence of water vapor or other hydrocarbon combustion products. In the absence of such products, the processes are generally slow and endothermic. In product gases where water vapor and hydrogen fluoride are present, chemical processes could lead to surface coating of the particle if temperatures remain low after chemistry with oxide layer ensues. Lingering surface coatings, such as condensed boron nitrides, could then further limit oxide layer removal as well as combustion under kinetically controlled combustion conditions.[13]

While the relatively cold particles are first being heated by the surrounding hot gases, the solubility of oxygen in the liquid boron oxide layer is expected to increase[9] as the partial pressure of O_2 is increased thereby initially thickening the oxide layer. Particle heating is accelerated by the exothermic reaction of this dissolved oxygen with dissolved boron in the liquid oxide layer. At low ambient temperatures, the limiting rate of $B_2O_3(g)$-product diffusion away from the particle surface[9] will slow oxide layer removal especially as pressure is increased, but at high ambient temperatures and with water vapor present there is notable dissociation of $B_2O_3(g)$ and conversion to $HBO_2(g)$.

An imbalance in the heating terms, either cooling by evaporation or endothermic oxide layer decomposition reactions, or heating from the surrounding gases or by boron reactions into sub-oxides, will dictate whether the particle fails to ignite (oxide layer thickens) or proceeds toward full-fledged combustion (oxide layer vanishes). Therefore although boron ignition is made difficult by several physiochemical processes, anything which can be done to accelerate heating rates or lower the temperature for effective oxide layer removal will have the largest effect on reducing ignition delays.

If the ambient gases or particle self-heating raise the particle temperature above 2350 K, the oxide layer will be quickly expelled and the boron particle will liquefy and there exists the process of boron droplet combustion. Boron gasification occurs by evaporation and chemical reaction with oxidizers. Boron gasification will be predominantly by heterogeneous surface chemistry since the boiling point of pure boron is so high as to preclude much boron vaporization. During the combustion stage, where "clean" boron is oxidizing in the absence of an oxide layer, competition occurs between oxidizer diffusion to the particle surface and chemical reaction on the surface. It is calculated in detailed modeling studies[13,14] that both kinetics and diffusional processes are important during combustion stage at elevated pressures. At temperatures between 2200 and 2600 K, it is possible for boron nitrides to form on the particle surface and remain there for long times, as supported by certain experimental observations.[15] Thus for particle combustion in lower temperature systems, the process of surface coating could also pose problems to boron oxidation.

A more detailed look at boron particle ignition and combustion and the underlying competing processes will be treated in later sections.

Compare this sequence for boron to that for aluminum particulate ignition and combustion.[2] Aluminum particles like boron are covered by a thin oxide layer. For aluminum the oxide layer is considered impermeable at room temperature because the oxide volume is greater than the volume of the metal from which it is formed. During heating however, the base Al metal expands more rapidly than its Al_2O_3 coating. This means the oxide layer will be stressed and crack thereby exposing nascent metal where heterogeneous reactions with oxidizer can occur. Ignition of aluminum particles is considered to occur when the melting point of the oxide (T_{mp,Al_2O_3} = 2327 K, 1 atm) is reached. Ignition

is defined as the transition from slow heterogeneous reactions of the pre-ignition heating period to the fast detached gas-phase reactions marked by a substantial increase in particle luminosity. This definition is consistent with the use of metal additives in propellants and explosives where relatively short residence times are afforded by the application.

Aluminum particles burn in a detached gas-phase regime and in only mildly convective environments the molten metal will be spherically shaped. A lobe of retracted oxide will form since Al_2O_3 has a low solubility in molten Al and also has a high surface tension, causing the molten oxide to retracts onto itself exterior to the molten Al-droplet.[2] Surrounding the droplet is a detached flame envelope in which the metal vapor and oxidizer react to form small sub-micron to 2 micron diameter condensed oxide droplets (see also recent work by Bucher, et al.[16,17]). The consumption of the metal droplet proceeds by Al evaporation followed by oxidation reaction to form Al_2O_3 which coalesces into small droplets in a cloud surrounding the particle, where the cloud is convected away from the vicinity of the droplet in convective environments. As with boron, the precise nature depends on the properties of the oxidizing atmosphere to which the particles are exposed.

1.3 Boron Thermophysical Properties

An understanding of complexities involved in boron particle ignition and combustion can be gained by a comparison of boron thermophysical properties to aluminum, where aluminum is a widely used metal propellant additive.[2] Important thermophysical properties of these two Group III elements and their respective oxide are tabulated in Table 1.2.

Firstly, boron and aluminum have greatly different oxide melting points. Whereas boron oxide liquefies at low temperature (723 K at 1 atm) and forms a barrier to oxide attack, aluminum oxide remains solid up to much higher temperatures (2327 K at 1 atm) and cracks as the melting base metal expands making the surface permeable. However this high melting temperature for aluminum oxide requires high ambient temperatures for particle ignition to occur. Secondly, the boiling point of boron oxide (2316 K at 1 atm), being ~900 K lower than that for aluminum oxide (3253 K at 1 atm), leads to evaporation from the particle surface at flame temperatures. The aluminum oxide on a particle typically retracts into a lobe on a particle and does not dissolve in its base metal. Thirdly, boron oxide typically dissociates into sub-oxides at higher combustion temperatures and low chamber pressures whereas aluminum oxide does not. Aluminum oxide in fact condenses out in the gas stream contributing significantly to the overall energy release. Compare the vapor pressures of the elements and their oxides in Fig. 1.3. Even in hydrocarbon environments, $Al_2O_3(s)$ is the preferred product whereas for

boron $HBO_2(g)$ forms and lowers overall energetics. Fourthly, boron's extremely high boiling temperature (3931 K at 1 atm) leads to very little evaporation during the combustion stage which makes heterogeneous reactions for clean surface oxidation all the more dominating for boron combustion than for aluminum, which vaporizes at 2791 K (1 atm) and typically burns in the vapor phase. Aluminum appears to have a distinct ignition temperature, 2327 K which is the melting temperature of the oxide layer, whereas boron is found to ignite over a range of temperatures which depends strongly on the oxidizer, particle diameter, and oxygen partial pressure.

Further important details of boron particle ignition and combustion are available from previous research and modeling efforts conducted to date, and these are described in the following two sections.

Table 1.2: Thermophysical properties of crystalline boron and aluminum and their oxides, B_2O_3 and Al_2O_3, respectively.

Physical Property		Crystalline Boron	Boron Oxide	Aluminum	Aluminum Oxide
ρ	[gm/cm^3] @ 300K	2.35(α) [a]	1.81, 1.85 [d,g]	2.70 [e]	3.97 [d]
k	[W/m K] @ 300 K	27.0 [c]	-	2.37 [c]	36 [h]
	600 K	10.6 [c]	-	2.31 [c]	15.8 [h]
	900 K	9.85 [c]	-	2.10 [c]	~7.9 [h]
c_p	[J/gm K] @ 300 K	1.055 [b]	0.904 [b]	0.899 [b]	0.779 [b]
	1000 K	2.311 [b]	1.733 [b]	0.995 [b]	1.224 [b]
	2000 K	2.725 [b]	1.863 [b]	1.177 [b]	1.340 [b]
T_{mp}	[K]	2350±50 [b]	723 [b]	933.4 [b]	2327±6 [b]
T_{bp}	[K]	3931 [a], 4139 [b]	2316 [b]	2790.8 [b]	3253 [d]
T_{ign}	[K]	1650 [g]	n/a	2327 [j]	n/a
H_{fus}	[kJ/mol]	50.2±1.7 [b]	24.1±0.4 [b]	10.7±0.2 [b]	111.1±4 [b]
H_{vap}	[kJ/mol]	480.3 [b]	362.04 [b]	294 [b]	-
$\Delta H^0_{f,298}$	[kJ/mol]	0.0 [b]	-1272±2 [b]	0.0 [b]	-1675.7 [b]
W	[gm/gm-mol]	10.81 [b]	69.62 [b]	26.98 [b]	101.96 [b]
α	[m/m K] 300-570 K	4.8E-6 [a]	-	25.3E-6 [j]	~7.3E-6 [k]
	[m/m K] 570-1070	6.3E-06 [a]	-	-	~7.8E-6 [k]
	[m/m K] 1070-1270	7.0E-06 [a]	-	-	~8.3E-6 [k]
ε		0.84-0.88 [a,f]	0.43 [i]	0.06-0.07 [e]	0.30 [e]
p_{vap}		see Fig. 1.3 [l]	see Fig. 1.3 [g]	see Fig. 1.3 [l]	see Fig. 1.3 [l]

[a] Reference (18)
[b] Reference (19)
[c] Reference (21)
[d] Reference (23)
[e] Reference (25)
[f] Reference (15)
[g] see Reference (9)
[h] Reference (20)
[i] Reference (22)
[j] Reference (24)
[k] calculated from data Ref. (26)
[l] Reference (27)

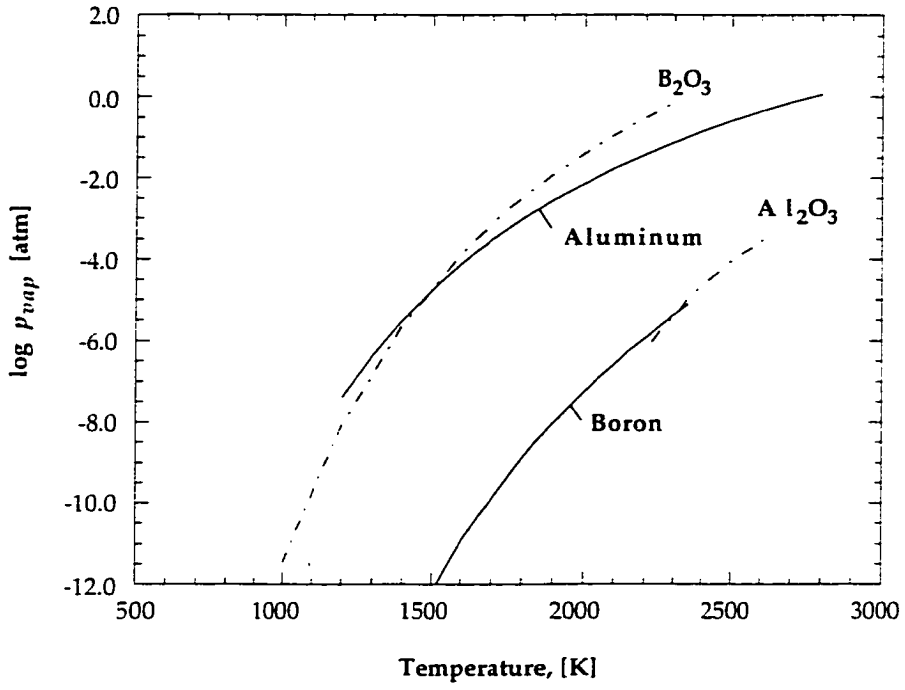

Fig. 1.3: Comparison of vapor pressures as a function of temperature for crystalline boron and aluminum and their oxides, B_2O_3 and Al_2O_3. The vapor pressure of boron is much lower than its oxide whereas the reverse is true for aluminum. The high temperature vapor pressure of boron is poorly known.

1.4 Review of Previous Research

In the following two sections a brief survey of boron particle ignition and combustion experiments and separately theoretical developments is presented. Emphasis is on particle studies since propellant additives will typically be small particles. The articles discussed will be presented in chronological order where it will be possible to highlight continuing contributions to growing knowledge of boron particle ignition and combustion behavior.

1.4.1 Survey of Experimental Boron Particle Ignition and Combustion Research

In this section previously published boron particle combustion measurements are reviewed to gain insight into boron particle ignition and combustion dynamics. Knowledge of many of the important trends measured at low pressure is required to see where possible advantages at elevated pressure and gas temperatures might be exploited. Since the interest is with combustion of metallized propellant additives, mainly small particle combustion work is reviewed, although there have been impressive

and enlightening works conducted on other specimens and on very larger particles as well. A review of more general boron combustion researches may be found in the review article by Yeh and Kuo, Ref. (10). As dictated by the application to high speed propulsion systems, where residence times may be limited to ~10 msec, particles of diameters less than 30 μm are of most interest. It is important to note from the outset that no research reporting boron particle ignition and combustion at high pressure with small particulate boron has been reported in the literature.

Macek and Semple[4] experimentally found boron ignition times in wet flat-flames to be reduced compared to dry flames between 2200 and 2900 K at 1 atm pressure. All times reported for the ignition stage consider only the time when the particles are luminous and therefore exclude the time for particle heat up. Reported times for the luminous first combustion stage for 34.6 μm diameter particles were found to decrease from 4.5 to 3.5 msec in dry flames and from 4.0 to 2.5 msec in wet flames over this temperature range. The combined quantity of oxygen and water vapor in the wet flames was roughly twice the oxygen concentration in the dry flames, however. For 44.2 μm particles in dry flames the times decreased from 5.5 to 5.0 msec. Combustion times in these atmospheric pressure flames were seen to vary approximately inversely as the partial pressure of O_2, to vary linearly as the initial particle diameter, and to decrease with water vapor present. Gas CO_2-laser ignition studies[6] at elevated pressures in cold ambient gases showed increased ignition delays as pressures were increased from 1 to 35 atm, with combustion diffusion-controlled and times decreasing as a function of pressure. The ignition result is in direct contrast to the results obtained in the present study, where there are high temperature ambient gases such as in typical combustor chambers.

Gurevich, et al.[28] measured large crystalline boron particle (50 - 260 μm) ignition delays and combustion times at 1 atm in hot gas streams containing H_2O or O_2 plus nitrogen mixed with arc heated argon. They recorded particle streak marks on film photographs and sometimes observed particles to shatter in water vapor. Some evidence was found for a transformation from surface chemistry to vapor-phase burning. Measured ignition gas temperature limits for various particle sizes are reported and it was found that this temperature in H_2O is higher than in O_2, decreases with increasing X_{H2O} or X_{O2} between 0.15 and 0.45, and decreases to larger particle sizes. Ignition delays between 1530 and 2230 K initial gas temperature in H_2O/Ar streams were generally much shorter than combustion times, and both t_{ign} and t_{comb} varied less than the initial diameter-squared. For 145 μm particles in X_{H2O} = 0.36, ignition delays decreased from 19 to 11 msec as ambient temperature was raised from 1530 to 2230 K, and combustion time remained approximately constant at 97 msec. Gas temperatures in the stream were fairly constant during ignition but decreased to 530-730 K during the particle combustion life. For 105 μm diameter particles at 1830 K initial gas temperature, combustion times decrease from 82 to 34 msec as X_{H2O} increased from 0.25 to 0.47, suggesting water vapor assists combustion as well as ignition. The observed trends for decreased ignition delays with increasing gas temperature and decreasing

combustion times with increased water vapor content agree with Macek's findings and those to be reported here. Unfortunately, particles of the size investigated by Gurevich, et al. are far too large for use in propellants or explosives. Generalizations from their observations cannot be straightforwardly extended to smaller particles and high gas temperatures.

It is widely agreed based on the low volatility of boron that surface reactions and not gas phase reactions control the particle combustion history and also dictate the mix of intermediate species which are liberated. In order to clarify some of the controlling issues, Yuasa and Isoda[29] performed ignition studies of larger boron lumps of 5 to 8 mm size in impinging oxygen streams at one atmosphere pressure where the lumps were continuously heated by a Xe lamp. Most significant in their study was the success of using optical bandpass filtering to spatially resolve and observe emissions from the BO and BO_2 molecules in the reacting mixture surrounding the boron lumps. Photographs revealed that BO formed on the liquid surface and then reacted away in the gas phase quickly, while BO_2 formed adjacent to the surface in the gas phase. The resulting combustion diagram for boron was found to be different from either magnesium or lithium, which burn as metal vapor diffusion flames, and be most similar instead to that of coal lump burning. Although this research did much to elucidate the sequence of boron oxidation, it provides little quantitative information on small particulate ignition and burn characteristics which could be used by propulsion system designers.

Li and Williams[7-9] measured boron ignition delays of very small ~0.1 μm diameter boron particles versus temperature from 1900 to 2500 K, and found a 3-fold decrease in delays from 5.8 to 1.6 msec at 1 atm.[9] Ignition delays were found to be insensitive to ambient oxygen concentration. The small-particle data, where particle lifetimes are predominantly ignition delay, were used assuming one-step Arrhenius ignition theory to extract the reaction rate constant for boron full-fledged combustion as a function of temperature. Ignition delays of 7 and 10 μm boron particles were found to decrease as a function of temperature between 1900 and 2050 K[7] and to be independent of ambient oxygen concentration.[8] Combustion times of these larger particles were measured and found to decrease significantly with increasing oxygen partial pressure from 0.25 to 0.63 atm. Combustion times were found to be independent of ambient temperature, vary inversely as O_2 mole fraction, and increase linearly with increasing initial particle diameter. Mie scattering measurements showed that particle diameters decreased linearly with time during the combustion stage, suggesting surface kinetics-controlled combustion under those conditions.

Yeh and Kuo[10] conducted experiments on ~3 μm boron and magnesium-coated boron particles at lower temperatures in atmospheric pressure flames to study boron particle combustion dynamics under kinetically-controlled combustion conditions. They found small-particle (~3 μm) ignition delays, where t_{ign} is the sum of t_i and t_1 defined in Ref. (10), for boron to decrease with increasing temperature

between 1770 and 1990 K, to decrease weakly with increasing ambient oxygen mole fraction between X_{O_2} = 0.18 and 0.28, and to decrease strongly in the presence of water vapor. No ignition delays were reported for the Mg-coated particles, but up to 5% Mg coating produced a noticeable decrease in particle combustion times at the lower temperature. In addition they carried out a low temperature study in an oven to investigate boron dissolving in its oxide layer. It was concluded that production of boron oxides during the ignition stage is controlled by boron dissolving in the oxide layer and molecular transport outward through the oxide layer rather than by oxygen diffusion inward toward the boron substrate. Using rate parameters extracted from their study and extending the Li and Williams model, they predict small particle ignition delays near 1800 K to be a strong function of pressure up to 10 atm and to be essentially independent of pressure at higher pressures. The data presented here show that ignition delays at high temperature in fact continue to decrease as pressure is raised up to 150 atm.

Krier, et al.[30] have studied boron ignition in a shock tube at pressures up to 34 atm and have provided further evidence of the ignition-enhancing effects of water vapor and fluorine. Although test times were too short (less than 900 μsec) to study the entire ignition process,[11] results from the shock-initiated combustion of ~24 μm boron particles indicate that increasing the pressure from 8.5 to 34 atm leads to a reduction in the time for the onset of oxide layer removal over the temperature range of 2200 to 3000 K in pure oxygen. Water vapor (30%) in oxygen only marginally shortens the onset of oxide layer removal at ambient temperatures above 2600 K at 8.5 atm, whereas traces of fluorine in oxygen significantly reduce this time between 1400 and 2700 K at 8.5 and 34 atm, when compared to pure oxygen alone. Hydrogen fluoride (HF, 6 and 12%) added to oxygen did not alter the onset of oxide removal between 2500 and 3100 K at 8.5 atm.

More recent tests in the same shock tube facility using smaller particles were conducted by Rood, et al.[11,12] in 100% O_2 mixtures. Particles of ~1 μm, 7.2 μm, and 11.8 μm were ignited behind the reflected shock where ignition was monitored via emissions in the infrared bandpass-filtered at 5.0 ± 0.15 μm, corresponding to B_2O_3 molecular bands, and simultaneously in the visible at 546.1 ± 4 nm for the BO_2 molecular band. Rood observed that infrared emissions attributed to B_2O_3 lead BO_2 emissions by ~250 μsec for the two larger particle sizes (and only 10 μsec for ~1 μm particles), suggesting that B_2O_3 removal precedes BO_2 molecule liberation from the gasifying oxide layer. Interestingly, the peak B_2O_3 emissions closely corresponded to the point of ignition based on the measured visible signal. Over a limited temperature range between 2500 and 2700 K, the 7.2 μm boron particle ignition delays determined from the visible signal decrease from 770 to 580 μsec and the 11.8 μm particle delays from 760 to 720 μsec. A sharp decrease in delay time for the 7.2 μm particles between 2400 and 2500 K was observed, in agreement with observations by Macek and in this study (to be discussed in Section 3.12). It is obvious that particles of these sizes are suitable for propellant applications, although unfortunately only tests in pure oxygen were conducted. From the measurements it was determined that ignition

delays vary as $d_p^{1.4}$ and $d_p^{1.5}$, as determined from the infrared and visible signals respectively, at 2550 ± 100 K and 8.5 ± 0.5 atm which agrees well with predictions from detailed modeling.[13] Under the conditions studied both oxidation kinetics and oxidizer diffusion control the overall oxide layer removal.

The previous measurements at atmospheric pressure described above provide keen insight for further research efforts and a necessary database of boron particle ignition and combustion behavior. Many of the present theoretical modeling efforts to be described briefly below have been guided by details gleaned from the described investigations. The measurements also provide a useful tool for validating particle combustion models. One stark truth evidenced from the various experimental efforts is that boron particles take a long time to ignite and that particle lifetimes are long. It appears that operation at elevated temperatures, with water vapor, and with small particle sizes reduces ignition delays. Additional measurements at intermediate pressures[11,30] and typical combustor chamber temperatures have pointed out the behavior at pressures more suitable to rocket chamber and propellant applications. These studies in hot ambient gases have shown that operation at elevated pressures, in addition to certain gaseous compounds such as fluorine, lead to reduced ignition delays in line with requirements of high speed propulsion systems.

No small particle ignition delay and combustion time data are available however at high pressure in mixtures containing both water vapor and hydrocarbon combustion products, with little excess oxygen, and at temperatures much above 2600 K. Many of the issues remaining unresolved due to lack of basic ignition delay and combustion time data are investigated and addressed in the present study, as will be outlined in Section 1.6 below. The experimental trends discussed above will be compared in detail to newer measurements at high pressure and high temperature.

First, however, a brief overview describing previous modeling efforts is given to gain an appreciation of and further insight into the complex processes dictating rapid boron particle ignition and oxidation at high temperatures. This is the topic of the next section.

1.4.2 Survey of Theoretical Boron Particle Ignition and Combustion Research

Detailed surveys of previous theoretical modeling efforts are beyond the goals of the present work. Good surveys of previously published modeling efforts are available from King[1,31] and Yeh and Kuo[10]. Here several studies are described for the purposes of gaining a further understanding of the processes involved in boron particle ignition and combustion.

Most of the models developed are similar in the way the competing physical processes are considered during the ignition stage, see Fig. 1.2, the main differences then being in the handling of chemical processes and the reaction rate expressions which couple the energy and mass transport processes, in handling of diffusional processes, and in the subsequent solution technique for solving the set of governing equations. In general, at first there is a heat up stage where particles are being heated by convective and radiative fluxes from the hot ambient surroundings. This heating is augmented above 1500 - 1800 K by particle self-heating from exothermic oxidation reactions. Oxygen for this exothermic process must diffuse to the particle surface where it is absorbed and can diffuse inward through the oxide layer to subsurface boron while at the same time boron may dissolve in the boron oxide layer and diffuse outward toward the gas. Oxidation of dissolved boron causes the oxide layer to thicken but at the same time this layer is being consumed by evaporation and product diffusion away into the gas phase, at a rate which depends on particle temperature. If the particle temperature rises enough, thermal runaway is generally assumed to rapidly expel the remaining oxide layer and full-fledged combustion ensues. In water vapors, the H_2O is considered to react with the oxide layer exothermically and produce gaseous HBO_2 product, assisting with overall oxide layer removal.

As shown in Fig. 1.4, the chemical processes which are important to boron ignition are oxidation reactions at the liquid oxide layer/gas interface, where gaseous species are absorbed and boron and boron suboxides are released into the gas phase, oxidation reactions at the subsurface boron/boron oxide interface, and water vapor oxide layer removal-enhancement. Gasification can also occur by evaporation of the boron oxide liquid layer. The various models to be discussed vary in the approach to formulating the chemistry and diffusional competitions at and between the various interfaces, as shown in Fig. 1.4. Similar mass and enthalpy balances are used in the models to obtain the time dependent equations for change in oxide layer thickness, particle radius, and particle temperature. In some models these equations are integrated once chemical reactions and rates are defined while in others limiting cases are analyzed using gross simplifying assumptions.

The early particle model of Mohan and Williams[32] is a two-stage model which considers oxide layer removal separately from full-fledged combustion. Equilibrium vaporization of B_2O_3 is assumed and diffusion of $B_2O_3(g)$ away in the gas phase is considered rate limiting. Oxygen is assumed to diffuse inward across the liquid oxide layer to react exothermically with the underlying boron either balancing or exceeding cooling by evaporation. Use is made of stationary states (quasi-equilibrium) analysis applied to the particle energy (temperature) and oxide layer thickness equations, allowing stability analysis by linear perturbation of the equations to be performed without directly solving the system of equations numerically. This type of analysis breaks down at higher pressure according to review by King,[31] and does not lead to information on ignition delay times.

The combustion stage model assumes boron reacts with oxygen at the surface to form $B_2O_2(g)$ which diffuses away and reacts to form $B_2O_3(g)$ in a detached flame sheet. The boron droplet burning problem is formulated similarly to hydrocarbon droplet combustion in terms of a transfer number, B, where the surface burning rate is given by $\dot{m} = (\overline{\rho D}/r_p)\, ln(1+B)$. In order to solve the set of equations analytically, it was assumed that the burning stage droplet temperature is fixed at 2500 K and that boron droplet burning is diffusion-controlled. Condensation of oxide products and enhancement from water vapor are neglected. The simplified model does not contain an explicit pressure dependency in the formulation.

Mohan and Williams obtained agreement between model predictions and dry-flame data only for larger particles in ambient gases hotter than the boiling temperature for the oxide, conditions where the simplifying assumptions hold the best. This early modeling effort points out that such simplifying assumptions lead to poor predictive capabilities in the general case.

The King model[1,31] like previous models considers the boron particle oxidation process as occurring in two stages where the first stage is particle ignition, which consists of particle heating and subsequent oxide layer removal, and the second stage is combustion, where the "clean" oxide-free boron surface is oxidizing. Both stages are viewed as consisting of multiple step chemical and diffusional processes, where during combustion the major heat release is modeled to occur in the vapor phase in a detached reaction zone.

During particle ignition, oxide evaporation and diffusion away from the surface into the ambient gases compete with oxide production from the subsurface boron. King models the oxide evaporation process with a kinetic rate instead of assuming liquid-vapor equilibrium, as was done by Mohan and Williams. Boron oxide is produced by chemical reactions with oxygen molecules which must first dissolve into the molten oxide layer and diffuse across the molten layer to the subsurface boron. The overall subsurface boron oxidation process is viewed as a series of resistances, between O_2 diffusion inward through the liquid layer and chemical oxidation at the boron surface, as shown in Fig. 1.4. The overall process, $B(s,l) + 3/4\ O_2(g) \rightarrow 1/2\ B_2O_3(l)$, is assumed rate-limited by the diffusion of O_2 through the liquid layer. The subsurface boron reaction and boron oxide layer removal can be enhanced by water vapor, which reacts exothermically with $B_2O_3(l)$ to produce $HBO_2(g)$ or $H_3B_3O_3(l)$ within the liquid layer, thereby converting non-volatile $B_2O_3(l)$ to volatile $HBO_2(g)$.

The combustion stage is modeled as the reaction between boron and gas phase B_2O_3 at the droplet surface to form the two suboxides $BO(g)$ and $B_2O_2(g)$, where the $B_2O_2(g)$ diffuses outward toward a flame sheet where it oxidizes further into $B_2O_3(g)$. The overall exothermicity is assumed to come from this flame sheet oxidation process. The burn stage is modeled as being rate controlled by the diffusion of O_2 to the flame sheet.

The resulting system of equations is integrated numerically once the chemical production rates and diffusional rates are specified. King finds that for ignition, if B_2O_3 evaporation controls oxide layer removal (which can only occur for high particle temperatures) then ignition delays (t_{ign}) should be dependent on pressure since evaporation is enhanced at higher pressure. Otherwise the model suggests ignition delays are weakly dependent on pressure at best. Comparison of model predicted first stage combustion times (t_1, ignition delay less the particle heat up times) to Macek's flame studies shows adequate agreement as a function of ambient temperature, but the model predicts too-large of a temperature dependence below 2400 K, does not predict the sharp decrease in times near 2450 K, and over-predicts the subsequent decrease with increasing temperature above 2600 K. Combustion times in cold ambient gases (Macek's laser-ignited particles) are modeled very well for larger particle sizes, following a d_p^2-law, but not so well for smaller sizes and higher ambient O_2-concentrations where chemical kinetic effects set in and the model begins to break down. The model unfortunately has not been extensively exercised against burn time data at high ambient gas temperatures.

Li and Williams[7-9] developed a boron particle ignition and combustion model which is fully described in Chapter 4 and which has been chosen in this study as one of two approaches for making predictions at elevated pressures. Li and Williams propose that it is not the O_2-diffusion process across the oxide-layer which is rate dictating during oxide layer removal but rather the equilibrium dissolution of boron in the liquid layer and outward transport of dissolved BO. Based on this premise, a five-step ignition model is developed, where first boron dissolves in the oxide layer to form a vitreous BO-BO-BO complex, then diffuses outward to react exothermically with absorbed oxygen and water vapor to form $BO_2(g)$ and $HOBO(g)$ at the outer particle surface, where reactions between dissolved boron sub-oxides within the oxide layer and with dissolved oxygen and water vapor take place, followed by the formation of $B_2O_3(g)$, and evaporation and diffusion of this product outward in the gas phase. Based on an extracted burn rate parameter from their own experimental study with ~0.1 μm diameter particles, they were able to propose a global reaction rate constant for boron oxidation at high gas temperatures. In this formulation several competing chemical kinetic and diffusion processes are treated as series resistances precluding assumptions on the dependency over a range of conditions. The equations are numerically integrated after stipulation of diffusion and other thermophysical parameters and can be exercised to determine time-resolved oxide layer removal and particle temperature profiles.

The burn stage model proposed by Li and Williams considers particle gasification by oxidation where the competition between gas-phase diffusion of an oxygen molecule to the surface and chemical reaction at the surface to produce $B_2O_2(g)$ are included, but particle melting and boron vaporization at high flame temperatures are neglected. It is assumed that oxidizer diffusion and reaction at the surface occur in series, and based on reasonable simplifications for parameters varying only weakly

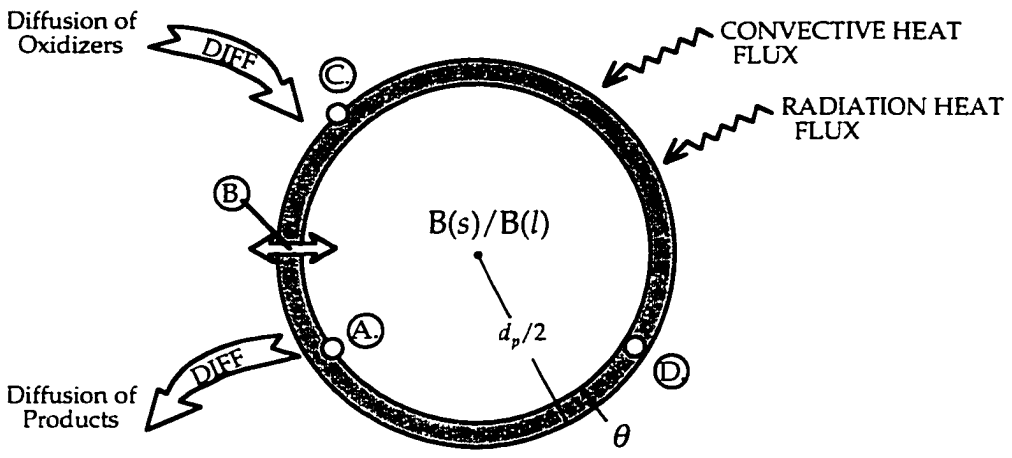

PARTICLE IGNITION STAGE

	King Model	Li and Williams Model	Yeh and Kuo Model
A.	$B(s,l) + \frac{3}{4} O_2(g) \rightarrow \frac{1}{2} B_2O_3(l)$ $\frac{4}{3} B(s,l) + \frac{1}{3} B_2O_3(l) + H_2O(g) \rightarrow \frac{2}{3} H_3B_3O_3(g)$ $\frac{2}{3} B(s,l) + H_2O(g) \rightarrow \frac{1}{3} B_2O_3(l) + H_2(g)$	dissolution process, $B(s) + B_2O_3(l) \leftrightarrow 3\ BO(d)$	dissolution process, $B(s) + B_2O_3(l) \leftrightarrow \frac{3}{n} (BO)_n(l)$
B.	$O_2(g)$ diffusion inward	$BO(d)$ diffusion outward $O_2(g)$ diffusion inward at low T_p	$(BO)_n(l)$ diffusion outward
C.	$B_2O_3(l) \rightarrow B_2O_3(g)$, vaporization $B_2O_3(l) + H_2O(g) \rightarrow 2\ HBO_2(g)$	$B_2O_3(l) \rightarrow B_2O_3(g)$, vaporization $B(s) + O_2(g) \rightarrow BO_2(g)$ $\frac{4}{3} B(s) + \frac{4}{3} B_2O_3(l) + 2\ H_2O(g) + O_2(g) \rightarrow 4\ HBO_2(g)$	$\frac{2}{n} (BO)_n(l) \rightarrow B_2O_2(g)$, vaporization $B(s) + O_2(g) \rightarrow BO_2(g)$ $\frac{4}{3} B(s) + \frac{4}{3} B_2O_3(l) + 2\ H_2O(g) + O_2(g) \rightarrow 4\ HBO_2(g)$
D.	layer is $B_2O_3(l)$	layer is solution of $BO(d)$ in $B_2O_3(l)$	layer is solution of $(BO)_n(l)$ in $B_2O_3(l)$

Fig. 1.4: Comparison of chemical schemes employed in several boron particle ignition and combustion models which make use of semi-global chemistry.

with temperature, an analytical expression for the burn time of small particles could be derived explicitly in terms of the sum of diffusion and kinetic timescales.

The burn stage model proposed by Li and Williams considers particle gasification by oxidation where the competition between gas-phase diffusion of an oxygen molecule to the surface and chemical reaction at the surface to produce $B_2O_2(g)$ are included, but particle melting and boron vaporization at high flame temperatures are neglected. It is assumed that oxidizer diffusion and reaction at the surface occur in series, and based on reasonable simplifications for parameters varying only weakly with temperature, an analytical expression for the burn time of small particles could be derived explicitly in terms of the sum of diffusion and kinetic timescales.

Agreement between the model predictions and Macek's flame data and laser-ignited particles in cold atmospheres shows good agreement,[9] but the model predicts both ignition delays and combustion times to become independent of pressure above ~30 atmospheres for particle sizes of interest to this study at high ambient temperatures.

The boron particle ignition and combustion model of Yeh and Kuo[10] is similar in many respects to the Li and Williams model but it considers slightly different chemistry and diffusional transport (see Fig. 1.4). During the ignition stage where the oxide layer is being removed, Yeh and Kuo argue that it is not $B_2O_3(l)$ which is gasified but instead $B_2O_2(g)$ which is liberated from the vitreous liquid oxide layer. Boron is considered to dissolve in the $B_2O_3(l)$ layer, similarly to the way Li and Williams propose, to form a complex which gasifies at the oxide layer/gas interface as $B_2O_2(g)$, where the rate of $B_2O_2(c)$ evaporation is taken to be the rate of diffusion outward away from the particle surface into the ambient gas. In addition, a series of in-solution reactions also converts boron to partially oxidized intermediates, starting with dissolution in the liquid layer, net outward transport of $(BO)_n(l)$ units to react at the gas interface with oxygen molecules (the rate limiting step, as in Li model), and rearrangement of bonds to produce $B_2O_3(l)$, net oxide layer build up, and $BO_2(g)$, resulting in net gasification. Water vapor ignition-enhancement is treated similarly to Li and Williams with slightly different underlying fundamental chemistry, starting with the reaction of $(BO)_n(l)$ with H_2O to form $HOBO(g)$, the rate limiting step, and several fast absorbed species interaction reactions which effectively split a water vapor molecule and recombine the parts with BO to form $HBO_2(g)$. The overall reaction is exothermic and concurrently removes boron and boron oxide from the particle by producing gas-phase products. The governing system of equations, where the effect of oxide layer thickness is included explicitly in the equations to relax the stipulation of Li and Williams model that the layer remain thin throughout ignition, is then solved numerically for the first stage combustion time which includes the time to remove the oxide layer and to melt the particle, but excludes the particle heat up time.

The "clean" surface oxidation or burn stage model is similar to that of Li and Williams where again the underlying chemistry has been reevaluated and additional elementary reactions proposed. The overall reaction and rate are the same as for Li; the oxidation of a B(*l*) producing B_2O_2 in the gas phase. The competition between gas-phase diffusion of an oxygen molecule to the surface and chemical reaction at the surface are considered and particle melting and boiling are neglected. By approximating diffusive terms and using the temperature independent rate constant obtained by Li, the equation for the change in particle size (boron mass balance) is integrated analytically to obtain an algebraic expression for the combustion time, as the sum of two terms which are the kinetic-controlled contribution and the diffusive term. Similar Damköhler number analysis as that performed by Li suggests that combustion of ~24 μm particles at high pressure (30 -150 atm) should be O_2-diffusion controlled.

The model predicts ignition delays and combustion times from Macek's flame experiments very closely. From Yeh's analysis for small ~3 μm particles at the low temperature of 1800 K, boron particle ignition delays are predicted to become independent of pressure above ~10 atm, be independent of O_2, and be independent of H_2O molar-concentrations above 30% H_2O. The high pressure data of this study for larger particles will show that at high temperatures (2400 K - 2850K) ignition delays are in fact a strong function of pressure.

A-priori assumptions concerning rate limiting chemical and diffusional processes and subsequent simplification of complex chemistry into semi-global schemes limit the extent of applicability of semi-global ignition and combustion models developed for boron particle combustion. These models have been developed using inputs for chemistry and diffusion parameters based on low pressure studies, and like any good engineering works, have been tailored through the choice of these inputs to produce agreement with low pressure data. Up to now no high pressure data has been available for extension of these models to other conditions. However, since kinetic mechanisms within the particle oxide layer and at liquid and gas interfaces cannot be neglected, more chemical and diffusional detail is required.

An attempt to address the complex competing chemical and physical interactions which control boron particle ignition and combustion on an elementary chemical reaction level for the general case is being pursued by a group of researchers at Princeton University and Aerodyne Corp., who have been assembling a detailed chemistry and multi-phase molecular transport model.

The Princeton/Aerodyne model has been developed in stages to address individually various physical and chemical processes involved in particle ignition and combustion. These processes include: oxidation reactions among gas-phase species and boron gas-phase products (Yetter, et al.[33,34]); heterogeneous ignition-stage reactions on the liquid oxide surface including elementary physical and chemical absorption, desorption, and surface complex rearrangement reactions[35,36] applied to gasifying

$B_2O_3(l)$ droplets and boron droplets; dissolved species liquid-phase transport in the oxide layer; and subsurface chemical reactions. Modeling of the combined oxide-coated and subsequent "clean"-surface boron particle scenario in hydrocarbon environments[14,37] has more recently been extended to include fluorine species chemistry[38-40] and nitrogen chemistry[13] with the oxide layer and the "clean" boron surface, processes which are important for boron burning in propellant product gas environments. The formulation makes minimal pre-assumptions about rate-limiting processes and allows determination of competing processes and sensitivities to the input rate expressions over a range of generalized operating conditions. A drawback of the model to date is the dearth of either measured or calculated fundamental reaction rate constants, most of which must be estimated instead. Nevertheless, the detailed formalism provides a mechanism to determine which reactions are critical steps and must therefore be investigated more closely.

The Princeton/Aerodyne Model has been exercised successfully to model Macek's flame data and Yeh and Kuo's measurements at 1 atm and shows good agreement with the data.[14] In addition the model has been used to model the high pressure ignition delays and combustion times measured in this study[41] and further investigate competing processes during the ignition stage. The model shows agreeable comparisons in several areas over the range of conditions which are studied.[13]

Much research has been conducted at low pressures to elucidate the processes controlling particle ignition and combustion at typical combustion temperatures. Experiments and theoretical modeling to date have shown that boron ignition is an extraordinarily complex process, which involves the balancing of dissolved species chemistry, multi-phase diffusional transport, heterogeneous chemistry at several interfaces on the particle, and gas-phase chemistry and species transports. Although the competing physical and chemical processes are sufficiently well understood to allow boron models to accurately predict and mimic experimentally determined trends at low pressure, there is great uncertainty in extending these predictive capabilities to high pressure. Typically current models predict ignition delays to become independent of pressure above ~10 to 35 atm.[1,9,10] Since interest has branched into using boron for explosive grain additives, where conditions are undoubtedly at higher temperatures and pressures than in propulsion applications, it has become crucial to study the ignition delay and burn characteristics of boron particles at higher pressures and temperatures than previously reported. There is virtually no experimental data at elevated pressures, especially data where ignition is caused by high temperature reactive gases, conditions representative of combustor chambers, or explosives conditions.

1.5 The Role of Boron Particle Ignition-Enhancers

A review of previous research and related modeling efforts reveals that small boron particle lifetimes are fairly long compared to residence times in high speed propulsion devices. Since the outset of boron particle investigations, techniques have been proposed to alleviate this problem by enhancing particle ignition and combustion. These include use of gas-phase ignition-enhancers such as certain halogens which appear in propellant product gases (F_2, Cl_2, and HF, HCl), thin metal coatings of Mg or Ti, and particle impregnation with Ti or LiF. As will be shown here, operation at elevated pressures also reduces ignition delays.

The use of metal coatings is based on the premise that these coatings will readily ignite and provide additional particle surface heating to assist with boron oxide layer removal. Magnesium, titanium, and zirconium coatings have received attention[1,42] in this regard. Chemical impregnation of the boron particle with titanium or lithium fluoride (LiF) works on a chemical basis instead of by enhanced energetics,[42] where the coatings assist with oxide layer removal by decomposing in the presence of the oxide, via $B_2O_3(l)$ + LiF(l) –> $LiBO_2(l,g)$ + OBF(g) for example. A further discussion of these effects is reviewed in Ref. (10).

Certain gaseous species react exothermically with the liquid boron oxide layer, increasing particle heating and assisting oxide removal, and thereby reducing particle ignition delays. Fluorinated propellant gas-phase products show the most promise for providing chemically assisted ignition-enhancement since fluorine reactions with the oxide layer and the underlying boron produce greater overall energy release. Several theoretical studies[9,14,36] and more recent experimental findings[30,43] have warranted re-examination of these oxide layer removal-enhancing agents toward reducing boron ignition delays.

Although small quantities of fluorine (~6%) produced by the shock dissociation of SF_6 in oxygen mixtures were seen to hasten oxide layer removal compared to pure oxygen,[30] no such decrease was observed with hydrogen fluoride in oxygen. Smolanoff, et al.[43] have found that HF is quite reactive with boron oxide clusters in cluster beam experiments, but reactivity decreases as temperature is increased and falls off sharply as surface hydrogen-speciation increases. It was further reported that boron clusters show little reactivity with HF and that the reaction requires a significant activation energy. Newer experiments are reported here in an attempt to further elucidate the effects of HF on a macroscopic scale.

1.6 Thesis Research Objectives

Much of the previous research involving either atmospheric pressure flames or laser initiation in cold gases has indicated fairly lengthy boron particle ignition delay times on the order of 2 to 10 milliseconds[6] for particles of mean diameter of 34.5 to 44.2 μm and between 1 and 10 milliseconds for particles of 7 to 10 μm size in moist flames.[7] These ignition delays coupled with long burn times between 3 and 20 msec lead to very long particle lifetimes which would preclude the use of even small particles in high speed propulsion devices. Unfortunately these atmospheric pressure flames where gas temperatures were mostly below 2600 K are not representative of propellant applications and further study at elevated pressure and high temperature are needed. To make matters worse many theoretical models predict that operation at higher pressures produces no improvements in boron particle ignition and combustion.

Toward the goal of extending the experimental boron combustion database and understanding boron particle ignition and combustion at conditions more representative of propellant and explosion conditions, new experiments are performed at higher pressures than previously reported and at high ambient temperatures. Particle experiments at elevated pressures are conducted in the products of nitrogen-diluted premixed hydrogen/oxygen gas combustion at constant volume in an enclosed combustion bomb. In this system the high temperature and high pressure conditions for particle study are provided by rapid gas-phase chemical reaction. Although the shock initiation technique is ideal for particle studies, since pressure and temperature equilibrate essentially instantaneously behind the shock front and gas compositions, pressure, and temperature can be easily and independently varied,[11,24,30,44-47] the high pressures required for this study precluded the use of shock dynamics which could be produced in a feasibly sized shock tube facility.†

In this work the ignition and combustion of particulate crystalline boron are investigated experimentally to measure ignition delay and combustion times over a range of pressures higher than reported previously, specifically between 30 to 150 atm, to study and document the effect of pressure on these variables. The experiments are conducted at high temperatures (2400 to 2850 K) for several excess but low oxygen concentrations (5 to 20%) on nominally 24 μm particles. Test mixtures contain excess oxygen plus water vapor, OH, nitrogen, and nitrogen compounds such as NO, which are typically found in propellant combustion products. The newer data are compared to previous determinations at lower pressures and to the predictions from two boron ignition models. It is not the intent here to develop new models but rather to evaluate predictive capabilities of existing models at high pressure and

† The shock tube in the UIUC Shock Tube and High Pressure Combustion Lab is capable of producing reflected shock conditions up to 34 atm and 3400 K. Pressure limitations in the driver section, condition p_1, preclude tests at higher reflected shock pressures.

temperature. Particle size effects (10-50 μm) and the influences of two proposed ignition-enhancing agents (CO_2, HF) are also studied. With these newer data, the range of pressures under which particle tests have been documented has been significantly expanded, as shown in Fig. 1.5.

This work represents a direct contribution to the boron and metal particle combustion field. A new experimental injection technique is described which allows for small particle ignition and combustion to be studied at high pressure and temperature. The technique involves rapid injection of the particles after sufficient delay to allow gas-phase combustion transients to equilibrate in the chamber so that particle ignition and combustion dynamics can be measured at nearly constant pressure and temperature conditions. To the author's knowledge this is the first study where boron particle ignition and combustion times are measured at pressures up to 150 atm at high ambient temperatures. The effects of increased pressure operation and proposed gas-phase ignition-enhancers are investigated for crystalline boron particles where the methodology can just as easily be applied to the study of metal-coated or chemically-impregnated particles.

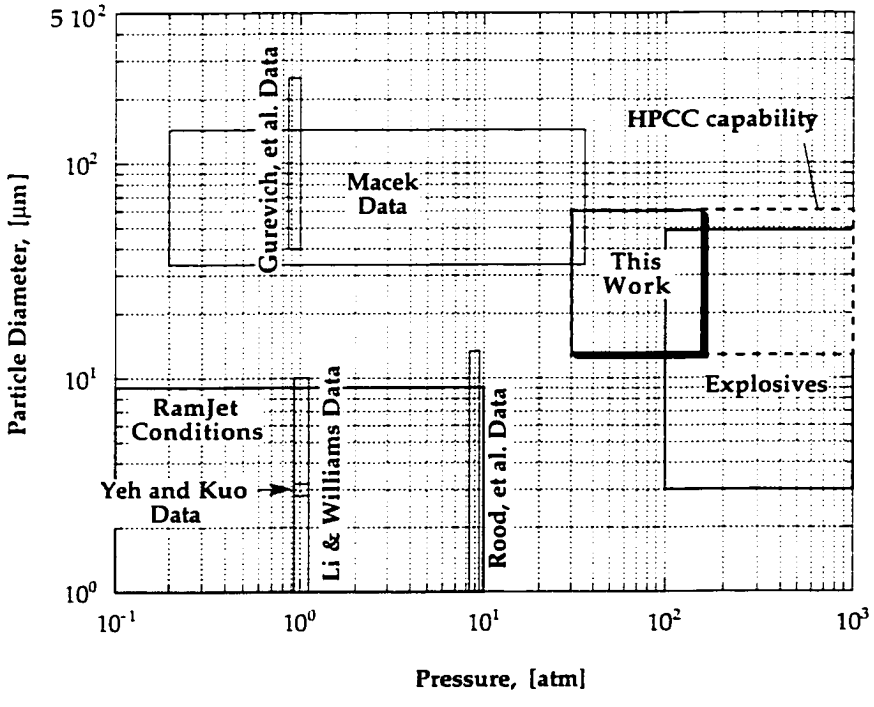

Fig. 1.5: Range of conditions for which boron particle combustion data exist highlighting the contributions of the present study. The dashed box represents the capability of the high pressure combustion chamber facility developed as part of this work.

2. EXPERIMENTAL FACILITY

2.1 Discussion of Experimental Technique

In this study boron particle ignition and combustion are investigated at high temperature and high pressures formed by the spark initiated combustion of nitrogen-diluted premixed hydrogen/oxygen mixtures in a constant volume combustion chamber. This technique is suitable for very high pressure combustion studies in that final pressure is only limited by the fill pressure and strength of the pressure vessel; a 6 - 8 fold increase in pressure is easily achieved without reliance on detonations or shock physics. The reflected shock technique used in related studies at intermediate pressure[11,30,44,46] is not capable of producing the hundreds of atmospheres pressure anticipated in the present and future studies in a cost effective manner. Unlike the shock initiated particle ignition technique however, where the rise in ambient pressure and temperature is on the order of a microsecond, in the combustion chamber the establishment of quasi-steady conditions takes several milliseconds. Consequently, in order to avoid particle combustion during gas-phase ignition transients, a novel particle injection technique has been developed where the particles are injected into the hot ambient gases after a sufficient time delay.

The experimental process is illustrated schematically in Fig. 2.1. An initial combustible gas mixture is metered into the chamber and allowed to mix for 10 minutes after which it is ignited by a spark discharge. The resulting expanding combustion front is unsteady in nature, but the final test

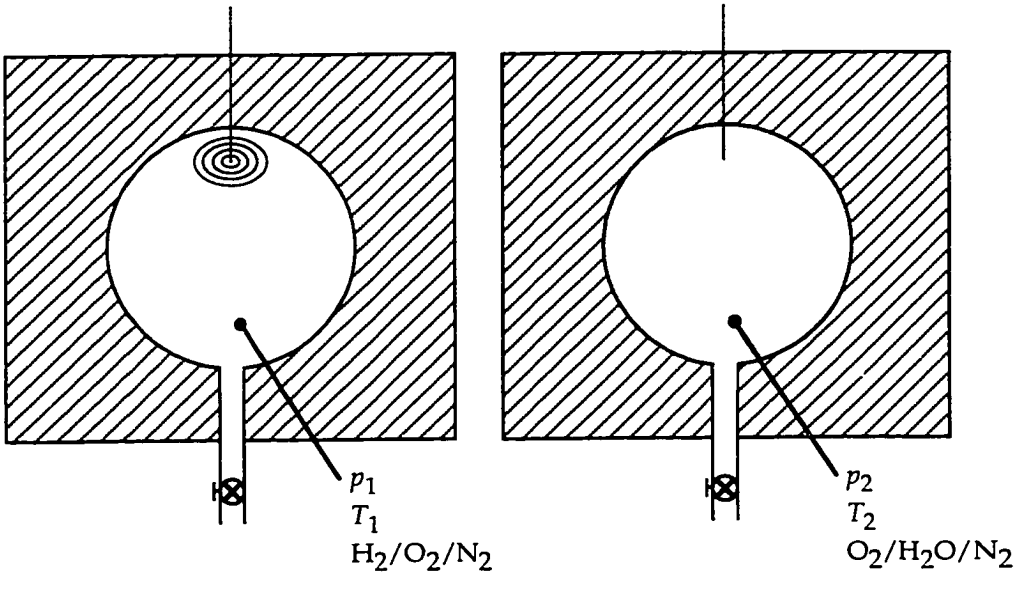

Fig. 2.1: Idealized constant volume combustion initiated by spark ignition source. State "1" is the initial undisturbed mixture and state "2" after fuel plus oxidizer have been converted to products. The gas-phase combustion process is assumed adiabatic.

conditions can be estimated by constant volume combustion relation if heat losses are neglected. The initial conditions are treated as state "1" and final conditions, after the expanding combustion front and transients have died down, are referred to as state "2". State "2" is not constant because of subsequent heat losses to the chamber walls but is seen to be quasi-steady and ideal for studying the ignition and combustion of small particles such as those of interest here. The slowly time-varying conditions are referred to as p_∞ and T_∞. Test mixtures typically reach peak combustion pressure within 1 to 4 msec, the longer times occur when large nitrogen dilution is used to provide low combustion temperature.

A measured pressure signal from a typical experimental condition is shown in Fig. 2.2 a. In the figure spark ignition of the initial gas mixture occurs at approximately -0.5 msec followed by the pressure rising in the combusting mixture (t_{pr}), reaching a peak, and then decaying slowly. The total test time or stay time (t_{ps}) is determined by the degree of pressure fall-off which is determined acceptable ($t_{ps} \approx 10$ msec). The oscillations in the pressure signal are thought to be from sound waves ringing in the metal transducer housing and chamber itself, and not pressure oscillations in the gas-phase. The frequency of this noise is 4.00±.05 kHz and is independent of initial chamber pressure and mixture stoichiometry for those mixtures where the ringing occurs. In Fig. 2.3, a filtered photodiode signal of net-particle emissions (to be discussed in Section 3.3) is shown where the particles were mounted on a sting exposed to the advancing combustion front. According to interpretations of the collected emissions, it is seen that particles ignite before ambient pressures peak. During this time the initial gas mixture is still being combusted and conditions in the chamber are very non-uniform and ill-defined globally up to the time when quasi-steady conditions are reached. It was determined from preliminary particle experiments that measurements and interpretations under such conditions were incompatible with goals of the study. This led to the development of a particle injection technique.

In order to study particle ignition and combustion dynamics at well defined conditions, particle injection is delayed. The delayed injection sequence is shown schematically in Fig. 2.2 b. The figure shows two cross-sections of the chamber where the first instant is prior to particle injection, during which time the particles are not exposed to the hot and rapidly changing pressure conditions. The pressure rise in the chamber due to gaseous mixture combustion drives a tiny piston to inject particles as shown in the second half of the figure. The particles are injected into the hot and slowly decaying pressure gases where they ignite and burn to completion within the conical field-of-view of the optical window and fiber-optic assembly.

The long test times afforded by the slowly decaying pressure (and temperature) allow for the study of boron ignition and complete combustion for particles up to ~50 μm in diameter. The next section describes the combustion chamber and diagnostics used in this study. Following this description, the compositions and characteristics of the boron powders used in this determination are discussed.

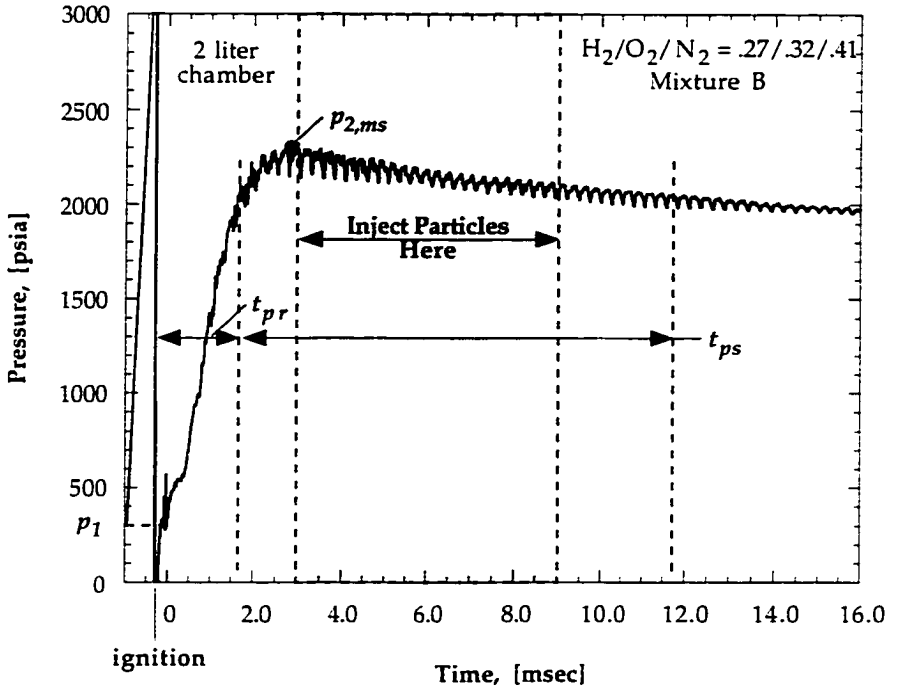

(a)

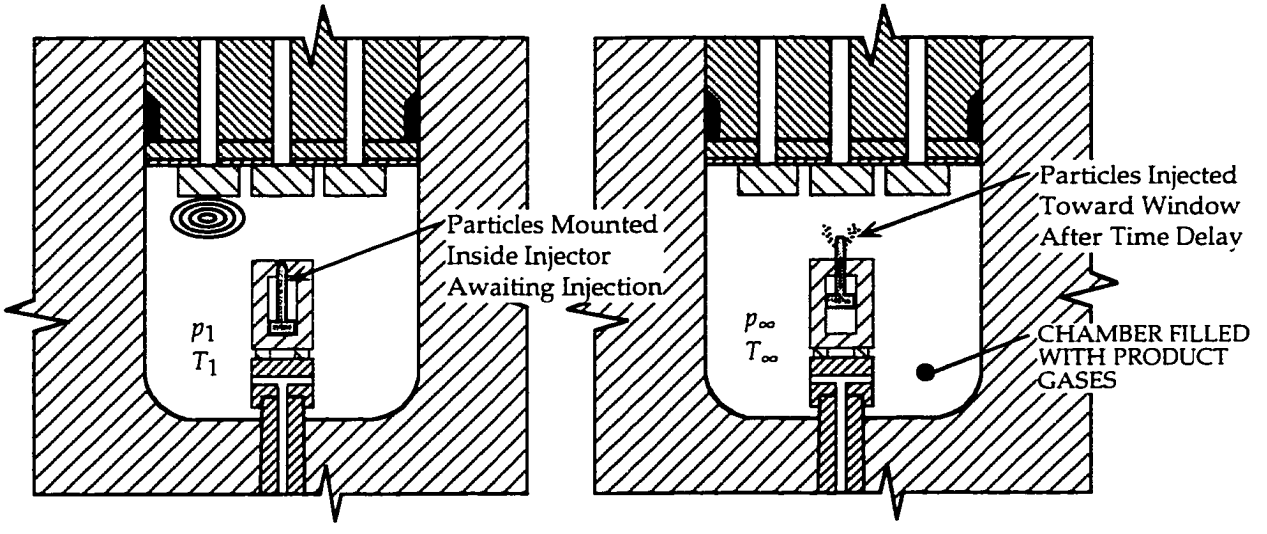

(b)

Fig. 2.2: Scenario for studying small-particle ignition and combustion at high pressures. (a) A typical smoothed pressure rise signal in the combustion chamber shows millisecond timescale to reach peak pressure in a mixture initially containing 2.0 H_2 + 2.4 O_2 + 3.0 N_2, at 20.4 atm. (b) The particle injection sequence is shown where injection is delayed during gas mixture combustion and occurs after peak pressure is reached.

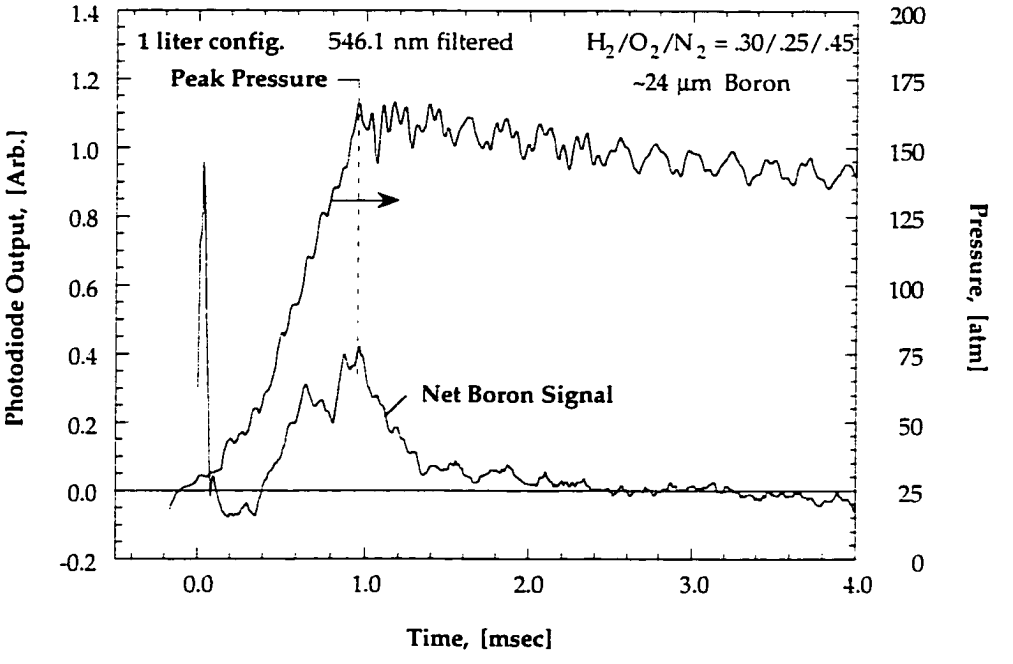

Fig. 2.3: Typical pressure and net filtered-photodiode signal traces from the combustion chamber. Here ~24 μm boron particles were mounted on a sting and exposed to the developing gas mixture combustion. The photodiode signal shows that the particles ignite during the pressure rise while gas-phase conditions are being established.

2.2 Description of High Pressure Combustion Chamber

2.2.1 Combustion Chamber Design and Fabrication

The particle combustion experiments are performed in a newly fabricated and instrumented high pressure combustion chamber (hpcc) facility which has been designed for transient combustion studies and high pressure chemical synthesis investigations.

A photograph of the chamber is given in Fig. 2.4. The combustion chamber is a high pressure, constant volume combustion bomb designed for transient pressures up to 3,400 atm and transient peak temperatures to 4,000 K for 1 MJ energy release. The main vessel is fabricated from 4340 carbon-steel (gun barrel steel) which has been heat treated to Rockwell Hardness R_C = 36. The vessel measures 66 cm tall by 51 cm diameter and is capped by a 25 cm diameter top plug which closes the central 2.0 liter cylindrical chamber cavity, as shown in Fig. 2.5, where the combustion chamber cavity has a diameter of 14 cm. Chamber inserts were fabricated which can reduce the effective combustion volume to 1.0 or 0.5 liters. The main vessel wall thickness is 18 cm giving a chamber-to-vessel wall diameter ratio of 3.6.

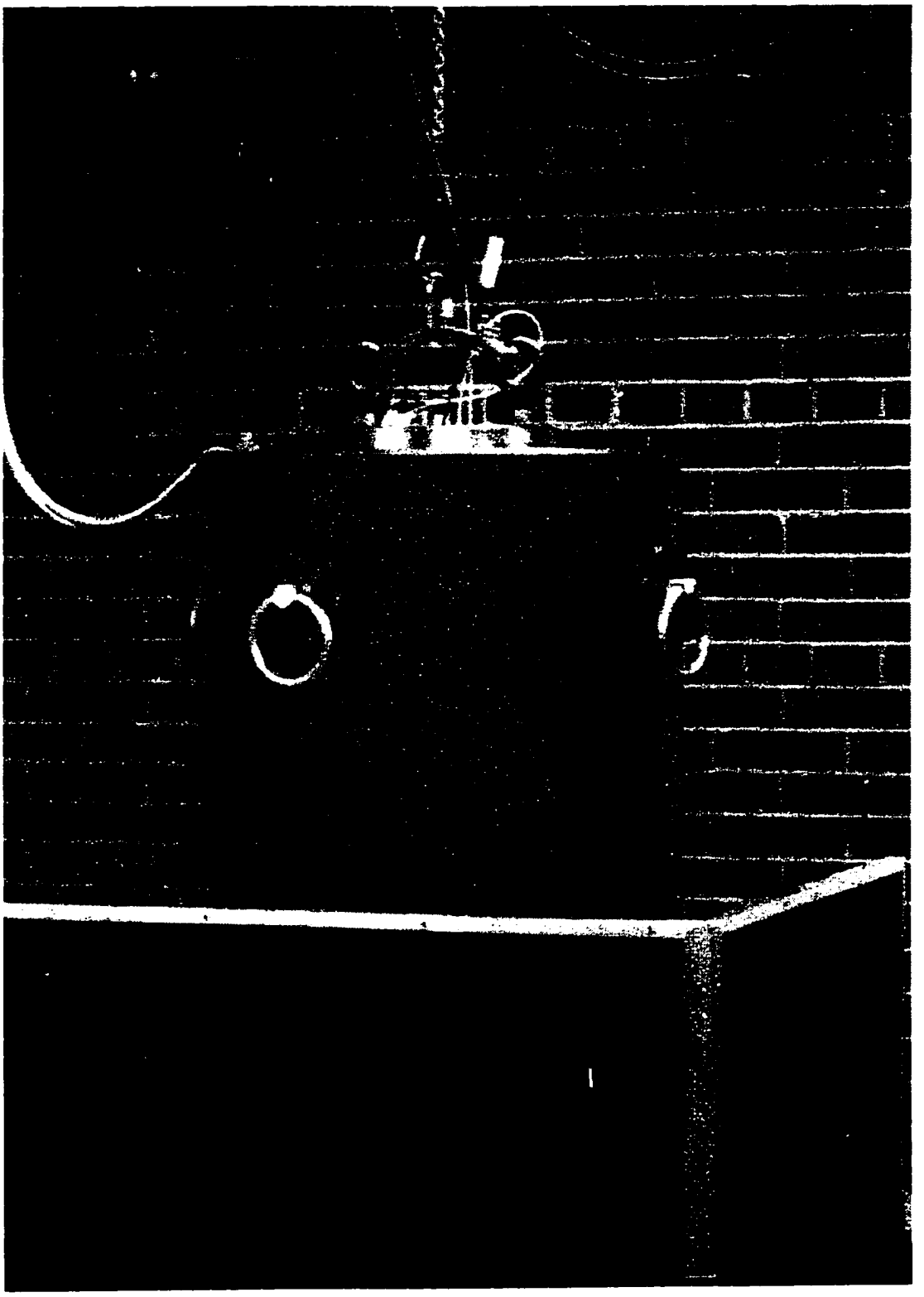

Fig. 2.4: Photograph of high pressure combustion chamber (hpcc) with top plug and retention pins installed. All diagnostic access is through the top plug. The black panels are used for protection in case of exhaust line rupture.

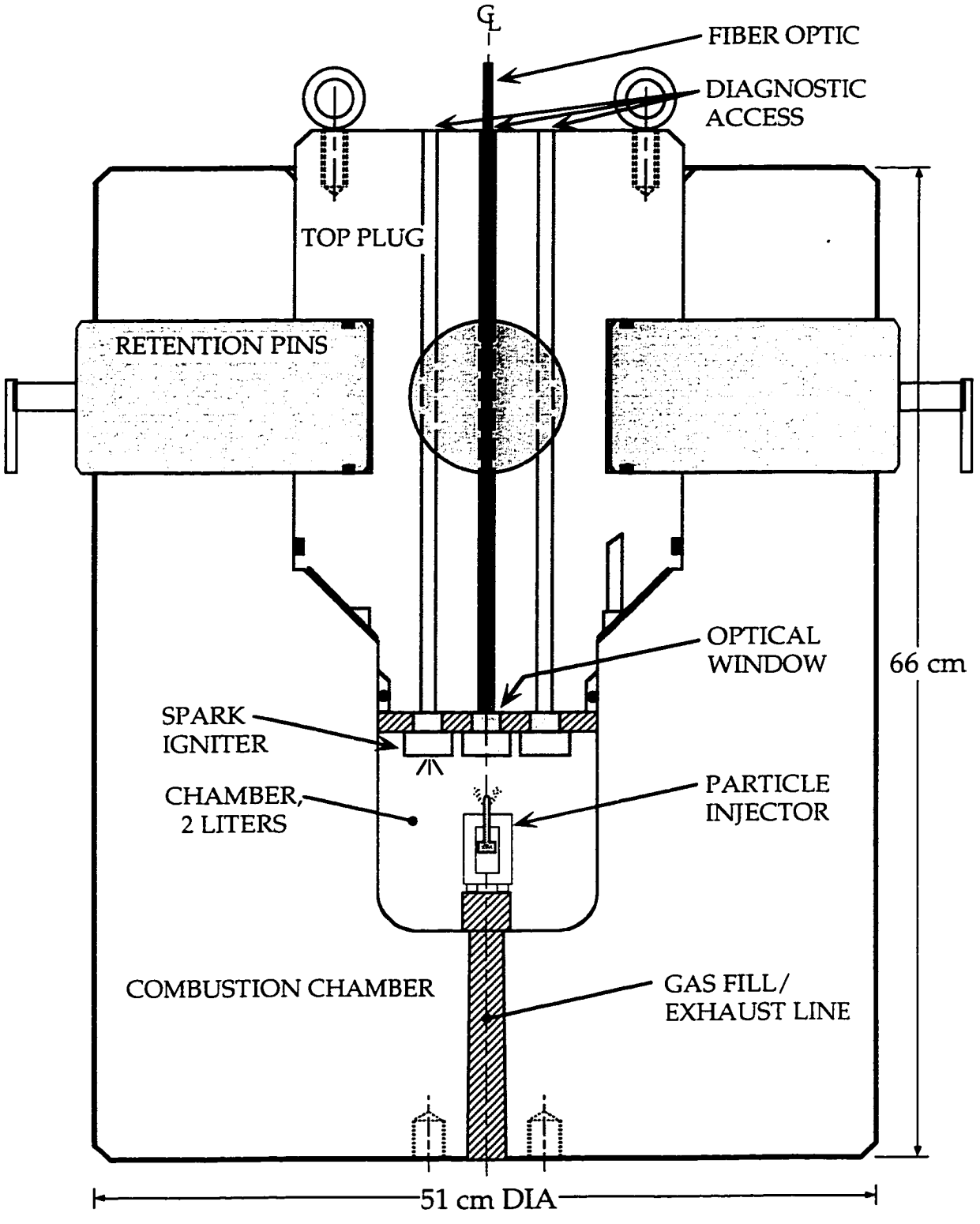

Fig. 2.5: Schematic of high pressure combustion chamber (hpcc) showing 2.0 liter test chamber and diagnostic access through the top plug. Gas inlet and exhaust are through the bottom.

The chamber top plug is also fabricated from 4340 carbon-steel hardened to $R_C = 36$ and this plug provides all diagnostic access. The chamber vessel and top plug are assembled as shown in the photograph and held together by four 10.2 cm diameter, high strength A2 tool-steel retention pins. These four pins carry the entire load due to pressure acting on the top plug and were hardened to $R_C = 60$ so that no lip would form on the barrels under impact loading, something which might make disassembly after an experiment impossible. The four retention pins have been fabricated with through holes to allow hydraulic extraction in the event they become jammed in place, something which has never happened.

All diagnostic access is through the top plug as shown in the photograph in Fig. 2.6. Present diagnostic capabilities consist of dynamic pressure measurement, particle injection timing (not shown), spark ignition, and centerline-viewing optical emission detection through a high pressure quartz window. Spectral emissions are collected and transferred to remote detectors through a six core fiberoptic cable; detection is by narrow bandpass filtered photodiodes and optical multichannel analyzer for spectral decomposition. Special design considerations for all diagnostic accesses were required to prevent accidental blowout at high pressures, as will be discussed in upcoming sections. Initial gas fill pressure and temperature are measured in the gas fill line adjacent to the chamber slightly upstream of the chamber inlet.

Fig. 2.6: Photograph of installed diagnostics showing pressure port (right), igniter (bottom), blank (left), recess for injection timing electrical feed (top), and optical window (center). Diagnostics cover caps have been removed from the window and igniter. Copper heat shield also removed.

The combustion chamber is sealed with a high pressure, high temperature sandwich-like seal composed of a polycarbonate (Lexan) wedge-ring, an ethylene propylene o-ring, and a packing or "piston" ring (Teflon or polycarbonate). This seal packing is shown schematically in Fig. 2.7 a and in the accompanying photograph in Fig. 2.7 b. The o-ring provides the true seal at low pressure. Initial o-ring compression is provided when the diagnostic cover plate is screwed into place. Further compression is provided at elevated pressures by the packing ring; small pressure transfer holes on the periphery of the diagnostic cover plate allow pressurized gases to push upward on the packing ring causing the o-ring to compress further, similar in principle to a technique used in race car engine pistons. This packing ring also helps to protect the o-ring from direct exposure to the high temperature combustion gases; Teflon material provided superior temperature resistance over extended uses. By design at even higher transient pressures, the wedge-ring will extrude along its chamfered edge into the slip clearance to produce additional sealing there. This wedge-ring can also be physically pre-energized during installation to force additional interference fit, although this was never found necessary under the conditions tested up to 600 atm. The main seal has been designed for very high pressures although particle combustion tests have not been conducted above 300 atm to the date of this writing.

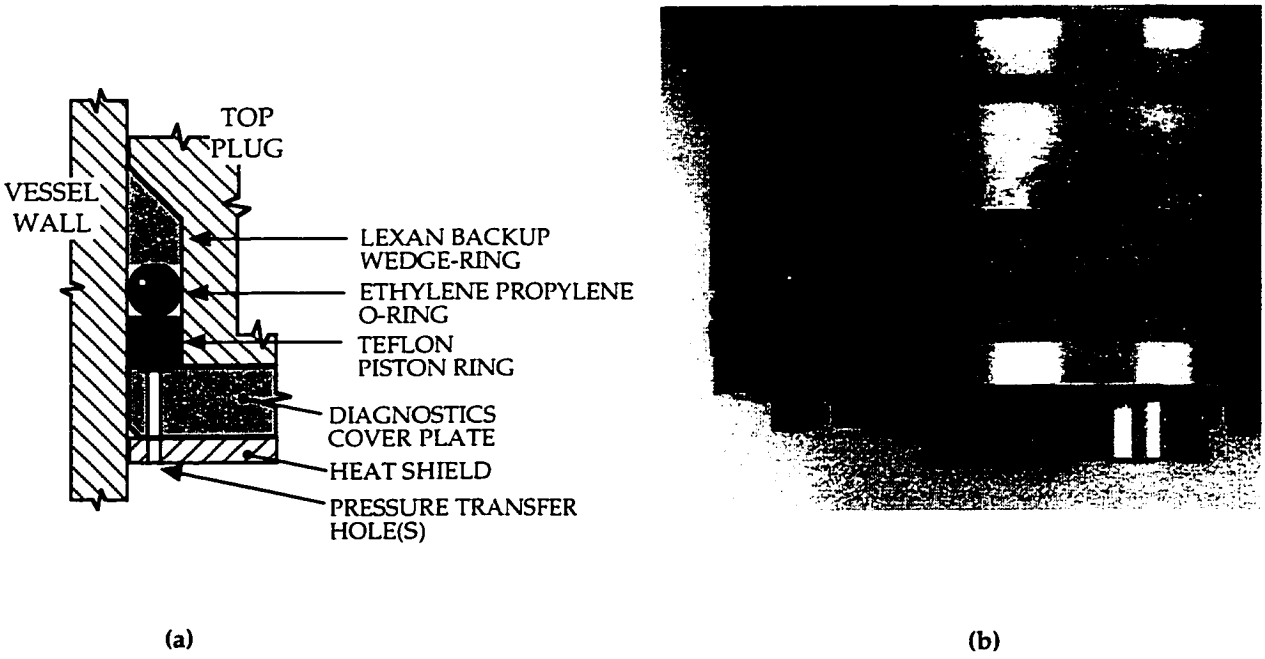

Fig. 2.7: Detail of the hpcc main seal assembly indicating wedge ring, o-ring, packing ring, and cover plate with pressure transfer holes. (a) Schematic of seal sandwich, and (b) photograph of assembled main seal.

The high pressure combustion chamber has a single gas fill and exhaust port at the bottom of the chamber. The gas port is lined with a removable, specialty dispersion-strengthened copper liner to protect the 4340 carbon-steel from high temperature, high velocity corrosive exhaust gases. This specialty copper, type AL-60 Glid-Cop® (SCM Metal Products, Inc.), has almost 80% of the thermal (and electrical) conductivity and nearly identical melting temperature to pure copper. However the Glid-Cop® is interspersed with micron sized aluminum oxide particulates which provides excellent material strength properties. Type AL-60 retains 67% of its room temperature yield strength at 1273 K, which is 24 times the high temperature strength of normal oxygen-free copper, making it an excellent choice for high temperature applications where high strength and excellent heat transfer capabilities

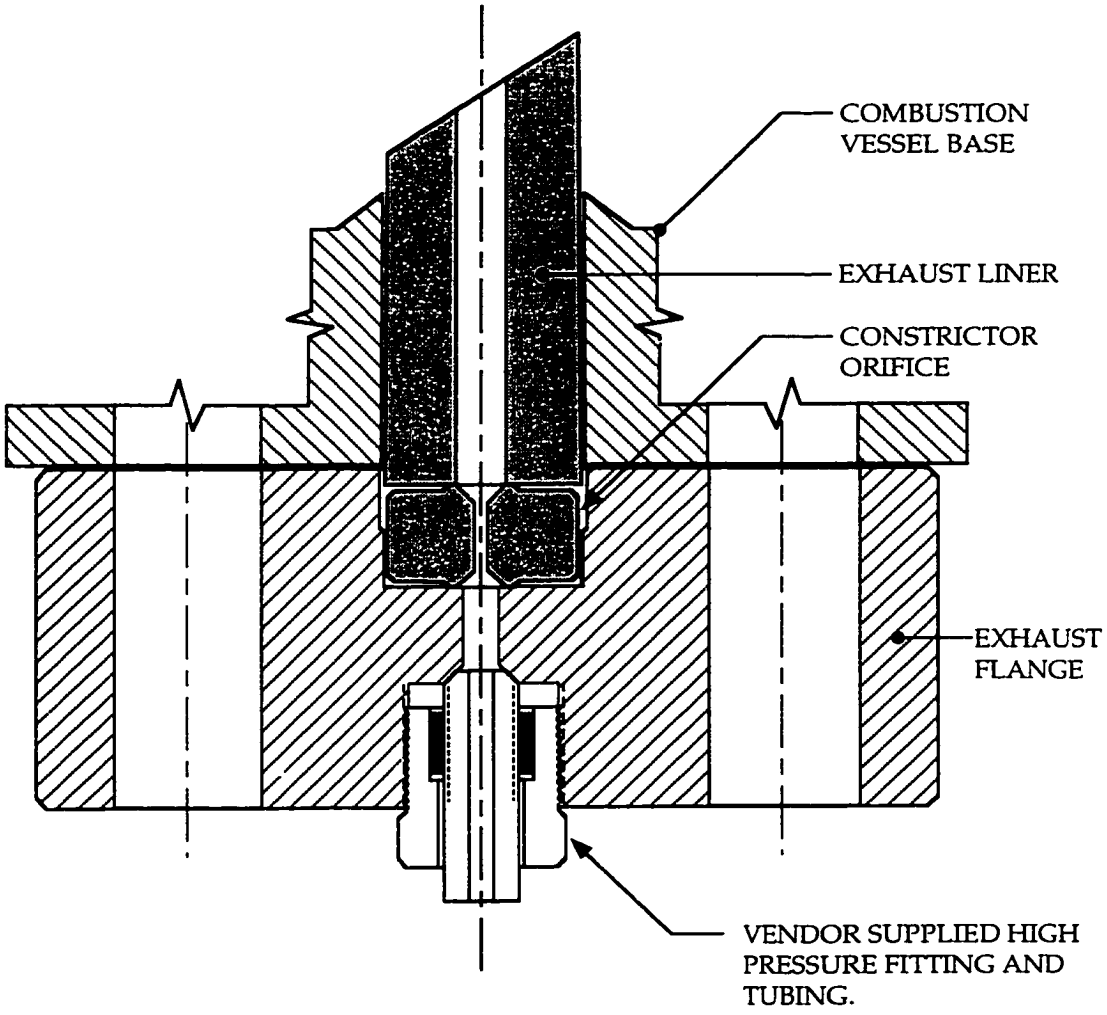

Fig. 2.8: Detail of the hpcc exhaust seal showing tapered exhaust liner, flow-limiting orifice, and exhaust flange. Note collar/gland mechanism on the vendor supplied 60,000 psi (4080 atm) exhaust line connection.

are needed. The copper liner is tapered to allow for easier removal and is threaded at the top to accept an exhaust cap. The exhaust cap is fabricated from type HD-18 tungsten alloy (Mi-Tech® Metals, Inc.), and has four radial exhaust ports to reduce the possibility of clogging. This tungsten alloy has excellent elevated temperature properties but is much easier to machine than pure tungsten. Both the exhaust liner and exhaust cover cap have been used in over 400 high pressure (150 atm), high transient temperature (2600 K and above), oxygen-rich combustion experiments without excessive wear making these material choices very effective.

Pressure sealing at the exhaust port is provided by two separate metal-to-metal seals. On the upstream or chamber side, the first seal is made between the base of the copper exhaust port liner and a flow-constricting orifice, see Fig. 2.8. The tightening torque on the adapter flange fastening screws provides the compression required for the constrictor orifice seal. The second seal on the downstream side is made at the bottom of the exhaust flange between a coned nipple and matching tapered receptacle in the flange, which accepts a standard high pressure fitting composed of a collar and gland assembly. The inlet and exhaust lines are composed of high pressure, 316 stainless steel tubes and fittings (High Pressure Equipment Co.) rated to 60,000 psi (4080 atm) at room temperature.

Exhaust flow is constricted by a 0.16 cm diameter orifice which is also fabricated from AL-60 Glid-Cop® specialty copper. This is done to limit thermal loading on the exhaust line by reducing the exhaust gas flow rate. The exhaust line is water cooled along its entire length from the chamber exhaust adapter flange up to the water-filled exhaust blowdown tank. Only a single constrictor orifice has been used for all the tests conducted to date.

The post combustion gases are exhausted automatically after an experiment through a self-rupturing burst disc, with a typical delay time of 0.4 second, and vented through a radial-flow exhaust nozzle into a water-filled cooling tank. This tank doubles as a neutralization system filled with a sodium-hydroxide solution when caustic gases such as hydrogen fluoride are involved. The chamber can also be vented remotely through an electrically activated, pneumatic flow control valve (see diagram in Fig. 2.25). The exhaust system is kept at slight negative pressure to avoid leaks into the laboratory. Currently the maximum pressure operation of the facility is limited by the exhaust system cooling requirements, which are dictated by the mass throughput of hot exhaust gases, and not by chamber design strength. Tests up to 600 atm have been conducted with no problems as long as the exhaust line is water cooled, and there have never been any line failures (ruptures, metal erosion, etc.).

2.2.2 Design of Gas Mixture Ignition System

The gas mixtures used to establish ambient conditions for particle combustion are ignited with a foil-type igniter energized by the discharge of a capacitor bank. As initial pressures are increased during the course of the investigation, the ability to produce a spark becomes more and more difficult. The ability to arc in a given gas is a function of gas pressure, gas composition, voltage between the electrodes, and gap size between the electrodes. The required potential difference to create a spark between two electrodes is often displayed in the form of a graph called a Paschen curve, a plot of break down voltage (V_t) versus the product of pressure and gap size (pd). Such a Paschen curve for several individually tested gases[48] is shown in Fig. 2.9, which covers the conditions for the present set of experiments. In order to avoid the difficulties of continually adjusting the igniter gap size as a function of initial gas pressure and composition, a foil igniter is used which when energized produces its own gap. The current discharge through the anode-foil contact melts the foil producing a gap which leads to a spark, and thereby precludes the use of unmanageably high voltages. Typically 4,000 volts at 15 Joules total energy produces very repeatable ignition (over 99%). The initial spark energy is a small fraction of the chemical energy release in the chamber, where for example in a nominal 300 psia (20.4 atm) initial pressure gas mixture this release is ~110 kJ.

The igniter used in the hpcc experiments is encased in a stainless steel housing which fits into any of the diagnostic access ports in the top plug. Referring to Fig. 2.10, a double o-ring seal composed of a primary plus backup seal is used to prevent hot gas leakage at even very high peak pressures and temperatures. The igniter electrical lead is fabricated from the center lead of a Belden RG-58 U coaxial cable. This lead is silver soldered to a more robust and chemically inert brass igniter head. The igniter head is encased in a high temperature, high extrusion strength, Yorolite grade G-11 composite insulator which is affixed to the igniter housing with high temperature epoxy (Loctite 445). The igniter foil, typically an aluminum foil disc of 0.05 mm thickness, is pressed across the igniter head and held in place with a brass shim washer and igniter screw cap as shown in Fig. 2.10. The igniter head and its tapered insulator packing are backed up by 1.1 cm of steel from the igniter housing to prevent blow-out over the entire design pressure range of the chamber.

A photograph of the spark produced by the igniter in open air is shown in Fig. 2.11 indicating the spark's spread and intensity. It is noted that the spark at chamber fill pressures and mixture compositions will be quite different. The igniter is powered by a capacitor bank which provides a fast discharge, see Fig. 2.12. A power supply located inside the control room is used to establish capacitor voltage remotely. The capacitor bank is composed of four 2 μF capacitors, where two capacitors in-series are arranged in parallel with another two in-series. This configuration gives an overall 2 μF capacitance. Each capacitor alone is rated to 2000 volts and the selected arrangement provides a very

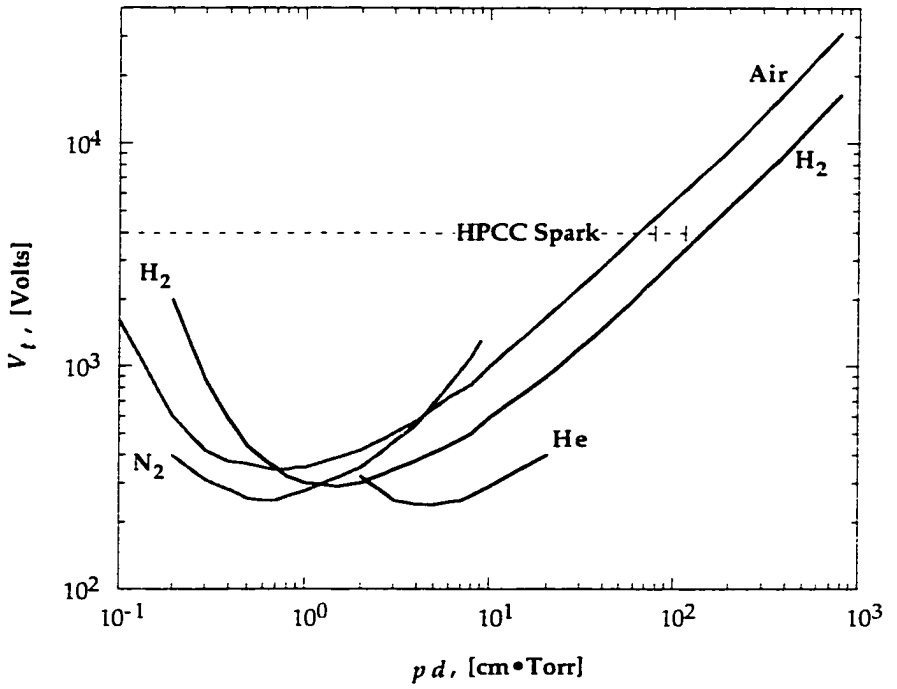

Fig. 2.9: Paschen curves for various gases indicating required breakdown potentials between electrodes, from Ref. (48). To avoid problems associated with precise gaps at various pressures, a foil-type igniter is used.

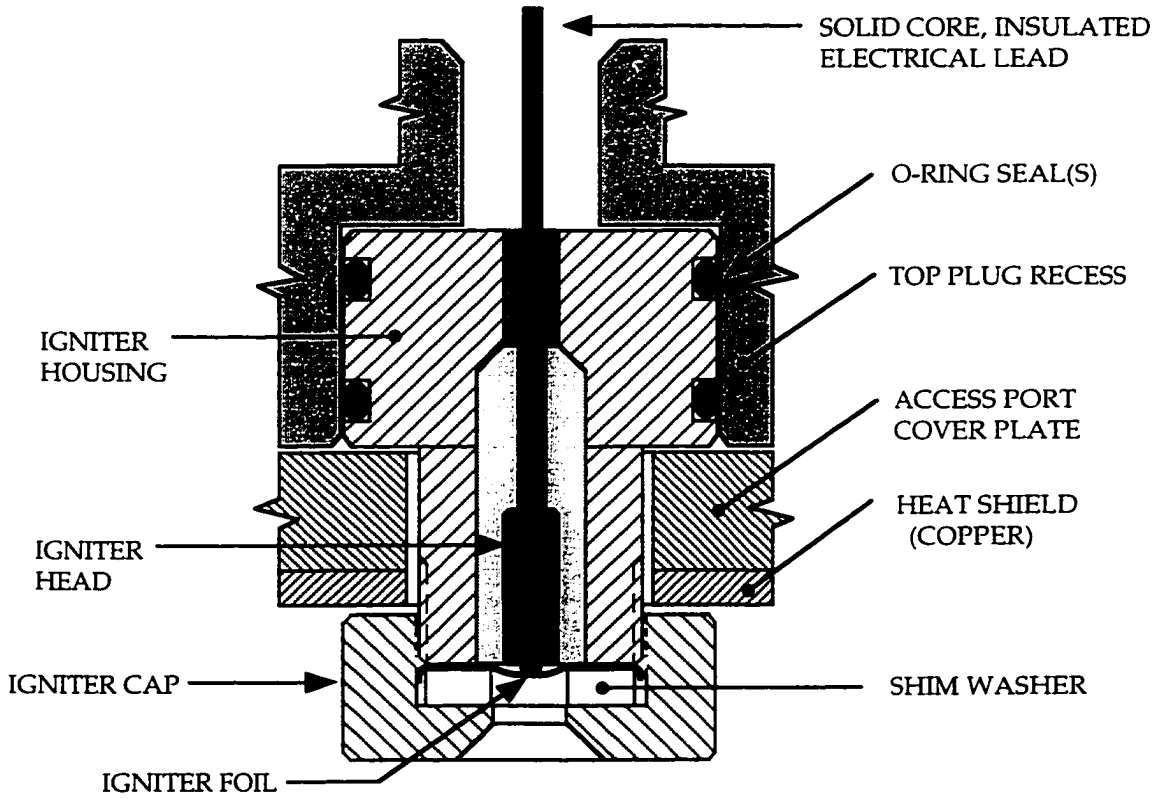

Fig. 2.10: Schematic of foil-type igniter used in the combustion chamber experiments. Igniter assembly is shown installed in top plug access port.

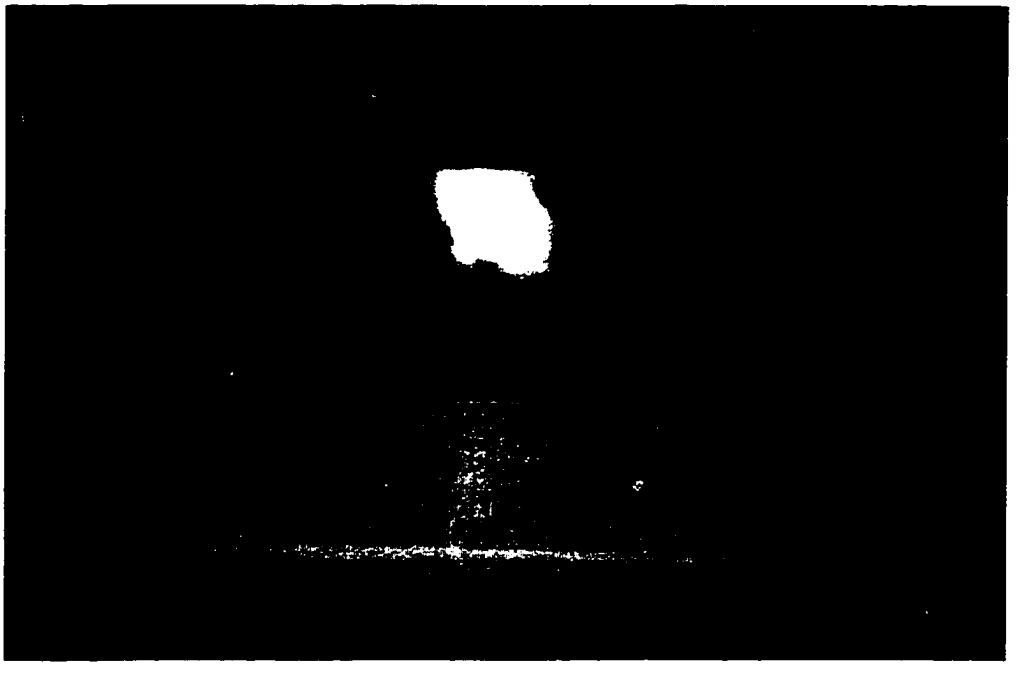

Fig. 2.11: Photograph of igniter spark discharge in open air at 1 atm.

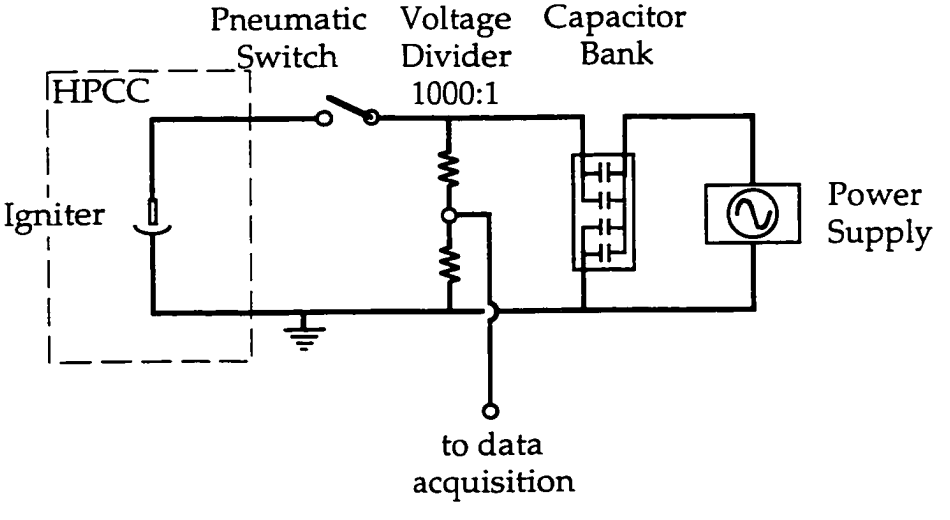

Fig. 2.12: Schematic of igniter power supply circuit.

robust configuration. With the inductance of the related wiring and switching circuitry the bank has a typical measured discharge time constant of only 16 μsec.

2.2.3 Design of Observation Window

The ignition and combustion characteristics of particles are monitored by optical means. Particle combustion emissions are monitored as a function of time with fast-response photodiodes to determine ignition delays and combustion times and are spectrally decomposed to identify key intermediate species in the combustion process. As such a key aspect of the particle combustion study is the ability to extract optical information from the high pressure, high temperature combustion region.

To this end, a high pressure, high temperature optical port has been designed which is shown schematically in Fig. 2.13. Optical access is achieved through a quartz window and collected light emissions are transmitted through fiber optic cables to corresponding detectors. The quartz piece is a high quality, A-1 quartz cylinder (Esco Products, Inc.), 0.95 cm diameter by 0.95 cm length, which is housed in the optical window housing as shown. Two 0.16 cm thick polycarbonate (Lexan) washers are used to provide cushion for the window. A threaded 5.1 cm long common-end fiber optic coupler is tightened flush with the polycarbonate washers to produce a snug fit. The window piece is sealed on the periphery of the quartz cylinder by the window o-ring, with secondary sealing provided between the window and its polycarbonate washer backing. The window o-ring requires replacement every four to five shots at high pressure conditions because it becomes thermally charred.

The cylindrical quartz window and fiberoptic coupler (ferrule) are contained in the stainless steel optical window housing. This housing fits into any of the five diagnostic access ports in the top plug (except pressure port). A double o-ring seal composed of a primary seal plus backup is used on the optical window housing similar to the sealing arrangement employed on the igniter housing. A stainless steel cover cap is tightened down on the window assembly to energize the seals by compressing the window o-ring and firmly seating the quartz cylinder against its polycarbonate backing, enclosing the entire assembly. The key design consideration here is the quartz window's soft backing which is needed to avoid window shatter when the unit is exposed to "shock" from rapidly rising pressures. It was found that the two polycarbonate washers provide sufficient cushion when the quartz cylinders have generously ground and beveled edges, whereas these edges chipped easily along an axial direction when they were left un-ground.

The angular field-of-view (f.o.v.) of the fully assembled optical window and fiber optic has been measured for several separation distances between a point source of 0.16 cm diameter and the

assembled optical window. The intercepted light intensity was measured with an unfiltered photodiode, to be described below, and the result is given in the plot in Fig. 2.14 a. From Fig. 2.14 a it is seen that the f.o.v. is approximately ±15 degrees of-center for the nominal 3.3 cm window separation used in the experiments, indicating a cone of light with ~30 degree cone-angle is collected. Light collection within this cone is not uniform about the central cone axis however. Calculations show that glowing particles which are dispersed upon injection re: ıain in this f.o.v. during their entire lifetime.

A restricted optical field of view is an important parameter in the present high pressure and high temperature combustion study. The hot gas emissions measured in the absence of particles cannot be neglected in comparison to the particle-laden signal, even within the filtered bandwidths which correspond to boron species molecular transitions, to be discussed below. Fig. 2.14 b shows how the optical f.o.v. has been restricted so that the particle injector housing blocks out all of the hot gas radiation originating from *gases behind* the particle injector. This effectively limits the depth of view (optical path) to 3.3 cm, the distance between the optical window and the top of the injector, the region where particles are igniting and burning.

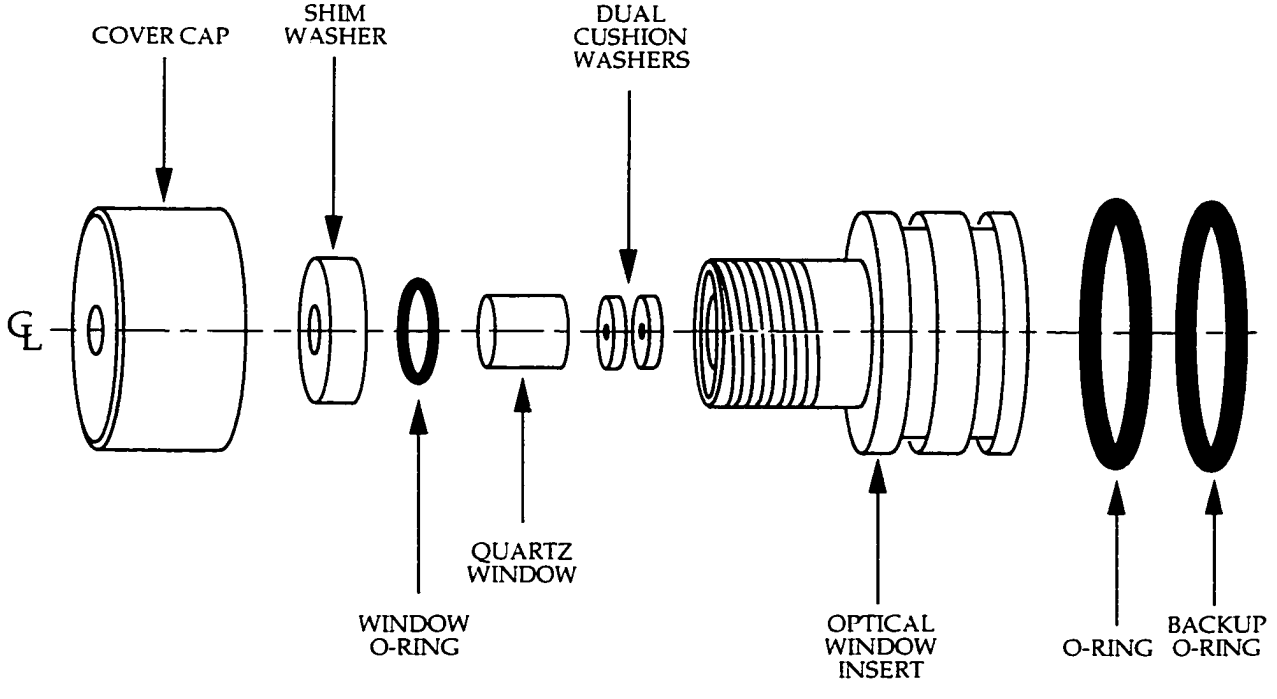

Fig. 2.13: Schematic showing assembly of high pressure, high temperature optical port. On the front side are two polycarbonate cushion washers, the cylindrical quartz window piece, and window o-ring. The fiberoptic coupler screws into the back side of the housing until it snugs up against the cushion washers. A cover cap screws down onto the quartz piece to hold the window components in place and energize the seals.

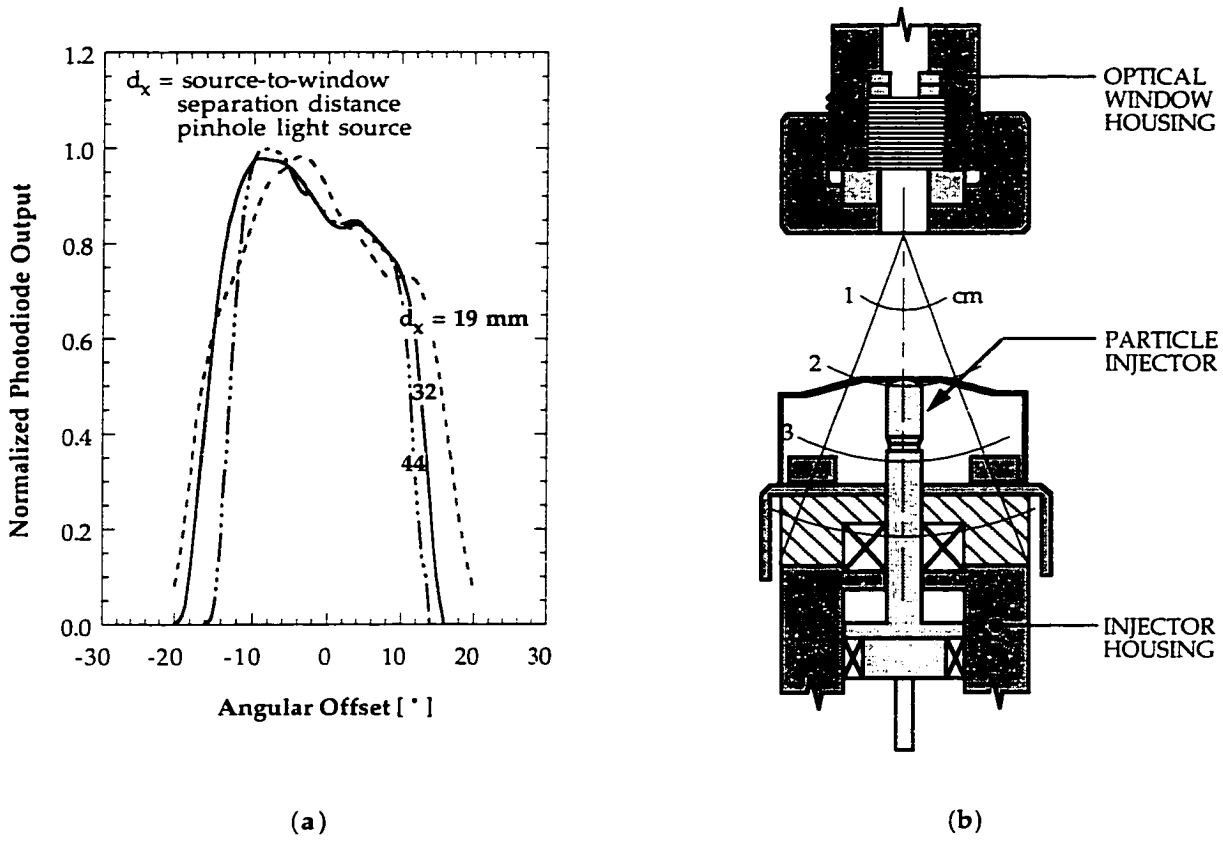

Fig. 2.14: (a) Measured angular field-of-view of combustion chamber optical window for various window-to-source separation distances. (b) Configuration for viewing igniting and combusting particles showing restricted field-of-view.

2.2.4 Design and Predicted Performance of Particle Injector

As mentioned previously, particles are injected into the hot chamber gases after sufficient delay to allow peak pressure to be reached. This is accomplished with the particle injection device shown in Fig. 2.15. Particles are initially loaded into a shallow annular groove (1.8 mm length by 0.8 mm depth) in the shaft of the injector piston and are injected at moderate velocity into the hot quasi-steady high pressure ambient gases. Particles are protected from the hot ambient gases until the instant of injection by a tight seal which guides the shaft during the injection stroke. The pressure rise in the chamber forces gases through the orifice at the base of the injector (Figs. 2.16) into the piston bore pushing the particle piston upward. By tailoring the bore dimensions, particle piston mass, and orifice size, the injection delay can be suitably configured for the range of tests conducted in this study.

The injector is a novel device comprised of a housing, a piston/plunger which contains the supply of particles, a sharp-edged orifice, a piston base seal and top guide collar seal (Teflon), a high

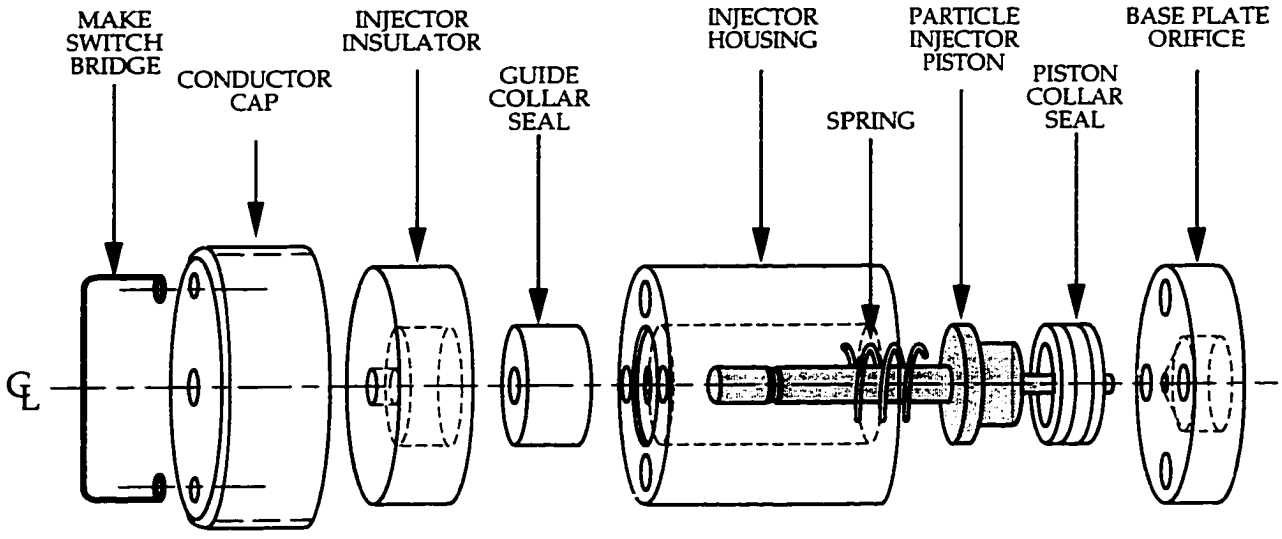

Fig. 2.15: Schematic of particle injection device and the make-switch modification to measure injection timing. The injector's dynamics were matched to the pressure rise history in the chamber.

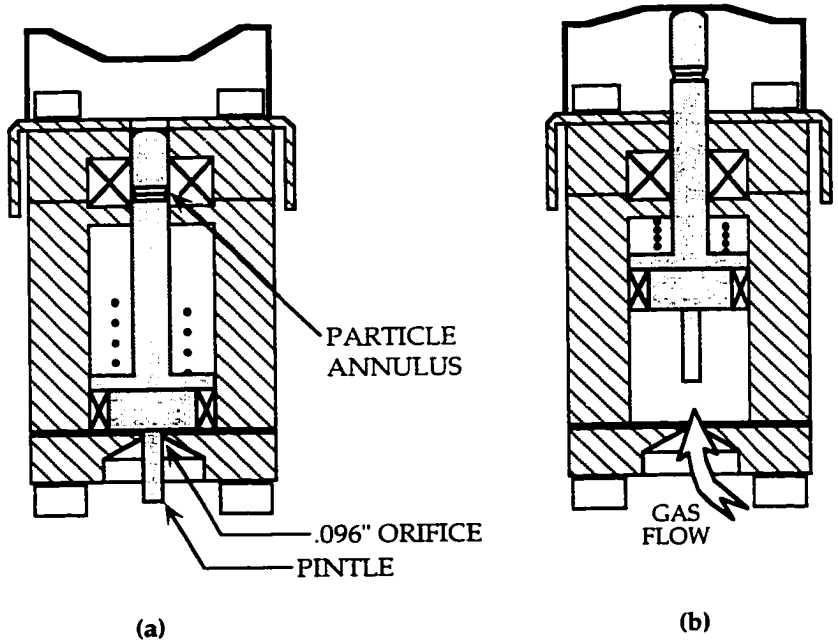

Fig. 2.16: Schematic of particle injector (**a**) before particles are injected, with particles loaded into the narrow annular groove in the plunger shaft. The pressure rise in the chamber from H_2/O_2 combustion drives the particle-laden piston to inject particles. (**b**) Configuration after particle injection with timing switch is in closed position.

temperature electrically insulating ejector plate, and a cover cap. The injector piston in Fig. 2.15 is fabricated from HD-17 tungsten alloy because this material is very dense - its large mass provides lower acceleration and therefore longer injection delay. The material has good chemical and thermal resistance too. Best results have been obtained when the orifice plates are made from either the same material or Glid-Cop®, and each orifice usually lasts for 4 to 5 shots before the hole is worn. Teflon material is excellent for the two seals because one can achieve a good tight seal with low sliding friction. The high temperature electrically insulating ejector plate is made from G-11 grade Yorolite, a laminated composite material, which stands up to high temperature for ~5-8 high pressure shots and can be tapped and threaded to accept four bolts which hold the injector together. The Yorolite ejector-plate is covered with a protecting cover cap made from a shortened 1.38 in. (3.50 cm) copper pipe end-cap fitted with holes for the injector and injection timing bridge-wire retaining screws. This piece typically survives ~20-30 high pressure shots before it is chosen to be replaced. The timing bridge-wire is fabricated from 0.047 in. diameter (0.12 cm) paper-clip wire which has the chrome plating removed. This wire will not melt and is quite resilient, it can typically be used for ~30 shots.

The tailored injector time history is produced by a variable orifice diameter, providing both a long injection delay and fast injection. Figure 2.17 shows predicted piston kinematics for a typical pressure rise. The orifice gap is initially annular, ~0.2 mm^2, because the pintle at the base of the

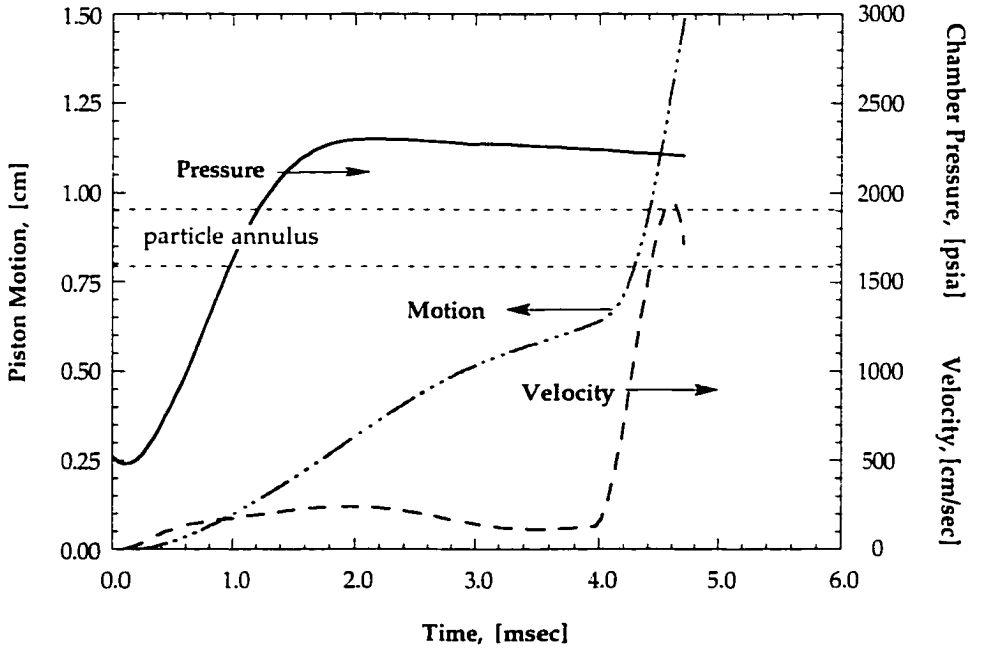

Fig. 2.17: Calculated particle injector piston motion. Initially the injector moves slowly, giving the required injection delay, followed by a rapid increase in velocity to ~12 m/sec to inject particles with good dispersion.

particle piston protrudes through the orifice (Fig. 2.16). Just prior to injection this pintle is retracted by the rising piston, increasing the orifice flow area 25-fold. A 4 to 8 msec injection delay is therefore achieved with injection velocity ~12 m/sec. Injection timing is provided by an external circuit connected to a bridge wire which is then shorted to ground by the rising injector piston. The axial length of the particle-containing annulus requires ~100 μsec to inject the entire sample.

Special Design Considerations

The particle injector is a critical part for successful particle combustion studies and there are several design considerations worth mentioning. The two most critical aspects of the injector which could lead to failures are the three seals and excess wear on the pintle.

Both the Teflon guide collar seal and the plunger base seal must be carefully and precisely fabricated. It was found that reaming the through hole in the guide collar seal undersize to 0.186 in. (0.472 cm) provided the best results. This seal must be tight and the inner barrel surface free of scratches and very uniform or else excessive particles will be lost in the seal during the injection stroke. Also critical is alignment of this through-hole and the center hole in the Yorolite ejector plate. Misalignment resulted in many problems concerning injector use. The piston base seal is epoxied to the plunger base and is generously chamfered at the base as shown in Fig. 2.18 a. Pressures acting on the base of this seal produce a radially-outward force component which energizes the seal even more as pressure rises. The two shallow circumferential grooves in this seal temporarily delay any gas leakage into the cavity above the rising injector. Leakage into this cavity slows the piston by dampening the upward stroke, resulting in poor injection. The outer diameter of the seal is typically fabricated to produce a 0.005 in. (0.013 cm) interference fit when installed into the housing bore. By working the plunger in-and-out of the bore several times before an experiment, the outer surface of the plunger seal becomes nicely polished, much smoother than could be machined, and it is squeezed to the intended dimension. A single tiny, circuitous leak groove is added by scratching the surface axially to prevent the injector from unseating during chamber filling.

The seal between the base of the injector housing and the orifice plate is also very important. Since the initial gap between the pintle and orifice is typically only 0.003 in. (0.008 cm), the slightest leakage past the seal between the two metal surfaces will result in premature injection. Best sealing is achieved by machining a 0.010 in. (0.025 cm) standoff lip into the base of the housing (Fig. 2.18 b) and using a 0.004 in. thick (0.010 cm) brass gasket fabricated from standard sheet shim stock. The lip plus shim avoid possible complications from orifice plate warping which was observed after just a few uses.

It is imperative to have a clean orifice. Of the metals which were used, 17-4 stainless steel, Glid-Cop®, and HD-17 tungsten alloy, the tungsten alloy functioned the best (lowest hole wear and

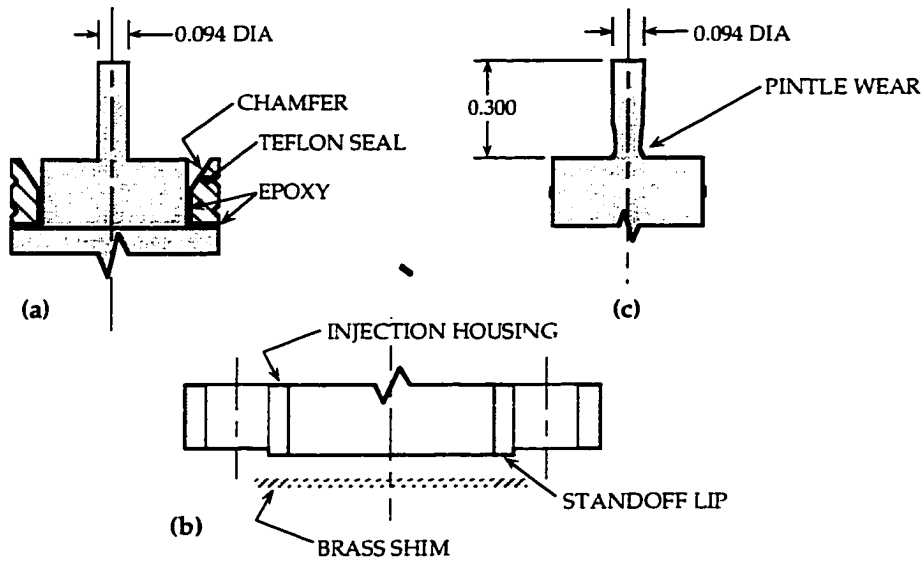

Fig. 2.18: Special issues concerning particle injector. (a) Sketch showing epoxy adhesive and chamfer on inner edge of plunger base seal. (b) The standoff lip on bottom sealing surface of injector housing and brass shim provide superior sealing there. (c) Schematic showing typical mode of wearing on the injector pintle. The taper is exaggerated for clarity; it is usually difficult to detect because of its proximity to base.

least warping). Stainless steel proved to be the poorest choice because the orifice holes wore the most quickly (diameter opened after repeated uses). The through holes in the orifice plates were always reamed to within ±0.0005 in. (0.0013 cm) to provide the very precise dimensions required. As will be shown below, an increase in the gap width by only 0.001 in. (0.003 cm) results in a 25% decrease in injection delay time and thus premature injection. The orifices are repeatedly cleaned with these reamers (by twirling them between fingers) to remove very slight foreign matter buildup during an experiment.

The pintle at the base of the injector/plunger is an integral part of the injector which provides the desired kinematics. As the pintle retracts from the orifice as the piston/plunger rises, the effective orifice area changes dramatically. The pintle is fabricated from 17-4 PH stainless steel; it was originally desired to be fabricated from HD-17 tungsten alloy but this proved to be too brittle for such a small part. The stainless steel suffers from fast wear so this part requires replacement every 5-8 shots, unless one uses a variety of orifice sizes. The pintle tends to wear first at its base in a taper, as shown in the schematic in Fig. 2.18 c, which is difficult to detect and can lead to premature injection for a given orifice size. The pintle size needs to be within ±0.001 in. (0.003 cm) to provide acceptable injection delays. The nominal gap width between the pintle and orifice is selected to be 0.003 in. (0.008 cm) for a nominal 150 atm pressure experiment and 0.080 in. (0.203 cm) for 38 atm shot.

Injection Timing Device

To determine particle ignition delays it is imperative to know when the particles are injected. The time when injection occurs is measured directly by the closing of a make-switch inside the chamber. This switch is composed of a bridge-wire (with applied ~0.4 volt potential) and the particle piston (ground potential). The rising particle piston contacts the bridge-wire at the instant when the particle annulus is exposed, shorting the potential on the bridge-wire to ground through the piston, a coiled spring, and the injector housing which complete the circuit to the chamber vessel wall (see circuit diagram in Fig. 2.19). The drop in voltage is recorded by the transient data recorder along with other measurements.

The make-switch voltage supply is shown schematically in Fig. 2.19. A voltage divider is used to step down the battery voltage and a capacitor to reduce the electrical current load on the battery. The typical full-scale response of the make-switch circuit is measured to be ~20 μsec; however, measured injection timing uncertainty from the signal itself is only ±2 μsec since the full scale response is not required. The recharge time-constant of the power supply capacitor is ~100 μsec, which was designed to be fast enough so that multiple injections can be measured should the injector oscillate.

The make-switch electrical feed into the chamber is shown in Fig. 2.20 and consists of a modified igniter, anode post (brass), insulating washer (Teflon), and contact-lead arm. The contact-lead arm is also made from paper-clip wire and is bent using needle-nose pliers into the shape of a generous letter "L", which is compressed like a cantilever spring when it is lowered down onto the copper cap covering the injector housing. The loop at the top of the contact-lead arm is for attaching it to the anode post, with a tiny screw, and the loop on the other end provides a large electrical contact surface which rests on top of the injector cap when installed in the chamber.

Design Calculations for Injector Motion

The piston injector's kinematics have been modeled and optimized for the nominal 150 atm condition where the pressure rise time is ~2.5 msec. The time dependent kinematic equations governing the piston's acceleration were developed (see Appendix A) and integrated numerically using the measured pressure rise history as the piston driving potential. The piston mass (density of material), plunger cross-section (net forces due to acting pressures), bore dimensions, and the ratio of orifice size to pintle diameter are key design variables. The most critical variable effecting the injection delay is the orifice gap size as shown by the predictions displayed in Fig. 2.21. The figure demonstrates how sensitive injection delay time is to this ratio.

The piston experiences very high accelerations which are dictated by the pressure acting on its base area of the plunger. The use of an effective variable area orifice provided by the retracting pintle

produces a relatively long delay at first followed by a great increase in piston velocity just prior to particle injection. The design is constrained by the overall length of the injector housing, which must fit inside the chamber, and the possibility for oscillation near the point of injection. The bore length above the moving piston dictates the compression ratio at the instant of injection. If this length is too

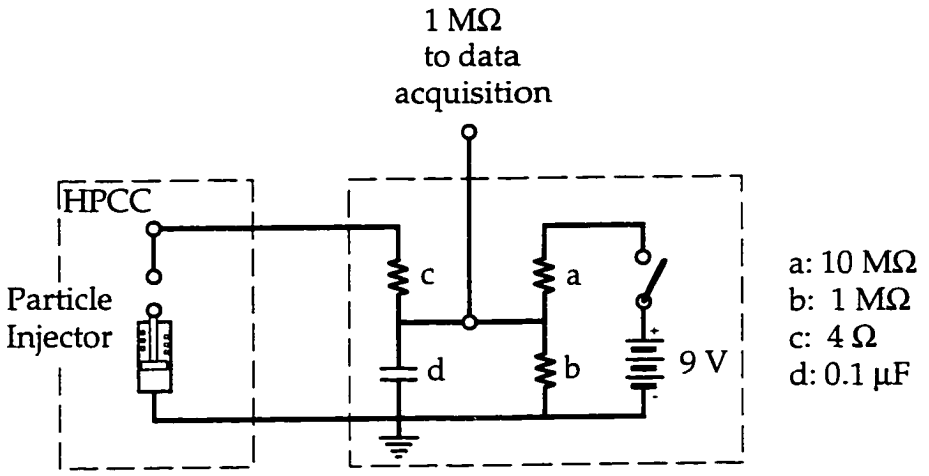

Fig. 2.19: Circuit diagram for make-switch (and voltage source) used to time when particles are injected.

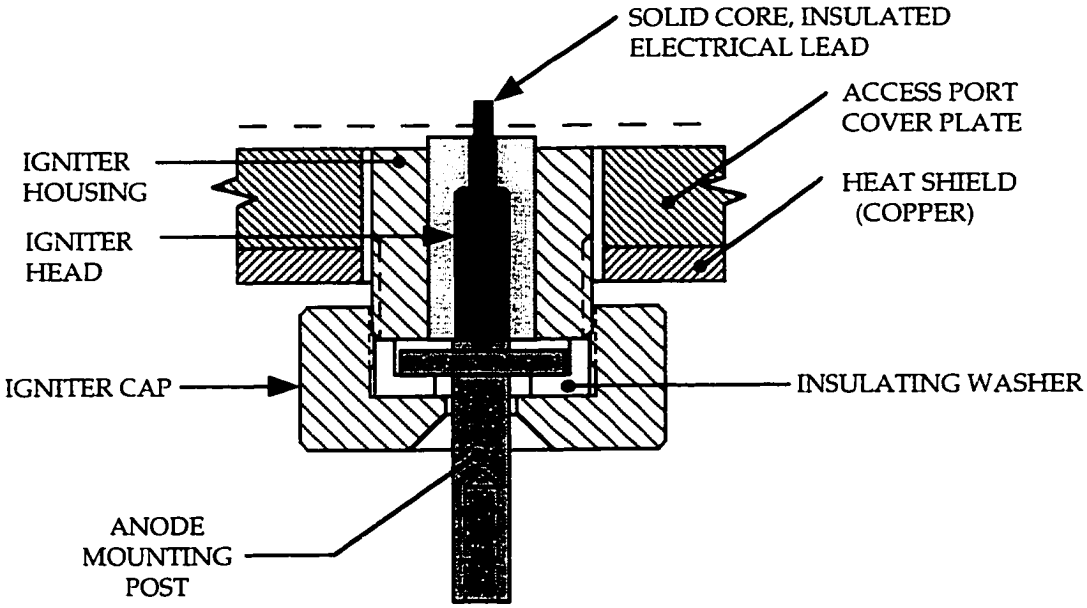

Fig. 2.20: Schematic of make-switch electrical feed into the chamber. The feed is a modified igniter with insulator washer, anode mounting post, and cantilever contact wire.

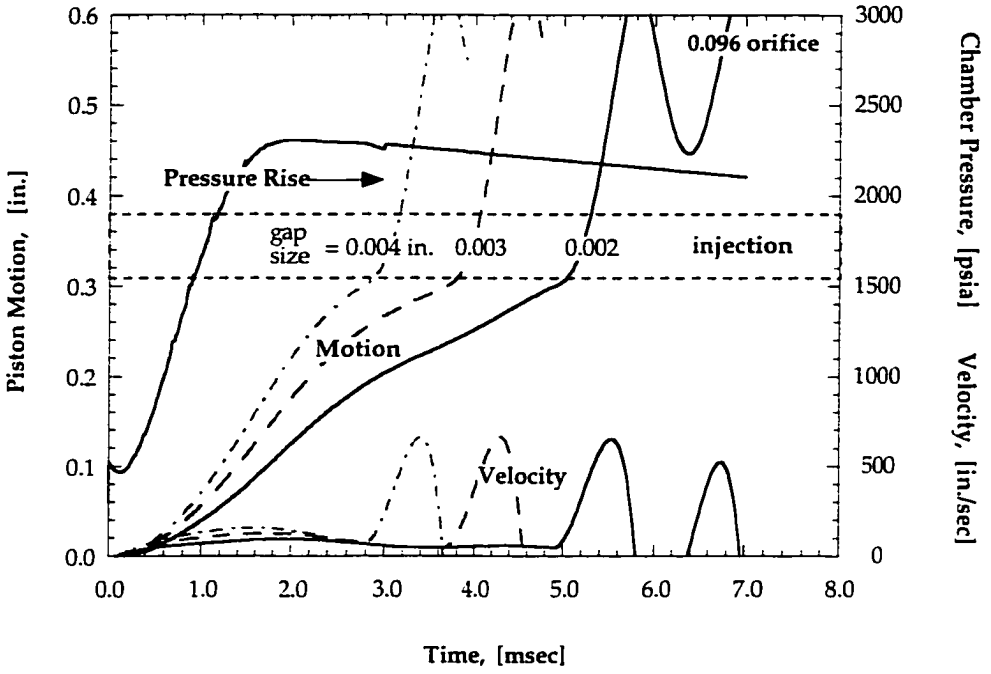

Fig. 2.21: Injector design calculations showing the effect of variable gap size between the pintle and orifice. The various curves demonstrate the sensitivity of injection delay time to the gap size.

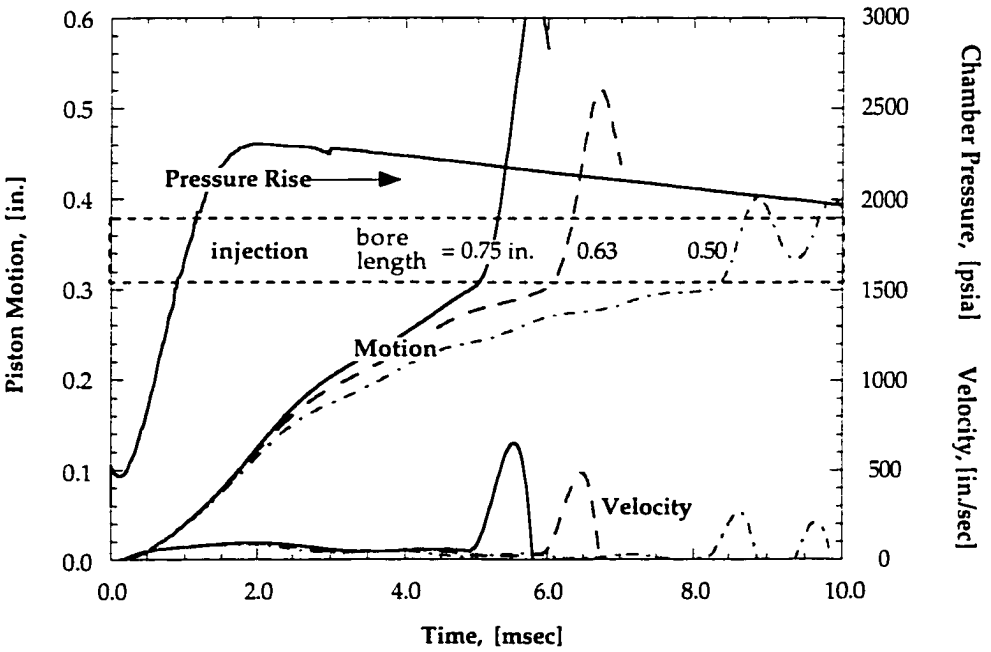

Fig. 2.22: Injector design calculations showing the effect of variable bore length on injection. The dashed curves demonstrate how poor injection is achieved if the bore length is too short, due to excessive compression of gases above the rising plunger.

short then compression of gases above the piston will slow the injector on approach to injection, leading to poor injection. Fig. 2.22 compares the dynamics for several injector bore length configurations. The dashed curves in the figure demonstrate that a short bore length can cause the injector to inject particles with essentially zero velocity and perhaps retract them back inside the injector. The injector can also oscillate with damping as shown by the predictions.

Poor injection due to over-compression of the gases above the plunger will also occur if gases leak past the plunger base seal. The result is slow injection and poor particle dispersion as will be discussed further in Section 3.12. Moderate injection velocities are needed to disperse the particles sufficiently so that they may ignite and burn independently of one another and of the injector itself. Injection velocities between 8 and 14 m/sec were typical for the various test conditions studied. These velocities are shown in Chapter 4 to increase particle heating rates by convective heat transfer. This effect must be properly accounted for in the analysis of measured ignition delays.

2.2.5 Description of Combustion Chamber Operation

This section describes the basic operation of the high pressure combustion chamber experiment. To prepare the combustion chamber for an experiment the chamber cavity is thoroughly cleaned before a new experiment is begun. The chamber is then wiped down with ethyl alcohol to remove any residual grease. The gas inlet and exhaust line is blown out with compressed nitrogen to clear out any residual humidity. A burst disc suitable for the upcoming experiment is installed and the exhaust line is reconnected to the chamber. Burst discs are fabricated on-site from 0.010 in. thick (0.025 cm) Mylar sheet in a hand operated press to form the shape suitable for the angled-seat burst disc holder.

The plug and diagnostics are prepared next. The main seal assembly is inspected and re-assembled after each part is covered with a thin layer of vacuum grease. The piston ring usually experiences some heat damage from the previous test and its thickness is verified with a micrometer. The ring is normally good for about 10 to 20 tests before it is replaced; rings made from Teflon last the longest. The o-ring is also inspected carefully before every run for heat damage, which rarely occurs. The wedge-ring typically shows no wear and rarely requires replacement.

The optical window, igniter head, and make-switch electrical feed are inspected and cleaned with alcohol between experiments. The integrity of the quartz window is checked (for cracking) and the window o-ring is examined for heat damage. If the quartz window has cracked it was likely caused by over-engaging the threaded fiberoptic coupler, which should just tighten snugly up against the quartz window but not unseat the window and quartz cushion-washers from the lip on which they rest.

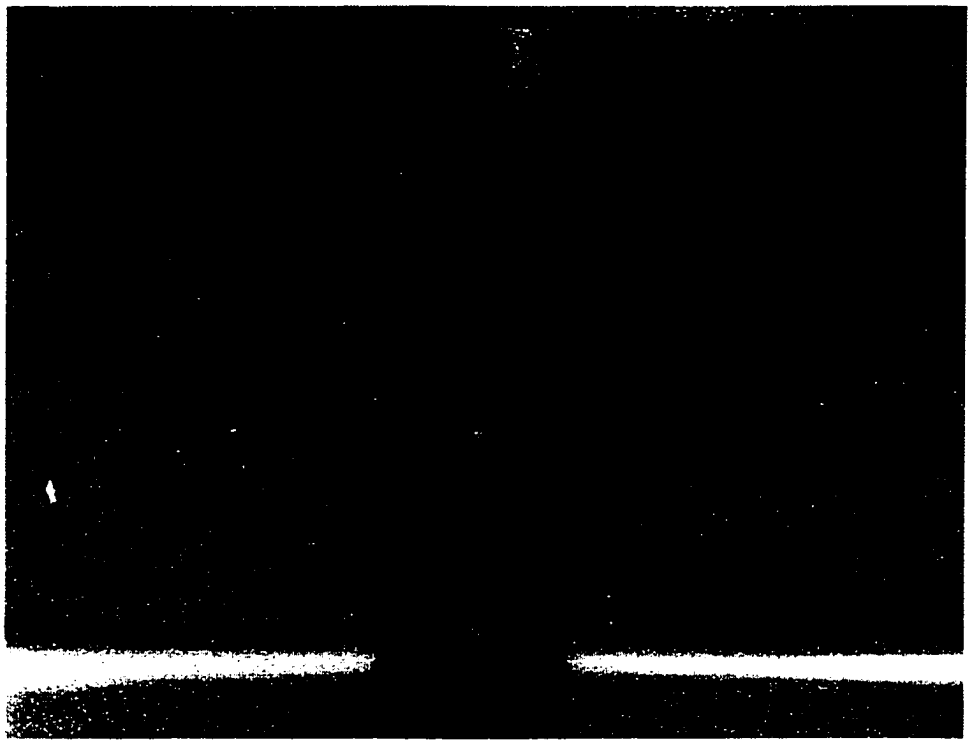

Fig. 2.23: Photograph of assembled make-switch electrical feed showing how the contact wire rests atop the injector cover cap when installed in the chamber.

The igniter head and make-switch electrical feed are usually covered with some charred epoxy and the igniter has some aluminum foil residue which should be removed. The igniter and make-switch electrical feed tips are then polished lightly with very fine sandpaper to provide a clean electrical contact. The pressure port is inspected and the column prepped with vacuum grease if necessary according to manufacturers directions (see Section 2.3.2).

The window, igniter, and make-switch electrical feed ports are installed and then the diagnostic cover plate and heat shield are tightened down into place with twelve grade-8 cap screws. The stainless steel cover plate must be inspected for warping before installation. This warping is caused by uneven thermal stresses between the outside surface exposed to hot gases and the inside surface which contacts the cold plug base metal. Warping of the plate effectively reduces the squeeze on the main seal and this can lead to seal failure at combustion pressures. To avoid the uneven heat loads on the diagnostics cover plate, a 0.125 in. (0.318 cm) thick copper "heat shield" plate is used which has been found to effectively alleviate plate warping. After the two plates are installed, the igniter is fitted with a foil and the igniter and optics cover caps are screwed in place, where care is taken to center the respective shim washers when tightening the cover caps. The igniter foil is pricked to form two tiny pinholes which prevents the foil from tearing during gas purging and filling.

The make-switch electrical feed is assembled as shown in the photograph in Fig. 2.23. The anode mounting post and Teflon insulating washer shown in Fig. 2.20 are tightened down onto the electrical tip of a second "igniter" insert, ensuring the post is centered. Then the contact wire is attached to the anode post using a small screw in the tip of the post, and the offset distance between the foot of the contact wire and the optical window cover cap is set to 4.0 cm. Then when the plug is lowered down into the chamber, the foot of the "L" shaped cantilever-like contact wire comes to rest on the injector's cover cap with ~1 cm interference. This interference produces a spring-like compression which has been found necessary to ensure the contact wire remains in contact with the injector cover cap during gas-phase combustion. Once diagnostic installation is completed and prior to closing the chamber, the electrical continuity of the pressure transducer, igniter, and make-switch leads should be verified.

The particle injector is then readied for assembly where this can be done independently of the chamber preparation. The particle injector components must be closely inspected and may require significant preparation depending on the previous experiment. The housing barrel through which the piston/plunger travels must be smooth and scratch free. Typically pitting occurs at the base of this barrel and this should be removed by polishing the barrel bore with extra-fine sandpaper on a rubber mandrel. It is also important to inspect and possibly replace the plunger base seal and remove entrained boron particles from the guide collar seal. The plunger base seal surface must be smooth, scratch-free, and pit-free or else finite leakage past the seal into the cavity above the rising injector-plunger will slow (dampen) particle injection.

As was previously mentioned in Section 2.2.4, the pintle on the injector is susceptible to wear and this wear is difficult to detect, necessitating careful inspection of the pintle diameter with a micrometer. Close inspection of the injector components is stressed because if the injector components meet specifications then the injector will function properly and reliably, and based on experience, there is greater than a 90% chance of a successful particle combustion measurement (other "failure" modes include make-switch timing failure or improper gas mixture metering). Operation with worn injector seals, or pitting on the base seal or injector bore, and/or wear on the pintle will likely result in poor injection or no injection.

To load particles into the injector the piston/plunger is pushed part way down into the housing bore and the plunger tip inserted into the guide collar seal just deep enough to expose about two-thirds of the particle annulus. This temporary configuration is then inverted and particles are placed into the exposed annular particle groove using the tip of a hobby-knife blade as shown in Fig. 2.24 a. Once ~5 mg sample are loaded, the injector is slowly depressed deeper into the guide collar seal just far enough to cover the entire annulus. Then the injector housing and ejector plate are pushed back together to seat

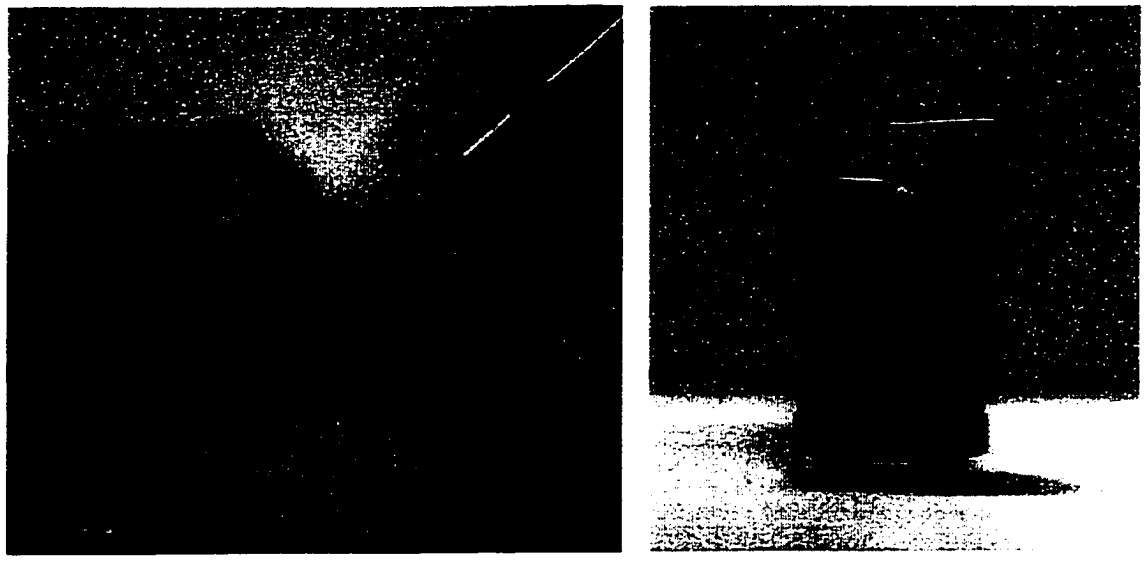

(a) (b)

Fig. 2.24: Left photograph (a) showing particles being placed into the inverted, partially assembled particle injector. Right photograph (b) shows the fully assembled particle injector and timing mechanism which is ready to be installed in the chamber.

the plunger in the piston bore at its proper starting position. The orifice plate, housing, and ejector plate are fastened together using four screws which are threaded into holes in the ejector plate. Then the copper shield and injection-timing bridge-wire are attached using short screws and the bridge-wire height is set precisely with a micrometer. The fully assembled injector is shown in the photograph in Fig. 2.24 b. The injector is mounted onto the chamber exhaust cover cap using two mounting posts which remain affixed via metal-to-metal press fits. At this point the injector is fully assembled and all exposed surfaces on the injector are wiped clean with alcohol before installation in the chamber.

The particle injector will be properly positioned in the chamber with respect to the optical window and make-switch contact wire when the exhaust cap is screwed down onto the threaded copper exhaust liner. Once the injector is mounted inside the chamber, then the main seal on the top plug is readied for closing the chamber. The main seal's outer surface is greased liberally to allow for easy insertion into the chamber throat when the top plug is lowered into place. Once the plug is seated, the four retention pins are inserted and the chamber is ready for pressurization. The chamber is first purged with 300 psia of nitrogen during which time the entire system is examined for leaks. The chamber is vented and a second and final purge of 300 psia is applied and fully vented. A residual of ~8 psia of purge gas remains in the chamber at this point (there is a check valve in the exhaust tank) and the chamber is ready for loading with combustion gases for that experiment.

The gas handling system for the high pressure combustion chamber is shown schematically in Fig. 2.25. All of the gas supply bottles are located in an adjacent room removed from the experiment.

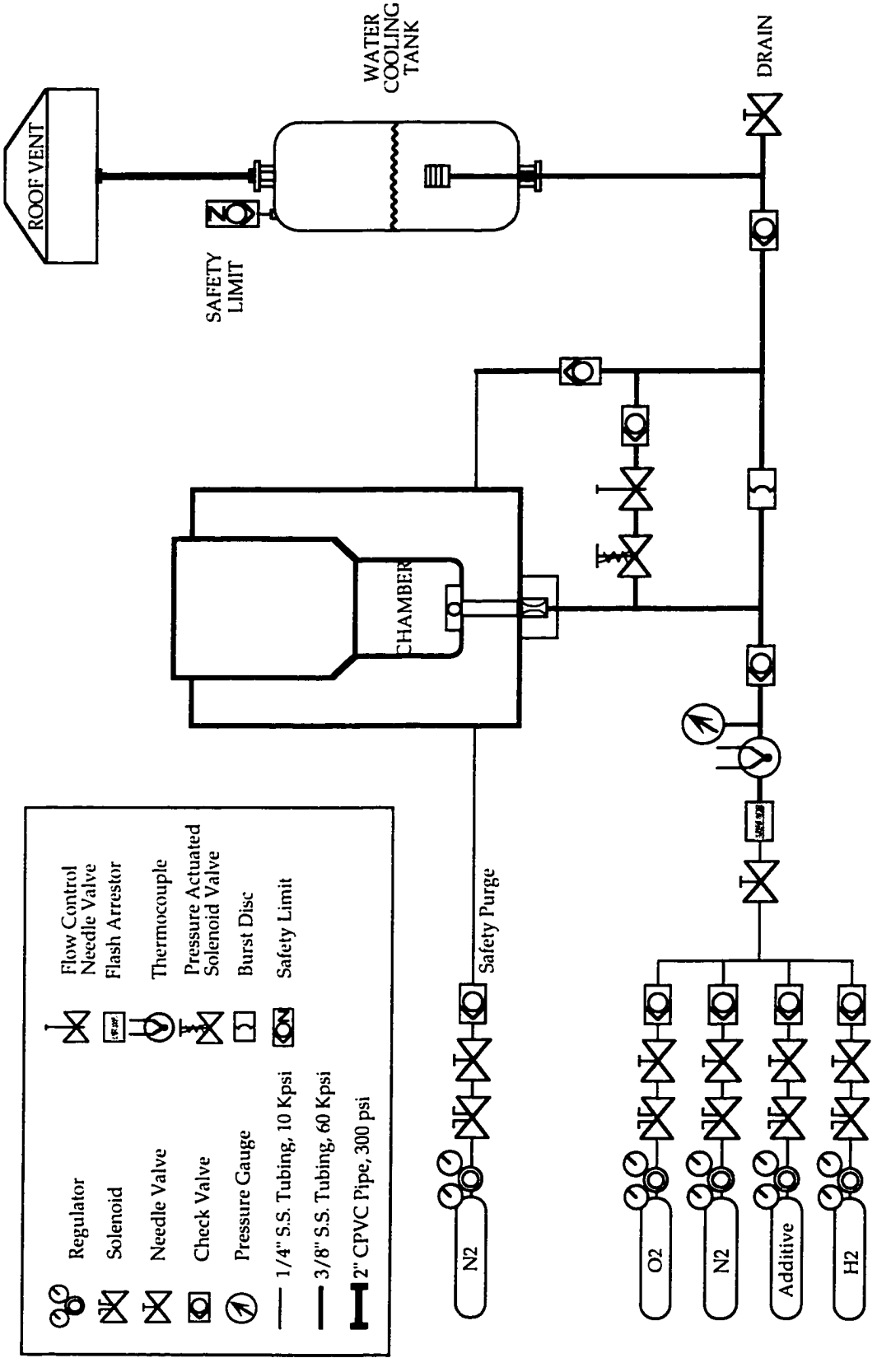

Fig. 2.25: Schematic of high pressure combustion chamber gas handling system.

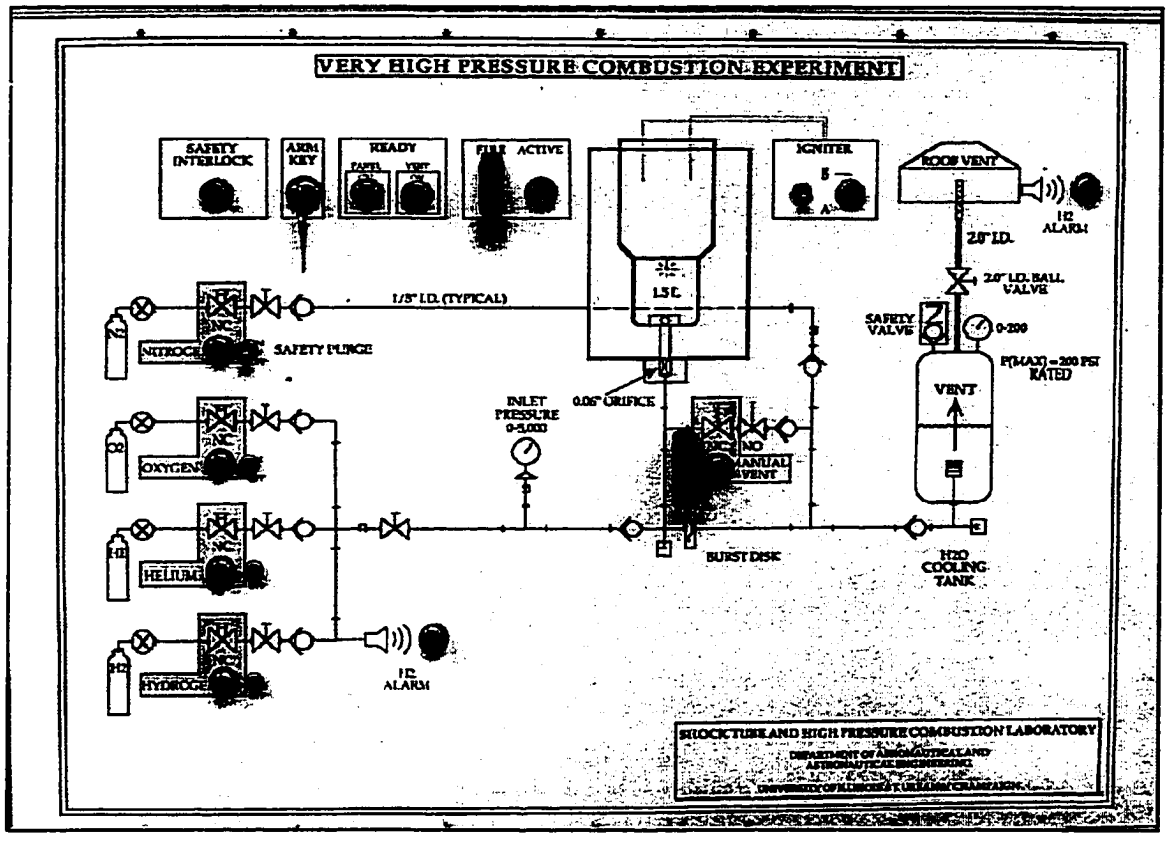

Fig. 2.26: Photograph of the hpcc control panel showing gas feed actuation switches on the left, two hydrogen-alarm interrupts, manual vent switch under the chamber schematic, and safety interlocked FIRE switch to the left of chamber schematic. Small lights are used to indicate active processes. Since the photo was taken, helium was replaced by nitrogen and gas lines for particle ignition-enhancing gases were added.

Water is added to the exhaust line cooling system which simply consists of a tubular enclosure of PVC pipe along the entire length of the exhaust line. This cooling is required for operation at and above 300 atm, where convective heating from the flowing exhaust gases thermally stresses the exhaust line to a noticeable extent. Cooling is used at all pressures to equilibrate the line temperature during gas filling. The gas supply lines from the tank farm up to a break off point which then feeds into the combustion chamber are 1/8" I.D. by 1/16" wall thickness, 316 stainless steel tubes rated to 10,000 psia (680 atm). The inert, oxygen, and any benign additive gases share a common manifold whereas the hydrogen gas line is coupled in at a later point. Where the gas inlet line breaks off toward the chamber, and continuing through the exhaust system, 1/8" I.D. by 1/8" wall thickness, 316 stainless steel tubes rated to 60,000 psia (4080 atm) at room temperature are employed. A surge valve (snubber) and flash arrestor separate the inlet and exhaust lines to protect the inlet pressure gauge from rapid pressurization and hot combustion gases.

All gas loading is accomplished remotely from the control room via electrically actuated solenoids. The control panel from which gas loading is controlled is shown in the photograph in Fig. 2.26. The gas fill system has two safety interrupts where the first interrupt is either of two hydrogen leak detectors and the second interrupt is the lab ventilation system. One of the leak detectors is located in the gas supply room and the other directly above the chamber. If either a hydrogen leak is detected or flow in the exhaust ventilation system ceases then power to the gas-filling system will be interrupted and all gas fill solenoids will return to their normally-closed position. Control wires from the control panel are distributed to respective actuators through a cable tray which hangs from the ceiling and is electrically isolated form the building. Diagnostic signal carrying wires are contained in a separate 5.1 cm diameter hard copper pipe cable guide which is grounded commonly with the chamber vessel and data acquisition system.

Fill gas pressure is measured slightly upstream of the chamber with a Sensotec model TJE, intrinsically safe, pressure transducer. The model TJE transducer has a diaphragm with a 4-arm bonded-foil strain gauge bridge. The unit has a measuring pressure range of 0-5,000 psi and quoted infinite resolution. A model GM-A single channel digital display and amplifier with 1 psi readout resolution is used in combination with the transducer. Special care must be taken during gas filling to allow pressure to equilibrate inside the chamber - the gases will cool as discussed below. Gas temperature is measured in the inlet line near the pressure transducer with a K-type thermocouple which is monitored with an Omega digital HH-81 readout with a readout accuracy of 0.1 °C. Figure 2.25 shows the placement of the inlet line pressure transducer and thermocouple.

The gas fill pressure is monitored from the GMA unit's digital readout located adjacent to the control panel. A snubber valve is used to isolate the gauge from the combustion event and exhaust gases. The snubber is normally open but the ball effectively seats with an instantaneous 2 psi over-pressure from the downstream side. Gases are loaded sequentially and pressure allowed to equilibrate before the next gas is added, typically for 180 sec. All gases used in the experiments are obtained from a local distributor and originated from MG Industries. The hydrogen gas has a stated purity of 99.99%, the oxygen and nitrogen have stated purity 99.95%, and the helium 99.995%. The mixture additives are obtained directly from MG Industries; the carbon dioxide, methane, and sulfur hexafluoride are respective grades with stated purity 99.99%. All gases were used as delivered without additional purification.

Prior to gas mixture loading, the chamber is purged twice to 300 psia to flush and dilute any residual air in the chamber cavity. The resulting effect of the residual gas in the chamber is very small and is neglected. The desired gas composition in the chamber is determined by Dalton's Law of Partial Pressures, where the mole fraction of each constituent X_i is given by

$$X_i = \frac{p_i}{p_1} \tag{2.1}$$

where p_i is the gas partial pressure for the i^{th} gas and p_1 the total pressure. The gas loading sequence is nitrogen purge(s) and venting, then partial fill with nitrogen, hydrogen fill, oxygen fill, additive fill, and nitrogen top-off to clear the inlet lines of combustible gases. The gas temperature typically varies less than ±0.3 °C throughout the filling process, which can last up to 30 minutes, and this variation is neglected because gases are allowed to equilibrate with the chamber wall temperature between successive gas fills.

Once the last gas to be added has reached its steady specified pressure, the gas mixture is allowed to molecularly mix for at least an additional 600 seconds (1200 seconds for highest nitrogen dilution). During this time the data acquisition system and triggering are double-checked by cold-firing (no voltage on the capacitors) to check zero-readings on the instruments and proper functioning of the high voltage switching. Just prior to firing, the capacitor bank is charged to full voltage (4000 volts), the control panel FIRE switch is armed, and the data acquisition system's triggering reset. When the chamber is ready to fire, the capacitor power supply is shut off with a quick interrupt switch and the control panel FIRE toggle switch activated. Data acquisition is automatically initiated and ignition of the combustible gas mixture ensues providing the high pressure, high temperature ambient conditions into which particles are injected, ignited and fully combusted. Typically transient pressure, combustion emissions bandpass filtered at several wavelengths, particle injection timing, and occasionally capacitor discharge are measured.

Chamber venting is accomplished automatically through the burst disc which is rated to rupture for the test conditions anticipated. An inert purge of the exhaust system is initiated immediately subsequent to firing to purge the exhaust lines and chamber, and especially to cool the injector. Manual venting can also be initiated from the control panel should problems arise with automatic venting. Once venting is completed all recorded data is downloaded from the digital recorder and saved to computer for analysis.

Subsequent to an experiment the combustion chamber is disassembled, cleaned, and dried off. It is ideal to disassemble and clean the injector soon after an experiment to avoid further degradation of seals and the inside barrel surface of the injector. The diagnostics cover caps are also removed for cleaning and inspection of components. All transducer leads are stowed and the exhaust line is flushed out with water flow for ~300 seconds and blown dry with compressed air to purge the exhaust line of any remaining water. The chamber is then wiped clean, scrubbed out and neutralized with alcohol to prevent rusting, and blown out with compressed air to dry.

In the experiments where hydrogen fluoride (HF) is produced to study the effects of fluorine compounds on boron ignition and combustion, special care must be taken during disassembly of the chamber. HF resistant gloves, full face and eye protection, and a respirator are worn to ensure no remaining HF vapors are inhaled. The chamber is flushed with a solution of sodium hydroxide and then purged with fresh water prior to physically opening the chamber. Subsequently all parts and especially the injector are handled with gloves and flushed with sodium hydroxide solution and are then rinsed with fresh water.

2.2.6 Gas Loading, Mixing, and Ignition Issues

There are several important safety and practical operation issues concerning filling potentially explosive gases into the combustion chamber. These issues include safely handing explosive gas mixtures, providing sufficient mixing times, and repeatable ignition, and they are discussed here.

Gas leaks are potentially dangerous and steps are taken to reduce the associated dangers. The initial nitrogen purges not only dilute the residual air in the chamber but are also used to check the system for leaks which could prove disastrous due to the use of hydrogen. Leaks are rare but sometimes the burst disc leaks because it was crimped during the burst disc holder assembly - if this occurs it is simply replaced. Gas lines are limited to 0.125 in. (0.318 cm) diameter to prevent flashback in the event pre-ignition occurs somewhere in the system. All gases are slowly metered into the chamber to prevent pre-ignition induced by rapid mixing, and are added sequentially in a prescribed order. Hydrogen is added after the chamber has been filled partially with nitrogen and before oxidizer is added, so that this initial fuel mixture is both diluted and free of oxidizer. Then oxygen and any boron particle gaseous ignition-enhancers are added followed by the final percentage of nitrogen diluent to purge the gas fill lines.

Experience has taught that gases which have flowed through the narrow gas lines cool considerably once inside the chamber. This causes the chamber pressure to drop initially between gas fills and one must allow sufficient time for the pressures to equilibrate and stabilize prior to adding subsequent gases. A time of ~180 seconds has been found sufficient to allow pressures to equilibrate. Without this pause to allow for mixing, partial pressure readings will be inaccurate and result in incorrect mixture ratios since gases are added in succession. This effect although seemingly insignificant becomes evident in measured pressures and background hot gas emissions which are not repeatable between experiments when insufficient time was given for cooling.

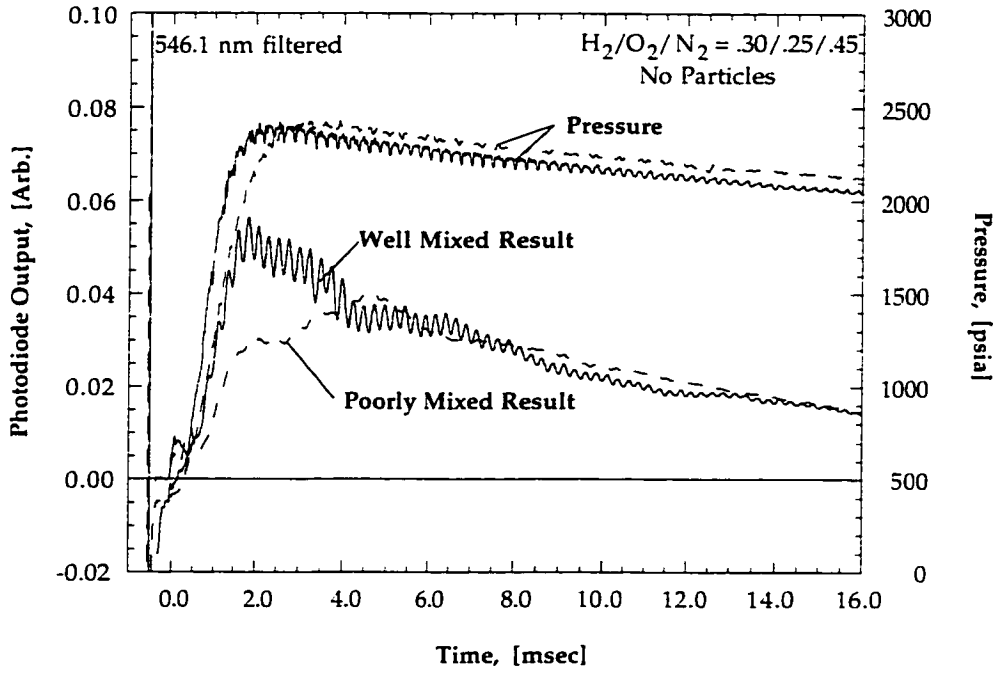

Fig. 2.27: Measured pressure rise and hot gas emission from two experiments with different degrees of initial gas mixing. When gases are allowed to mix for only ~180 sec (dashed curves), the resulting pressure rises more slowly than in the well mixed case (~600 sec, solid curves), especially near peak pressure, and the filtered hot gas emissions exhibit a double hump or "hiccup". Hot gas emissions are similar after 5 msec but the well mixed case displays greater oscillations. The results from the poorly mixed case are indicative of unmixed nitrogen at the bottom of the chamber, where nitrogen is the last component added to the mix.

Once all gases are filled the final mixture must be allowed to mix molecularly for good premixed combustion to occur. A pause of ~600 sec was determined by trial and error to be sufficient for this mixing. It was observed that gases mixed for only 300 sec typically resulted in a slower pressure rise during gas-phase ignition than if gases were mixed longer, whereas mixing for 1200 or 2400 sec resulted in no discernible differences from 600 sec mixing. If the final gas mixtures are not allowed to mix sufficiently, the measured pressure rise and photodiode signals will be different than anticipated, as shown in Fig. 2.27. The pressure rises more slowly in poorly-mixed gases than in well-mixed gases and the filtered photodiode signals (without particles) typically exhibit a double hump, or "hiccup", as shown in the figure. This behavior is thought to be caused by unmixed nitrogen at the bottom of the chamber, where nitrogen is the last gas added to the mixture.

The false results due to insufficient gas mixing cannot be more clearly demonstrated than in a few cases where nitrogen was replaced with helium to achieve even faster pressure rises. When the gases were not allowed to mix sufficiently, it was possible to obtain very nice and rapid combustion in the chamber. However, when the gases were allowed become well-mixed, *detonation resulted*!

Filling gases slowly, pausing between filling subsequent gases, and allowing ~600 sec for gases to molecularly mix after the final mixture is reached, have all shown to give repeatable measurements when no particles are present. Such measurements provide baseline hot gas emission levels which are required to determine net-particle emissions, as will be discussed in the next chapter. Numerous measurements were conducted without particles present and these "no-particle" signals were averaged to determine nominal average hot gas emissions.

2.2.7 Discussion of Gas Mixture Combustion and Pressure Decay

The achievable final pressure, pressure rise time, and pressure stay time are important parameters for the particle combustion experiments. Mixtures of nitrogen-diluted premixed hydrogen and oxygen are combusted to provide various high temperature, high pressure mixtures of prescribed gas composition for conducting particle combustion experiments. The fuel and oxidizer choice provides rapid combustion, simple products, and high temperatures. Nitrogen is a convenient detonation-preventer and is furthermore used to control test temperatures while providing similar mixture properties to air. The mixtures used are detailed in Table 2.1 and will be further discussed in later chapters. The chamber could just as well be configured to use solid propellants to establish ambient product mixtures, but there the pressure rise times are significantly longer.

Achievable peak pressure performance measured in the high pressure combustion chamber is displayed in Fig. 2.28 for the various combustion mixtures used in these experiments. In the figure

Table 2.1: Premixed nitrogen-diluted hydrogen/oxygen mixtures used for establishing high pressure and high temperature conditions for particle combustion. The product distributions for these mixtures are given in Table 2.3.

Mixture	Initial Mix Mole Fractions								
	p_1 [atm]	H_2	O_2	N_2	CO_2	SF_6	p_2 [atm]	T_2 [K]	$p_{2,ms}$ [atm]
A	10.9	0.30	0.25	0.45	0	0	90	2860	86
A	20.4	0.30	0.25	0.45	0	0	166	2875	160
B	5.8	0.28	0.32	0.40	0	0	46	2725	44
B	10.9	0.27	0.32	0.41	0	0	84	2665	80
B	20.4	0.27	0.32	0.41	0	0	158	2675	153
C	22.8	0.26	0.24	0.50	0	0	176	2655	164
D	23.8	0.24	0.22	0.54	0	0	167	2475	156
E	20.4	0.28	0.29	0.39	0.044	0	158	2665	151
F	5.8	0.29	0.34	0.37	0	0.007	58	2750	43
G	22.8	0.26	0.18	0.56	0	0	169	2660	158

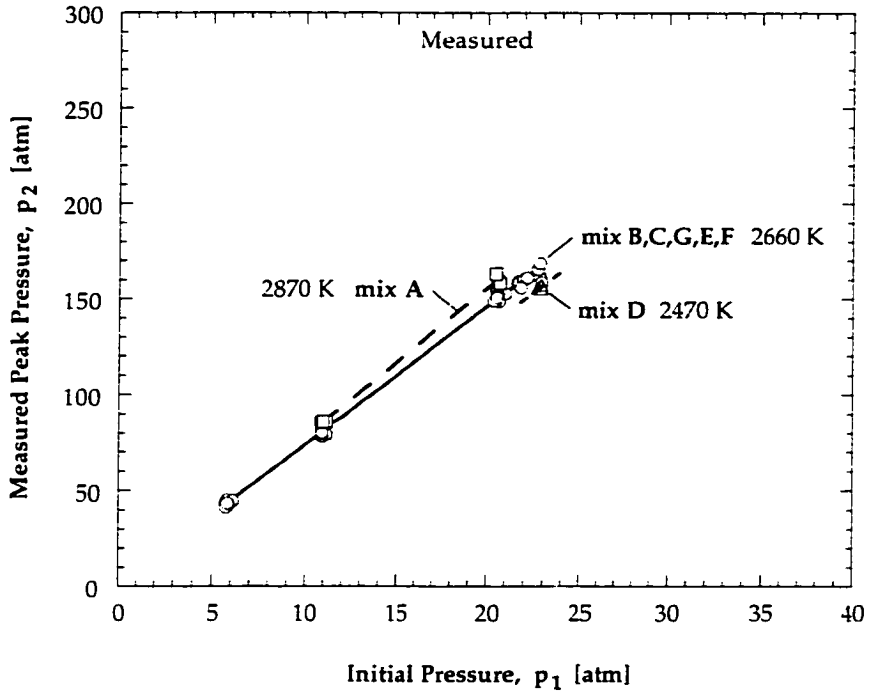

Fig. 2.28: Combustion chamber peak pressure performance as a function of fill pressure for various combustible mixtures used for particle experiments.

measured peak pressure is plotted as a function of initial chamber fill pressure. It appears that the achievable peak pressure in the chamber is more a function of combustion temperature than the initial gas mixture or the percentage nitrogen dilution; mixtures with average peak temperature ~2660 K (T_2) all lie on the same trend-line whereas higher peak pressure is achieved in mixtures with 2870 K peak temperature, and lower peak pressure at 2470 K. The measured performance can be expressed as a function of initial fill pressure by a formula of the type

$$p_{2,ms} = \text{fctn.}(T_2, p_1) = \text{const.}(T_2) \cdot p_1 \qquad (2.2)$$

where $p_{2,ms}$ is the measured peak combustion pressure. For 2870, 2660, and 2470 K the constants are 7.78, 7.30, and 6.84 respectively. The constant is truly invariant to the initial gas pressure and it is believed that this invariance is a good indication that heat losses can be neglected during gas-phase ignition and combustion.

Measured peak pressures are always lower than equilibrium predicted values and are typically between 90 to 95% of the ideal values. Such differences have been noted previously[49,50] and in particular are noted in light gas gun experiments[51] using H_2/O_2/He mixtures, which were used as a baseline for the expected performance in the hpcc. The ratios of measured peak pressure to equilibrium calculated peak pressure, averaged over many tests, are .940, .936, and .924 for the

hydrogen/oxygen/nitrogen mixtures producing 2870 K, ~2660K, and 2470 K peak combustion temperatures. As will be discussed below, even lower ratios are indicative of incomplete mixing of fill gases. Heat loss timescales are several orders of magnitude longer than the global gas-phase combustion timescales, as will be discussed below.

In the particle experiments it is desirable to have fast pressure equilibration from the standpoint of particle injection given the limited physical configurations of the injector. Then also heat losses during gas-phase ignition and combustion will be small simplifying chemical equilibrium calculations.

A typical pressure measurement for a 300 psia (20.4 atm) initial pressure mixture was shown in Fig. 2.2 a where the pressure rise time (t_{pr}) and pressure stay time (t_{ps}) were indicated. It is seen in the figure that pressure equilibration is on the order of several milliseconds and that pressures peak and remain fairly constant for some time. The pressure rise time is defined as the time from initial pressure rise to 90% of peak pressure. The pressure rise times for the various mixtures tested are plotted in Fig. 2.29 as a function of peak pressure. The pressure rise times are generally between 0.9 and 1.4 msec and are fairly invariant to final pressure. They are not simply a function of combustion temperature either (generally shorter t_{pr} for higher peak temperature mixtures), but are highly dependent on the percentage nitrogen dilution in the initial mixture. Mixtures D and G have long pressure rise times which are at least double those of the other mixtures used and both mixtures have ~55% initial nitrogen. These mixtures are used to establish conditions of low final temperature and low excess oxygen conditions for particle combustion.

Although local chemical timescales are very short, a deflagration front must first traverse the entire chamber and completely burn the gases, establishing a uniform peak pressure in a time limited by the flame front propagation across the chamber. The characteristic deflagration speed over the 2 liter chamber is ~50 m/sec. The time required for full gas-phase combustion is on the order of particle heating and ignition times for the small particles (10-50 μm) of interest to propulsion devices, and this inevitable fact has necessitated the development of an injection technique which allows for particles to be injected after sufficient delay to allow ambient conditions to be fully established.

Since pressure rise times are so short compared to typical heat loss timescales (see below), heat losses during this "pressure-rise" are neglected when performing equilibrium calculations to predict mixture compositions. State "2" is assumed to hold when maximum pressure is reached, and the temperature there is T_2, the calculated peak combustion temperature, as is done in common practice.

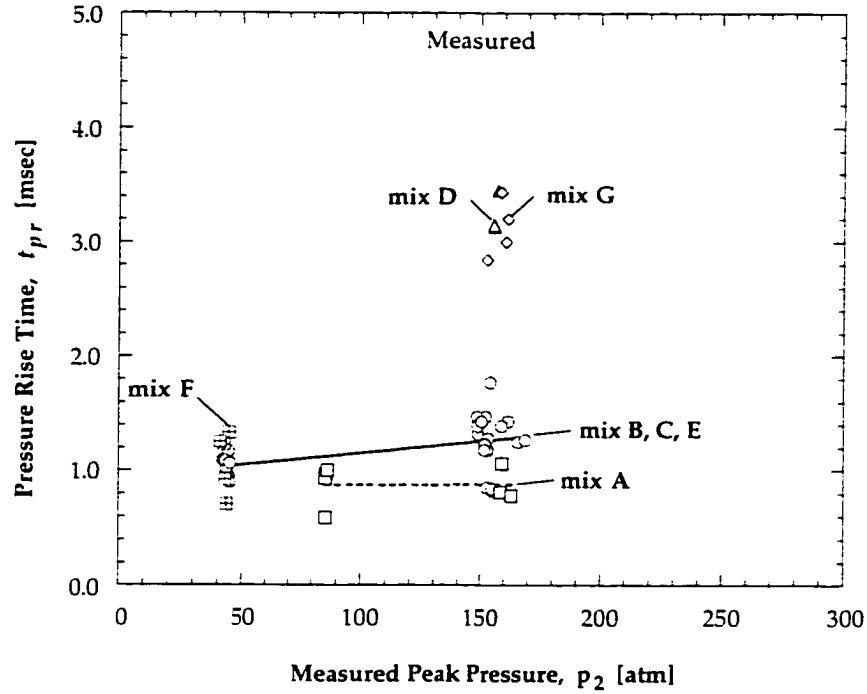

Fig. 2.29: Plot of nominal pressure rise time (t_{pr}) as a function of peak pressure for various combustible gas mixtures.

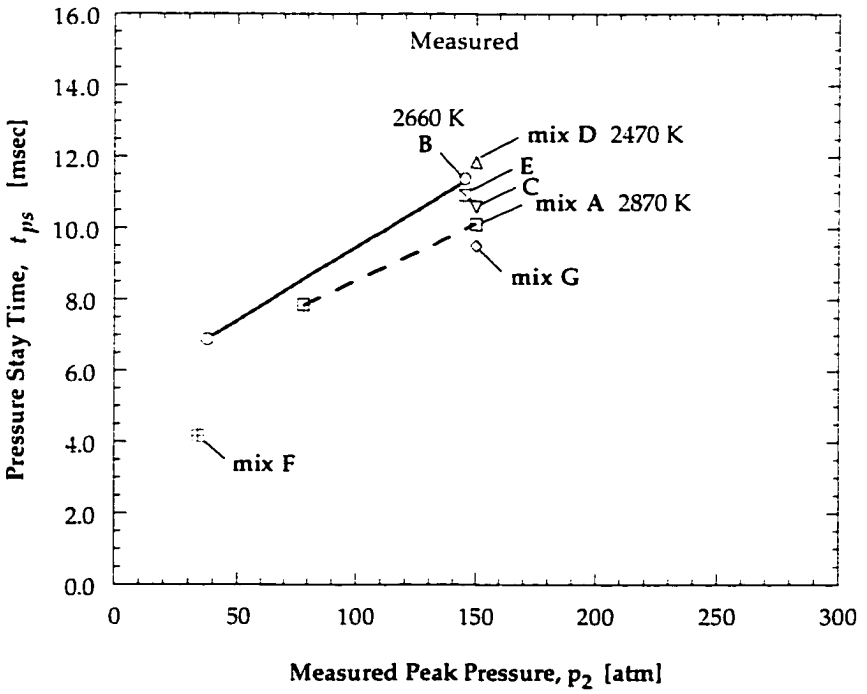

Fig. 2.30: Plot of nominal pressure stay time (t_{ps}) as a function of peak pressure for various combustible gas mixtures.

It is also desirable to retain a fairly constant pressure over the particle ignition and combustion lifetime because it is the intent to determine particle ignition and combustion at constant pressure. Since chamber pressures decay slowly with time (see Fig. 2.2 a) particle combustion does not occur at constant pressure but *nearly* constant pressure. In Fig. 2.30 the measured pressure stay times are plotted as a function of peak pressure and they are seen to be typically 8 to 12 msec. Higher pressure mixtures display longer pressure stay times (slower pressure decays), where typical pressure fall-off rates are ~1.4 atm/msec. By definition of t_{ps} the pressure does not change more than ±5% over the times plotted in the figure. Over the span of boron particle lifetimes measured pressures typically vary less than ±2.5 atm of the mean. In practice an average pressure is determined for the ignition or combustion event and this average is treated as a constant where the small variation about the mean is treated as part of the uncertainty in the measurement.

The achievable nearly constant pressure regime in the combustion chamber is much longer than in a comparable shock tube. In the combustion chamber pressures fall as a result of gas heat losses near the chamber walls and these are comparably slow processes, whereas in the shock tube shock wave interferences typically limit test times to 0.6 to 1.5 msec.[12,24] These longer test times in the combustion chamber come at the expense of longer pressure rise times however.

After peak pressure is reached within ~1.5 to 4 msec of H_2/O_2 gas ignition, the chamber pressure is seen to decay slowly at a rate of ~0.2% per msec. This is likely a result of gas heat losses where the possible heat loss mechanisms include conduction, radiation, and condensation on the surrounding metal chamber walls. Simple transient one-dimensional conduction heat transfer analysis[52] for a hot sphere of gas conducting to a cold wall at constant temperature (since the wall thermal conductivity $k_w >> k_g$ the gas thermal conductivity) gives a characteristic conduction heat loss time constant of between 30 and 80 seconds for mixture B at 37.5 and 145 atm (see Table 2.1). The corresponding characteristic radiation heat loss time constants, assuming the gas volume radiates as a black body with zero optical depth which corresponds to the greatest heat loss case possible, are 0.9 and 3.3 sec. These numbers indicate heat losses occur on long timescales compared to the particle ignition and combustion times. Condensation losses in the growing thermal layers along the chamber walls (see Section 3.5.1) are confined to a region less than ~0.2 mm thick during the time-frame of particle injection and combustion resulting in a fractional mass loss less than ~0.1% from the 30% water vapor gas mixture, which is negligible.

The question remains whether the observed pressure drop in the chamber can be accounted for by conduction and radiation. For mixture B at high pressure, the total chemical energy release is ~110 kJ. The heat transfer analysis for a conducting sphere predicts a heat loss of approximately ~16 J/msec and heat transfer from a sphere radiating as a black body ($\varepsilon = 1$) is ~750 J/msec, so that the fractional loss

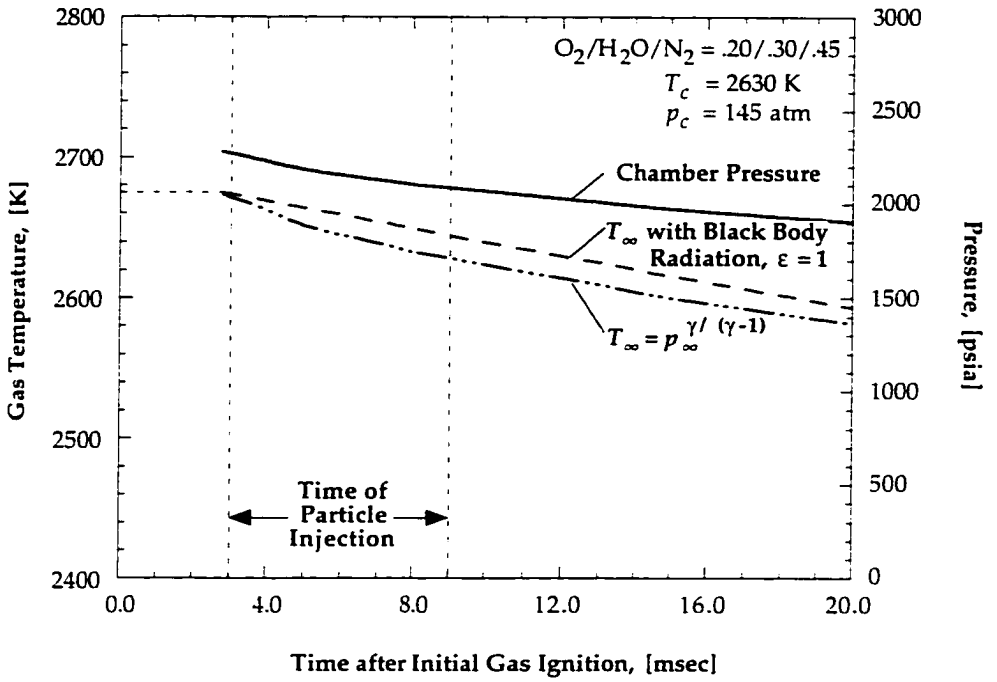

(a)

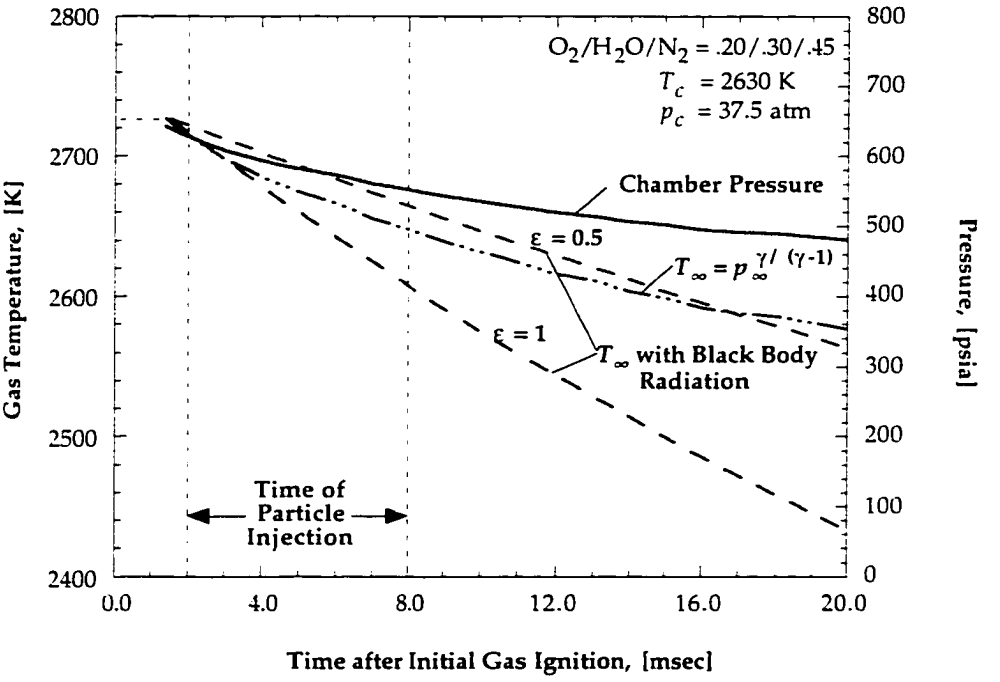

(b)

Fig. 2.31: Comparison of ambient gas temperature fall-off based on measured pressure decay to calculated temperatures based on radiation loss from a sphere of zero optical depth of equivalent surface area/volume to the combustion chamber. Pressure and temperature profiles at (a) 145 atm and (b) 37.5 atm. The assumed radiation loss mechanism at low pressure (ε = 1) far over-predicts the temperature decrease with time.

per msec is 0.7% of the total energy. In the ~20 msec time-frame for particles to be injected, ignited, and burned to completion the energy lost will therefore be small compared to the gas total energy. This energy loss rate is compared to the measured pressure decay for the same mixture which is 1.1% per msec. These rough calculations suggest the pressure drop in the chamber is a result of gas heat losses.

Both estimates of energy losses are based on cumulative heat transfer at the edges of the mass of hot gas to the cold chamber walls. The resulting temperature drop will be much less at the center of the chamber where particles are injected than at the periphery. Heat lost at the periphery of the hot gas core will cause gases in the chamber to expand to remain at uniform density (constant volume). Based on the long characteristic heat loss timescales for conduction and radiation, it is assumed that gases at the center of the chamber where particles are injected are expanding adiabatically and ambient temperatures $T_\infty(t)$ are calculated from the measured pressure decay by $p_\infty / T_\infty^{\gamma/(\gamma-1)} = \text{const.}$ With this assumption the differential temperature loss rate for mixture B at high pressure is $\Delta T_\infty / T_\infty$ = 0.2% per msec.

The resulting temperature decay rate for most mixtures is ~5 K/msec. For tests conducted with HF, heat loss rates calculated from the measured pressure decay are much higher initially than in all other mixtures studied; the temperature decreasing as rapidly as ~30 K/msec over the first 6 msec and then leveling out to ~10 K/msec thereafter. The resulting calculated temperature decays from heat losses are shown in Figs. 2.31 a, b for mixture B compared to temperatures calculated assuming an adiabatic process at the center of the chamber. It is seen that the agreement at high pressure (145 atm) is very good, within 20 K, and except for the initial 3 to 4 msec, the heat loss rate also agrees very well. At lower pressure (37.5 atm) the temperatures calculated from measured pressures decrease much less rapidly than radiation losses predict ($\varepsilon = 1$), indicating the gases are likely not radiating as strongly as assumed ($\varepsilon = 0.5$).

2.2.8 Discussion of Nitrogen Dilution and Detonable Mixtures

Nitrogen is added to the initial gas mixtures in the combustion chamber experiments to control post-combustion gas temperature *and to prevent detonation.* Hydrogen/oxygen mixtures are very detonable and Nettleton[53] gives the detonation limits for confined detonations as 15 to 90% H_2 in oxygen and as 18.3 to 58.9% H_2 in air. A graph taken from Ref. (53) showing the amount of nitrogen required to suppress detonation in hydrogen/oxygen mixtures is shown in Fig. 2.32. Also shown in the figure are the hpcc gas mixtures used in this study where it can be seen that all mixtures lie outside the detonation limit for nitrogen-diluted hydrogen/oxygen mixtures. Nettleton cautions that the curve in

the figure is not a sharp boundary since enclosure geometry and initial mixture pressure also effect the detonation limits.

Inert gases such as helium and argon are much less effective detonation inhibitors than nitrogen.[53] Tests were performed in the combustion chamber with helium replacing nitrogen in two mixtures and it was observed that these mixtures became detonable when the gases were allowed sufficient time to mix molecularly. The mixtures were mixture A' (45% He, replacing the N_2) and mixture B' (41% He, replacing the N_2).

Detonations can be studied in the hpcc but they lead to additional operational complications. Typical measured pressures and photodiode signals are very "noisy" due to the detonation wave(s) reflections within the chamber. Gas temperatures behind the reflected detonation front were so high that the exposed quartz window surface fogged. The high temperatures also caused the diagnostics cover plate to warp in such a way as to reduce main seal o-ring squeeze, which could lead to seal failure. Although the window surface became fogged, the integrity of the optical window seal was never compromised in the detonation experiments.

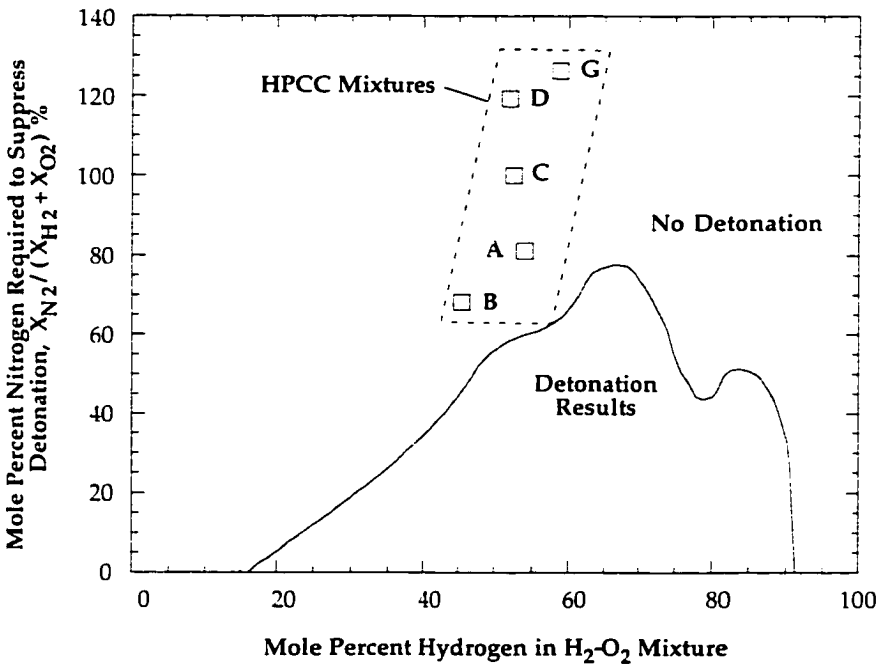

Fig. 2.32: The amount of nitrogen additive required to suppress confined detonations in hydrogen/oxygen mixtures, from Nettleton.[53] The hpcc gas mixtures used to produce high pressure and high temperature ambient mixtures for particle combustion lie outside the limits for detonable mixtures.

2.3 Diagnostics and Data Acquisition System

2.3.1 External Trigger and Digital Recorder System

Data acquisition consists of a single time resolved chamber pressure measurement, particle injection timing, and multiple photodiode measurements of the combustion event. A diagram of the data acquisition system used in the particle combustion experiments is shown in Fig. 2.33. At the heart of the system is the Soltec ADA-1000, an 8-bit, 10 MHz sampling digital transient waveform recorder. The recorder is equipped with four independent channels each with 64 kbyte memory length for use in the time resolved measurements. Typically 1 MHz sampling is used for the experiments described. A single channel is reserved for transient pressure measurement, two channels are reserved for centerline-viewing photodiode measurements, and the remaining channel is used for either off-axis photodiode measurement, monitoring the capacitor discharge powering the spark igniter, or measuring particle injection timing. The Soltec recorder is interfaced with an IBM-AT computer through an IEEE-488 parallel interface port. Recorded data is downloaded to this computer for first-glance analysis and data storage.

An external triggering source is used to initiate data acquisition by the Soltec ADA-1000 recorder. The trigger is located inside the high voltage FIRE switch. Figure 2.34 shows a schematic of the pneumatically actuated, high voltage firing switch which connects the capacitor bank to the combustion chamber igniter. The switch consists of a pressure supply port, an electrically actuated flow control solenoid, an Omega model PSW-523 pressure actuated switch, a gas operated linear acting piston, and brass high voltage contact leads. The high voltage switch is remotely operated from the control panel located in the control room. The build up of line air-pressure which actuates the linear piston to close the high voltage switch also triggers the data acquisition via the pressure switch. A TTL signal from the Soltec external trigger port is shorted onto itself when the pressure switch closes, thereby triggering the Soltec to initiate data acquisition. The pressure switch's activation pressure can be adjusted so as to effectively adjust the triggering delay.

At the periphery of the data acquisition system shown in Fig. 2.33 are the combustion diagnostics which consist of a high speed pressure transducer and the multiple photodiode optical detection system. The other "diagnostic" is the make-switch which has been previously described in Section 2.2.4. The spectrometer setup with the optical multichannel analyzer, to be discussed below, can be used interchangeably with the photodiodes.

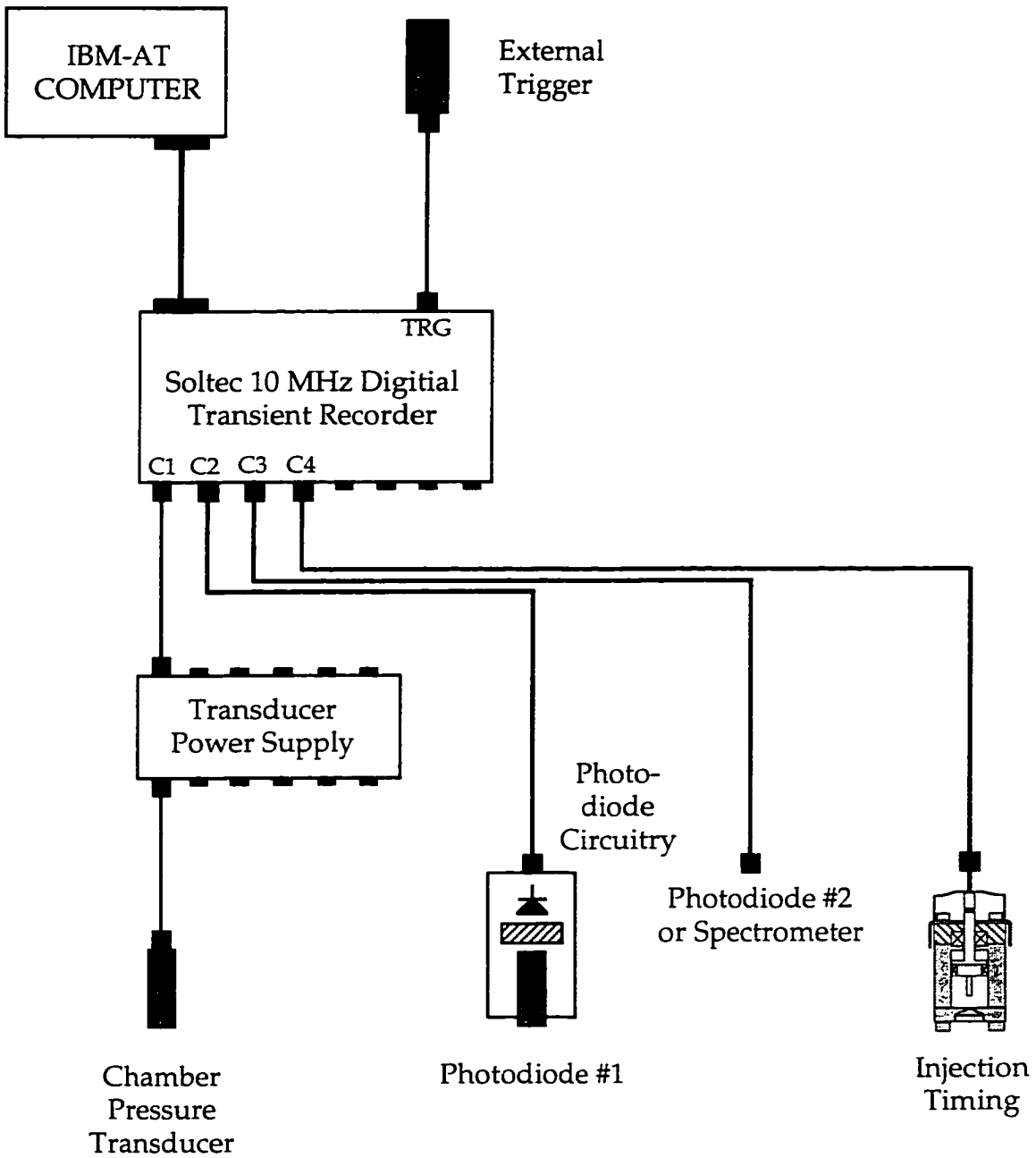

Fig. 2.33: Schematic of data acquisition system used to record transient chamber pressure, bandpass filtered emissions from the particle combustion event, and particle injection timing.

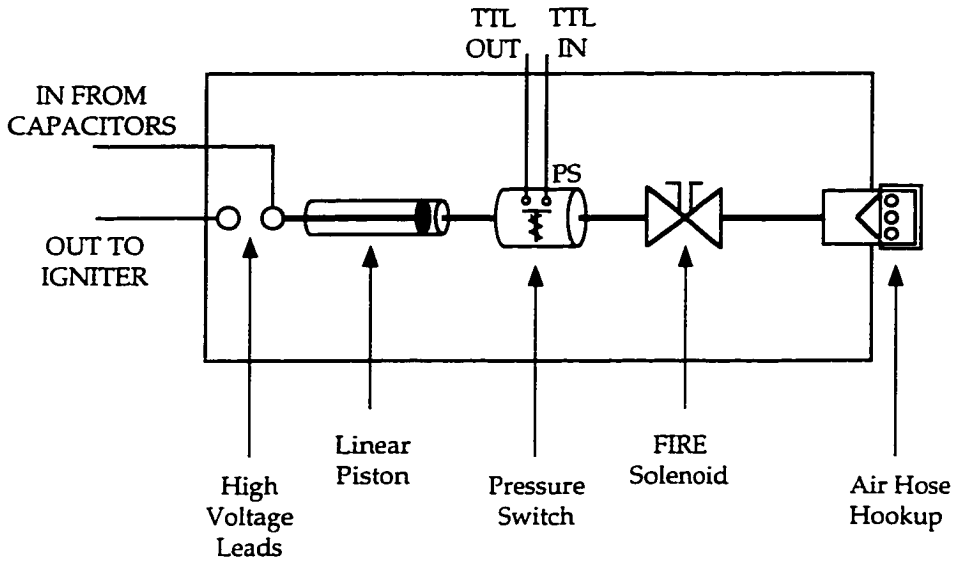

Fig. 2.34: Schematic of the pneumatic, high voltage firing switch. Pressure buildup behind the linear piston actuator activates pressure switch at preset delay, thereby sending signal to trigger data recording.

2.3.2 Pressure Transducer System and Measurement of p_2

Combustion pressure is measured with a single high speed piezocrystal pressure transducer purchased from PCB Piezotronics, Inc. The model 109A transducer makes use of a quartz sensing element with a built-in unity-gain amplifier and works in the voltage mode. The unit shown in Fig. 2.35 has a quoted rise time of 1 μsec, a pressure range of 0-80,000 psi, and a 1 psi resolution. The model 109A transducer has a long 2000 sec decay time, however in combination with the model 483A02 power supply the system has a much shorter maximum decay time of 110±10 msec, obtained from measurement (see Fig. 2.37). The sensing element surface has a diameter of 0.62 cm and is coated with a ceramic layer to shield the sensor from flash combustion temperature.

The pressure transducer is mounted in the top plug in one of the four off-axis transducer ports as shown in Fig. 2.36. Due to the high flash combustion temperatures achieved in the hpcc, the pressure transducer is recess mounted to protect the sensing element and built-in amplifier from the hot combustion gases. Thermal stresses on the transducer would lead to incorrect pressure measurement by changing the piezocrystal response. A 0.32 cm diameter, 1.1 cm long column provides access to chamber pressures and this column is filled completely with vacuum grease to further protect the transducer sensing surface from heat, as per the manufacturer's suggestion.

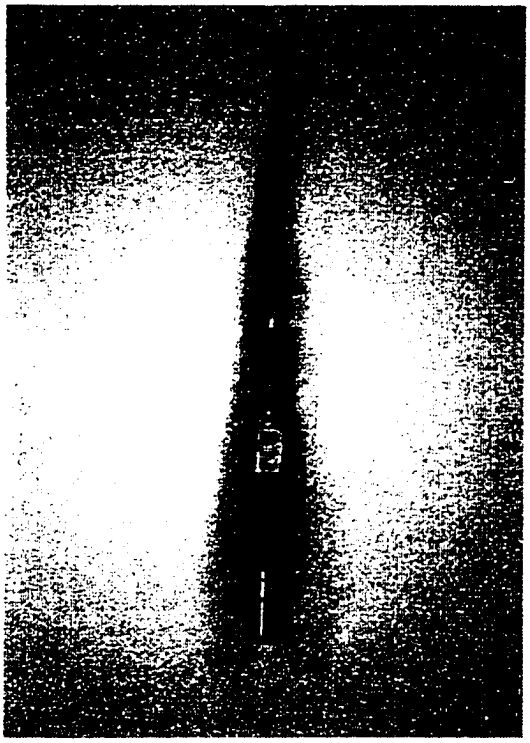

Fig. 2.35: Photograph of piezoelectric pressure transducer with cable. Transducer threads into transducer mount which gets installed in the top plug of the chamber (see Fig. 2.36).

Fig. 2.36: Pressure transducer insert installation in diagnostic port. Note the 0.063 in. (0.16 cm) diameter pressure tap which is filled with vacuum grease to protect the transducer from heat.

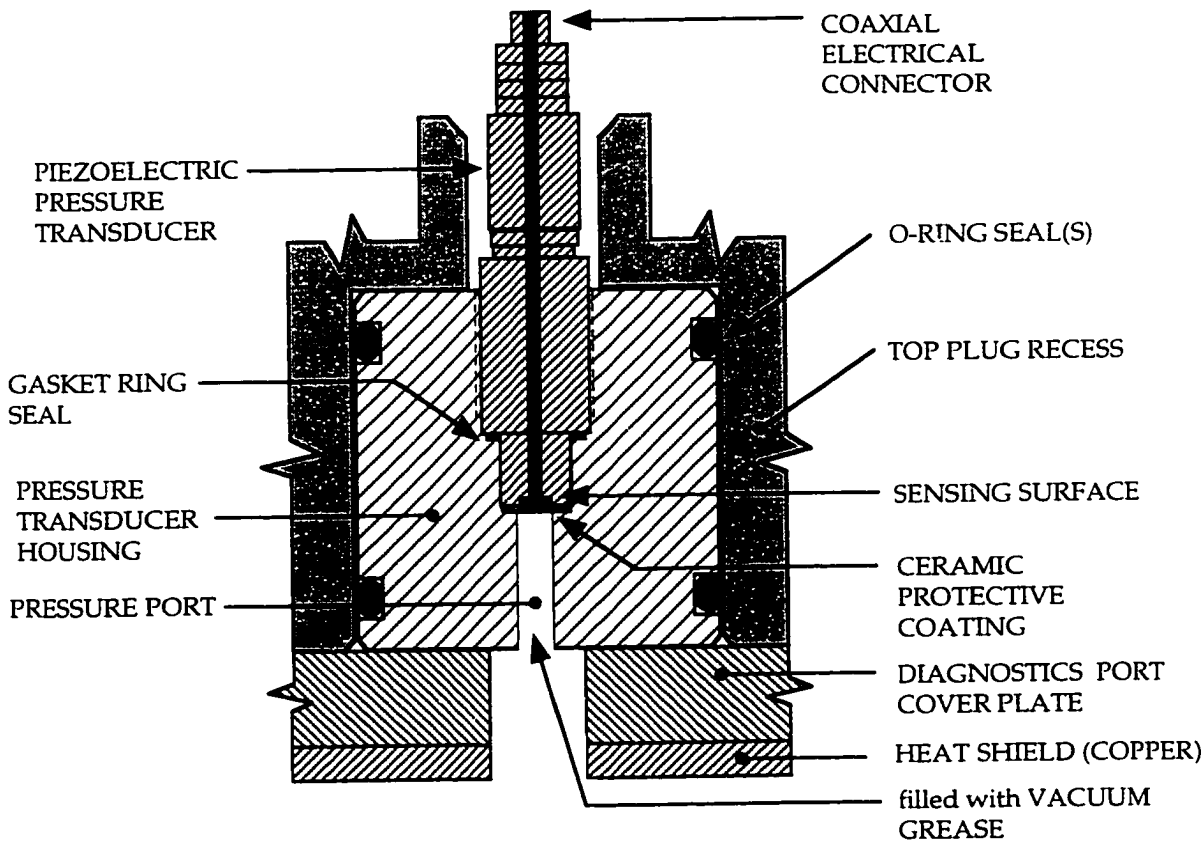

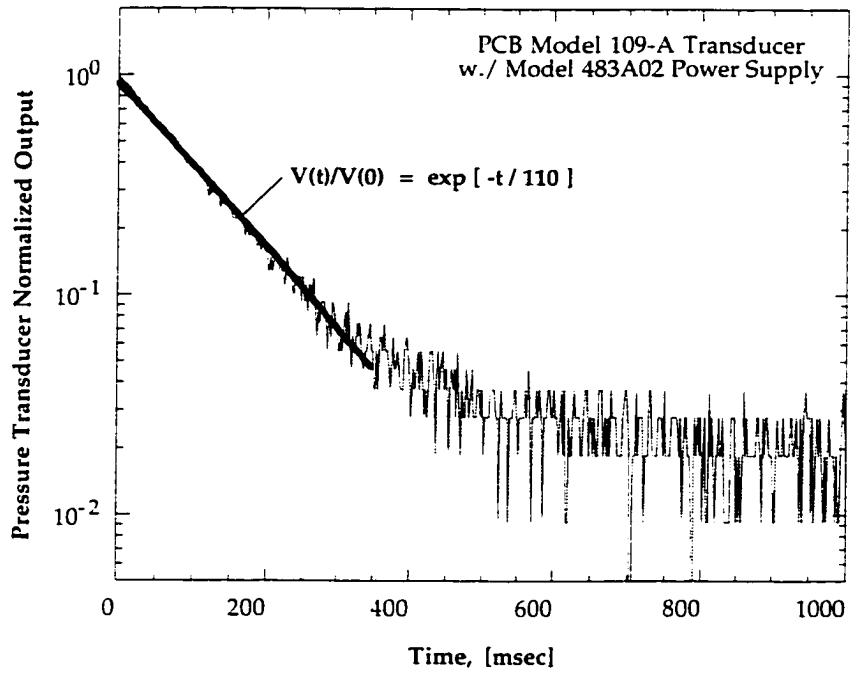

Fig. 2.37: Measured decay time constant of pressure transducer and power supply.

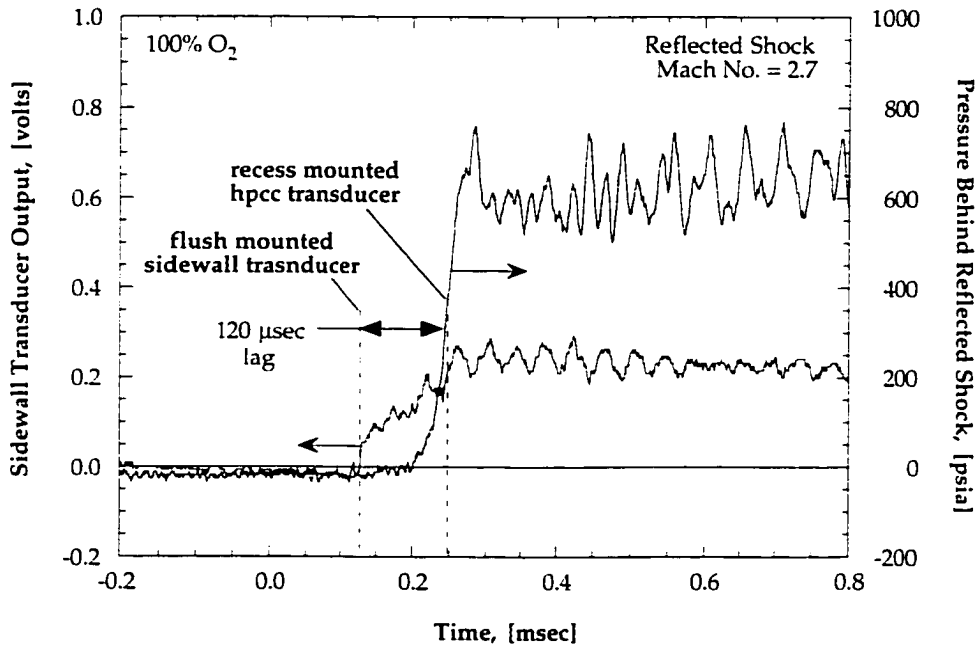

Fig. 2.38: Measurement comparing pressure response of recess-mounted hpcc pressure transducer to pressure response of flush-mounted shock tube sidewall transducer to a pressure jump across a reflected shock wave traveling at Mach 2.7. The plot indicates the recess-mounted transducer's response lags the flush-mounted transducer by 120 µsec, but reaches peak in only 60 µsec.

The 1.1 cm long pressure access column leads to a pressure rise lag for the recess mounted pressure transducer. According to the manufacturer this lag for an air-filled column is ~100 μsec for the present column dimensions. The lag has been measured with the pressure jump across a reflected shock wave where the model 109A transducer is mounted in a side-wall port of a shock tube, retaining the same pressure column configuration, and comparing the response to a flush-mounted sidewall transducer. The flush mounted transducer responds essentially instantaneously to the shock wave as shown in Fig. 2.38. The measured lag of the recess mounted transducer is 120 μsec and the peak pressure reading is reached in only 60 μsec, for a combined lag of 180 μsec. In the hpcc experiments, where the pressure rise timescale is three-orders of magnitude longer than the microsecond pressure rise time across a shock, this 180 μsec lag is neglected.

2.3.3 Photo Optical Detection System

Particle emissions are collected through a high pressure, high temperature optical window mounted in the top plug. Collected light from the chamber is transferred from the experiment to photodiode detectors and a spectrometer through fiberoptic cabling as shown in Fig. 2.39. A 6-core, 7 m long fiber optic cable is used which was obtained from General Fiber Optics, Inc. (GFO). This fiber has six identical 600 μm diameter silica/silica HOH type quartz cores which have a minimum transmission of 99% per meter below 0.90 μm where most of the measurements are taken. The wavelength transmissivity of the HOH fiber is shown in Fig. 2.40. The primary combustion measurement is obtained on-centerline with some measurements being made through one of the off-axis ports as well.

One type of light measurement performed in the particle combustion experiments is time resolved emission measurement. This is accomplished with an array of individual photodiodes each one filtered at selected wavelengths. Selectively bandpass filtered emissions are measured by fast response, GFO Series 5T PIN photodiodes. The photodiodes have a spectral range between 0.40 and 1.05 μm, with peak relative response near 0.82 μm. Vendor supplied spectral response curves are given in Fig. 2.41. A transimpedence amplifier with ±15 V bias is used to transform the diode current source into a voltage source with 250X amplification; the circuitry of such an amplifier is shown schematically in Fig. 2.42. Voltage signals are transferred through approximately 18 meters of Belden RG-58 U coaxial cabling to the data recorder. The advantage of transimpedence amplification is that the unit's response time is not affected by the amplification and capacitance in the transmission lines; the measured response time of these amplified diodes plus the associated circuitry is still less than 1 μsec (measured).

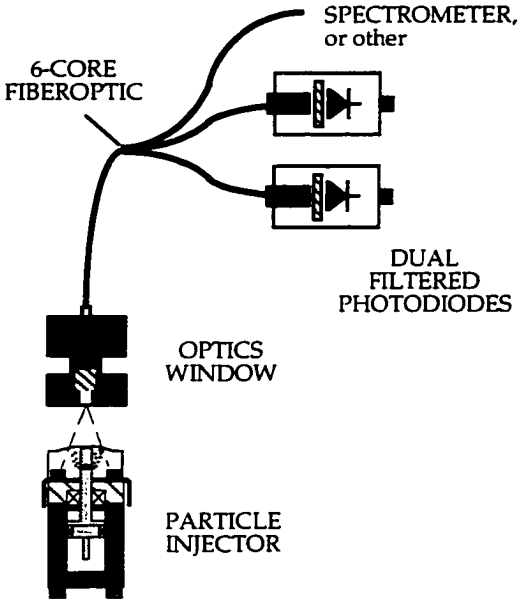

Fig. 2.39: Schematic of light collection system for the hpcc experiment.

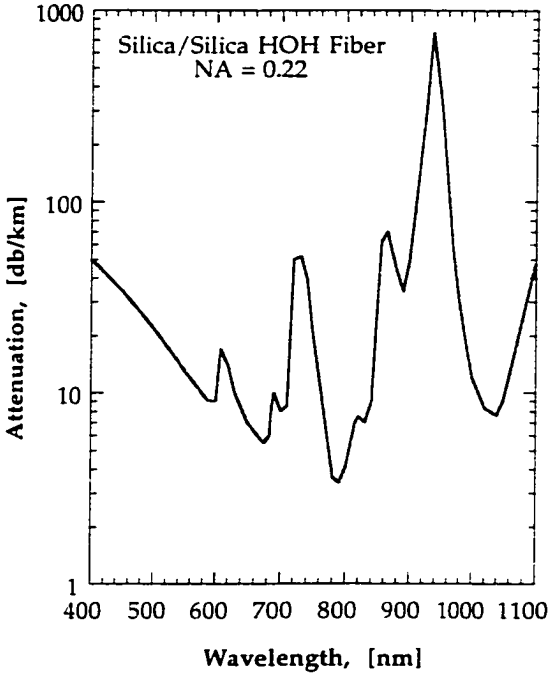

Fig. 2.40: Attenuation data for fiber optic cable material used in the optical data collection system.

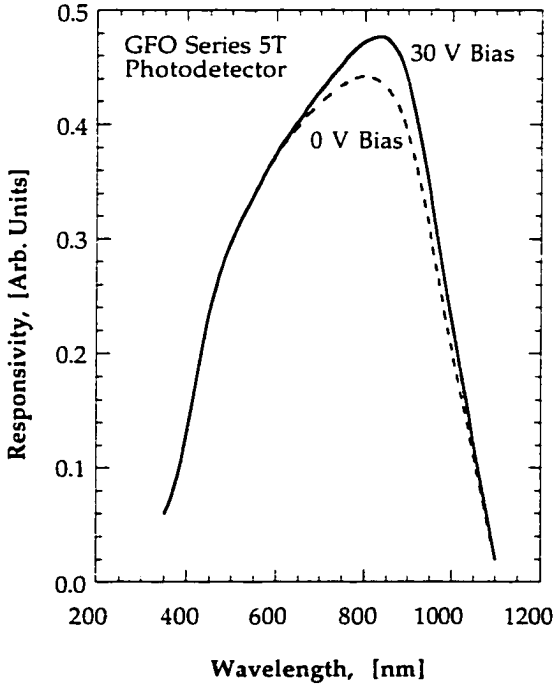

Fig. 2.41: Spectral response of Series 5T photodiode detector. Data furnished by supplier.

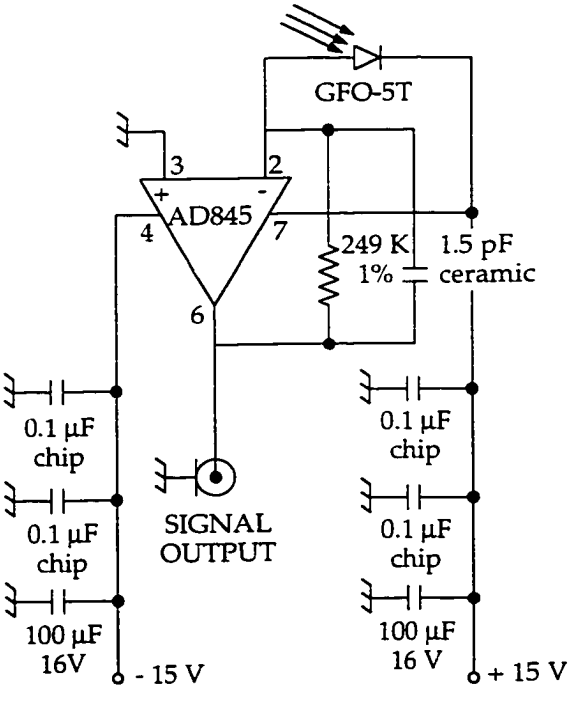

Fig. 2.42: Schematic of transimpedence amplification circuit for use with photodiodes.

Particle combustion time histories are measured indirectly by monitoring combustion emissions at selected wavelengths in order to filter out as much of the hot ambient gas radiation as possible. Measurements of hot chamber gas emissions indicate that background radiation, i.e., when no particles are present, is not negligible. Optical narrow bandpass filters are used to monitor emissions centered on the 545 and 518 nm bands of the BO_2 molecule, where BO_2 is a reactive intermediary gas-phase species formed throughout boron particle ignition and combustion. According to the model for boron particle ignition and combustion presented in Chapter 1, boron particle reaction processes liberate BO_2 and HBO into the gas phase where these intermediates are quickly converted further into products. The BO_2 spectrum[54] is readily observable in both the ignition and combustion stages. The choice of bands is based on analysis of spectra obtained with a gateable optical multichannel analyzer,[55,56] and observations in atmospheric pressure flames[8] and flow streams[29] prior to our own work. In the aluminum particle tests which were also conducted, hot gas and particle emissions are filtered about the 484 nm band of the AlO intermediate. For aluminum combustion AlO is a similar transient molecule to BO_2 for boron combustion.

Our premise for using filtered emission signals as an indicator of particle combustion *without directly viewing the disappearance of representative particles* is as follows. According to detailed chemical modeling, BO_2 is an intermediary sub-oxide formed during both the oxide removal stage (ignition) and clean particle surface oxidation stage (combustion stages) and BO_2 is a short lived molecule which is oxidized rapidly to form $B_2O_3(g)$ or $HBO_2(g)$, depending on the amount of water vapor present. Hence any BO_2 formed will only be present in the gas phase while its source, the combusting boron particle or droplet, is finite. Once this source disappears so will the $BO_2(g)$ through conversion to products. This process is not immediate in atmospheric pressure flames where $B_2O_3(g)$ dissociates and $BO_2(g)$ lingers in the flame plume at high temperatures but is found to be fast at high pressure. In addition to the contribution from excited $BO_2(g)$, there is a significant contribution to the collected particle emissions from the particle "black-body" continuum, as is evident from spectra such as the one shown in Fig. 2.45 to be discussed shortly. For boron combustion once the droplet is consumed, then so is the black-body radiator because unlike aluminum, no condensed smoky product cloud forms out of the products.

Even so the concern remains whether monitoring the BO_2 molecule reveals true details about particle combustion dynamics or whether just the dissociated products are being measured. To answer this concern tests have been conducted using amorphous B_2O_3 particles, where the B_2O_3 vaporizes and could dissociate into $BO_2(g)$ at chamber temperatures. Bandpass filtered emissions are shown to be quite different between combusting boron and the evaporating B_2O_3 even though both produce $BO_2(g)$. A typical measurement is shown in Fig. 2.43. For vaporizing B_2O_3 some net BO_2 signal is measured but

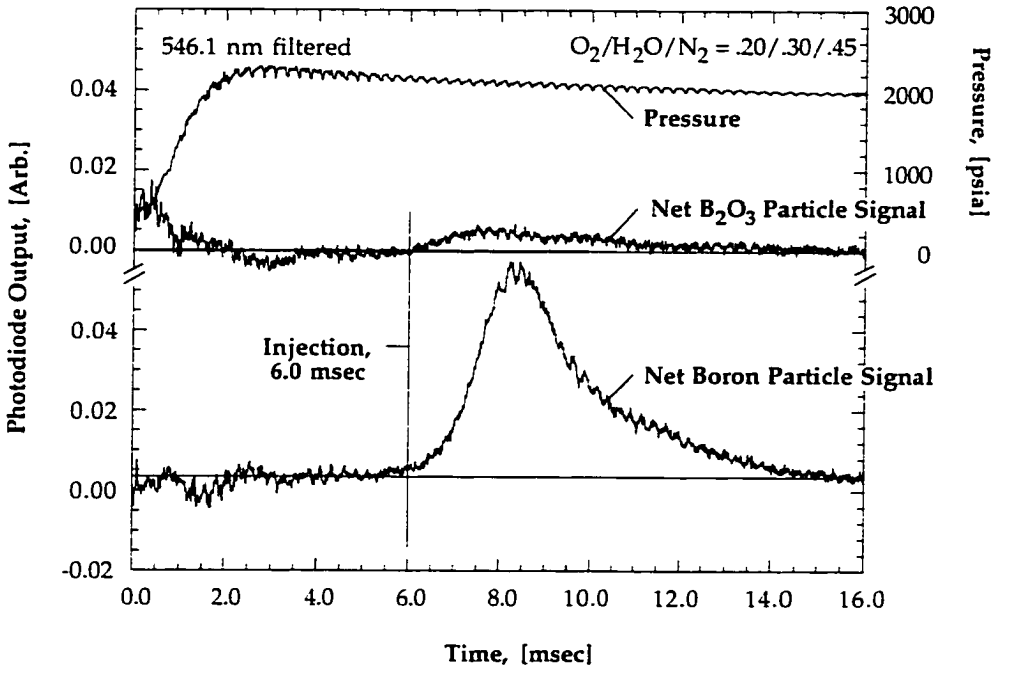

Fig. 2.43: Overlay of particulate boron oxide and particulate boron combustion signals filtered at 546.1 ± 4 nm. For the case of B_2O_3 (top curve), the particles merely vaporize at high temperature but show very little BO_2 emissions whereas for boron (bottom curve), the particles ignite and combust and the filtered emissions show a clear and distinguishable peak.

emissions rise slowly and never reach a true peak but level out instead. In contrast for combusting boron the emissions rise quickly, peak, and decrease back to background levels.

Therefore based on the preceding three arguments (resolved BO_2 emissions, the black-body contribution, and difference from the B_2O_3 particle produced emissions) it is possible to obtain a clear indication of the particle lifetime by monitoring particle emissions near the molecular bands of the BO_2 molecule. In addition it has been shown in particle laden experiments that BO_2 emission signatures are discernible above the background at the pressures and temperatures studied.

The choice of the two molecular bands for BO_2 (and the band for AlO) is based on the easily observable BO_2 (AlO) spectrum in a shock tube at 8.5 atm[55,56] and spectra obtained at elevated pressures in the hpcc. The filters used for bandpass filtering collected emissions are 0.5 in. (1.27 cm) diameter interference bandpass filters, at 546.1 ± 4 nm and 514.5 ± 5 nm respectively, obtained from Ealing Electro-Optics, Inc. Here the ± X nm are roughly the filter bandwidths. These are ideal for use with fiber optics because they are small and inexpensive. In the aluminum particle tests a 486.1 ± 4 nm filter from Ealing is employed.

The bandpass filtered photodiode output is recorded as a function of time and then analyzed to determine particle ignition and combustion times for the hpcc experiment. The process of interpreting measured emissions and obtaining combustion characteristics from these measurements is described fully in Section 3.3. Such measurements, where particle emissions from well dispersed particles in a high pressure, high temperature ambient can be differentiated from the background emissions, are made possible by optically filtering collected emissions and restricting the field-of-view to minimize hot gas contributions to the signal.

2.3.4 OMA and Spectral Data Recorder System

Another type of light measurement performed in the particle combustion experiments is spectral decomposition of the emissions to identify key intermediary species. For this purpose an optical multichannel analyzer (OMA) configured as shown in Fig. 2.44 has been used. Spectral data acquisition is accomplished with a 0.3 meter Instruments S.A., Inc. HR-320 coma-corrected Czerny-Turner configuration spectrometer and analyzed on an EG&G PARC model 1254 intensified vidicon array which can resolve into 500 pixels in the spectral dimension and 512 pixels in the spatial direction. An optical grating with 100 grooves/mm is used to give a spectral range approximately 250 nm wide. The detector is controlled and scanned by a model 1216 detector controller which is in turn controlled by an EG&G PARC model 1460 OMA console.

The OMA is gateable with the addition of a model 1211 high voltage pulse generator which permits 50 to 1000 μsec snapshots in the preselected ignition or combustion phases of particle burning. A timing circuit was also added to sequentially trigger the OMA gating and detector reading, both initiated by the same triggering signal which initiates data acquisition on the SOLTEC data recorder. Such a configuration could be used to obtain a series of snapshots giving partially time-resolved information about evolution of boron product species, as was done by Spalding.[55,56] However only one exposure per experiment is possible and the procedure proves very unreliable. Problems with reliable OMA gating and the poorly resolved spectra at the elevated pressures in the hpcc experiments precluded anything further than identifying the BO_2 spectrum at high pressure.

A sample combustion chamber spectrum from ~24 μm crystalline boron particles obtained over a 400 μsec exposure initiated 1 msec after particle exposure to hot gases is shown in Fig. 2.45. The ambient mixture contains $O_2/H_2O/N_2$ = .11/.34/.51 (products) at ~2850 K and ~150 atm. A typical hot gas emission spectrum is shown for comparison where in that case there were no particles present. The magnitudes of the two curves are to scale. It can be seen that several BO_2 bands are identifiable at 493, 518, and 545 nm, although they are weak and poorly resolved. It was judged that the 518 nm and 545 nm bands stand out the best when compared to the hot gas emissions.

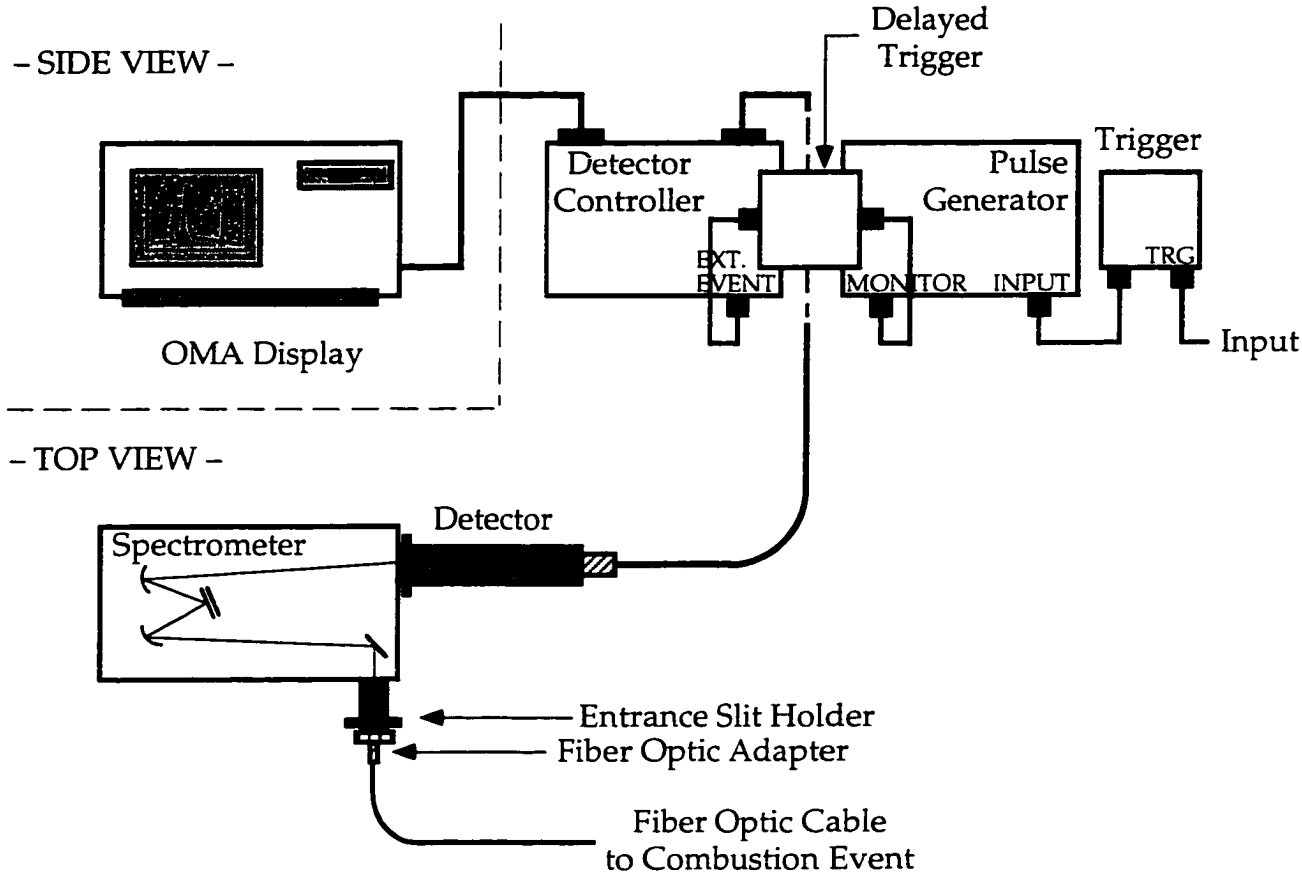

Fig. 2.44: Schematic of spectral data collection system showing gating pulse generator, detector controller, vidicon array detector, and spectrometer arrangement.

The spectra reveal several important characteristics. Firstly the glitches in the spectra near 410 and 440 nm are due to premature initiation of detector reading, and should thus be ignored. It is seen from the relative amplitudes of the two spectra that the particle-laden signal not only shows boron emissions but higher overall intensities as well, attributed to black-body emissions from the glowing particles. There is weak band structure apparent near expected transitions for the BO molecule, at 436, 502, and 530 nm, but BO emissions were not observed in the shock tube which makes connection of these bands to BO here rather speculative. Some very weak band-like structure is also observed in the particle-free spectrum near 485, 516, 530, 536, and possibly 615 nm. These may be bands arising from excited N_2, OH, NO, or NO_2 according to the tabulation of transitions in Appendix B. There are a few percent OH and NO in the product mixtures used to establish the environment for particle combustion.

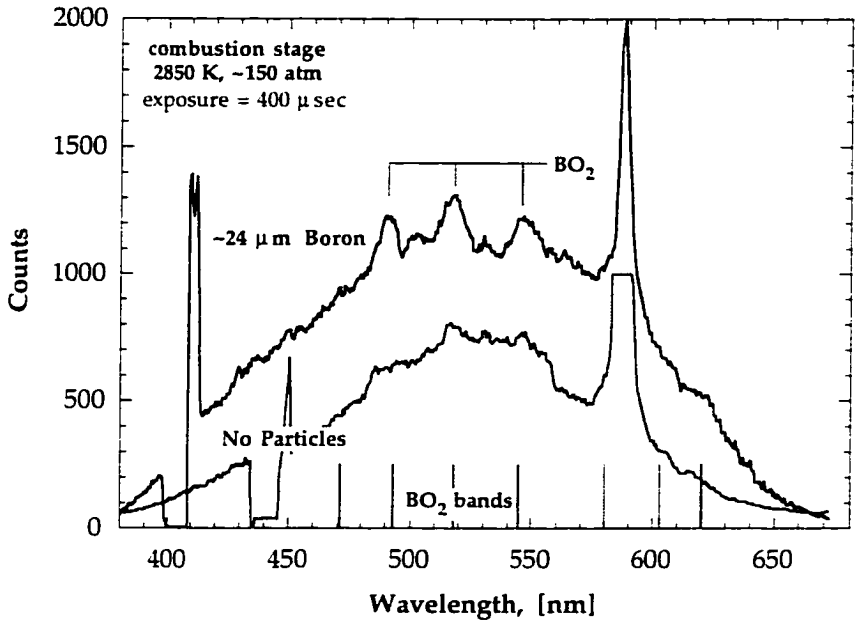

Fig. 2.45: Sample emission spectrum from combusting boron particles (~24 μm) obtained in the hpcc, in $O_2/H_2O/N_2$ = .11/.34/.51 at ~2850 K and 150 atm. Also shown is hot-gas emission spectrum where no particles were present. The relative amplitudes of the two spectra are to scale.

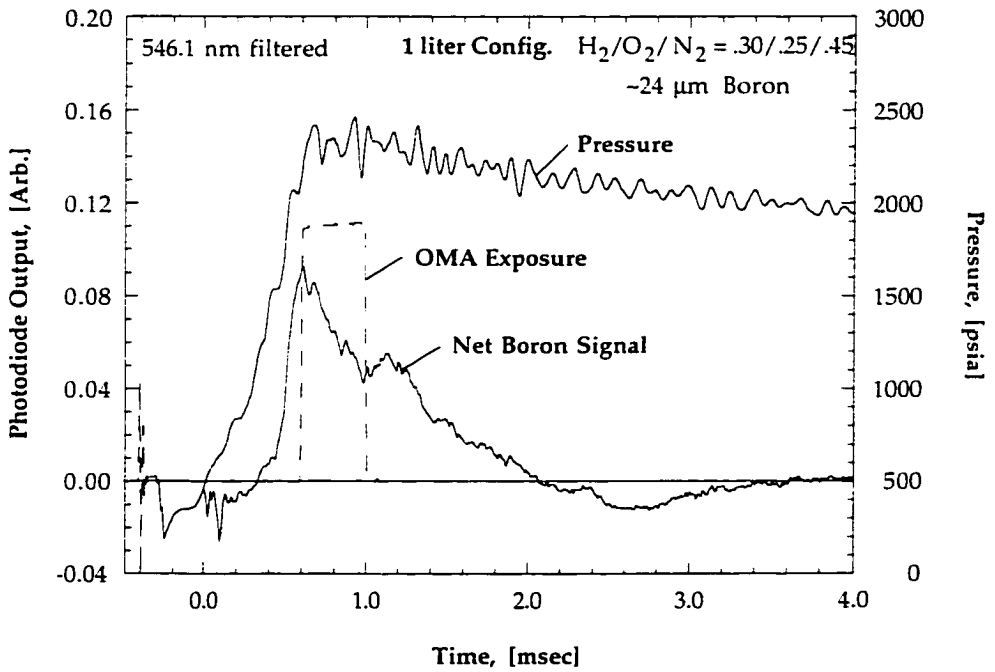

Fig. 2.46: Sample 546.1 ± 5 nm filtered photodiode signal from combusting boron particles (~24 μm) obtained in the hpcc, in $O_2/H_2O/N_2$ = .11/.34/.51 at ~2850 K and 150 atm. The measured square pulse indicates the boundaries of the gating window for the spectrometer-detector exposure time used in Fig. 2.45.

The last feature to point out in the measured spectra is the most glaring feature, namely the strong and sharp band or line near 587 nm which is present both with and without particles. In the boron-particle spectrum this line is shown to be very sharp suggesting it may be an atomic transition superposed on the BO_2 band at 580 nm. The most likely atomic source is sodium where the transitions are the Na doublet at 589 and 589.6 nm, which cannot be individually resolved into two lines with the spectrometer grating used. The slight shift between 587 and ~589 nm can easily be attributable to detector calibration. It is unclear what the source of sodium could be but it is possible it arises from finger oil residue on the particle injector housing. All parts in the chamber are cleaned with methyl alcohol before installation in the chamber, so this seems unlikely. The sodium could also originate from the quartz window whose outer surface is directly exposed to the high gas temperatures. There are several transitions of N_2 and NO near 590 nm but it is doubtful that they would be so strong and isolated from other N_2 and NO transitions elsewhere in the spectrum which are not observed.

2.3.5 Boron Gas Phase Species Emission Wavelengths

Wavelengths of known molecular transitions of the BO_2 and BO molecules are listed in Table 2.2 and are useful to identify emission bands from experimental measurements. From recorded spectra such as the ones shown in Fig. 2.45, the resolved structure near 493, 518, and 545 nm can be readily attributed to the BO_2 emission spectrum. These three clearly identified BO_2 bands arise from the two electronic transitions, ($A^2\Pi_u$ - $X^2\Pi_g$) and ($B^2\Sigma_u^+$ - $X^2\Pi_g$), involving exchanges between vibrational states as shown in the table. The very faint structure at 436, 502, and 530 nm may be due to BO molecule. BO molecular bands expected at 436, 462, 504, and 536 nm, among others, are never clearly discernible and so early attempts at monitoring BO molecule emissions were abandoned. BO molecular bands at these wavelengths were never observed in shock tube experiments combusting boron in pure oxygen. Based on the observations at high pressure, it was decided to monitor the time resolved bandpass filtered emissions about the 545 nm and 518 nm bands because these are the best resolved of the bands listed.

It would be ideal to monitor the appearance of other gas-phase products as well as be able to identify changing product routes when various ignition-enhancing agents are employed. Detailed chemical modeling studies[14] predict that HBO_2, HBO, OBF, and BN, among others, are formed during boron combustion in our system. The primary emissions from product species such as HBO_2 are in the infrared and for the boron-fluorides in the far infrared where it is predicted there will be interferences from water vapor emissions. Based on limited detection capabilities of the present system however, and the restricted range of infrared wavelengths transmitted through the fiber optic, the optical

Table 2.2: Prominent emission bands of BO and BO_2 molecules at combustion conditions. The 493, 518, and 545 nm bands of the BO_2 molecule are observed in spectra from the hpcc at 150 atm. Na, N_2, and NO bands are included in the list for reference to the unknown emitter observed near 587 nm.

Species	Bands λ [nm]	Lines λ [nm]	Comments	Refs.
BO	404	401.5, 403.7	weak in flames	a
BO	434	433.9, 434.2	weak in flames	a
BO	436	436.0, 436.3, 436.6	weak in flames	a
BO	461	461.3, 461.5	weak in flames	a
BO	504	504	weak in flames	a
BO	555	547.8, 555.2	weak in flames	a
BO_2	452	-	strong band	a
BO_2	471	-	strong band	a
BO_2	493	492.9, 494.1, 496.5, 497.4	strong band	a,b
BO_2	518	516.9, 518.1, 519.6, 520.7	strong band	a,b
BO_2	545	545.7, 547.1	strong band	a,b
BO_2	580	579.1, 581.3	strong band	a,b
BO_2	603	-	strong band	a,b
BO_2	620	617.2, 620.2	strong band	a,b
BO_2	639	637.7, 639.6	strong band	a,b
Na	589.5	589.0, 589.6	strong lines	a
N_2	580	575.5, 580.4, 581.5	-	a
N_2	590	585.4, 590.6, 595.9	-	a
NO	600	600.1	-	a

a: Reference (54)
b: Reference (57)

system is presently limited to detection in the range of 400 to 1300 nm. Table B.1 in Appendix B lists selected wavelengths for other boron product gas-phase species which may be of interest for further study. Rood[11,12] for example developed a B_2O_3 detection capability which may be applied to the hpcc at a future date.

2.3.6 Hot Gas Emission Measurements

It will be shown in the next chapter where particle measurements are discussed that the hot ambient gas emissions cannot be neglected in comparison to particle emissions. A series of measurements

were thus performed to obtain average hot gas emissions for each of the mixtures in which particle combustion is studied. These experiments were conducted with the particle injector in place to block out hot-gas contributions from elsewhere in the chamber (see Section 2.3.3).

Experiments without particles are quite reproducible if proper care is taken during gas metering and sufficient time is allowed for molecular mixing of the constituents. In Fig. 2.47 are shown measured pressures and hot gas emissions from four individual experiments without particles in a mixture initially containing $H_2/O_2/N_2$ = .27/.32/.41 at p_1 = 20.4 atm, mixture B of Table 2.1. The composite formed from these signals is shown in Fig. 2.48 c below. Measurements of interest in the absence of particles include the pressure rise and decay rate, bandpass filtered photodiode measurements, and the hot gas spectrum. The average hot gas emission measurements for all gas mixtures are shown in Figs. 2.48 a - i where between 2 and 6 individual measurements were combined for each average. Only the final composite for each of the two wavelengths of most interest are shown along with the average pressure measurement. Wavelengths of interest are near 546.1 nm and 486.1 nm where boron and aluminum combustion intermediates have strong emission bands. The mixtures referred to in the figure captions were given in Table 2.1. Product gas compositions for these mixtures are given in Table 2.3.

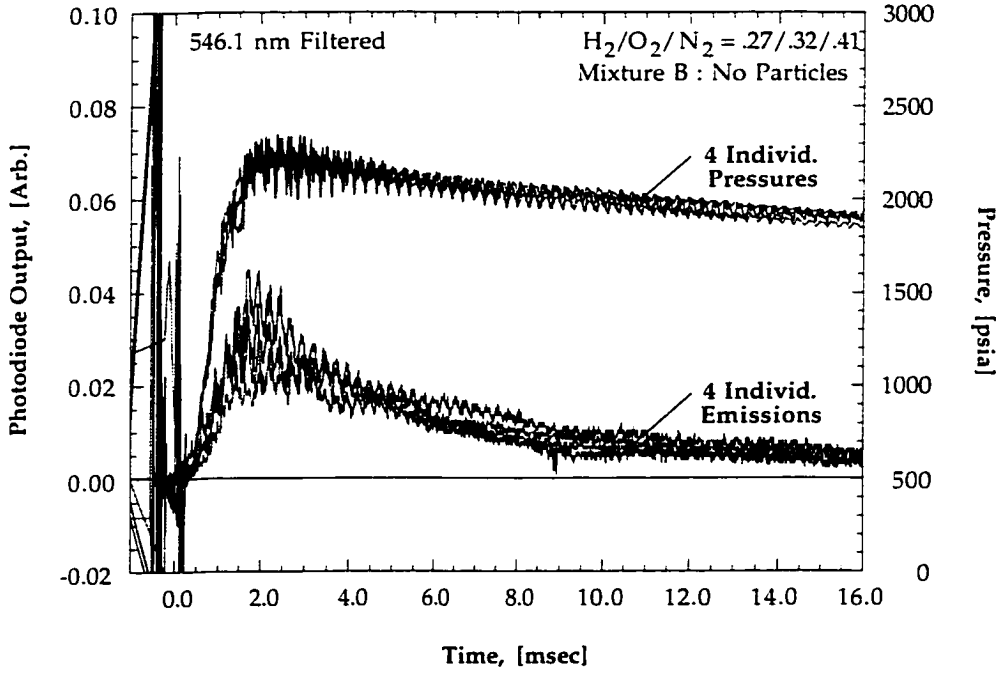

Fig. 2.47: Collection of four individual pressure and hot-gas emission signals used to produce a composite average background for mixture B at high pressure. The individual measurements without particles are shown to be repeatable.

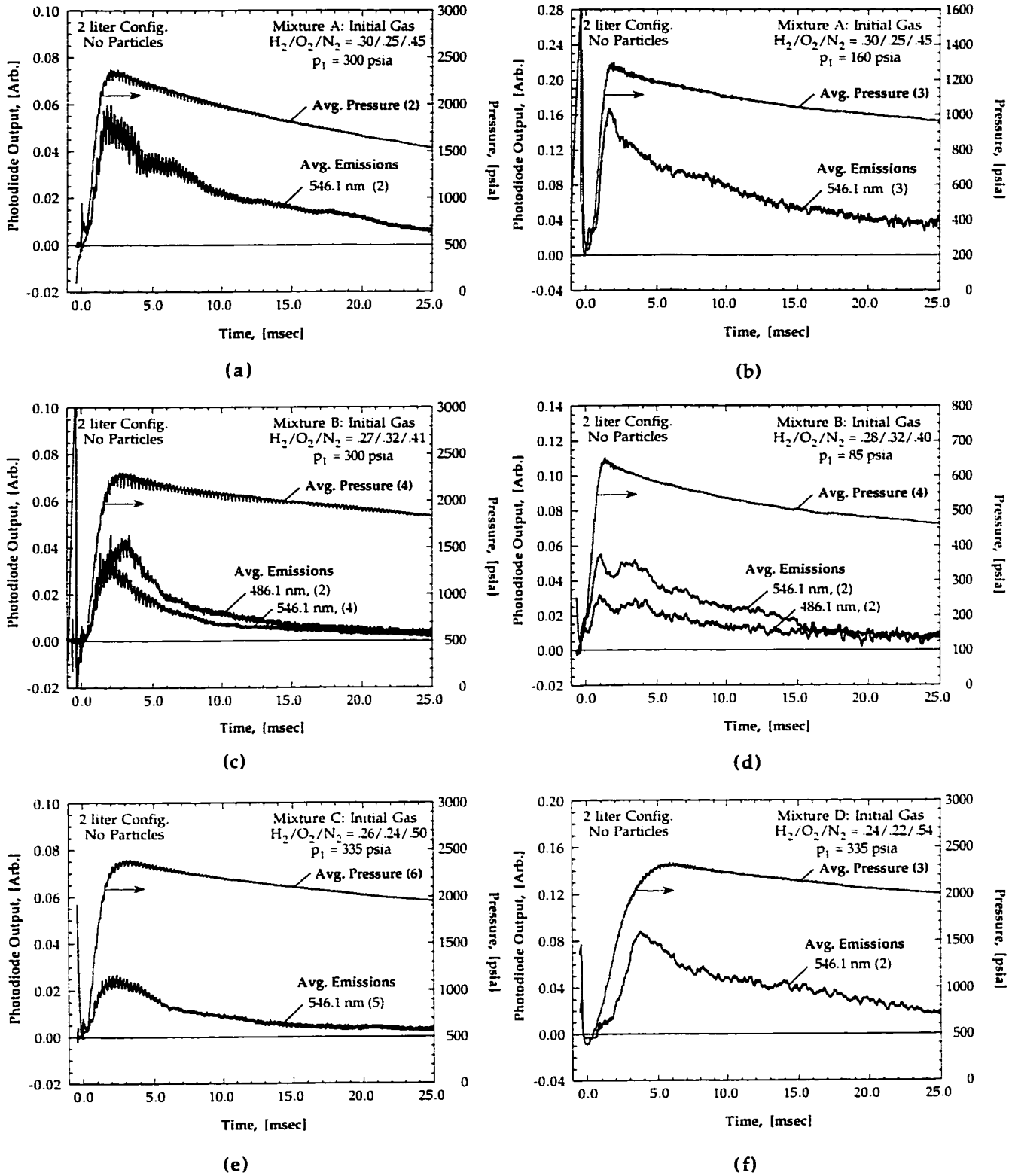

Fig. 2.48: Composite pressure measurement and hot-gas emissions in various mixtures: (a) mixture A, 150 atm; (b) mixture A, 78 atm; (c) mixture B, 145 atm; (d) mixture B, 37.5 atm; (e) mixture C, 150 atm; and (f) mixture D, 150 atm; cont. -

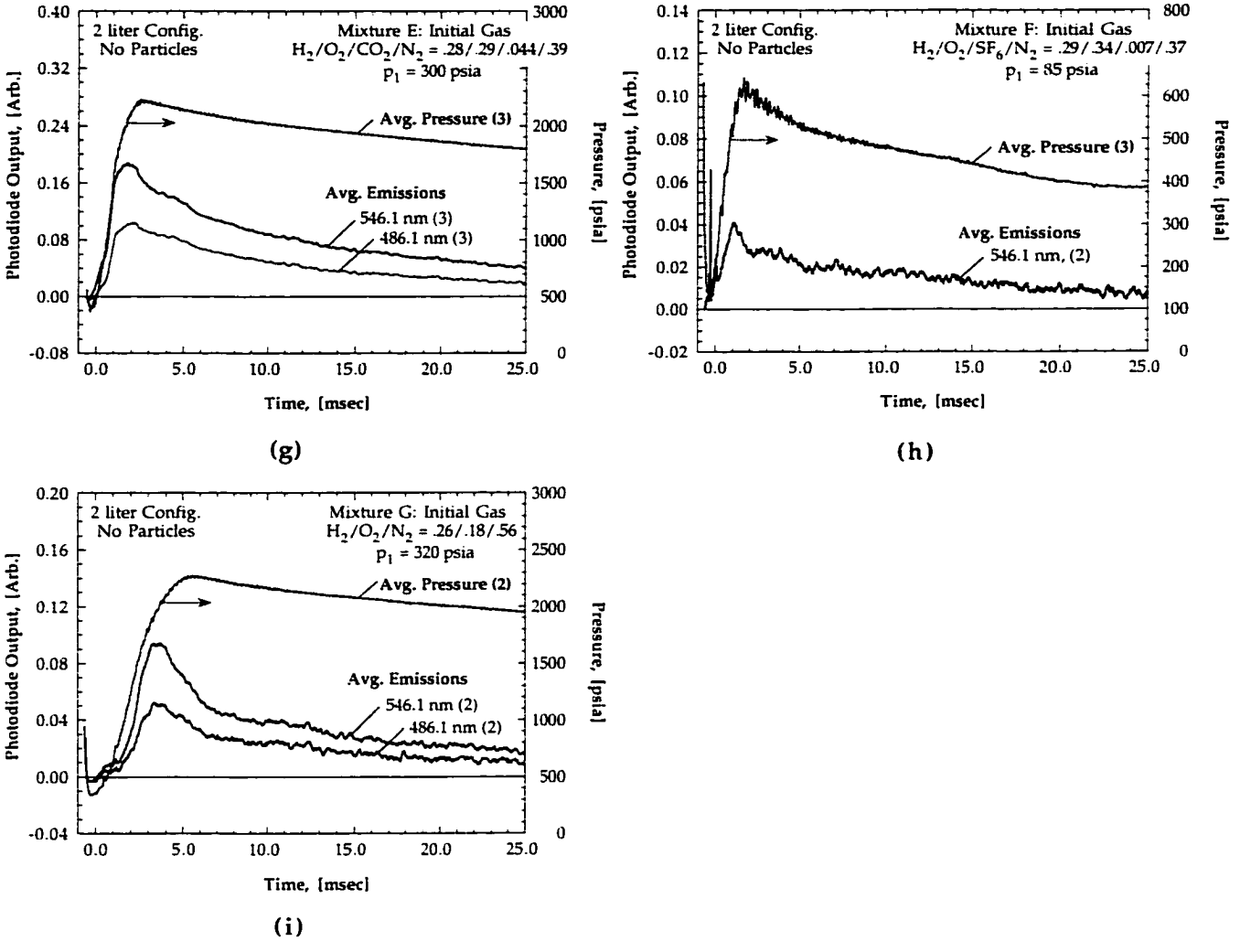

Fig. 2.48: cont. - Composite pressure measurement and hot-gas emissions in various mixtures: (g) mixture E, 145 atm; (h) mixture F, 34 atm; and (i) mixture G, 150 atm. See Table 2.3. Nominal pressures quoted are those when particle ignition and combustion occur.

2.3.7 Determination of Product Mixture Properties

No product gas species concentration measurements are performed in the hpcc experiments. Instead all information about chamber gas speciation after initial mixture ignition and combustion is obtained from equilibrium calculations using measured initial gas compositions. All equilibrium calculations are performed using the CHEMKIN II Chemical Kinetics Package[58] and thermodynamic database[59] along with the STANJAN equilibrium program.[60] The gas-phase combustion process is constant volume and assumed to be adiabatic - that is there are no bulk gas heat losses during gas-phase combustion. The resulting post-combustion chamber product gas mixtures are listed in Table 2.3 and are composed primarily of water vapor, oxygen, and nitrogen, with a few percent NO and OH. These mixtures are used to ignite the boron particles under study.

Shifting equilibrium calculations were performed to monitor gas-phase speciation during the slow pressure and temperature decay following peak pressure. Measured pressure and calculated temperatures were used as inputs for the time-dependent calculations which assumed equilibrium at every instant in time. These calculations indicate that stable species mole-fractions (O_2, H_2O, and N_2) change negligibly during the time for particles to inject, ignite, and burn to completion whereas the reactive radical species concentrations (O, OH, NO) typically dropped less than 10% from their peak values, mainly due to the temperature decrease with time. This change has been neglected in the subsequent discussions.

Table 2.3: Combustion chamber product gas mixtures indicating calculated peak temperature and species mole fractions, assuming adiabatic constant-volume premixed-gas combustion. The initial reactant mixtures used to produce these product gases are given in Table 2.1.

Mixture	p_1 [atm]	T_2 [K]	$p_{2,ms}$ [atm]	O_2	H_2O	N_2	NO	OH	CO_2	HF
A	10.9	2860	86	0.11	0.33	0.51	0.02	0.02	0	0
A	20.4	2875	160	0.11	0.34	0.51	0.02	0.02	0	0
B	5.8	2725	44	0.19	0.31	0.45	0.02	0.02	0	0
B	10.9	2665	80	0.20	0.30	0.45	0.02	0.01	0	0
B	20.4	2675	153	0.20	0.30	0.45	0.02	0.01	0	0
C	22.8	2655	164	0.11	0.30	0.56	0.02	0.01	0	0
D	23.8	2475	156	0.11	0.26	0.61	0.01	0.01	0	0
E	20.4	2665	151	0.16	0.31	0.44	0.02	0.01	0.048	0
F	5.8	2750	43	0.20	0.28	0.43	0.02	0.02	0	0.047
G	22.8	2660	158	0.05	0.29	0.63	0.01	0.01	0	0

2.3.8 Uncertainty Analysis in Measured p_c, and Calculated T_c and X_i

Chamber pressure $p_\infty(t)$ is measured throughout an experiment for up to ~30 msec after gas phase ignition. The piezocrystal pressure transducer measures the dynamic pressure and the system produces a voltage which is measured by the transient data recorder, where the maximum analog/digital conversion used was 1.2 mV/bit. This voltage is converted to pressure through a transducer calibration constant (0.076 mV/psia, linearity < 2% full-scale) and the result corrected for the transducer system time constant which was measured to be 110±2 msec. The pressure $p_\infty(t)$ is the sum of the measured dynamic pressure and the initial chamber pressure. The resulting formula with uncertainties for each term is given by

$$p_\infty(t) \pm \Delta_{p_\infty} = \left[\frac{V(t) \pm \Delta_{VD/A} - (V_0 \pm \Delta_{VD/A})}{0.076 \pm \Delta_{cal}}\right] \cdot \exp\left(\frac{t \pm \Delta_t}{110 \pm \Delta_\tau}\right) + p_{0,g} \pm \Delta_{p0,g} + p_{atm} \pm \Delta_{patm} \qquad (2.4)$$

where the voltages $V(t)$ and V_0 are in mVolts, $\Delta_{VD/A}$ = ±0.6 mV, Δ_{cal} = ±1%, $\Delta_{p0,g}$ = ±1 psia, Δ_{patm} = ±0.2 psia, Δ_t = ±0.5 μsec, and Δ_τ = ±2 msec. Processing the various uncertainties for a typical experiment at ~150 atm, the overall uncertainty in a pressure measurement is ±1.2% which corresponds to ±1.8 atm. For a typical low pressure experiment (37.5 atm) the errors are ±3.0%, or ±1.3 atm.

The manufacturer claims there is no loss of sensitivity due to the recess mounting but a small response time lag has been measured, as discussed in Section 2.3.2. The response time lag is a factor of ~10 shorter than the characteristic pressure rise times in the chamber and is therefore neglected. The fall-off in pressure during particle ignition and combustion is calculated for every experiment and is typically 3.0 atm. Pressures quoted for the particle ignition and combustion events throughout this thesis are time averaged values (p_c) and the fall-off is ascribed to an additional uncertainty $\Delta_{pf\text{-}o}$ = ±1.5 atm. The overall uncertainty then is typically Δ_{p_c} = ±3.3 atm at high pressure and Δ_{p_c} = ±2.8 atm at low pressure. These uncertainties, using actual $\Delta_{pf\text{-}o}$ for each experiment, are the ones shown as error bars on the respective plots.

For larger particles, especially boron particles over ~32 μm in diameter and also at lower pressures, particle combustion times are fairly long and there the assumption that pressure remains nearly constant is not very good. This can also be said about studies in mixtures with HF, where the pressure fall-off is greater than in all other mixtures tested. For these cases the corresponding uncertainties are greater than quoted in the preceding paragraph.

Temperature in the chamber is not constant over time due to slow gas heat losses near the chamber walls but is nearly constant over the timescales of particle ignition or combustion. The ambient

temperature at every instant $T_\infty(t)$ is calculated from the measured pressure decay by assuming an adiabatic process at the center of the chamber, and the relation for temperature at time t is then

$$\frac{T_\infty(t) \pm \Delta_{T_\infty}}{T_2 \pm \Delta_{T_2}} = \left(\frac{p_\infty(t) \pm \Delta_{p_\infty}}{p_2 \pm \Delta_{p_2}} \right)^{(\gamma-1)/\gamma} \tag{2.5}$$

where T_2 is the equilibrium adiabatic temperature, p_2 the peak *measured* pressure, and Δ_i are the corresponding uncertainties. The measured pressure p_2 is uncertain to 1.2 to 3.0% and $p_\infty(t)$ to 2.2 to 7.5% depending on the initial gas pressure (150 to 37.5 atm) and T_2 is calculated from the measured values T_1, p_1, and X_i. The peak chamber temperature T_2 is based on an equilibrium calculation and has been found to be insensitive to the measured temperature $T_1 \pm 1$ K. The initial gas temperature T_1 is measured prior to each experiment with a thermocouple and has an associated uncertainty of only $\Delta T_1 = \pm 0.2$ °C. The calculated equilibrium temperature is most sensitive to uncertainties in the partial pressure of initial hydrogen, and the largest uncertainty occurs when H_2 is underfilled and O_2 correspondingly overfilled by the same amount. If the uncertainty in the hydrogen partial pressure is taken to be ± 1 psia H_2, (which is twice the pressure gauge uncertainty, $\Delta_{p0,g}$) then T_2 will be uncertain to ±35 K (±1.3%) at high pressure (~150 atm) and ±75 K (±2.8%) at low pressure (37.5 atm). Processing the various uncertainties in Eq. (2.5), the resulting uncertainty in $T_\infty(t)$ will be ±40 K (±1.3%) and ±80 K (±2.9%), respectively.

As is the case for pressures, quoted temperatures (T_c) for ignition and combustion are time averaged values and the temperature fall-off is ascribed to an additional uncertainty; typically this uncertainty is $\Delta_{Tf\text{-}o} = \pm 10$ K. The overall uncertainty then is typically $\Delta_{T_c} = \pm 50$ K at high pressure and $\Delta_{T_c} = \pm 90$ K at low pressure. Uncertainties using actual $\Delta_{Tf\text{-}o}$ for each experiment are shown as error bars on the respective plots.

The important oxidizing species are O_2, H_2O, and OH and the effect of initial gas pressure measurement uncertainties on the equilibrium calculated product gas speciation must be considered. The greatest compounding effect of various uncertainties again occurs if H_2 is underfilled and O_2 overfilled by an equal amount, e.g., $\Delta_{pO_2} = -(\pm \Delta_{pH_2})$, taken to be ±1 psia. The resulting uncertainties Δ_{X_i} are given in Table 2.4 for both the high and low pressure cases. The change in speciation due to gas cooling (shifting equilibrium) has been previously shown to affect radical species concentrations the most, typically decreasing 10%, and the stable species decreasing less than 1% as the gases cool during the particle injection delay. This additional uncertainty in X_{O_2} and X_{H_2O} due to gas cooling is so small that it is neglected, and the error bars in the corresponding figures are those of Table 2.4.

A notable exception to these low species uncertainties is mixture F with hydrogen fluoride. The HF is produced by the dissociation of sulfur-hexafluoride (SF_6) and because of the large number of F-atoms per SF_6 molecule, very little SF_6 is required. To keep the relative pressure gauge reading uncertainty low, twice the amount of gas mixture is typically metered and then half is vented before

ignition. Even with this precaution, the uncertainty in SF_6 partial pressure is typically ±50%, resulting in an equilibrium calculated uncertainty of ±48% for X_{HF} and an additional temperature uncertainty of ±10 K. An alternative method for metering small amounts of SF_6 into the gas mixtures employed is suggested for future experiments.

Table 2.4: Calculated species mole-fraction uncertainties corresponding to a 1 psia initial H_2 under-fill coupled with a 1 psia initial O_2 over-fill, at high and low pressure. This scenario results in the largest compounding of uncertainties in the final equilibrium product gas speciation for a given mixture.

Variable	Baseline	Δ_i, %	Baseline	Δ_i, %
i	150 atm		37.5 atm	
P_2, [atm]	158	-1.0	45	-2.2
T_2, [K]	2674	-1.3	2728	-2.7
O_2	0.20	2.0	0.19	11.2
OH	0.01	-9.3	0.02	-17.0
H_2O	0.30	-2.0	0.32	-4.2
N_2	0.46	1.0	0.45	-0.4
NO	0.02	-3.7	0.02	-5.7

2.3.9 Uncertainty in Measured Injection Timing, t_{inj}

A technique to inject particles after a time delay has been described along with a timing device to measure when the particles are injected (Section 2.2.4). For this device injection timing (t_{inj}) is measured with a make-switch which closes at the instant when the annulus containing particles is first exposed. If the piston is operating near baseline design conditions, calculations show that the time to inject the entire sample, i.e., to expose the full length of the annulus (Δt_{inj}), is about 100 μsec . For faster injection, which is stipulated when the injection delay is 80% or less than the baseline, the calculated injection time reduces to ~80 μsec; for slower injection where the injection delay is 140% or greater than the baseline, it is ~120 μsec. These values were obtained by investigating off-design injector performance with the particle injector design computer program.

The finite amount of time required to inject particles will effect measured particle ignition delays if this time is a significant portion of the particle heat-up time. For the particle sizes studied this is not the case because $\Delta t_{inj} << t_{ign}$ (and $t_{heat\text{-}up}$), but obviously a lower limit on particle diameter exists. The acceptable lower limit on particle sizes below which corrections are needed to account for the finite injection time is approximately 8 μm for boron and less than 20 μm for aluminum. For the present experiments, the length of time to inject particles is ascribed to an uncertainty in the injection

time measurement. This uncertainty is stipulated to be $\pm\frac{1}{2}\Delta t_{inj}$ and is much larger than the ~2 μsec uncertainty in the measured injection timing mark.

2.4 Description of Boron and Metal Powders

The powders used in these experiments consist of either crystalline boron or amorphous boron oxide samples. Several tests were also conducted with spherodized aluminum particles identical to those used previously by Roberts, et al.[24,44] All powder samples were received containing particles ranging from sub-micron to approximately 100 microns in diameter and were subsequently sieved into tighter size distributions in order to produce experimental results tenable to meaningful analysis. Characteristics of the various samples are given in Table 2.5 along with the supplier. Samples were separated by sieving and classified under a scanning electron microscope as will be discussed.

The crystalline boron samples were obtained from two suppliers; the Goodfellow, Corp. boron has stated purity 99.6% and the Aldrich Chemical Co. boron has stated purity 99.0%. Both samples showed similar initial and final separated particle characteristics. The amorphous boron oxide (B_2O_3) powder was obtained from Aldrich Chemical Co. with stated purity 99.98%. The raw samples were dry sieved using a Gilson model SS-5 vibrating sieve shaker with stacked sieves of decreasing hole size positioned underneath the preceding mesh. With a raw sample loaded into the top sieve, the largest particles are trapped in the first few meshes with the very smallest needing to travel through the entire stack. Sieves with mesh sizes of #850, 570, 635, 500, 450, 400, 325, 270, 230, 200 were used with mesh openings of 10, 15, 20, 25, 32, 38, 45, 53, 63, and 75 μm. Although the shaker's afforded vibrating/tapping combination was sufficient for separating aluminum, magnesium, and boron oxide

Table 2.5: Characteristics of powder samples used in the combustion experiments.

Particles	Form	Mesh Size	d_{eff} [μm]			Supplier
			Mean	Median	St. Dev.	
B	crystalline	10 - 15	11.8	11.2	2.4	Goodfellow [a]
B	crystalline	20 - 25	23.4	23.0	4.0	Goodfellow [a]
B	crystalline	45 - 53	49.2	48.0	7.6	Goodfellow [a]
B_2O_3	amorphous	20 - 25	43.3	42.6	6.4	Aldrich [b]
Al	-	20 - 25	21.6	21.7	2.4	Valimet, Inc. [c]
Al	-	45 - 53	53.1	52.3	5.2	Valimet, Inc. [c]

[a] Goodfellow Corp., Berwyn, PA 19312.
[b] Aldrich Chemicals, Milwaukee, WI 53233.
[c] see Roberts, Ref. (24)

samples, this technique proved unsuccessful for boron powders due to the tendency of the samples to clump. For boron, sieving was manually assisted with more violent tapping than the shaker produced to dislodge clumps which are formed by the shaker vibration. Boron samples were continually de-clumped and resieved through preceding larger hole-size meshes in an attempt to dislodge tiny sub-micron and micron sized particles which comprised the majority of each raw and partially sieved sample.

It was determined that it is the much smaller particles (less than 5 μm) which are responsible for most of the clumping tendency. Samples were periodically inspected, clumps re-crushed, and re-screened until deemed acceptably separated. Inspection was performed visually and samples deemed separated when further sieving onto a clean white plastic insert showed minimal or no additional particle fall-through. The boron samples were generally sieved in excess of 20 hours with maximum tapping. Boron oxide powders were sieved under purge with un-purified Argon to preclude contamination by water vapor - particulate boron oxide is very hygroscopic. The majority of the boron particles used in the experiments are from 10-15 μm, 20-25 μm, and 45-53 μm meshes; boron oxide particles are from the 38-45 μm mesh; and aluminum particles from 20-25 μm and 45-53 μm meshes.

All boron and boron oxide powders were received sealed air-tight from the supplier and were stored prior to and after sieving in individual vessels. These vessels were stored in a sealed container filled with anhydrous silica gel desiccant. Sieving of 10 to 20 gram samples of raw particles produced a gram or two of the desired separated sample with most of the boron being smaller than 5 μm; however, this was sufficient for test purposes since very little powder is used for each experiment.

The boron particle samples were photomicrographed and analyzed to document sample constituency and size distribution. Photomicrographs were taken with an ISI-DS130 and Hitachi S-800 scanning electron microscope (SEM) at various magnifications. Size distributions were measured manually by counting 100 - 200 randomly chosen particles on the SEM photograph. Photomicrographs were scanned into a computer and two perpendicular dimensions recorded with the use of fine measurement grids, with dimensional error approximately ±0.5 μm. In each case two dimensions are recorded along with the approximate shape of the particle; either a prolate spheroid or a parallelepiped.

Figures 2.49 - 2.51 show photomicrographs (and corresponding particle size histograms) of the three main boron samples used in the experiments. Photomicrographs of the particles reveal that the boron particles are irregularly shaped granules, some with sharp edges, which have sub-micron sized parasitic particles clinging to the surface. Higher magnification exposures are inconclusive as to whether these smaller particles are actually fused to the large particle surface. Also seen are

agglomerates of smaller fused particles which could not be broken apart when ground between quartz surfaces.

Figure 2.52 shows a photomicrograph and corresponding particle size histogram of the single boron oxide sample used to compare particle emissions to those of boron samples. Photomicrographs of the boron oxide reveal "rounder" particles than the boron crystals, but the oxide particles have very rough and porous surfaces.

Figures 2.53 - 2.54 show photomicrographs and particle size histograms of the two aluminum particle samples used. Photomicrographs of the aluminum show that unlike the boron and boron oxide samples, the aluminum particles are much more uniform and are spheroidally shaped. The 20-25 μm sample is fully described in Ref. (44) and shows very uniform particles with an effective mean diameter of 21.6 ± 2.4 μm. The larger 45-53 μm sample shows considerably larger variation in shape and types of particles; these particles however were only used to validate particle injection as will be discussed further in the next chapter.

The jagged boron particles will remain irregularly shaped for the majority of the time they are heated to ignition since boron has such a high melting temperature, making these particles non-ideal for particle sizing studies. Several effective means of spherodizing the particles prior to undertaking the experiments were considered, such as melting the particles in an argon purge using an arc discharge, but it was not clear whether the product particles would not be altered dramatically, especially as concerns the oxide layer. Regardless, the type of boron used in propellant formulations would be the same as that used here since this is the form which is readily available commercially. It will be shown that this irregularity in particle shape partially masks expected results based on modeling predictions. For boron oxide and aluminum on the other hand, which have low melting points, the initially non-spherical particles will become spherical upon melting which occurs early in the overall "ignition" process.

It is assumed for particle sizing that particles can be classified by an equivalent spherically shaped particle. The effective particle diameter is defined to be equal to the equivalent spherical diameter which conserves the particle mass (volume). The original non-spherical particles are treated either as prolate spheroids (ps) or parallelepipeds (pp). The effective diameter of each particle is then calculated from the two measured perpendicular dimensions according to Eq. (2.6) and (2.7);

$$d_{eff}^{ps} = [\, l_1 (l_2)^2 \,]^{\frac{1}{3}} \tag{2.6}$$

$$d_{eff}^{pp} = \sqrt[3]{\frac{6}{\pi}} \left[\frac{1}{2} (l_1 + l_2)\right] \tag{2.7}$$

where l_1 and l_2 are the lengths of the major and minor axes respectively. Histograms were produced from the counted particles, which are shown in the accompanying upcoming figures, and statistical effective diameters calculated. Table 2.5 lists measured mean and median effective particle diameters and standard deviations for the samples. These effective diameters are referred to as the initial particle diameters ($d_{p,0}$) elsewhere in this thesis. The boron powders have relatively large variation of particle sizes whereas the aluminum particles are more uniform. It is noted that boron particle effective diameters measured as described for ~24 μm particles are nearly identical to values measured by a particle sedimentation technique using a Horiba CAPA-700 Particle Analyzer with glycerin as the dispersion fluid.

Higher magnification SEM photomicrographs were taken of select boron, boron oxide, and aluminum particles to more closely inspect the surface character of each sample, as shown in Figs. 2.55 - 2.56. The highly magnified 20-25 μm boron particles have smooth surfaces which are flat, typical of crystals. The composition of the small particles which cling to the larger particles is not known. High magnification pictures of the boron oxide powders show a distinctly different picture where the surface is rough, cracked with large crevices evident in some cases, and is apparently porous. High magnification photomicrographs of typical aluminum particles also show satellite particles clinging to the surface, but they are fewer in number than on the boron particles. The aluminum particles have wrinkled or blotchy surfaces which are rounded, unlike the flat surfaces and edges found on boron particles.

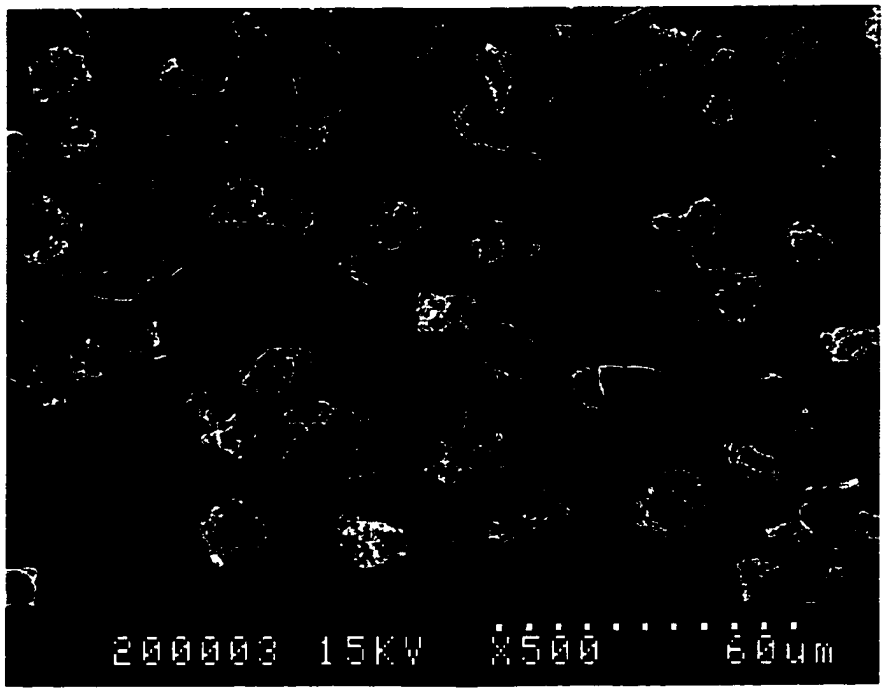

(a)

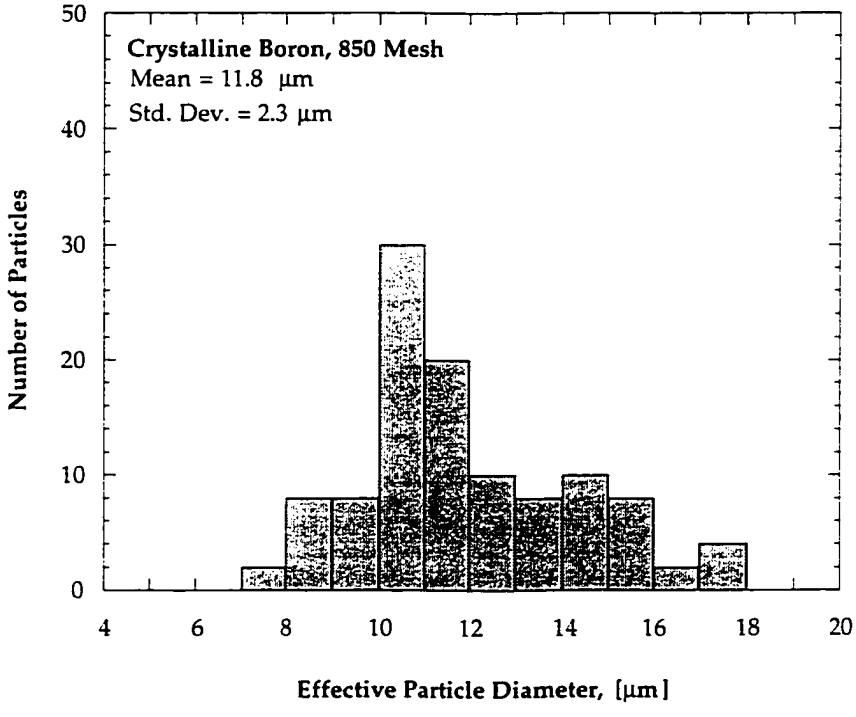

(b)

Fig. 2.49: Photomicrograph and particle size distribution of 10-15 µm crystalline boron powder. (**a**) SEM photomicrograph at 500X magnification. (**b**) Histogram based on 100 individual particle measurements.

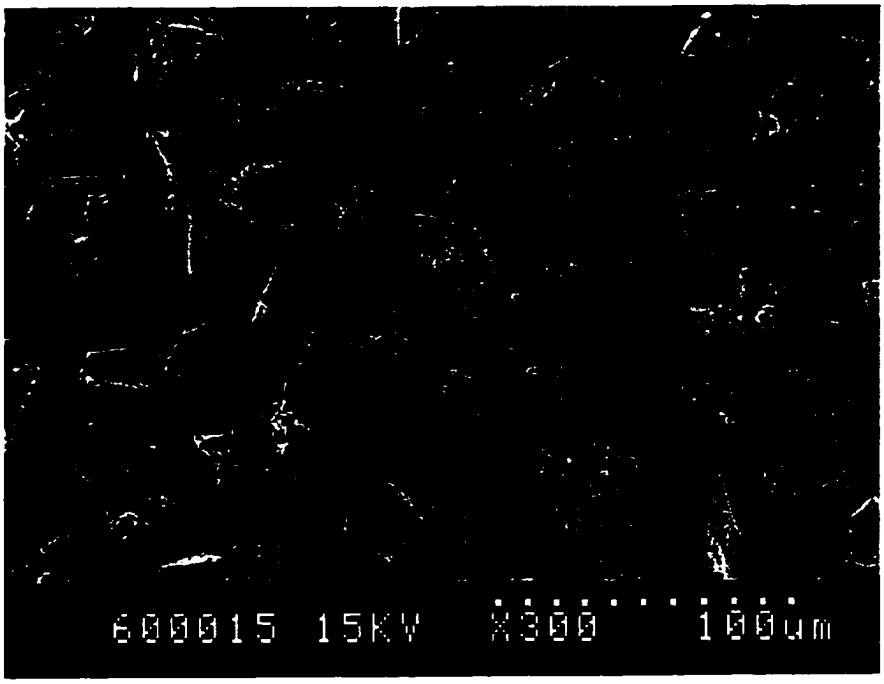

(a)

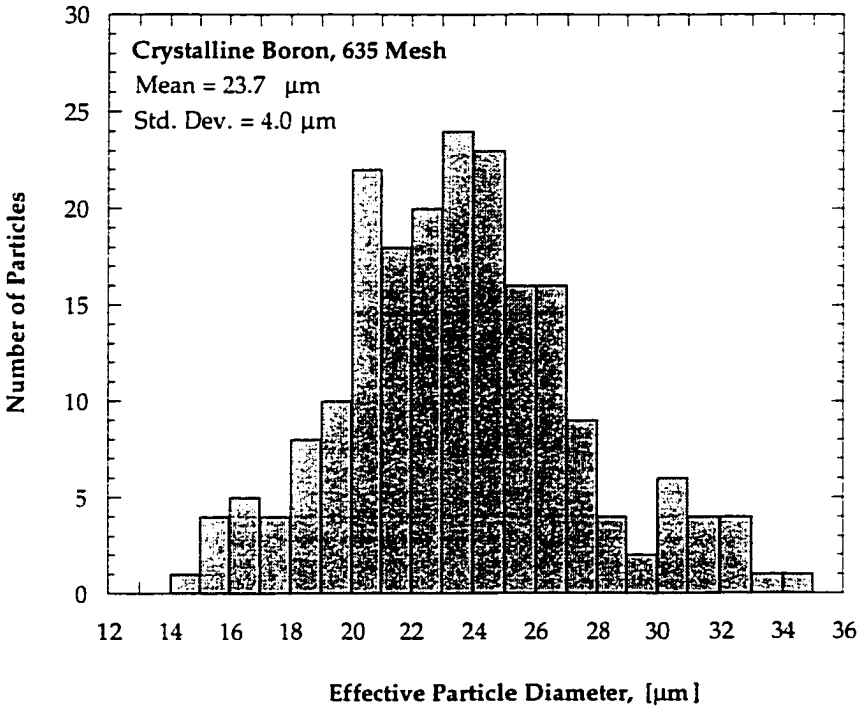

(b)

Fig. 2.50: Photomicrograph and particle size distribution of 20-25 µm crystalline boron powder. (a) SEM photomicrograph at 300X magnification. (b) Histogram based on 200 individual particle measurements.

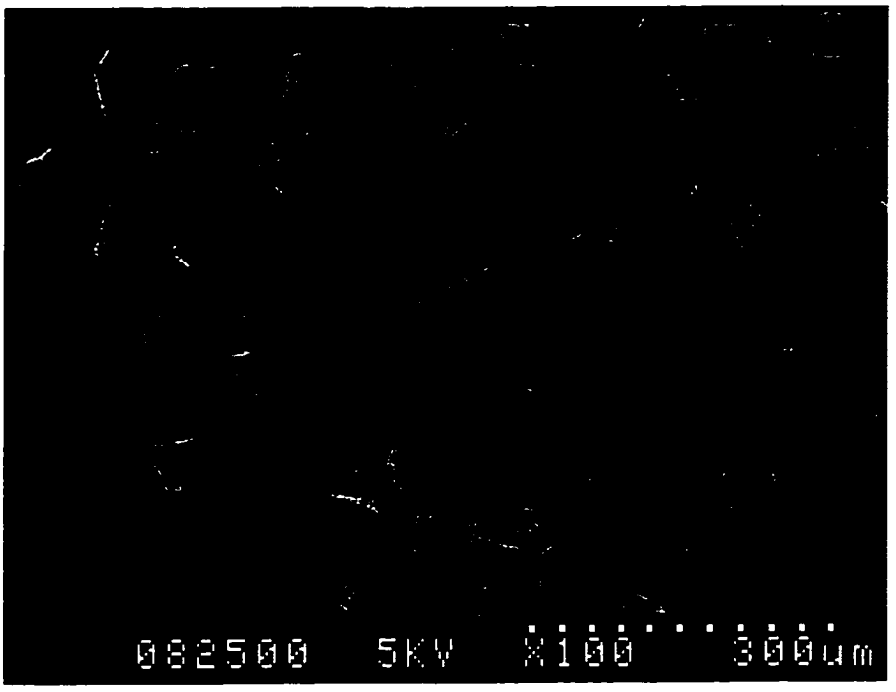

(a)

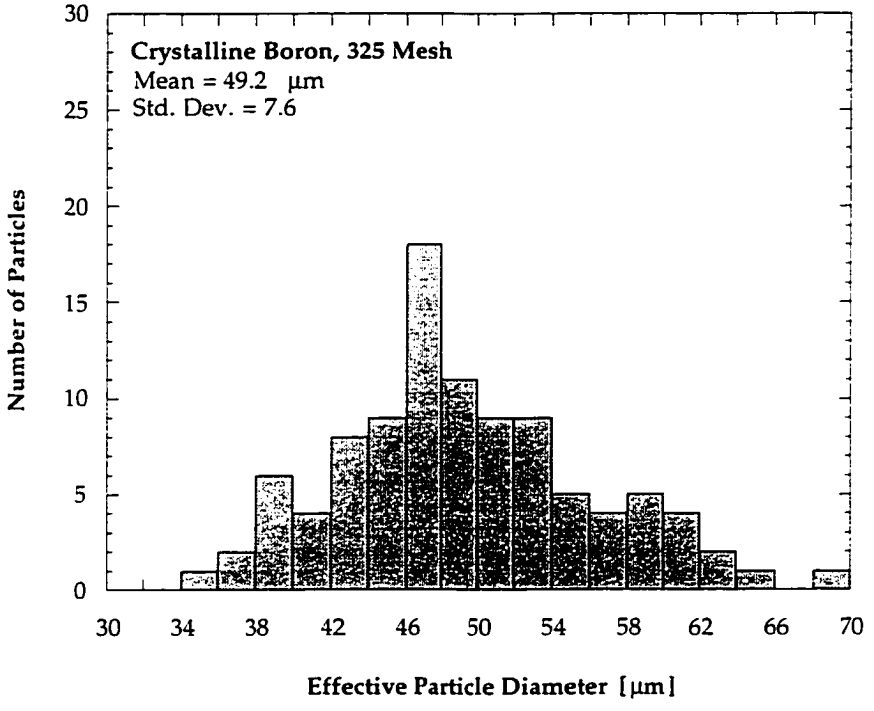

(b)

Fig. 2.51: Photomicrograph and particle size distribution of 45-53 µm crystalline boron powder. (**a**) SEM photomicrograph at 100X magnification. (**b**) Histogram based on 100 individual particle measurements.

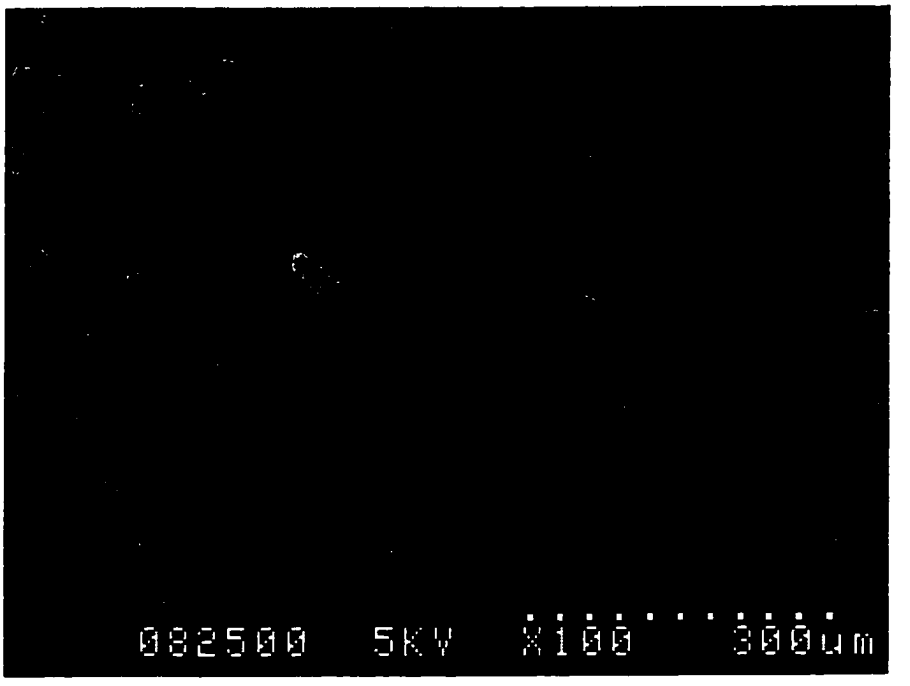

(a)

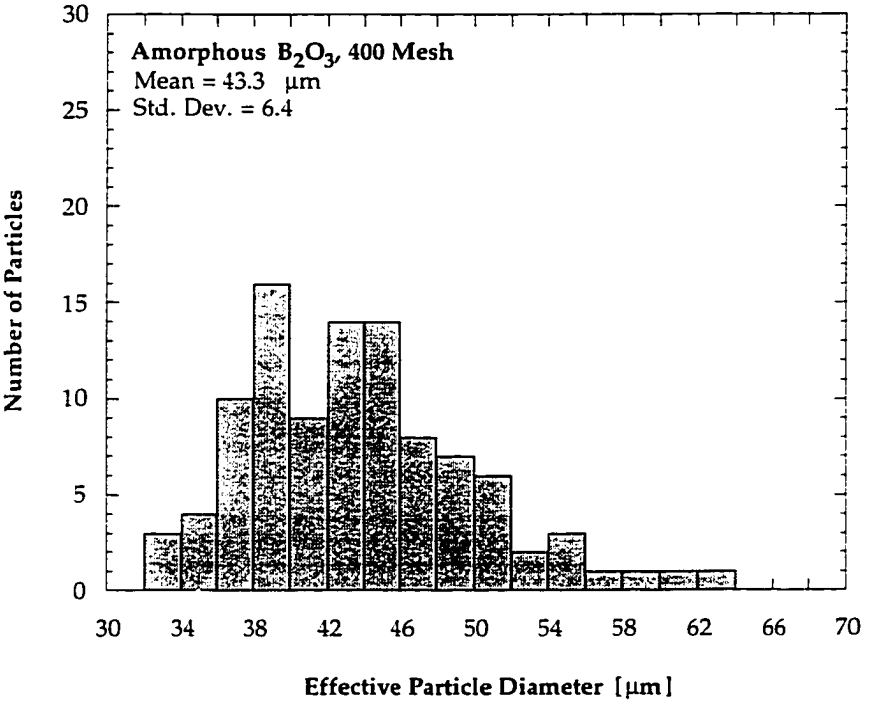

(b)

Fig. 2.52: Photomicrograph and particle size distribution of 38-45 µm amorphous boron oxide powder. (a) SEM photomicrograph at 100X magnification. (b) Histogram based on 100 individual particle measurements.

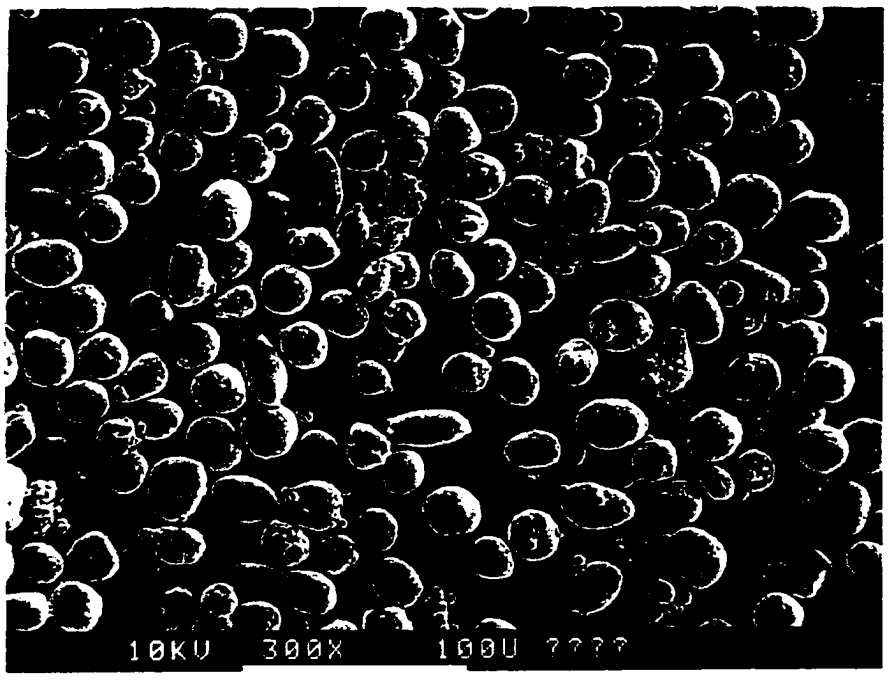

(a)

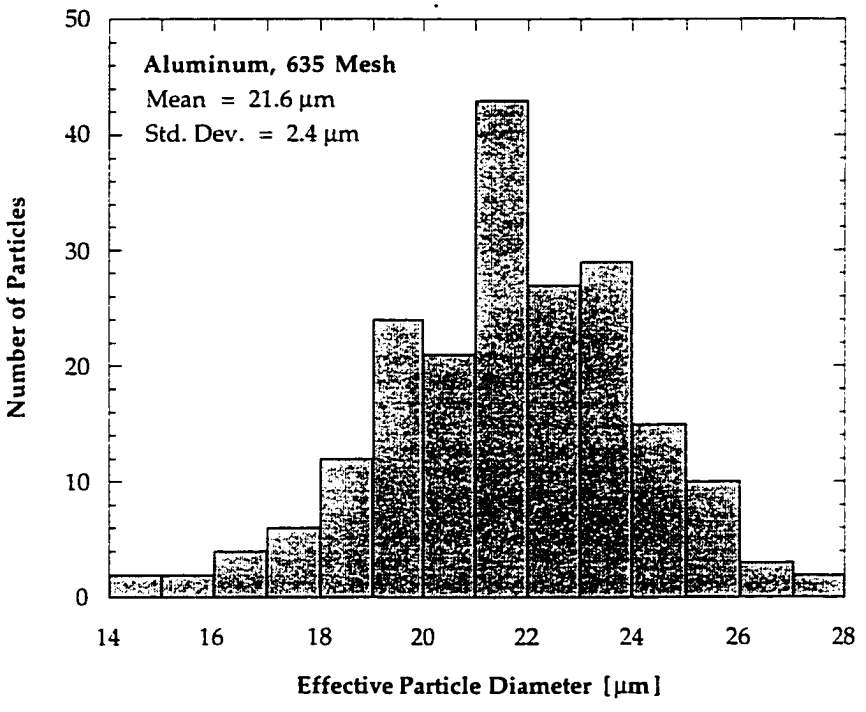

(b)

Fig. 2.53: Photomicrograph and particle size distribution of 20-25 µm aluminum powder from Roberts.[24] (a) SEM photomicrograph at 300X magnification. (b) Histogram based on 200 individual particle measurements.

(a)

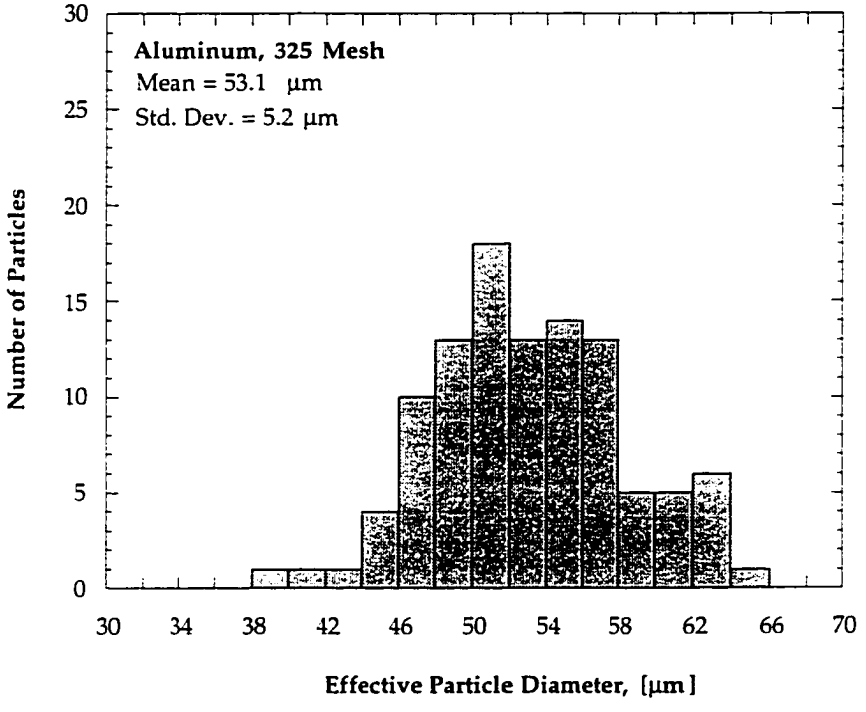

(b)

Fig. 2.54: Photomicrograph and particle size distribution of 45-53 µm aluminum powder. (**a**) SEM photomicrograph at 100X magnification. (**b**) Histogram based on 100 individual particle measurements.

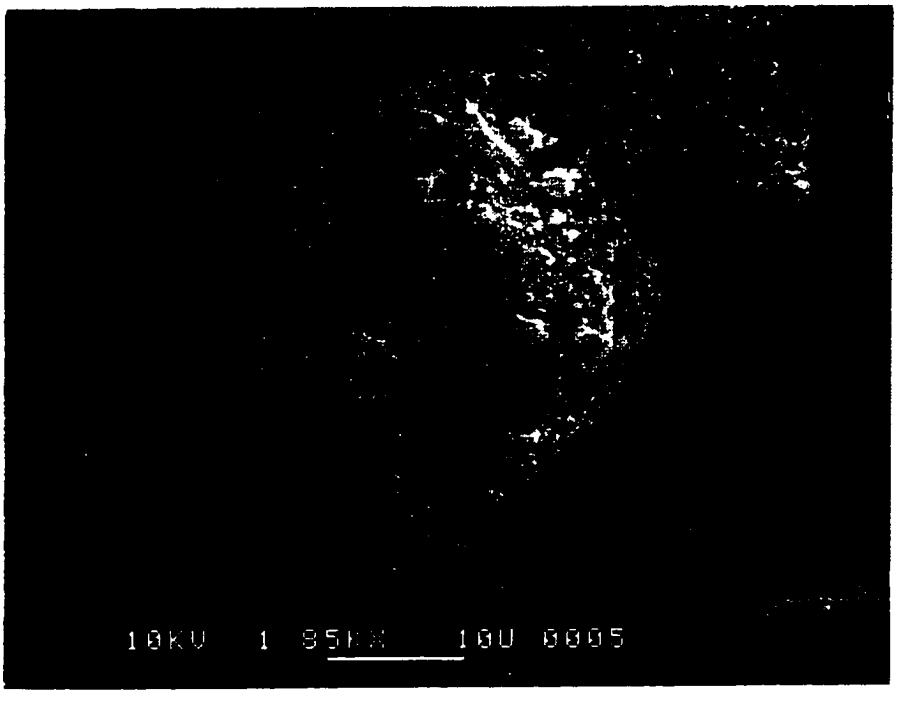

(a)

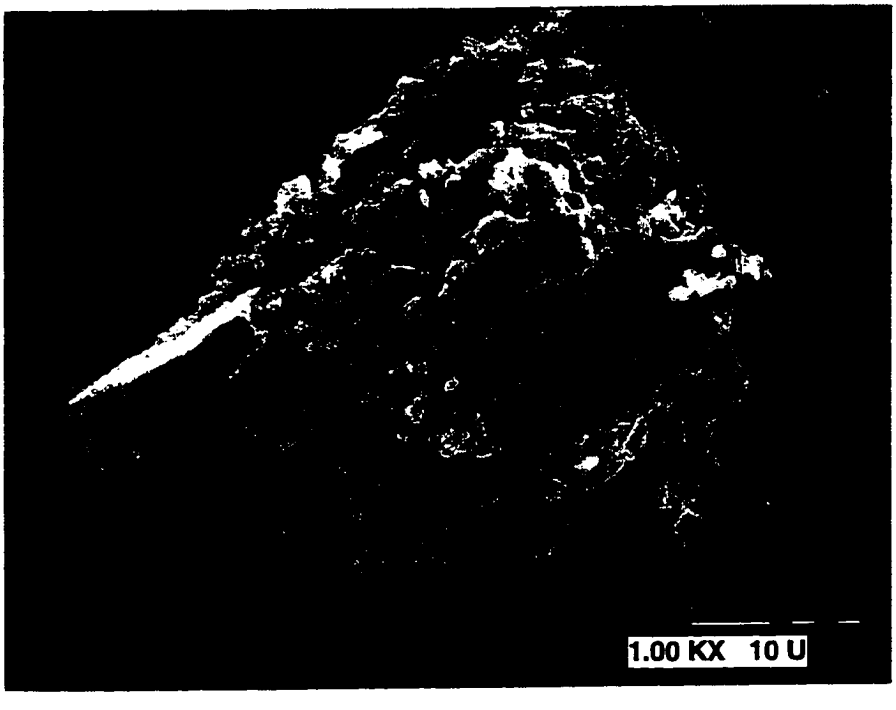

(b)

Fig. 2.55: High magnification photomicrograph of boron particles. (**a**) SEM photomicrograph of 20-25 μm boron particle at 1850X magnification showing flat edges and satellite particles. (**b**) SEM photomicrograph of an atypical 45-53 μm boron "particle" at 1000X magnification showing a chunk composed of a large number of smaller particles fused together, which did not break apart under grinding.

(a)

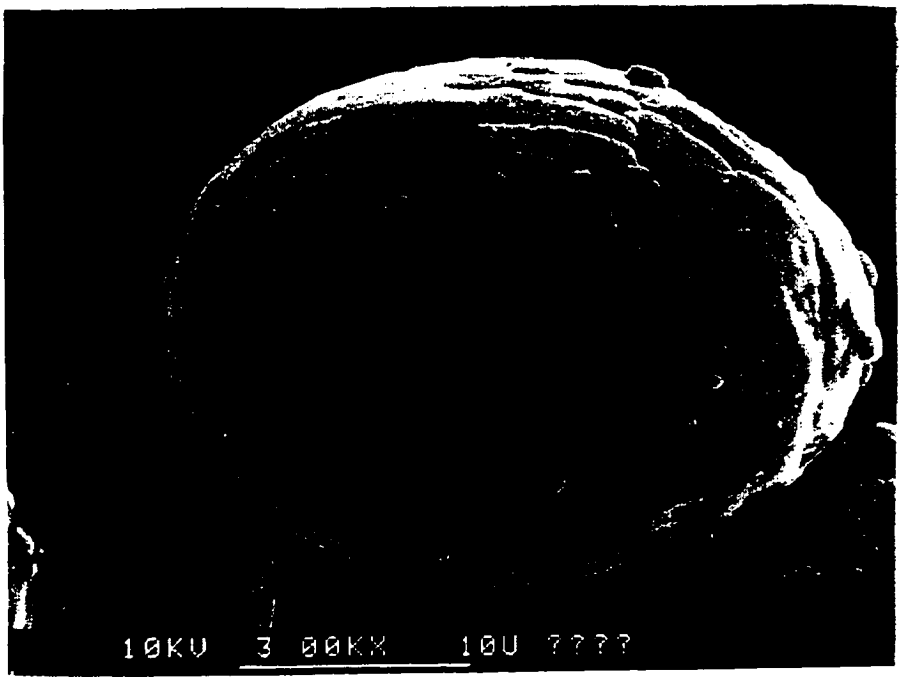

(b)

Fig. 2.56: High magnification photomicrograph of 38-45 μm boron oxide and 20-25 μm aluminum particles. (**a**) SEM photomicrograph of boron oxide particle at 1000X magnification showing rough surface and cracks. (**b**) SEM photomicrograph of spheroidal aluminum particle at 3000X magnification showing wrinkled surface and few satellite particles, from Roberts.[24]

3. EXPERIMENTAL DATA AND DISCUSSION

3.1 Typical Measurement of Gas Mixture Combustion

It is desired that particle combustion experiments occur at nearly constant ambient pressure and temperature. Therefore it is necessary to delay particle exposure to the reacting ambient gases until these mixtures have reached peak pressure and any gas-phase transients have sufficiently subsided. It is judged that this occurs typically ~4 msec after initial spark discharge, as will now be discussed.

Figure 3.1 shows a multi-shot average pressure and average photodiode measurement in the combustion chamber for a given initial gas loading (mixture B, $H_2/O_2/N_2$ = .27/.32/.41, p_1 = 20.4 atm; see Table 2.1) where there are no particles present. After spark discharge at t = - 0.5 msec in Fig. 3.1, gas-phase combustion takes place causing the pressure to rise and peak at 2280 psia (155 atm) within ~2.5 msec. Measured signals show 4.00±.05 kHz oscillations, which are very repeatable between experiments and whose origin is not well understood (see Section 2.1). Hot gas emissions which are monitored through narrow band-pass filters show a brightening in luminosity up to the point of peak pressure, as gas-phase chemical reaction proceeds, followed by a slow decay. Particle combustion tests performed after ~4 msec delay would be ideal, as this is when gas phase constituents are completely reacted and maximum pressure has been reached.

3.2 Particle Injection Technique

It is of interest to conduct particle combustion tests on particles in the size range of 10-70 μm, sizes which would be considered for use in propellant additives. It was initially found that in experiments where such particles were exposed to the igniting gaseous mixture, they ignited while chamber pressures were still rising (see Section 2.1). In order to study particle combustion in the chamber at well-defined nearly constant pressure and temperature conditions, particle introduction into the hot ambient gases is delayed until the hydrogen/oxygen gas-phase combustion transients have subsided. During this delay it is necessary to keep the particles isolated from the hot chemically reacting gases and to inject them rapidly, since particle heat-up times to ignition are on the order of 2 msec for the sizes of interest, compared to the ~2.5 msec rise time for chamber gas pressure and temperature. It is also important to disperse the particles beyond the injector surface thermal layer so they may react with the gas phase independently of one another and the particle injector body.

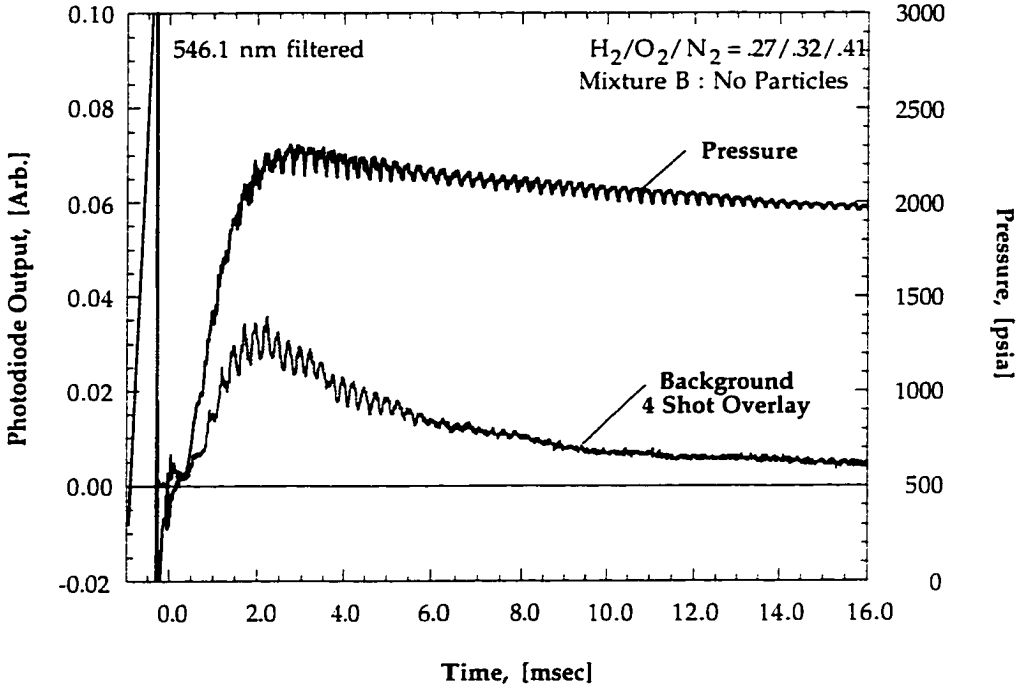

Fig. 3.1: Typical multi-shot average pressure and band-pass filtered photodiode signals in the combustion chamber with no particles present, in a mixture initially containing $H_2/O_2/N_2$ = .27/.32/.41 at 20.4 atm (mixture B). Background emissions come from radiating hot gases. Particle tests are conducted after sufficient delay to allow gas-phase combustion transients to subside.

To achieve the desired result an injector has been developed which uses the pressure rise in the chamber to accelerate a 1.6 cm dia. piston/plunger loaded with particles to high velocity. The dynamics of the injector have been configured to provide suitably long injection delay (4 to 8 msec) combined with fast injection (~12 m/sec). Particles are loaded into the shallow annular groove (1.8 mm length by 0.8 mm depth) in the shaft of the particle injector. The axial length of the particle-containing annulus requires ~100 μsec to inject the entire sample. Less than 20% of this groove is filled with particles (~4 mg boron) and not all particles are finally injected because some become embedded in the Teflon collar seal. Particle dispersion cannot be observed directly in the chamber at combustion conditions since such optical access is impractical at the pressures under study. To gain confidence in the injector's operation, several tests were performed to investigate the issues of sufficient injection, particle dispersion, and whether the injection technique alters particle ignition and combustion. A discussion of injector operation validation is deferred to Section 3.4 so that signal interpretation can be discussed first.

3.3 Interpretation of Particle-Laden Signals

3.3.1 Typical Aluminum Particle Signal

Typical aluminum and boron particle signals are shown in Figs. 3.2 and 3.3. Figure 3.2 shows an aluminum particle measurement and background measurement at identical ambient conditions of Fig. 3.1. It is seen that after spark ignition, the pressure and hot gas emissions rise to peak levels. Then at 4.1 msec aluminum particles are injected as indicated by the injection-timing mark (from the make-switch device) in the figure. Shortly after injection the band-pass filtered photodiode measurement centered at 486.1 nm shows a rapid increase in luminosity above the background level due to particle ignition. This is followed by a peak in the particle signal and an eventual return of measured luminosity to the background gas emission level, indicating particle combustion and conversion to gas-phase products is complete. In Fig. 3.2 the filtered background hot gas emissions are negligible compared to the aluminum-particle emissions.

Notice that chamber pressure is unaffected by particle combustion. Likewise, the bulk gas mixture composition is unaffected at long times as seen by the excellent match between particle-laden and background hot-gas emissions after particle combustion is completed. For all tests conducted, the mass of particles introduced is negligible compared to the bulk gas mass, ~1:2500 for the lowest pressures studied (37.5 atm).

3.3.2 Typical Boron Particle Signal

A sample boron particle measurement is shown in Fig. 3.3 at identical ambient conditions to Figs. 3.1 and 3.2. For boron experiments a band-pass filter centered at 546.1 nm is used. There is a longer delay before particle emissions appear than is the case for aluminum particles. Particle emissions also rise more gradually, peak, and decay more gradually to background levels. It is evident from Fig. 3.3 that there is only a single stage for boron ignition. A direct comparison of the two figures demonstrates that boron particle ignition and combustion dynamics are much slower than for aluminum particles.

The hot ambient gases exhibit significant luminosity levels compared to the boron particle signal which cannot be neglected throughout the particle ignition and combustion events. To determine particle combustion timescales, a net particle signal is obtained by subtracting out the average "no-particle" background emissions filtered at identical wavelengths to the particle-laden emissions. Background emissions for all gas mixtures were discussed in Section 2.3.6. Ignition delay and combustion times are determined from the net-particle signal for both boron and aluminum.

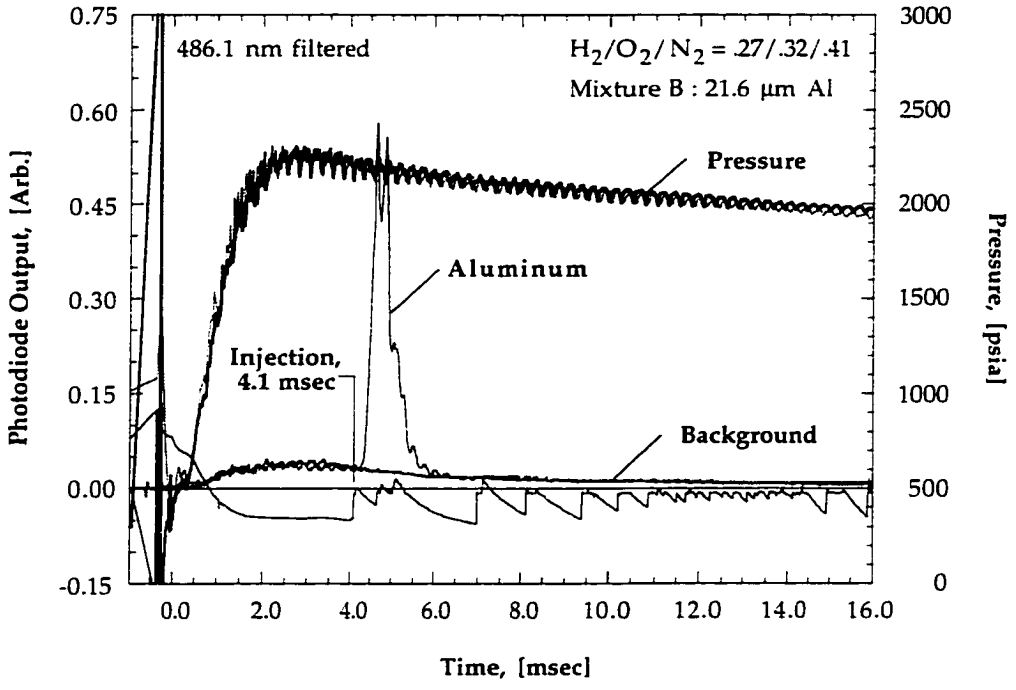

Fig. 3.2: Typical aluminum particle signal in combusting mixture identical to Fig. 3.1 but filtered at 486.1 nm. After injection at 4.1 msec, emissions increase to a peak and decay back to background level at 6 msec.

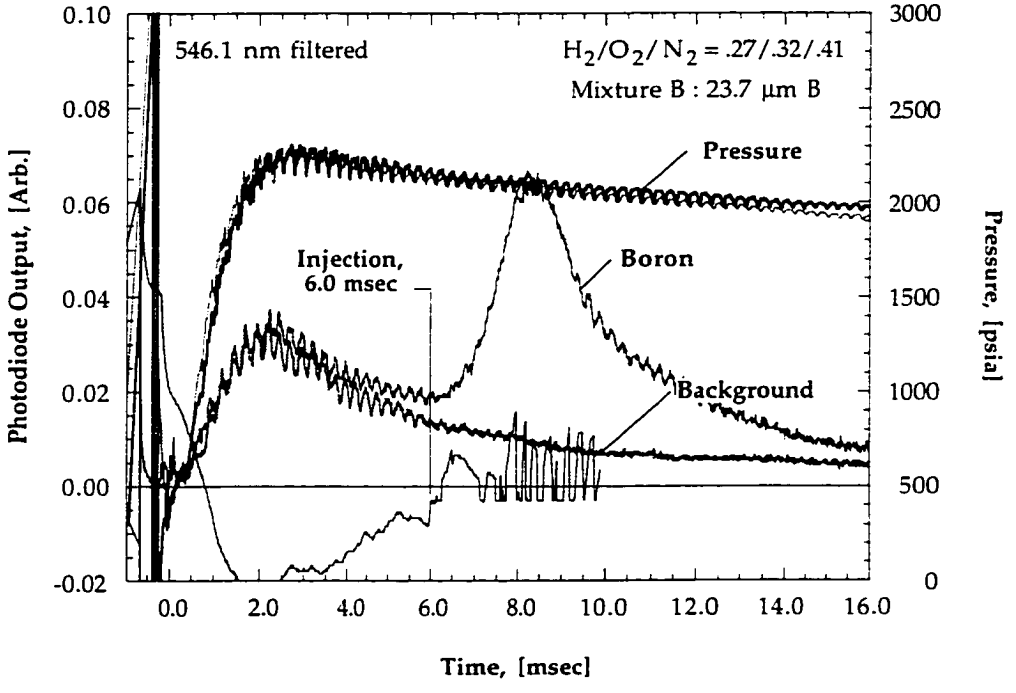

Fig. 3.3: Typical boron particle signal in combusting mixture identical to Fig. 3.1, filtered at 546.1 nm. Particle injection occurs at 6.0 msec and signal width is much broader than aluminum-particle signal at identical conditions.

3.3.3 Definition of Particle Ignition Delay and Combustion Time

The method for determining particle ignition delay and combustion times is illustrated in Fig. 3.4. Ignition is defined as occurring at the half-maximum point in the net filtered photodiode output signal. Then ignition delay is defined as the time from the temperature stimulus (time of particle injection) to the point of ignition, and combustion (burn) time is defined as the time from ignition to the time when the net filtered photodiode output signal has fallen back to half-maximum (see Fig. 3.4). This methodology is consistent with earlier particle combustion work at intermediate pressures.[30,44,46] Two additional methods to define when particle combustion is complete, using either a 90%-completion (90% of area under the net signal) or complete burn-out (when net signal returns to zero) are also considered below.

As discussed in the previous chapter, particle combustion time histories are measured indirectly by monitoring combustion emissions using narrow band-pass optical filters. For boron particle tests, emissions are monitored about the 545 and 518 nm bands of the BO_2 molecule. Recent work in a shock tube[11] typically with 100% O_2 at 8.5 atm and 2650 K using both infrared measurements filtered at 5.0 ± 0.15 μm (approximate B_2O_3 band) and also the 546.1 ± 4 nm (BO_2) filtering used in this study, show that the infrared signal rise precedes the visible signal rise by about 250 μsec, independent of

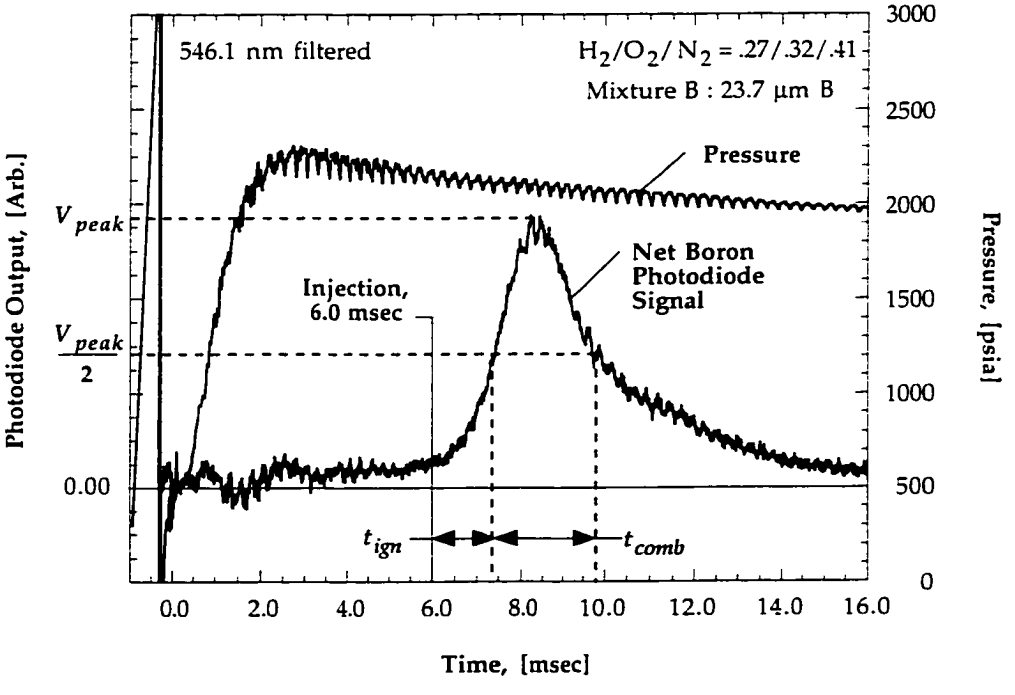

Fig. 3.4: Typical net boron particle signal in combusting mixture identical to Fig. 3.1 filtered at 546.1 nm, defining ignition delay and combustion times in terms of the time at half of peak amplitude.

particle size (7.2 and 11.8 μm). This indicates that delays determined for boron particles in this study may be long by ~0.25 msec. However, similar tests at ~2850 K showed that data could not be obtained from infrared measurements due to high background O_2-gas emission levels. Further discussion of the infrared measurements is given in Ref. (12). The reason for the discrepancy in ignition delay determinations based on monitoring emissions about the BO_2 molecule bands compared to B_2O_3 bands is unclear, but likely has to do with gasification dynamics at the particle surface during particle heat-up. Rood did not investigate the contribution to the infrared signal from the hot particle "glow". Infrared measurements are not possible at combustion chamber conditions due to expected significant interference from water vapor molecule emission bands near 5 microns at all temperatures.

Alternate Definitions of the Combustion Time

Combustion times are also determined using an approach which correlates the total area under the net-particle signal to the amount of energy released in a certain spectral bandwidth.[61] Then the particles are considered to be approximately burned to completion when the majority of their useful energy has been consumed *as determined by their luminous brightness*, where the remaining luminosity is considered as either negligible energy release or possibly as lingering emissions from the hot oxides which are formed. In this study a value of 90% of the total area under the net-particle signal curve is chosen as the point when particles burn to completion according to this definition. The combustion time $t_{c:90}$ then is defined as lasting from the point of ignition, still defined by the half of peak amplitude method, to the time when 90%-area is reached.

This approach can be extended to define completed combustion instead at the time when 100% of the total area under the net-particle signal curve is reached. Particle combustion is then considered completed when the net-particle signal curve returns to zero, and is referred to here as $t_{c:100}$. This definition coincides most closely with that used in practice by Macek[4,62] and Yeh and Kuo[10] in flat-flames at 1 atm where combustion was considered to have ended when luminous particle-streaks on photographic film vanished. In the high pressure experiments such a definition leads to serious problems interpreting the boron combustion stage for the following three reasons.

Firstly at high pressure the background hot gas emissions are not negligible compared to boron combustion emissions and they must be subtracted out to obtain the net contribution from combusting particles. The process entails subtracting two large signals (with associated uncertainties) to obtain an exactly zero result. Boron particle signals typically fade to zero gradually and this leads to very large interpretive uncertainty in the result. For boron particles a small non-zero net-particle signal is often observed to last for a long time which introduces large scatter into the determination of $t_{c:100}$. This lingering signal could be due to several factors which include emissions from iingering particle "embers", or smoke cloud emissions as discussed by Olsen and Beckstead[61] for aluminum, or from

lingering BO_2 molecules which do not recombine into HBO_2 or B_2O_3 at these high ambient temperatures.

Secondly although backgrounds are very reproducible in an overall sense, there is some variation between different experiments. The small mismatch in the tail of the signal, where hot gas emissions decay from the peak, introduces *negligible* uncertainty in measured maximum and half-maximum amplitudes determined from the net-particle signal, but conversely introduces *large* uncertainty in the time $t_{c:100}$ because the net-particle signal returns to zero very slowly.

Lastly, these are not single particle experiments and the individual boron particles show a large variation in sizes and shapes. By stipulating completed combustion to occur at the 100%-area point for all particles one is effectively measuring the burn time of the largest effective diameter particle component which is poorly known even after micro mesh sieving. Therefore it is believed appropriate to define combustion times in a statistical sense to indicate when the majority of the particles are consumed, by using the time between the half maxima similar to previously studies by Roberts[24,44] and Megli, et al.[45,46] The use of large numbers of particles (but still a small mass) alleviates the problems arising from individual particle variations by introducing statistical averaging.

For aluminum particles the difference between t_{comb} and $t_{c:90}$ is fairly small in an absolute sense but not in a relative sense because the measured times are so short. Even at ~145 atm measured $t_{c:100}$ are quite a bit longer than $t_{c:90}$. If this difference is an artifact of lingering emissions, then the problem of interpreting combustion measurements at low pressures[61] appears to persist even at high pressures.

Several measured particle combustion signals are presented in Appendix C where these issues can be further inspected. Now that signal interpretations have been presented, validation tests are discussed which were used to gain confidence in the particle injection methodology. This is followed by presentation of the measured particle ignition delay time and combustion time trends which were investigated as the thrust of this study.

3.4 Uncertainty in Measured t_{ign} and t_{comb}

Measured ignition delay (t_{ign}) and combustion times (t_{comb}) have associated uncertainties which are partly due to interpretation of the net-particle signals. These characteristic times are obtained from the recorded photodiode signals where the response time of the photodiode circuitry has been measured to be less than 1 μsec and so detector response is not of concern. To obtain a net-particle signal, a composite background average of several hot-gas emission signals (no-particle signals) is first

constructed where it was shown that these backgrounds are quite reproducible. The net particle signal is then obtained from the raw data by subtracting out the average no-particle signal. From the net particle signal the peak amplitude V_{peak} is determined from the trace. The peak is generally well defined except in cases where signal levels are low or there are excessive oscillations in the photodiode trace. The choice of V_{peak} has an associated uncertainty ΔV_{peak} leading to a value of the half-height ("hh") $V_{hh} \pm \Delta V_{hh}$. From this value, two times $t_{hh}^{(1)}$ and $t_{hh}^{(2)}$ are determined corresponding to the times which bracket the full-width at half-maximum. The resulting uncertainty in the $t_{hh}^{(i)}$ associated with the uncertainty in the half-height is generally *less than* ± 10 *μsec and is small* compared to the injection timing uncertainty and the interpretation uncertainty.

The uncertainty in the ignition delay time results from the finite time to inject the entire particle sample (Δt_{inj}) and the uncertainty in $t_{hh}^{(1)}$ attributable to interpretation. Values of the ignition delay time are calculated as the time between particle injection, t_{inj}, and ignition which is stipulated to occur at $t_{hh}^{(1)}$. There is generally a small interpretive-uncertainty in the choice of $t_{hh}^{(1)}$ because the resulting net-particle signal rises quickly and unambiguously toward the peak value; however in instances where the composite background is poor (noisy) and/or the measured particle signal contribution is weak, there may be cases when $t_{hh}^{(1)}$ corresponding to a value of $V_{hh} \pm \Delta V_{hh}$ is not singular and clearly defined (see Fig. 3.5), and where an average value is taken instead. The resulting interpretive-uncertainty in $t_{hh}^{(1)}$ is denoted by $\Delta_{hh\text{-}interp}^{(1)\,+/-}$. The uncertainties in t_{ign} are taken to be the maximum of the injection uncertainty and the interpretive uncertainty:

$$\Delta_{t_{ign}}^{+} = \text{MAX}\,(\Delta_{t_{inj}}\,,\ \Delta_{hh\text{-}interp}^{(1)\,+}) \qquad (3.1\text{ a})$$

and

$$\Delta_{t_{ign}}^{-} = \text{MAX}\,(\Delta_{t_{inj}}\,,\ \Delta_{hh\text{-}interp}^{(1)\,-}) \qquad (3.1\text{ b})$$

where because of the interpretive factor, $\Delta_{t_{ign}}^{+}$ is not necessarily equal to $\Delta_{t_{ign}}^{-}$. In most cases except those where the net-particle signal is weak and noisy, $\Delta_{t_{inj}}$ is the dominant uncertainty in t_{ign} and this is less than ± 60 μsec (see Section 2.3.7).

The uncertainty in the combustion time is likewise open to interpretive-uncertainty but here this uncertainty may be quite large due to the character of the boron signals. Whereas the particle emissions rise quickly on approach to peak levels, they decay more slowly for boron and often linger for quite some time. Thus the interpretive uncertainty in $t_{hh}^{(2)}$, given by $\Delta_{hh\text{-}interp}^{(2)\,+/-}$, may be comparatively large. The uncertainty in the combustion time is given by Eqs. (3.2),

$$\Delta_{t_{comb}}^{+} = t_{comb} - t_{c,min} = \Delta_{hh\text{-}interp}^{(2)\,+} + \Delta_{t_{ign}}^{-} \qquad (3.2\text{ a})$$

and

$$\Delta_{t_{comb}}^{-} = t_{c,max} - t_{comb} = \Delta_{hh\text{-}interp}^{(2)\,-} + \Delta_{t_{ign}}^{+} \qquad (3.2\text{ b})$$

where the uncertainty in $t_{hh}^{(1)}$ is now compounded with the uncertainty in $t_{hh}^{(2)}$. These uncertainties are shown schematically in Fig. 3.5.

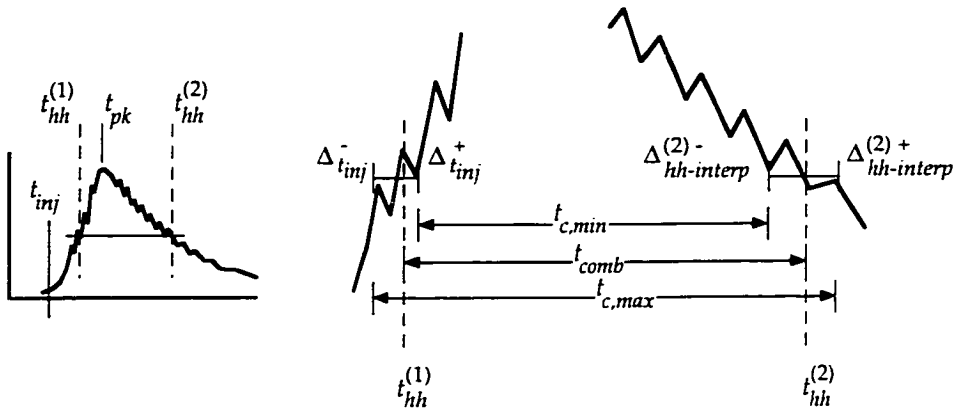

Fig. 3.5: Specification of uncertainties in ignition delay and combustion times.

3.5 Validation of Particle Injection Technique

3.5.1 Injector Operating Issues

It is desired to study individual particle ignition and combustion rather than group or particle cloud ignition and combustion. A fundamental requirement of the particle tests is that the particles do not interact with each other or the particle injector while they are being heated and combusted. The possibility for group particle interactions requires collection of evidence that group dynamics are in fact not occurring at combustion chamber conditions. Three key issues are identified which greatly affect measured particle ignition and combustion. They are: (1) sufficient particle injection, to ensure no interaction with the injector; (2) sufficient dispersion, to ensure individual versus group combustion; and (3) evidence that the injection technique does not itself affect the particle ignition process. These three issues along with the requirement for ~4 to 8 msec injection delay time played a crucial role during injector design.

To address the three issues identified, three sets of measurements were conducted to validate particle injector operation. To investigate sufficient particle injection and dispersion, high speed photography was conducted on particles injected through a propane flame sheet at atmospheric pressure. Dispersion concerns were further addressed by injecting a bimodal mixture of particles into the chamber at high pressure conditions and comparing the characteristics of the two-constituent mixture to those measured separately for the individual parts. Furthermore, measurements at chamber conditions

were performed with aluminum particles to validate Al-particle ignition and combustion time dependencies on pressure by comparison to independent data. All injector validation tests are performed using either 21.6 μm (with tight size distributions) and 45-53 μm spherodized aluminum particles. Aluminum was chosen for injector validation because a large Al-particle database at elevated pressures already exists in the literature and the Al-particle ignition processes are well documented, much more so than for boron particles.

To ensure sufficient particle injection, the injector was designed to impart a high enough velocity onto the particles to propel them through thermal layers forming above the particle injector and on the plunger itself. Based on predicted injector performance, particle trajectories were calculated assuming a drag coefficient formulation to model the deceleration (see Section 4.2.1). The particle velocity and distance traveled in the gas are given by solution of

$$\frac{dv_p}{dt} = -\frac{1}{2}\frac{\rho_g}{m_p} S_p C_D (v_p - v_g)^2 \tag{3.3}$$

$$\frac{dx_p}{dt} = v_p \tag{3.4}$$

where $v_p(t)$ the time dependent particle velocity, m_p is the particle mass, ρ_g the gas mixture density, S_p the particle frontal area, C_D the empirical drag coefficient, v_g the bulk gas velocity (≈ 0), and x_p the distance traveled (penetration depth). The two equations along with the energy and particle mass conservation equations are integrated numerically in Chapter 4 and yield among other information the depth to which particles penetrate into the ambient gases. Boron particles with 23.7 μm initial diameter typically come to rest within 1.5 to 2 msec after injection between 0.5 and 0.8 cm above their release point (see Fig. 3.6).

Simple one-dimensional transient thermal heat conduction analysis is applied to calculate growing thermal layers forming above the injector body and along the exposed plunger. The growth of the thermal layer above the injector is calculated from the analytical solution of Luikov[52] where the thermal layer height is taken to be the point at which the gas temperature reaches 99 percent of the far-field temperature. For the gas mixtures containing $O_2/H_2O/N_2$ = .20/.30/.45 (*products* here) at ~145 atm and 2675 K peak combustion temperature, the analysis plotted in Fig. 3.6 shows the particles spend insignificant fraction of their lifetime within growing thermal layers, only ~30 microseconds. Thus the particles are propelled sufficiently far beyond the growing thermal layers and into the hot surrounding gases.

Furthermore calculations of the near-wall temperatures show that particles which adhere to the injector plunger or which reside in the thermal layer above the injector housing will not ignite on the millisecond timescales under study. The temperatures there remain too low for ignition, and this

was evidenced in tests using ~1 μm boron particles which were purposely "glued" to the plunger annulus using finger oil. During injection most of the particles remained stuck to the plunger and were recovered after the experiment (but not chemically analyzed). The measured particle combustion signal showed nearly indistinguishable net particle emissions, where the gas temperature was as high as 2650 K during particle exposure inside the chamber.

Particles at the instant of injection have an imparted velocity of ~12 m/sec subsequent to which they slow due to viscous effects. Initially the particle Reynolds Numbers, $Re_p = \rho_g d_p v_{p,0} / \mu_g$, where μ_g is the gas mixture viscosity, are between 40 and 150 depending on gas density ρ_g (for p_c varied from 37.5 to 150 atm) for 23.7 μm particles where the thermal layer has been neglected. For these Reynolds numbers the maximum surface-average particle Nusselt numbers are between 5 and 8.5, where Nu_p is given by

$$Nu_p = 2 + 0.459\, Pr^{0.33}\, Re_p^{0.55} \tag{3.5}$$

and $Nu_p = 2$ corresponds to the analytical result for pure conduction (Pr is the Prandtl number). As will be discussed in Chapter 4, this requires that convective (heating) effects be included in any analysis of particle heating. Analysis furthermore indicates that the thin oxide layer coating the boron and the aluminum particles themselves will liquefy while the particles are still in motion.

It is interesting to note that the particles in the hpcc experiments have average slip velocities

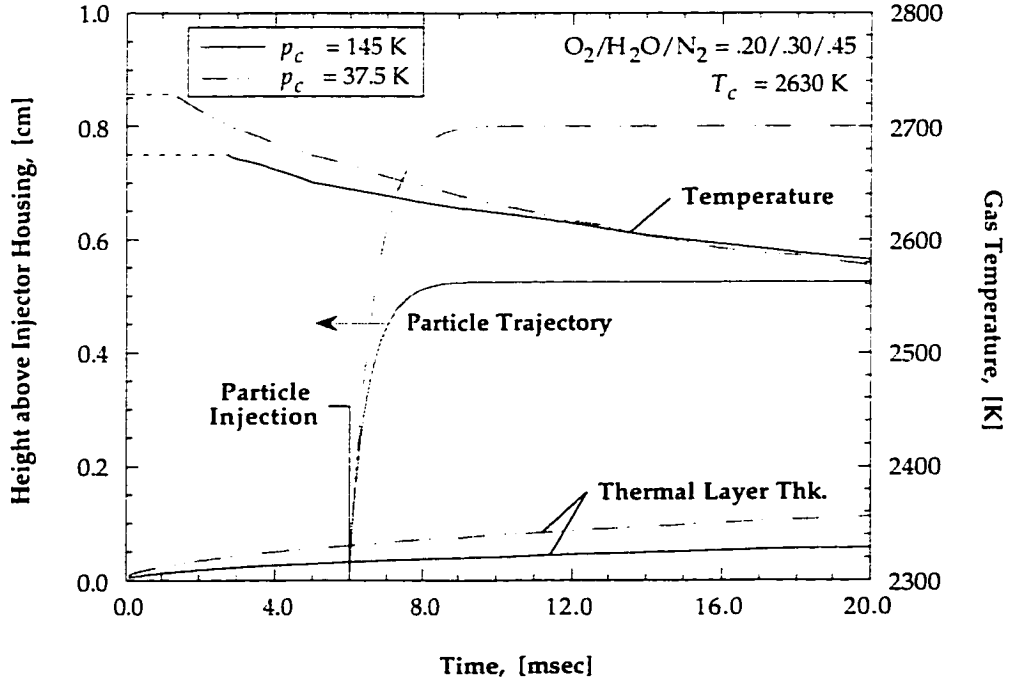

Fig. 3.6: Calculated particle trajectory and thermal layer growth. Particles spend negligible time in thermal layers and are decelerated by viscous drag.

$|v_p - v_g|_{avg}$ which are comparable to those experienced by particles emanating from the surface of HTPB/AP propellant (hydroxyl-terminated polybutadiene and ammonium perchlorate) driven combustion systems operating at 1000 psia (68 atm). This turns out to be merely a coincidence but is very useful from the standpoint of drawing analogies between the measured data and engineering applications. It will be shown in Chapter 4 that the magnitudes of convective heat transfer coefficients for the two cases are similar as well.

3.5.2 Investigation of Particle Dispersion

The second concern with injector operation is whether the particle injector sufficiently disperses particles so that they ignite and burn independently. Single-particle tests are not possible with the present injector and emission detection system. Sufficient numbers of particles are required to get strong enough signals to differentiate the contributions of combusting particles from the hot ambient background gasses. It was prohibitive to design sufficient optical access to the chamber to observe particle dispersion directly at high pressure conditions. Nevertheless, as a starting point, particles were injected through a propane flame sheet at atmospheric pressure and filmed with high speed camera sequencing system.

A camera system was developed in our laboratory to photograph combusting aluminum particles flowing in the exhaust products of burning propellants; details of this system can be found in Ref. (63). This camera has been used to photograph how particles injected with the particle injector are dispersed. According to the photograph in Fig. 3.7, 45-53 μm aluminum particles injected into the flame sheet are seen to ignite as distinct point sources and remain isolated from their neighboring particles as they become entrained in the gas flow. The flow of gases in the flame sheet was used to produce particle streaks for clarity. This leads us to conclude that particles are igniting and burning independently of one another and that the injector provides good dispersion, at least at one atmosphere.

Particle behavior at higher ambient temperature and gas density can be significantly different from the results obtained at one atmosphere. Much greater temperature and density gradients exist at chamber conditions. Two additional sets of experiments were thus performed to validate injector operation in the combustion chamber itself. Toward investigating whether group particle interactions occur at high pressure and temperature, particle ignition is studied with an aluminum powder sample containing a bimodal size distribution. Figure 3.8 shows the results of injecting a mixture of 20-25 μm and 45-53 μm Al particles into a hot gas mixture at ~145 atm (mixture B, $O_2/H_2O/N_2$ = .20/.30/.45, 2630 K). The photodiode signal in the figure displays two distinct peaks associated with the two

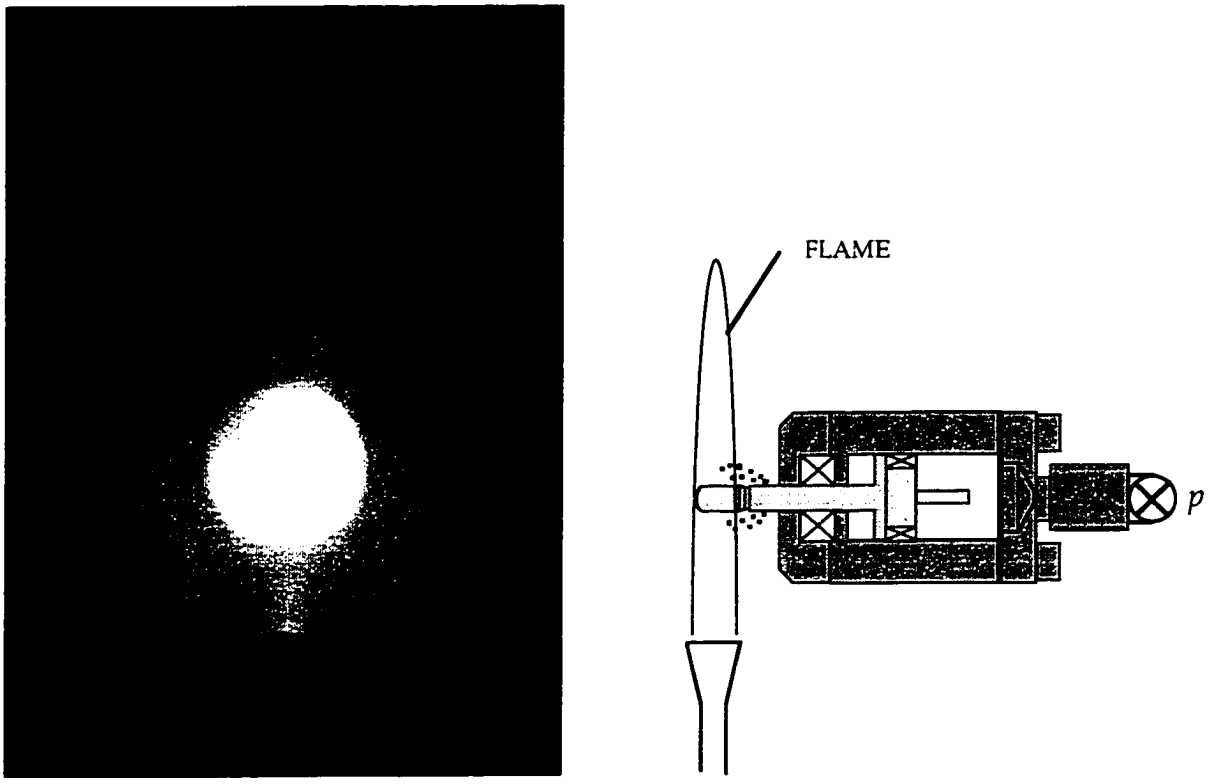

Fig. 3.7: Photograph of igniting 45-53 μm Al particles injected horizontally into a vertical propane flame sheet at 1 atm. The particles appear as distinct bright point sources which burn independently of their neighbors, indicating good particle dispersion.

distinct particle size distributions, as would be expected for particles which ignite and burn independently of one another. The particle sizes in the bimodal mixture were chosen so that the particle lifetime of the smaller constituent is shorter than the ignition delay of the larger constituent, and this is observed by the prominent valley separating the two peaks.

The measured ignition delay and combustion time corresponding to the first peak in Fig. 3.8 give $t_{ign}^{(1)}$ = 422 μsec and $t_{comb}^{(1)}$ = 450 μsec for the 20-25 μm particles whereas for the second peak $t_{ign}^{(2)}$ = 905 μsec and $t_{comb}^{(2)}$ = 825 μsec. The times for the 20-25 μm particles agree well with the data obtained separately for 21.6 μm Al, $t_{ign} = 350 \pm 130$ μsec and $t_{comb} = 530 \pm 240$ μsec, as is discussed further in the next section. The ignition time and combustion time for the second peak is in agreement with measurements on 45-53 μm particles tested separately, $t_{ign} = 975 \pm 80$ μsec and $t_{comb} = 930 \pm 145$ μsec. The measurements shown in Fig. 3.8 with the bimodal powders confirm that particles which are injected into the chamber at high pressure do in fact ignite and burn independently of one another. Similar tests with boron particles would not be expected to produce such clear-cut results because boron particle ignition and combustion times are not as strong functions of particle size. Ignition delays scale less strongly than d_p-squared, expected for particles heating under stagnant conditions (no relative motion), *indicating that*

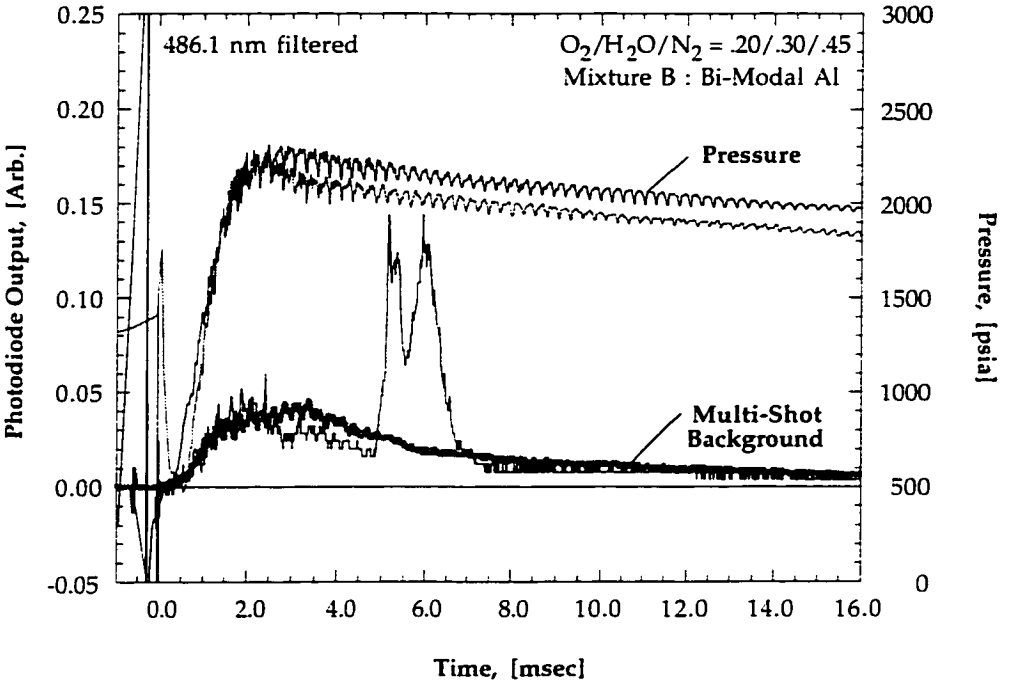

Fig. 3.8: Typical net particle signal for Al powder with bimodal size distribution, 20-25 μm plus 45-53 μm, in *product* mixture of O_2/H_2O = .20/.30 at ~145 atm and 2630 K. Two well resolved peaks correspond to the individual sizes igniting and combusting independent of the other, indicating good particle dispersion at high pressure.

delays are shortened significantly by convective heating. Thus one effect of particle injection is to shorten ignition delay times compared to stationary particles heated under stagnant conditions. The magnitude of this effect is elaborated on in Chapter 4.

Once the particle injection and dispersion issues were resolved, tests were run in a baseline mixture of oxidizers to study the pressure and particle diameter effect on ignition delay and combustion times. The pressure dependence of these ignition delays are compared to existing published data.

3.5.3 Measurement of Aluminum Particle Ignition Delay and Combustion Times

In addition to establishing that particles are well dispersed and ignite independently of one another, the third issue requires proof that the injection process itself does not alter particle ignition and combustion times. It was just discussed that finite injection velocities lead to accelerated particle heating. The particle injection approach was further validated by measuring aluminum particle ignition delays and combustion times for 21.6 μm particles at one gas mixture condition and comparing the results to independent measurements. These baseline tests are further used to check the consistency in our signal interpretations.

Table 3.1: Measured ignition delay and combustion times of Al particles as a function of pressure, for 21.6 μm diameter particles, at ~2640 K.

Shot #	T_1 [K]	p_1 [atm]	mix	O_2	H_2O	T_c [K]	p_c [atm]	t_{ign} [msec]	p_b [atm]	tcomb [msec]	$p_{b:90}$ [atm]	$t_{c:90}$ [msec]
3.17	293.7	20.7	B	0.20	0.30	2652	149.0	0.44	147.7	0.42	147.5	0.71
3.18	301.1	20.7	B	0.21	0.30	2613	133.8	0.21	133.2	0.80	132.8	1.25
4.11	293.5	20.6	B	0.20	0.30	2617	138.5	0.40	138.2	0.36	138.1	0.53
3.95	294.0	5.8	B	0.19	0.32	2680	40.3	0.66	39.6	0.90	39.6	0.85
3.96	293.8	5.8	B	0.19	0.31	2647	37.8	0.78	37.2	1.13	37.2	0.91
4.21	291.1	5.8	B	0.19	0.31	2621	37.8	0.88	36.7	0.99	36.6	1.30

The high pressure data obtained for aluminum (Table 3.1) are plotted in Fig. 3.9 a and show that aluminum ignition delays decrease by a factor of ~2 as pressure is increased from 38.5 ± 1.5 to 140 ± 10 atm in a mixture of O_2/H_2O = .20/.30, with the balance N_2 (mixture B) and average temperature 2640 K. It is not possible to perform tests with the present injector at even lower pressures, so these data are compared to independent measurements at lower pressures. The data of Robert's, et al.[24,44] in 100% oxygen show a definite pressure effect between 8.5 and 34 atm and that ignition delays increase with a decrease in temperature from 2775 to 2230 K. Megli's, et al. [46] data at 8.5 atm and 2700 K indicate that reducing the ambient oxygen to 60% in argon increases ignition delays compared to Robert's 100% O_2 data. Both Robert's and Megli's measurements were conducted behind reflected shocks in a 9-cm diameter test section shock tube with identical aluminum particles as used here.

In both the shock tube and combustion chamber experiments convective effects play important roles during particle ignition and combustion making it necessary to examine differences in these effects between the two experiments. According to Roberts' Fig. 3.21 of Ref. (24), during ignition in the shock tube time-averaged particle Nusselt numbers are typically ~4 and typical gas thermal conductivities fall between 0.14 and 0.20 W/m-K over the temperature range of interest, 2200 - 2800 K. The resulting convective heat transfer coefficients $\bar{h}_c = Nu_p\, k_g/d_p$ fall in the range 25 to 37 kW/m^2-K, *which are typical of those encountered for particles injected into the combustion chamber* at higher pressure (see Fig. 4.12 in Section 4.5.1, for example). Thus convective heating processes are similar in both experiments permitting a direct comparison of results. When the measured trend at high pressure, with 50% combined O_2 and H_2O at 2640 K, is extrapolated to still lower pressures, agreement is obtained with the shock tube data of Megli, et al.[46] in reduced oxygen mixtures (60% O_2 at 2700 K). The good agreement of the new data with these other independent studies, and the particle dispersion test results described previously, leads to the conclusion that the particle injection technique is valid.

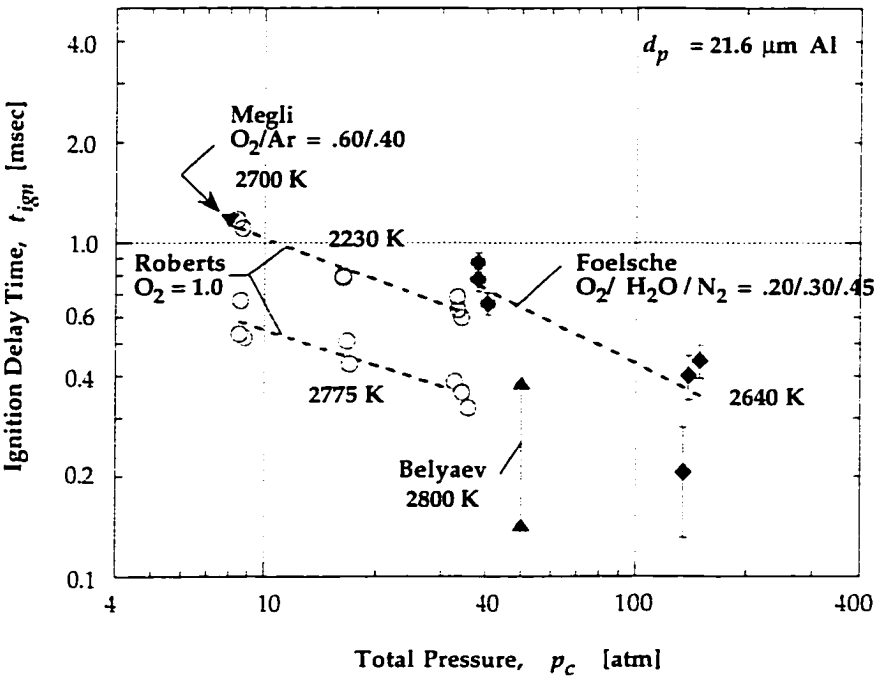

(a)

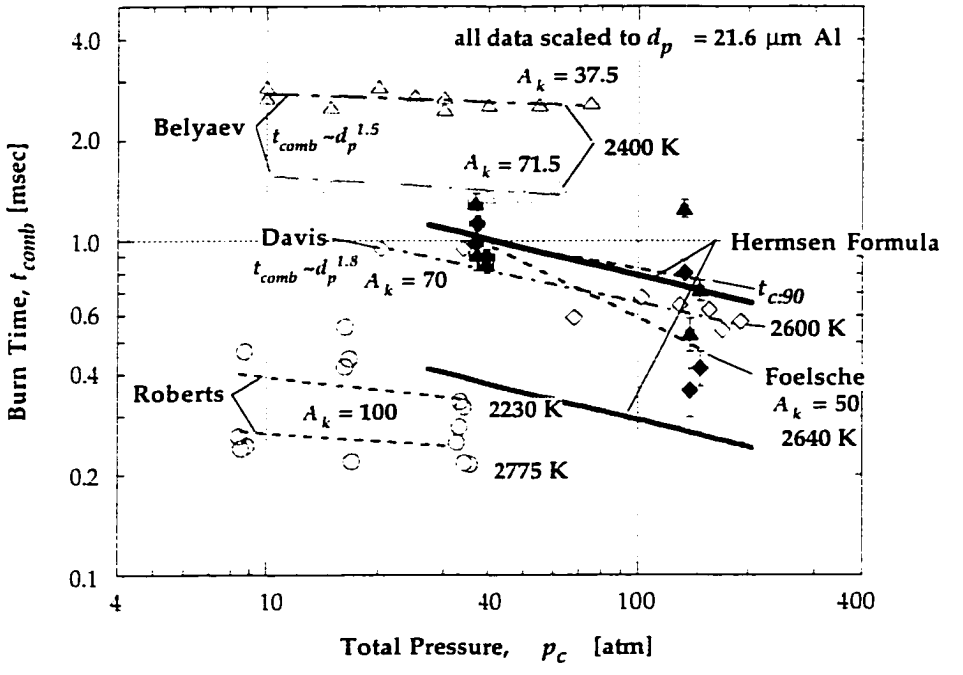

(b)

Fig. 3.9: Measured pressure effect on *aluminum* particle (a) ignition delay and (b) combustion times compared to data of other researchers. Ignition delay times decrease significantly as T_c increases (Roberts[44]) and also increase with decreasing X_{O2} (Megli[46]). The ignition data in the combustion chamber at higher pressure appear to be consistent with Megli data at similar temperature. Combustion times agree with data of Davis[64] but show larger pressure dependence than other studies indicate. Data of Davis and Belyaev, et al.[65] have been scaled to 21.6 μm diameter.

Combustion times defined by the times at half of peak amplitude are compared to similar high pressure data in Fig. 3.9 b and show good agreement with other determinations. The new data are compared to aluminum particle data of Davis,[64] who measured particle luminosity tracks in a closed bomb charged with nitrogen where pellets of propellant and oxidizer containing low loadings of Al particles were ignited and burned, and Belyaev, et al.,[65] who used similar techniques but in a half-closed bomb where the particles burned in a high temperature gas flow. These previous studies examined much larger particles than were used in the present study, between 53 and 140 μm, but particle size scaling relationships were determined in each case. The large particle data of Davis and Belyaev, et al. have been scaled to a diameter of 21.6 μm using the respectively determined scaling relationships; $t_{comb} \sim d_p^{1.8}$ (Davis), and $t_{comb} \sim d_p^{1.5}$ (Belyaev), to compare with data obtained in the shock tube[24,45] and combustion chamber. The data of this study compare most closely with Davis's determination, but show a larger pressure dependency than all other measurements.

The nature of the convective environments in Davis's and Belyaev's experiments is not known but is important even in an enclosed bomb where the burning propellant gases evolve from the propellant surface at a non-negligible velocity which exceeds the particle velocity. The nature of the relative slip flows in the shock tube experiments of Roberts and Megli are known however. For average particle velocities of ~10 m/sec during combustion in the reflected shock region, typical $Re_p \approx 4 - 8$, which are again typical of conditions in the high pressure experiments of this study. During combustion convective heating (or cooling) is not as important as the deformation of the reaction zone and product cloud surrounding the burning Al droplet - aluminum generally burns in the vapor phase.

The available aluminum particle combustion data have been determined over a large range of pressures, particle sizes, and differing oxidizing atmospheres. Hermsen[66] proposed an empirical relationship to calculate combustion times in terms of these parameters for various oxidizing atmospheres,

$$d_p^{1.8} = d_{p,0}^{1.8} - \beta t \tag{3.6}$$

where β is the combustion rate. The combustion time can be found by setting $d_p \approx 0$, giving

$$t_{comb} = \frac{d_{p,0}^{1.8}}{\beta} \tag{3.7}$$

where $\beta = 8.33 \times 10^{-5} R_k A_k^{0.9} p^{0.27}$ cm$^{1.8}$/sec

R_k = 1 - 2.7, a parameter

$A_k = (X_{O_2} + X_{H_2O} + X_{CO_2} + X_{Ox.}) * 100\%$, the mole fraction oxidizer, in %

p = gas pressure, in psia

$d_{p,0}$ = the initial particle diameter, in cm

The combustion time determined by Eq. (3.7) has units of seconds. The factor R_k is an empirically determined parameter to account for differences between the gas environments which typically exist in the laboratory and those in operating rocket chambers. For non-convective, low blackbody temperature environments typical of laboratory experiments a value of $R_k = 1$ is suggested. For the convective, high blackbody temperature environments of rocket chambers, the appropriate value of 2.7 is to be employed.[66]

For the conditions of mixture B (A_k = 50%, p = 145 atm) and for $d_{p,0}$ = 21.6 μm particles the upper and lower bounds on the calculated combustion times are 660 μsec and 245 μsec, respectively, compared to 500 μsec from the measurements. The new high pressure data agree more closely with the $R_k = 1$ value and are found to lie between the limits calculated with the empirical relation. Eq. (3.7) is plotted along with the various data in Fig. 3.9 b. The agreement between the new high pressure data and measured trends of Roberts and Davis and the empirical formulation of Hermsen provides more evidence that the particle injection technique and interpretation of results is valid.

Combustion times are also determined using an approach where particle combustion is considered to be complete when a certain high percentage of the total area under the net-particle emission curve is reached,[61] where the remaining luminosity is considered as either negligible energy release or possibly as lingering emissions from the hot oxides which are formed. In this study such combustion times are evaluated at the time corresponding to 90% of the total area, and are denoted $t_{c:90}$. The values so determined are compared in Fig. 3.9 b for 21.6 μm aluminum particles to Davis's measurement and show a much closer agreement than values determined using the times between half of peak amplitude. The pressure dependency in $t_{c:90}$ is reduced and falls in line with the other determinations and also Hermsen's empirical relation Eq. (3.7). Thus it seems that $t_{c:90}$ agree more closely with the combustion times measured in propellants product gases, which were measured up to the instant when luminous particles streaks on photographic film disappeared, even though the formalism used here is the same as that used by Roberts in the shock tube.

Several particle measurements are shown in Appendix C where the interested reader can judge for themselves which method provides a better specification of completed combustion. In this study the time between the half-peak amplitudes is used for combustion times.

3.6 Boron Particle Ignition and Combustion Results

Boron particle ignition delays t_{ign} and combustion times t_{comb} for particles injected as described are measured as a function of pressure p_c between 30 and 150 atm in two different high temperature mixtures. At ~150 atm, the effect of ambient temperature T_c is studied in mixtures with X_{O_2} = 0.11, and separately the effect of X_{O_2} is studied at T_c = 2630 K. The test matrix is delineated in Table 3.2. Pressure variation is accomplished by changing the initial gas fill-pressure, and temperature and ambient oxygen variation is accomplished by changing the amount of nitrogen diluent and excess oxygen in the initial gas mixture, respectively. When small quantities of ignition-enhancers are added to the baseline mixtures, only slight modification of $H_2/O_2/N_2$ gas ratios is required to keep p_c, T_c, and X_{O_2} fixed at their baseline values. Completely free variation of these three independent parameters is not possible without changing other post-explosion product gas mole fractions, namely X_{H_2O} and X_{N_2}.

Table 3.2: Test matrix for boron particle ignition and combustion experiments at elevated pressure.

Parameters Varied	Values [atm, K, %, μm]	Mixtures	$d_{p,0}$ [μm]	Parameters Fixed
p_c	37.5, 78, 150	A, B	~24	-
T_c	2440, 2630, 2830	A, C, D	~24	p_c, X_{O_2}
O_2	5, 10.5, 15.5, 20	B, C, E, G	~24	p_c, T_c
$d_{p,0}$	~12, ~24, ~48	B	-	p_c, T_c, X_{O_2}
CO_2	0, 5	B, E	~24	p_c, T_c
HF	0, 5	B, F	~24	p_c, T_c

Predicted gas-phase equilibrium product distributions for the various premixed gas mixtures are listed in Table 3.3. Major species distributions are assumed to remain unchanged during the time delay up to particle injection. Chamber pressures p_∞ are measured for the duration of each experiment and are used to calculate falling gas temperatures. For tests conducted with HF, the hydrogen fluoride is produced by the thermal dissociation of SF_6 and recombination of liberated fluorine with hydrogen compounds. At the pressures covered, HF recombination is very fast and therefore very little free fluorine exists. Approximately 1% SO_2 is also produced.

Boron particles are observed to exhibit single-stage ignition for all ambient conditions studied. At lower pressures it has been observed that boron ignites in two stages,[6,8] where the first very luminous stage is short-lived and whereupon the particle luminosity extinguishes, followed by a second stage where luminosity returns and continues throughout particle combustion. Macek[4] reported that at

Table 3.3: Combustion chamber product gas mixtures indicating temperature and pressure during particle experiments, and calculated species mole fractions assuming adiabatic constant-volume premixed-gas combustion.

Mixture	p_1	T_c	p_c	O_2	H_2O	N_2	NO	OH	CO_2	HF
	[atm]	[K]	[atm]							
A	10.9	2790	78	0.11	0.33	0.51	0.02	0.02	0	0
A	20.4	2830	150	0.11	0.34	0.51	0.02	0.02	0	0
B	5.8	2640	37.5	0.19	0.31	0.45	0.02	0.02	0	0
B	10.9	2630	76	0.20	0.30	0.45	0.02	0.01	0	0
B	20.4	2630	145	0.20	0.30	0.45	0.02	0.01	0	0
C	22.8	2610	150	0.11	0.30	0.56	0.02	0.01	0	0
D	23.8	2440	150	0.11	0.26	0.61	0.01	0.01	0	0
E	20.4	2620	145	0.16	0.31	0.44	0.02	0.01	0.048	0
F	5.8	2570	34	0.20	0.28	0.43	0.02	0.02	0	0.047
G	22.8	2630	150	0.05	0.29	0.63	0.01	0.01	0	0

1 atm the transition between the two stages became indistinguishable at low ambient oxygen concentrations, X_{O_2} ~0.1. Li[8] found the two stages to become indistinguishable for smaller particles above 2200 K flame temperatures.

Measured ignition delays are fairly reproducible and exhibit small absolute scatter at higher pressures. The shot-to-shot variation is attributed mainly to particle injector performance. Combustion times defined as the time between the half-maxima of the net filtered-photodiode signals (Fig. 3.4), display considerably more scatter than ignition delays. This is not uncommon even with single particle tests.[4] Unlike aluminum combustion times, boron particle combustion times are significantly longer, as can be seen by comparing the breadth of particle signals in Figs. 3.2 and 3.3. Measurements show that particle emissions linger much longer for boron than for aluminum, making definition of combustion time more uncertain. Since these are not single particle experiments, combustion times are defined in a statistical sense to indicate when the majority of the particles are consumed. Combustion times determined by an alternate method are compared later in Section 3.13 to the method chosen here.

Convective effects enhance particle heating and thereby reduce ignition times. For the 23.7 μm boron particles studied convective heating reduces ignition delays by approximately 50% compared to pure conduction as will be discussed in Chapter 4. Combustion times are effected to a much lesser extent.

3.7 Effect of Gas Pressure on Boron Particle Ignition Delay and Combustion Times

The variation of boron particle ignition delays as a function of pressure for 23.7 μm particles is shown in Fig. 3.10 a, with the data tabulated in Table 3.4. Measured ignition delays for the two different mixtures (A, B) decrease as p_c is increased from 37 to 156 atm. For 20% O_2 and T_c = ~2630 K, t_{ign} decreases from 2.1 ± 0.4 to 1.1 ± 0.2 msec as p_c increases roughly 4-fold. The decrease in ignition delay time with pressure is similar for the second mixture where t_{ign} decreases from 1.6 ± 0.3 to 0.99 ± 0.22 msec when pressure is doubled with 11% O_2 at T_c = ~2810 K. At high pressure the sum of the temperature variation and uncertainty in the data is ±40 K and at 37 atm it is ±80 K. In addition to molecular oxygen there is ~30% water vapor present in these mixtures plus a few percent NO and OH (see Table 3.3).

The dependence of boron particle ignition delays on pressure for the combined data from the two mixtures may be approximated between 37 and 156 atm by a power-law of the form $t_{ign} = c_o\, p_c^N$, where c_o and N are constants:

$$t_{ign} = 13.0\, p_c^{-0.5} \tag{3.8}$$

In Eq. (3.8), t_{ign} is in msec and p_c in atm. Temperature and ambient oxygen have no explicit effect on the pressure variation at the high temperatures investigated (i.e., both mixtures show the same trend). It will be shown in Chapter 4 that convective heating is not responsible for the measured pressure effect.

The variation of combustion times with pressure is shown in Fig. 3.10 b for both mixtures. The results for each of the two mixtures display markedly different characteristics however. For 20% O_2 and ~2630 K combustion time is a weak function of pressure between 37 and 145 atm. In contrast for the low excess-oxygen and high temperature mixture (11% O_2, ~2810 K), combustion time drops from 2.5 ± 0.9 to 1.4 ± 0.6 msec with a doubling of the pressure. These combustion times can be fit by a similar power-law in pressure, giving Eq. (3.9) and Eq. (3.10);

$$t_{comb} = 5.0\, p_c^{-0.13} \qquad \text{for 20\% } O_2\text{, 2630 K} \tag{3.9}$$

$$t_{comb} = 190\, p_c^{-1.0} \qquad \text{for 11\% } O_2\text{, 2810 K} \tag{3.10}$$

where it is seen that at higher temperature (and less oxygen) combustion times vary approximately inversely with pressure.

Table 3.4: Measured ignition delay and combustion times of boron particles as a function of pressure, for 23.7 μm diameter particles in two different oxidizing atmospheres.

Shot #	T_1 [K]	p_1 [atm]	mix	O_2	H_2O	T_c [K]	p_c [atm]	t_{ign} [msec]	p_b [atm]	t_{comb} [msec]	$p_{b:90}$ [atm]	$t_{c:90}$ [msec]
3.81	294.6	20.7	B	0.20	0.30	2594	-	-	135.5	2.35	134.1	6.84
3.83	294.0	20.5	B	0.20	0.30	2621	141.5	0.88	-	-	-	-
3.86 b	293.4	20.5	B	0.20	0.30	2627	144.9	1.38	142.0	2.67	141.1	7.12
4.10	293.7	20.6	B	0.20	0.30	2630	145.1	1.19	140.7	3.42	140.2	4.81
4.42	293.4	20.7	B	0.20	0.30	2623	145.1	1.07	141.9	2.21	140.9	4.05
4.00	294.3	6.0	B	0.18	0.31	2640	39.3	2.54	37.8	3.15	37.5	5.98
4.25	292.7	5.8	B	0.19	0.32	2669	38.8	1.74	37.2	2.35	36.6	6.20
4.45	294.1	5.8	B	0.20	0.31	2639	37.0	1.89	36.0	4.14	-	-
4.49 b	293.4	5.9	B	0.18	0.31	2629	-	-	36.7	3.01	36.8	4.38
2.77	299.3	20.6	A	0.10	0.34	2826	147.8	1.20	145.1	2.05	159.2	169.12
3.04	299.4	20.7	A	0.11	0.33	2818	148.3	0.99	146.0	0.92	158.5	169.60
4.04 c	293.7	20.5	A	0.11	0.33	2844	158.9	0.77	154.8	1.13	163.2	171.20
4.01	293.9	11.2	A	0.11	0.33	2816	83.2	1.43	80.0	1.69	85.9	92.49
4.02	293.6	10.9	A	0.11	0.34	2774	73.3	1.92	71.2	3.53	85.5	91.23
4.06 b	294.0	11.0	A	0.11	0.33	2795	78.8	1.19	76.8	1.74	86.3	91.33
4.68	294.4	11.0	A	0.11	0.33	2768	74.9	1.69	72.3	3.03	85.7	91.43

Table 3.5: Measured ignition delay and combustion times of boron particles as a function of temperature, for 23.7 μm diameter particles at ~150 atm and X_{O_2} = 0.11.

Shot #	T_1 [K]	p_1 [atm]	mix	O_2	H_2O	T_c [K]	p_c [atm]	t_{ign} [msec]	p_b [atm]	t_{comb} [msec]	$p_{b:90}$ [atm]	$t_{c:90}$ [msec]
2.77	299.3	20.6	A	0.10	0.34	2826	147.8	1.20	145.1	2.05	143.8	4.14
3.04	299.4	20.7	A	0.11	0.33	2818	148.3	0.99	146.0	0.92	144.9	2.14
4.04 c	293.7	20.5	A	0.11	0.33	2844	158.9	0.77	154.8	1.13	-	-
2.90	301.7	22.8	C	0.11	0.30	2614	-	-	146.6	2.01	146.6	1.95
4.34 b	293.8	22.7	C	0.11	0.30	2608	154.3	0.98	152.2	1.87	151.7	2.42
4.41 a	293.7	22.8	C	0.11	0.30	2611	158.3	1.06	155.6	2.15	155.3	2.41
4.41 b	293.5	22.9	C	0.12	0.29	2596	148.0	0.67	147.7	1.41	147.0	1.96
4.31	293.3	22.7	D	0.11	0.26	2435	151.1	2.89	146.0	4.64	146.1	4.52
4.32	293.5	22.9	D	0.11	0.26	2434	148.2	2.53	144.0	6.13	142.0	10.43
4.44	292.9	22.9	D	0.11	0.26	2448	154.1	2.34	150.1	4.10	149.4	4.24

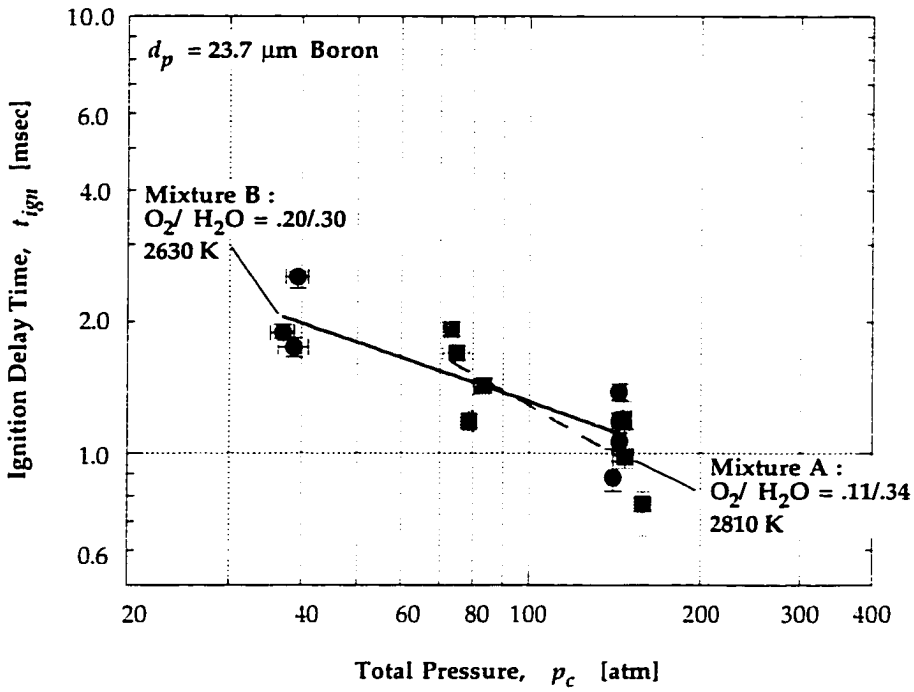

(a)

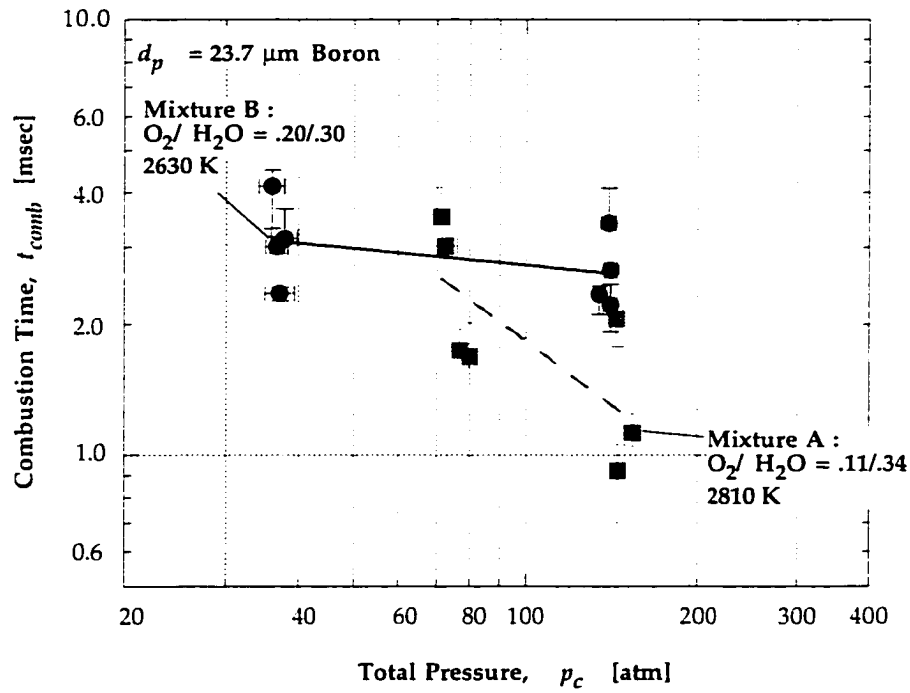

(b)

Fig. 3.10: Measured pressure effect on *boron* particle (a) ignition delay and (b) combustion times for two different oxidizing atmospheres. Ignition delays are a strong function of pressure in both mixtures, whereas combustion times show varied pressure dependence depending on the temperature and ambient oxygen present.

3.8 Effect of Gas Temperature on Boron Particle Ignition Delay and Combustion Times

The variation of ignition delay time with ambient temperature is shown in Fig. 3.11 for the data tabulated in Table 3.5. Measurements are conducted in three mixtures where p_c = 152 ± 4.5 atm, X_{O_2} = 0.11 and temperature is varied from 2440 ± 50 K to 2830 ± 60 K (mixtures A, C, and D). A marked 67% decrease in t_{ign} is measured as T_c is raised from 2440 K to 2610 ± 50 K while delays are nearly independent of T_c as temperature is increased further. A similar trend is measured for combustion times as temperature is raised from 2440 K to 2830 K. Combustion times shown in Fig. 3.11 decrease 60% between 2440 K and 2610 K followed by only a slight decrease as T_c is raised further. This behavior suggests that a transition temperature exists for boron combustion, where much shorter particle lifetimes are achieved above 2440 K ambient temperatures. Macek[6] also observed a similar step-like decrease in ignition delays and combustion times near 2500 K at 1 atm, as discussed below. Convective effects due to particle motion are not responsible for the measured trends.

3.9 Effect of Ambient O_2 on Boron Particle Ignition Delay Time and Combustion Times

Ignition delay times are shown to exhibit a weak but distinct dependence on ambient oxygen over a range of quadrupling X_{O_2}. The ignition delay dependence on ambient oxygen for 23.7 μm boron particles is shown in Fig. 3.12 where all measurements are at T_c = 2620 ± 55 K, p_c = 150 ± 8 atm, and X_{O_2} is varied between 0.05 and 0.20 (mixtures B, C, E, and G). Data are for the figure are tabulated in Table 3.6. Ignition delays decrease as X_{O_2} is raised from 0.05 to 0.11 and then increase again as X_{O_2} is raised further to 0.20. The delay at X_{O_2} = 0.11 is 0.85 ± 0.20 compared to 1.1 ± 0.2 at X_{O_2} = 0.20. A high level of confidence is placed on the data above X_{O_2} of 0.11 but less confidence at 0.05, where tests and analysis of measured emissions became more difficult.

Combustion times at high pressure shown in Fig. 3.12 follow a similar trend to measured ignition delays but increase almost 40% as post-combustion ambient oxygen X_{O_2} is raised from 0.11 to 0.20. For X_{O_2} = 0.11, t_{comb} = 1.9 ± 0.3 compared to 2.7 ± 0.5 for X_{O_2} = 0.20. There is considerably more uncertainty in the measured combustion times than ignition delays. The measured variation of boron particle combustion times with ambient oxygen is an unexpected result in light of the fact that most semi-global chemistry models consider the reaction of boron with $O_2(g)$ to be the rate limiting chemical step during combustion; combustion times should then decrease when more oxygen is available for boron consumption.

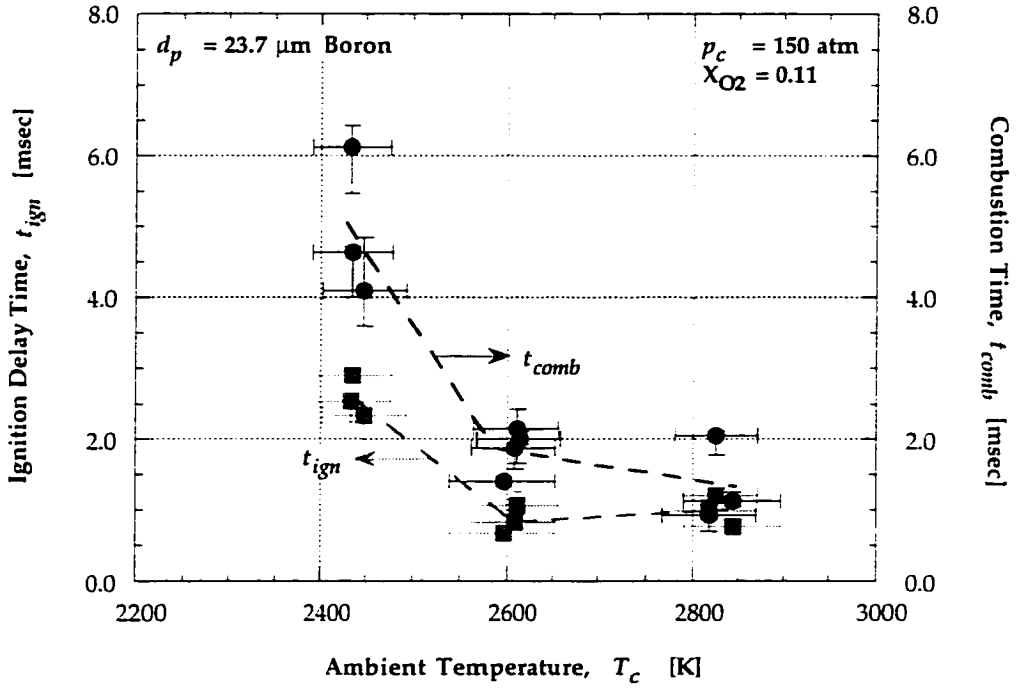

Fig. 3.11: Measured temperature effect on boron particle ignition delay and combustion times at high pressure. Both ignition delays and combustion times drop sharply above 2440 K, and are weak functions of temperature above 2600 K.

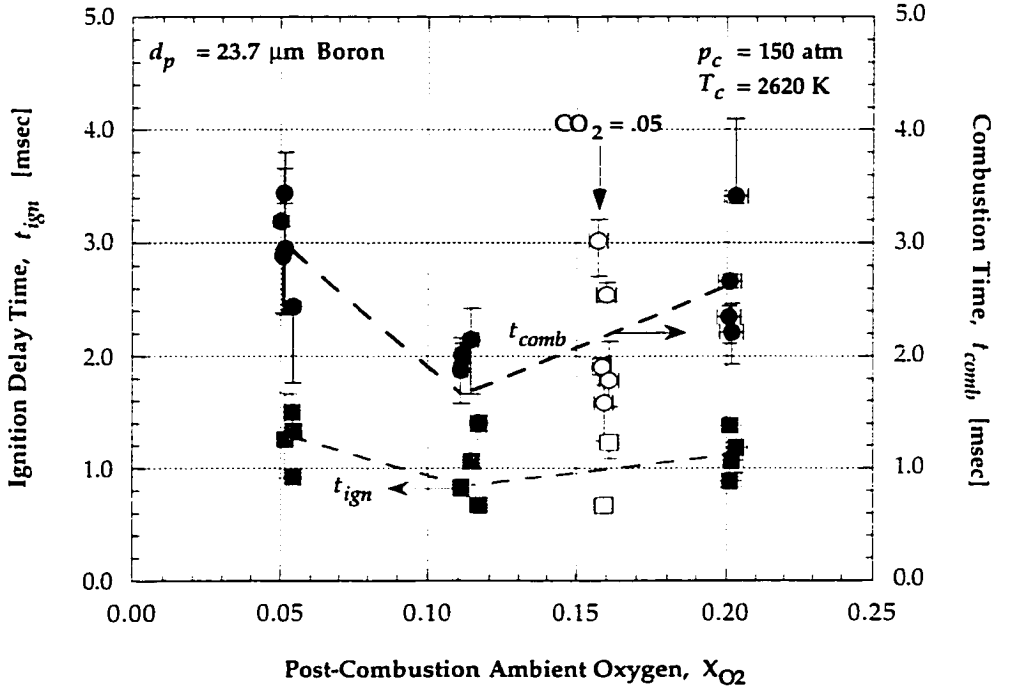

Fig. 3.12: Measured ambient oxygen effect on boron particle ignition delay and combustion times at high pressure. Measurements indicate an increase in ignition delays with increasing ambient oxygen mole fraction above $X_{O_2} = 0.11$.

Table 3.6: Measured ignition delay and combustion times of boron particles as a function of ambient oxygen mole fraction, for 23.7 μm diameter particles at ~150 atm and ~2620 K.

Shot #	T_1 [K]	p_1 [atm]	mix	O_2	H_2O	T_c [K]	p_c [atm]	t_{ign} [msec]	p_b [atm]	t_{comb} [msec]	$p_{b:90}$ [atm]	$t_{c:90}$ [msec]
3.81	294.6	20.7	B	0.20	0.30	2594	-	-	135.5	2.35	134.1	6.84
3.83	294.0	20.5	B	0.20	0.30	2621	141.5	0.88	-	-	-	-
3.86 b	293.4	20.5	B	0.20	0.30	2627	144.9	1.38	142.0	2.67	141.1	7.12
4.10	293.7	20.6	B	0.20	0.30	2630	145.1	1.19	140.7	3.42	140.2	4.81
4.42	293.4	20.7	B	0.20	0.30	2623	145.1	1.07	141.9	2.21	140.9	4.05
2.90	301.7	22.8	C	0.11	0.30	2614	-	-	146.6	2.01	146.6	1.95
4.34 b	293.8	22.7	C	0.11	0.30	2608	154.3	0.98	152.2	1.87	151.7	2.42
4.41 a	293.7	22.8	C	0.11	0.30	2611	158.3	1.06	155.6	2.15	155.3	2.41
4.41 b	293.5	22.9	C	0.12	0.29	2596	148.0	0.67	147.7	1.41	147.0	1.96
4.72	296.0	308.7	G	0.05	0.29	2641	-	-	147.3	2.89	143.7	9.32
4.76	293.3	318.7	G	0.05	0.29	2640	-	-	149.2	3.44	146.5	7.40
4.79	293.1	319.7	G	0.05	0.29	2615	148.6	1.33	-	-	-	-
4.80	293.6	319.7	G	0.05	0.29	2650	-	-	157.6	3.19	156.9	4.05
4.82	294.9	322.7	G	0.05	0.29	2634	160.6	0.93	157.5	2.44	154.5	5.60
4.83 b	293.1	325.7	G	0.05	0.29	2610	156.2	1.26	152.2	2.95	-	-
4.83 e	294.9	320.7	G	0.05	0.29	2610	144.9	1.50	-	-	138.5	6.92

The premixed gas mixtures used to produce mixture G with 5% excess O_2 exhibit long gas-phase combustion times (long pressure rise times, t_{pr}) compared to the other mixtures investigated, as was discussed in Section 2.2.7. This resulted in non-ideal performance of the particle injector for reasons which are not entirely understood. In those cases where good injection was achieved, particle emissions from the igniting boron particles generally rose to peak levels in a similar manner to the other mixtures investigated but the emissions remained high for some time (broad peak) and decayed much more slowly characterized by a long tail to the net particle curve. Representative signals displaying this feature are shown in Appendix C which may be an indication that full particle consumption takes significantly longer than with more oxygen present. The slow decay of emissions makes interpretation of particle combustion times more difficult than in cases where the emissions decayed rapidly after reaching a peak. Combustion times determined in terms of the time at half of peak amplitude do not clearly indicate this change in characteristics compared to other mixtures, perhaps supporting a different choice for defining when combustion has ceased. It is important to note that no "unburned" particle residue was ever found in these 5%-O_2 tests or in any of the other mixtures used so it is believed that the particles burned to completion even in this low oxygen environment.

These practical problems aside, it is significant to point out that boron was found to combust in product mixtures with excess O_2 as low as 5%. This is below the O_2-concentration limit for combustion observed by Macek[6] although it is pointed out that in the present tests there is ~30% water vapor present as well. This is a significant result for propellant applications where there is very little if any excess oxygen for particle combustion. The measured lifetimes for 23.7 μm particles are still below 10 msec and this suggests the possible efficient use of boron in O_2-lean high-speed propulsion systems.

3.10 Effect of Chemical Ignition-Enhancers on Reducing Boron Particle Ignition Delay Time

3.10.1 Ignition-Enhancement of Carbon Dioxide

Measurements with carbon dioxide additive, where ~5% O_2 has been replaced by an equal amount of CO_2 on a product-mole basis (mixture E), show that CO_2 neither accelerates nor inhibits boron particle ignition (Fig. 3.12 and Table 3.7). Measured $t_{ign} = 0.95 \pm 0.40$ msec, for $X_{CO_2} = 0.05$ in addition to $X_{O_2} = 0.16$, at $p_c = 143 \pm 3$ atm and $T_c = 2620 \pm 50$ K. The slight increase in delay time compared to $X_{O_2} = 0.11$ can be attributed to the observed increase in t_{ign} as ambient oxygen is increased. Carbon dioxide has been suspected to facilitate boron particle ignition by acting as a donor of O-atoms when CO_2 is chemically absorbed and dissolved into the liquid oxide surface.[14] Cluster beam experiments[43] show definite reaction of CO_2 with boron-oxide clusters by O-atom addition, and reaction seems to be thermoneutral. Similar experiments show definite reaction of CO_2 with boron by O-atom addition, but the process is found to be inefficient and endothermic.[43]

Carbon dioxide has no noticeable effect on measured boron particle combustion times at high pressure either (138 ± 5 atm); measured t_{comb} lie on the trend-line drawn between $X_{O_2} = 0.11$ and 0.20, and can be explained solely by the effect of increasing ambient oxygen. It is suggested that further tests

Table 3.7: Measured ignition delay and combustion times of boron particles in ambient mixture containing small quantity of CO_2, for 23.7 μm diameter particles at ~145 atm and ~2620 K.

Shot #	T_1 [K]	p_1 [atm]	mix	O_2	H_2O	CO_2	T_c [K]	p_c [atm]	t_{ign} [msec]	p_b [atm]	t_{comb} [msec]	$p_{b:90}$ [atm]	$t_{c:90}$ [msec]
3.64 a	294.4	300.7	E	0.16	0.31	0.048	2623	-	-	135.5	2.54	134.2	4.44
3.65	295.2	299.7	E	0.16	0.31	0.049	2617	-	-	132.6	1.91	130.3	5.88
4.52	293.0	302.7	E	0.16	0.31	0.047	2621	144.0	0.67	141.7	1.58	141.6	1.71
4.53	293.5	302.7	E	0.16	0.31	0.052	2611	-	-	138.9	3.02	138.4	3.69
4.54	293.3	301.7	E	0.16	0.31	0.047	2627	142.1	1.23	139.2	1.78	139.3	1.73

be conducted with little or no excess oxygen to more clearly differentiate the efficiency of CO_2 as an oxidizer. For the purposes here, CO_2 is considered as an additive to enhance ignition and not as a replacement for O_2. Propellant product gas streams would typically contain between 5 and 15% CO_2 and therefore CO_2 may be a crucial oxidizer for boron in the absence of free O_2.

3.10.2 Ignition-Enhancement of Hydrogen Fluoride

When sulfur-hexafluoride SF_6 is added to the combustible mix to produce fluorine compounds by dissociation, the liberated fluorine rapidly recombines into hydrogen fluoride (HF) by the time particles are injected. Fig. 3.13 shows that ~5% HF with 20% O_2, at p_c = 34 ± 3.5 atm and T_c = 2570 ± 110 K, lengthens boron particle ignition delays rather than shortens them. The figure also shows only a minimal reduction in boron particle combustion times. These findings agree with Anderson's group's determination that HF is unreactive with boron and also with boron oxide *in the presence of other hydrogenated compounds.*[43] Evidence from several sources now seems to suggest that free fluorine atoms are likely the active agent, and not necessarily fluorine compounds as suggested earlier.[31]

The boron particle ignition and combustion data in mixtures with ~5% HF (mixture F, Table 3.3) are at an average temperature of 2570 K and as was discussed in Section 2.3.8 the uncertainty in the temperature could be as high as ±180 K. This places the majority of the data in the narrow temperature range between 2600 and 2440 K where it was shown that ignition delay and combustion times increased sharply toward lower temperatures in similar mixtures without HF at 150 atm. It might also be speculated that HF could shift this temperature range where the phenomena were observed. The fact that average temperatures during ignition and combustion are below 2600 K and the large uncertainty in the HF concentrations (X_{HF} = 0.047 ± 0.022, or ~48%) tempers any definitive statement that small quantities of HF increase ignition delays, although *the data tend to indicate that trend.*

Table 3.8: Measured ignition delay and combustion times of boron particles in ambient mixture containing small quantity of HF, for 23.7 μm diameter particles at ~34 atm and ~2570 K.

Shot #	T_1 [K]	p_1 [atm]	mix	O_2	H_2O	HF	T_c [K]	p_c [atm]	t_{ign} [msec]	p_b [atm]	t_{comb} [msec]	$p_{b:90}$ [atm]	$t_{c:90}$ [msec]
4.56	294.8	89.7	F	0.20	0.28	0.039	2485	-	-	31.3	2.90	31.3	3.54
4.66	294.0	85.7	F	0.20	0.28	0.046	2542	34.1	3.55	32.2	2.30	32.0	3.16
4.67	293.9	84.7	F	0.20	0.28	0.047	2569	33.9	4.46	31.6	3.34	-	-
4.86	293.6	86.7	F	0.20	0.29	0.047	2599	34.6	3.44	32.3	2.60	31.9	3.64
4.88	295.4	85.7	F	0.20	0.29	0.047	2588	32.2	3.58	29.3	3.72	29.4	3.53

Fluorine is thought to reduce boron particle ignition delays and combustion times since the energetics of boron reacting with fluorine are higher than reaction with oxygen.[14] This has been shown by Golovko, et al.[67] to be the case with chlorine, which is found to reduce particle ignition temperatures. Fluorine compounds including HF were also thought to produce similar effect to free fluorine. As will be discussed further in Chapter 4, modeling efforts indicate that HF greatly assists oxide layer removal for small particles where ignition is kinetically controlled but has a much smaller effect on larger particles and slightly suppresses combustion in both cases.[13] It remains to be seen what beneficial properties, if any, are available from free fluorine at high pressure. To isolate fluorine's ignition-enhancing properties, tests are required in dryer environments where the fluorine will not recombine into HF as occurs in the present experiments.

A concern arose during tests with HF as to whether the HF will deactivate on the walls of the chamber (4340 steel) and on the injector housing during the time delay before particles are injected. Using simple 1-D diffusion analysis and assuming diffusion of HF through the mixture and treating the mixture ($H_2O/O_2/NO/OH/N_2$, mixture F) as an inert medium where the HF deactivates upon every collision with a wall, a characteristic HF diffusion timescale can be calculated. The HF diffusion timescale leading to deactivation on the injector housing, with a mixture averaged diffusion coefficient $D_{HF,mix} \approx$ 2.9e-3 m^2/sec as calculated from TRANFIT program,[68] is ~3.4 sec. This timescale is ~170X

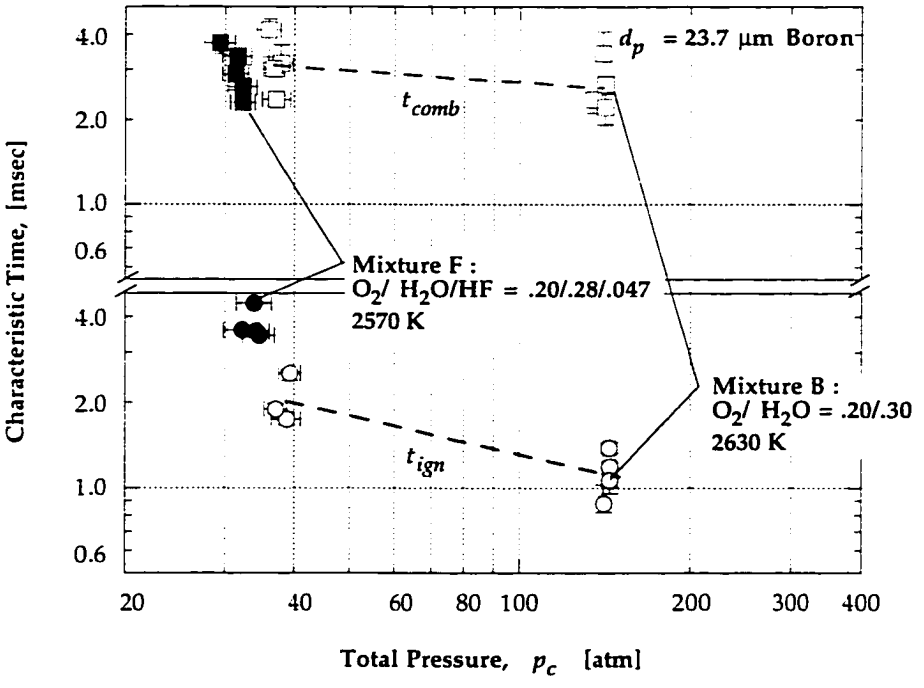

Fig. 3.13: Measured effect of ~5% HF on boron particle ignition delay and combustion times at lower pressure. Measurements indicate HF hinders ignition and produces only a minimal decrease in combustion times.

greater than the ~20 msec to inject, ignite, and burn the boron particles tested. Therefore, significant loss of HF to metal surfaces is not of concern.

3.10.3 Ignition-Enhancement of Water Vapor

There is much evidence that water vapor in oxygen enhances boron particle ignition and combustion.[4,7] Water vapor is known to actively react with the liquid boron oxide layer. However, it remains unclear from particle combustion experiments whether H_2O is actually a more efficient oxidizer than O_2 at high pressure. The experiments by Macek and Semple at 1 atm only compared dry to wet flames where the H_2O was in addition to equal amounts of O_2. No systematic study of water vapor concentration effects was conducted in the present investigation; all the mixtures studied were produced by premixed, nitrogen-diluted, hydrogen/oxygen combustion yielding between 26 and 34% water vapor in the products.

Observations from boron oxide droplet vaporization and cluster beam experiments have provided further evidence of water vapor enhancing ignition and combustion. Turns, et al.[22] measured boron oxide droplet gasification rates at temperatures between 1500 and 1950 K in moist and dry flames at 1 atm. The gasification timescales of ~1 mm diameter droplets with 12-16% H_2O present were found to be an order-of-magnitude shorter than in dry environments. The gasification in dry flames was very slow in comparison to the wet flames due to the low volatility of $B_2O_3(l)$ at these temperatures. Water vapor leads to the conversion of $B_2O_3(l)$ to HBO_x compounds which are much more volatile.

Brown, et al.[35] developed a model to simulate boron oxide gasification in hydrocarbon combustion product gases which includes detailed gas-phase and droplet surface kinetics and finite rate vaporization using measured and estimated rates. Modeling indicates that only reactions of $B_2O_3(l)$ with O, OH, and H_2O are competitive with vaporization below ~2200 K where these hydrogenated species are predicted to increase $B_2O_3(l)$ vaporization rates above the evaporation rate. For droplet sizes less than 50 μm at droplet temperatures between 1600 and 2000 K, such as during boron particle heat-up in hot ambient gases, the gasification rate due to reaction with OH/H_2O was as high as 10 times the vaporization rate. The most recent version of this model coupled with a boron particle model will be discussed further in Chapter 4.

Among several studies which measured the reactivity of water vapor with boron (see review in Ref. 10), Anderson and co-workers[43] measured reaction probabilities of H_2O with large boron clusters to be ~50% between 2000 and 3000 K, producing predominantly $HBO(g)$ in the products. Boron particle

ignition and combustion models to be considered in the next chapter further elucidate the important reactive species which lead to oxide layer gasification and oxidation.

3.10.4 Ignition-Enhancement of Nitrogen and Nitrogen Oxides

Macek found that the boron particle ignition temperature† was increased when N_2 was replaced by Ar in flames,[4] suggesting a possible exothermic reaction of boron with nitrogen or nitrogen compounds. Hsieh, et al.[15] found residues of hexagonal crystalline boron nitride (BN) in tests on the combustion behavior of strands of boron-based BAMO (3,3'bis(azidomethyl)-oxetane) and NMMO (3-nitratomethyl-3'-methyloxetane) solid propellants. They determined that BN was being produced from gaseous nitrogen and not fuel-bound nitrogen. Some evidence from molecular beam studies exists[43] for the reaction of boron with N_2O whereas reaction with N_2 occurs only at extremely high temperatures. Present experiments use nitrogen to prevent detonation and gas-phase combustion products typically contain 45 - 65% nitrogen. At temperatures covered, between 1 - 2% nitric oxide (NO) radicals are formed (but very little N_2O) which likely react chemically with the liquefied oxide layer, and NO chemistry may play a crucial role in this regard. In the present study no systematic investigation of nitrogen effects on boron particle ignition and combustion has been conducted. Subsequent tests with a suitable replacement for nitrogen are suggested to further elucidate the role of nitrogen chemistry.

Chemical modeling studies to be discussed in the next chapter indicate that surface reactions between boron and NO play an important role in the "clean surface" combustion stage between 2200 and 2600 K ambient temperature, where boron nitride (BN) may coat the particle surface thereby hindering combustion.

3.11 Effect of Particle Diameter on Boron Particle Ignition Delay and Combustion Times

Particle size scaling relationships are crucial for propellant and explosives designers since the balance between particle lifetimes and afforded residence times will dictate which particles will be most effective for the given application. In some instances where residence times are limited (less than ~10 msec), smaller particles will be required and in others, where particles are used to slow or tailor overall energy release rates, larger particles are appropriate. There may also be instances where a

† Here the temperature limit is meant as the minimum temperature to ignite boron.

mixture of both very small $d_p < 1$ μm and large $d_p > 100$ μm particles sizes are called for, such as is the case with aluminum in many aluminized propellants. It is impractical to experimentally investigate an entire range of particle sizes in addition to various other parameters (p_c, T_c, X_{O_2}), so it is useful to develop particle size scaling relationships. For Al particles for example, $t_{ign} \sim d_p^2$ and $t_{comb} \sim d_p^{nc}$, where $1 < n_c < 2$ as pressure increases have been determined.

It is possible that particle lifetimes ($t_{ign} + t_{comb}$) for 23.7 μm crystalline boron particles may be too long for many high speed propulsion applications where residence times are on the order of 10 msec. This is especially true at operating temperatures much below 2600 K and at low pressure. In addition to reducing particle lifetimes with ignition-enhancing techniques, whether by chemical assistance or higher pressure operation, smaller particles can be used. The effect of initial particle diameter $d_{p,0}$ on ignition delay time is investigated at 141 ± 5 atm, and T_c = 2615 ± 55 K with X_{O_2} = 0.20 (mixture B). Ignition delay is shown in Fig. 3.14 to increase linearly with $d_{p,0}$ between 10 to 50 μm (tabulated in Table 3.9). The data can be fitted somewhat loosely by Eq. (3.11)

$$t_{ign} = 0.04\, d_{p,0} \tag{3.11}$$

where t_{ign} is in msec and $d_{p,0}$ in μm. Ignition delay can be reduced to below 0.5 msec if smaller diameter particles (10-15 μm) are used. Combustion time also increases linearly with $d_{p,0}$ following the relation

$$t_{comb} = 0.095\, d_{p,0} \tag{3.12}$$

where there is uncharacteristically large uncertainty with this fit for smaller particles. Both curve fits have been forced to intercept the {0,0} axis.

It will be shown in Chapter 4 that convective heating reduces the apparent particle scaling exponent (n_i) for ignition delays. Corrections will be developed to account for the increased heat transfer rates compared to static conduction. It is interesting to note however that the slip velocities here are of the same order-of-magnitude as in propellant systems so that the convective effects are at least similar to typical applications where the particles might be used.

The fact that particles of all size-groups are not spherical, and that many have sharp edges (see SEM photomicrographs in Section 2.4), raises the issue of reliability of the diameter-scaling study. Spherical particles would produce superior results, lest such particles would need to be artificially produced and are not of the form commonly employed. Once full-fledged combustion ensues, surface tension tends to form a spherical droplet in the absence of significant convective forces. Not withstanding, if ignition were purely a result of ambient heating, ignition delays would vary as d_p^{ni} where $2 \geq n_i \geq 1.45$ depending on convective velocity (2 for pure conduction), indicating that for the range of particle sizes tested chemical reactions and/or self-heating quicken the transition to combustion.

Table 3.9: Measured ignition delay and combustion times of boron particles as a function of initial particle diameter, in ambient mixture containing O_2/H_2O = .20/.30, at ~140 atm and ~2615 K.

Shot #	T_1 [K]	p_1 [atm]	d_p [μm]	O_2	H_2O	T_c [K]	p_c [atm]	t_{ign} [msec]	p_b [atm]	t_{comb} [msec]	$p_{b:90}$ [atm]	$t_{c:90}$ [msec]
3.79	292.6	20.6	11.8	0.20	0.30	2612	139.0	0.26	137.8	1.67	-	-
3.80	293.7	20.7	11.8	0.20	0.30	2603	140.7	0.20	140.0	0.71	139.2	1.64
3.89	293.0	20.5	11.8	0.20	0.30	2614	142.9	0.25	142.4	0.66	139.5	3.72
4.50	292.6	20.6	11.8	0.20	0.30	2623	141.9	0.45	138.8	3.11	138.1	3.92
3.81	294.6	20.7	23.7	0.20	0.30	2594	-	-	135.5	2.35	134.1	6.84
3.83	294.0	20.5	23.7	0.20	0.30	2621	141.5	0.88	-	-	-	-
3.86 b	293.4	20.5	23.7	0.20	0.30	2627	144.9	1.38	142.0	2.67	141.1	7.12
4.10	293.7	20.6	23.7	0.20	0.30	2630	145.1	1.19	140.7	3.42	140.2	4.81
4.42	293.4	20.7	23.7	0.20	0.30	2623	145.1	1.07	141.9	2.21	140.9	4.05
3.91	294.0	20.9	49.2	0.20	0.30	2601	138.6	2.66	134.4	3.70	133.5	5.04
3.92	294.0	20.6	49.2	0.20	0.30	2600	137.0	2.13	132.3	5.17	132.6	4.71
3.93	293.9	20.7	49.2	0.20	0.30	2596	137.8	1.01	133.4	5.25	133.7	4.96

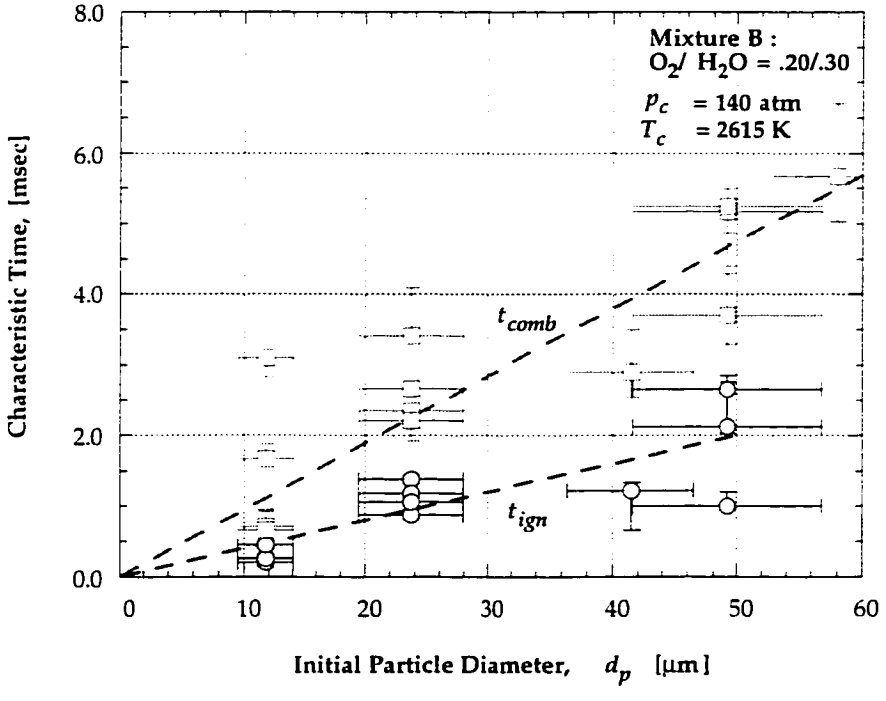

Fig. 3.14: Measured variation of boron particle ignition delay and combustion times with initial particle diameter, d_p, in O_2/H_2O = .20/.30, at ~140 atm and ~2615 K. Both t_{ign} and t_{comb} vary linearly with initial particle diameter.

3.12 Effect of Injection Delay Time on Particle Ignition Characteristics

An additional concern arising from use of the particle injector is what effect the length of the delay before particle injection has on measured particle ignition delay and combustion times. The particle injector has been designed to operate at ~150 atm given the chamber pressure rise histories of mixtures A and B. Slight adjustment of orifice size and seal tightness provide suitable performance when the pressure rise in the chamber is slower than and the final pressure lower than the baseline for which the injector was optimized. Even with knowledge of the required tailoring of injector operation, several compounding factors lead to variable injector performance for a given test condition. These factors include seal tightness and wear, pintle and orifice wear, and improper seating of the particle plunger (as is discussed in Section 2.2.4). Due to these factors, injection delay times have typically varied from less than 4 to as much as 12 msec for the gamut of tests conducted. During the injection delay, chamber pressure and temperature decay slowly and thermal layers grow above the injector housing and it is therefore important to investigate what effect these issues have on particle ignition and combustion dynamics.

The effect of injection delay time (t_{inj}) on particle ignition delay and combustion times is examined for all chamber conditions and the results for three cases in particular are shown in the following figures. Figures 3.15, 3.16 and 3.17 plot particle ignition delay and combustion times versus the injection delay time. The data in Figs. 3.15 and 3.16 are obtained in mixture B with $O_2/H_2O/N_2$ = 0.20/.30/.45, at ~145 and 37.5 atm, respectively. It is evident from Fig. 3.15 that at high pressure there is no systematic effect of injection delay on the measured times. At lower pressure, Fig. 3.16, there is also no systematic effect up to ~8 msec, but beyond this time there is a definite tendency for ignition delays to lengthen significantly the later the particles are injected. This could be caused by several effects, including thermal layer thickening and insufficient injection velocity. Based on calculated performance, the primary result of late injection is poor injection as was discussed in Section 2.2.4. To avoid the problems associated with poor injection, no data is retained for injection delay times greater than ~8 msec at this low pressure condition (~37.5 atm). Measurements at nominal temperatures of 50 K below the target test temperature are also not considered.

Measurements in mixture G which has the lowest excess O_2 were the most difficult to conduct and analyze for reasons already discussed in Section 3.9. The difficulty was thought to be caused by poor injector operation but this does not appear to have effected the measured times as shown in Fig. 3.17. The measured ignition delay and combustion times are found to be insensitive to t_{inj} even over the large span of injection delay times. Additional analysis of measurements for the other mixtures listed in Table 3.3 reveals there is no systematic effect of injection delay time on either ignition delays or combustion times when data for t_{inj} < ~10 msec are considered.

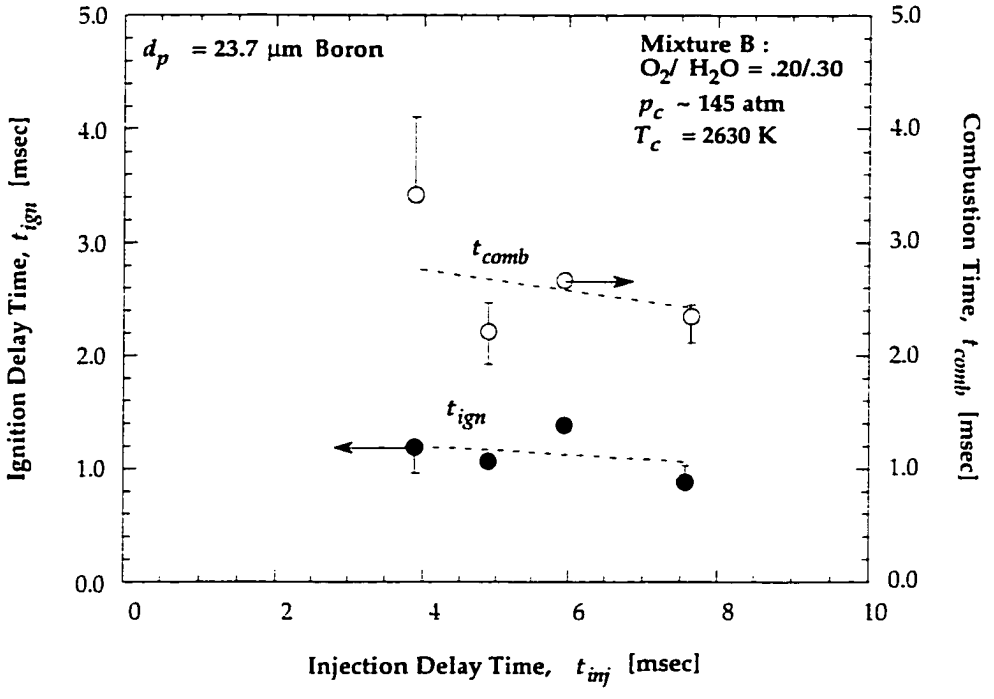

Fig. 3.15: The effect of injection delay time on measured ignition delay and combustion times for mixture B at ~145 atm. Measured times are essentially independent of injection delay between 4 and 8 msec.

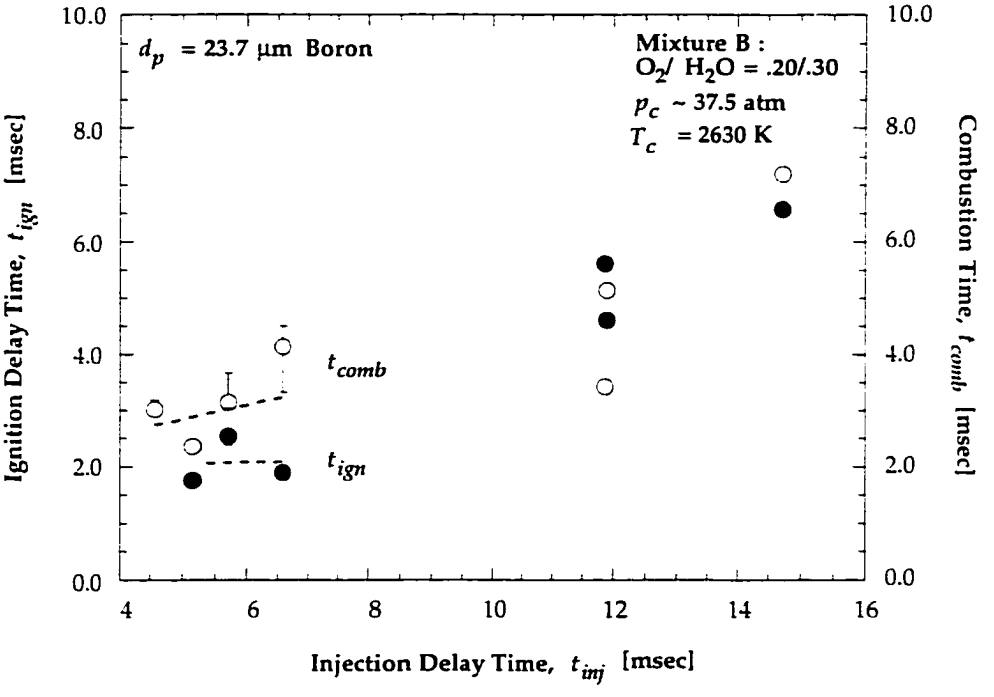

Fig. 3.16: The effect of injection delay time on measured particle ignition and combustion times for mixture B at ~37.5 atm. Measured times for t_{inj} > 8 msec are rejected because they show a strong dependence on the time when the particles were injected.

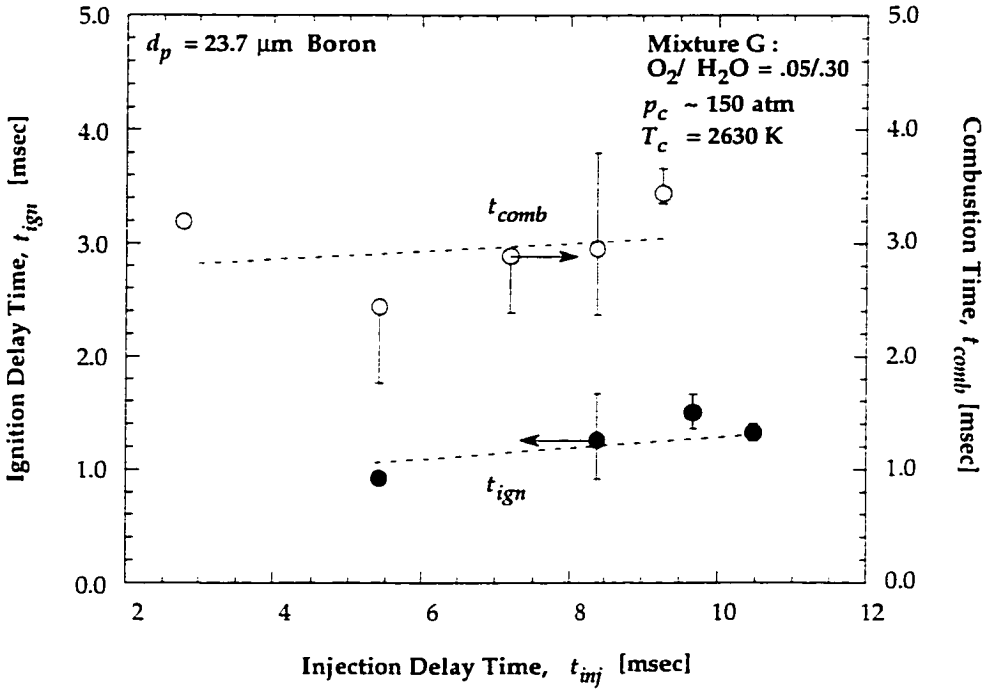

Fig. 3.17: The effect of injection delay time on measured particle ignition and combustion times for mixture G at ~150 atm. Mixture G has the slowest gas-phase combustion of all the mixtures tested. Measured times are independent of the injection delay between ~4 and 10 msec.

3.13 Comparison of Two Different Interpretations of Boron Particle Combustion Time

In this section the two different combustion times referred to as t_{comb} and $t_{c:90}$ are compared to point out differences in trends of measured combustion times versus changing pressure, ambient temperature, and ambient oxygen. It is recalled that t_{comb} is defined as the time from ignition to the time when the net filtered photodiode output signal has fallen back to half of peak amplitude and $t_{c:90}$ is the time from ignition to the time when 90% of the total area under the net-particle signal curve is reached. How these times are determined from measured photodiode signals was discussed in Section 3.3.3. It is found that the greatest differences between the two values occur at high temperature and pressure, and at high and low excess oxygen concentrations.

Figure 3.18 compares the measured pressure variation of t_{comb} to $t_{c:90}$ for the two ambient mixtures tested. The figure shows that $t_{c:90}$ are longer than t_{comb}. This is understandable since the point of 90%-area under the net boron particle combustion curve generally lies beyond the point where the half-maximum amplitude occurs. The largest difference observable in the figure however is the greatly reduced pressure effect for the high temperature mixture, mixture A at ~2810 K and O_2/H_2O =

.11/.34. The measured pressure variation in $t_{c:90}$ are comparable between the two mixtures at high ambient temperatures.

The measured variation of combustion times with ambient temperature at ~150 atm is compared in Fig. 3.19 for X_{O2} = 0.11. Again it is seen in general but not in all cases that $t_{c:90}$ are greater than t_{comb}. The two times are nearly indistinguishable below 2600 K, but $t_{c:90}$ is greater than t_{comb} at higher temperature, ~2810 K. The measured variations of the two differently defined times with temperature agree at low temperature but differ above 2600 K. It is not physically reasonable for the particle combustion times to increase with increasing ambient temperature. The apparent increase in $t_{c:90}$ might be explained if BO_2 does not recombine into products at higher temperatures and instead lingers, where it is then possible that lingering BO_2 emissions are being measured for the high temperature case and not particle consumption.

Figure 3.20 compares the measured variation of the two combustion times with ambient oxygen at ~150 atm and 2620 K. The figure shows that $t_{c:90}$ for X_{O2} = 0.05 are greatly increased. This is due to the fact that combusting particle emissions decayed much more gradually back to the background hot-gas levels as was discussed in Section 3.9. The $t_{c:90}$ are increased above X_{O2} = 0.11 as well up to X_{O2} = 0.20. Overall the measured trend with increasing ambient oxygen shows a larger decrease with increasing X_{O2} up to 0.11 and then a larger increase with X_{O2} for $t_{c:90}$ than was measured for t_{comb}. The increase in combustion times at low X_{O2} is understandable due to the nature of the signals but there is no physical reason why combustion times should increase at high temperature with increasing X_{O2}. It is again possible however that increased BO_2 concentrations in more oxygen-rich mixtures lead to lingering BO_2 emissions in the gas phase after the particles have burned to completion.

Based on physical and statistical arguments, presently more confidence is placed on the measured combustion times given by t_{comb}. It is obvious that uncertainties remain unresolved which might be reconcilable *with a direct measurement of particle sizes* as a function of time, by Mie scattering for example. Such an approach is feasible in the combustion chamber from an optical-access point of view using the fiber optics and backscattering, but issues need to be addressed concerning optical properties of the high temperature and pressure medium and the hot particles themselves.

The times t_{comb} are considered as most closely representing particle combustion and will be referred to beyond this point as the boron particle combustion time. The interested reader can inspect the nature of representative particle signals in Appendix C.

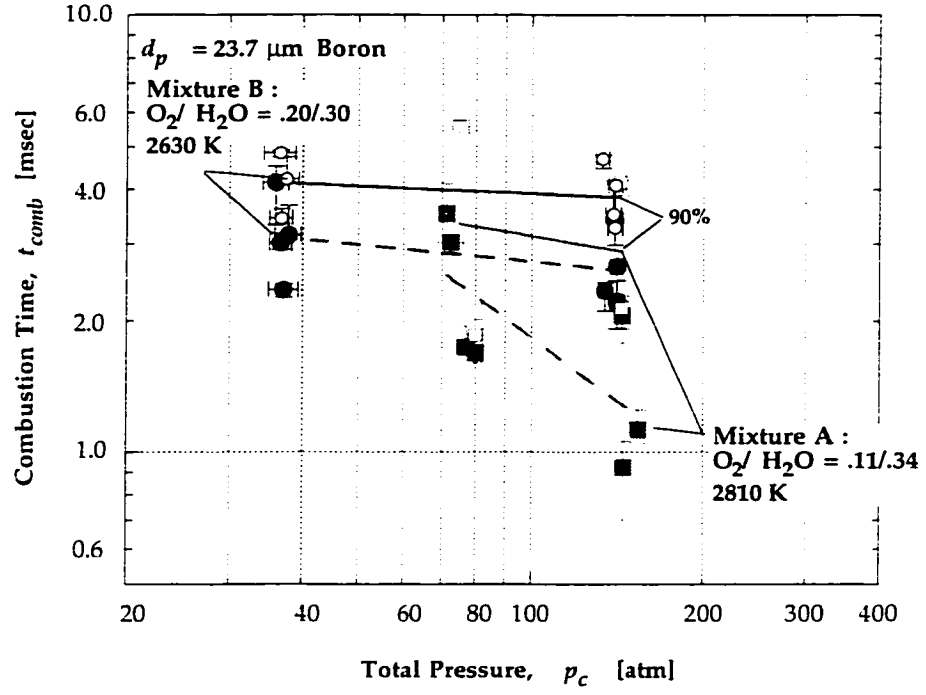

Fig. 3.18: Comparison of pressure variation of measured t_{comb} vs. $t_{c:90}$ for boron particles. Values of $t_{c:90}$ are greater than t_{comb}, but more importantly the pressure dependency of $t_{c:90}$ for mixture A is greatly reduced and comparable to mixture B.

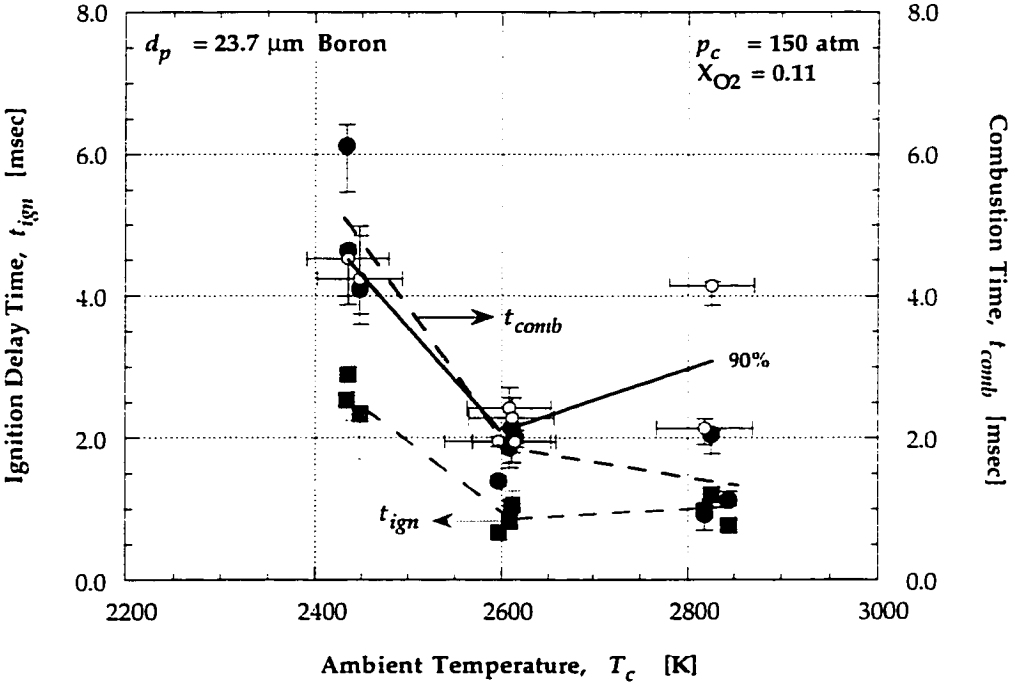

Fig. 3.19: Comparison of temperature variation of measured t_{comb} vs. $t_{c:90}$ for boron particles, at ~150 atm and O_2/H_2O = .11/.30. The two times agree at 2440 and 2610 K, but $t_{c:90}$ are significantly greater than t_{comb} at 2830 K.

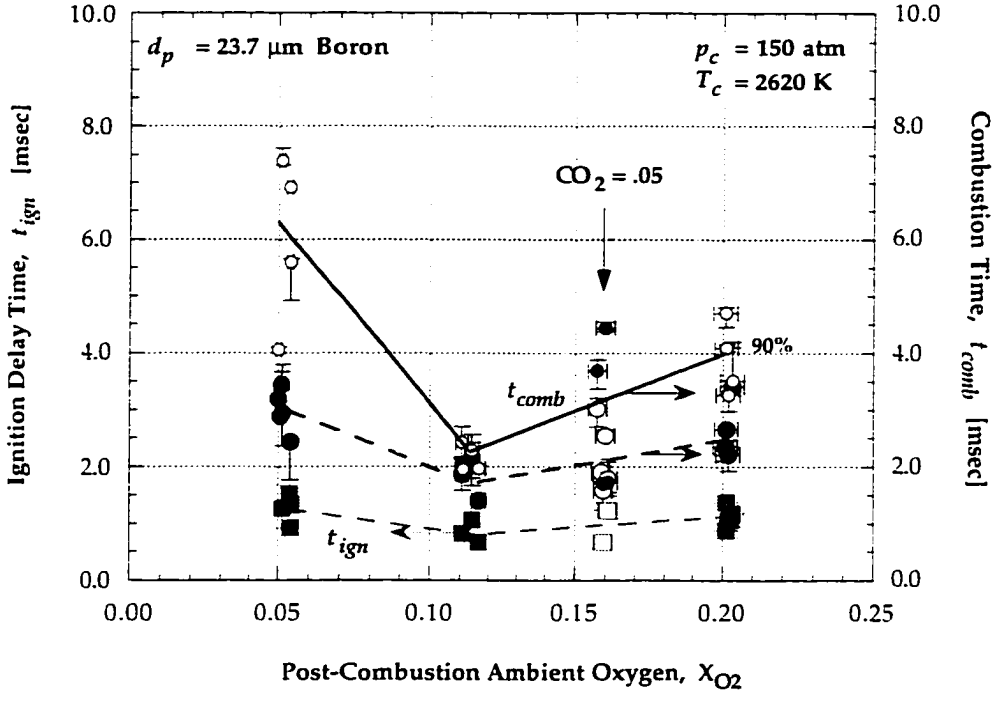

Fig. 3.20: Comparison of ambient oxygen effects on measured t_{comb} vs. $t_{c:90}$ for boron particles, at ~150 atm and 2620 K. Times for X_{O2} = 0.05 are greatly increased as is the apparent trend of increasing combustion times with increasing X_{O2} above X_{O2} = 0.11.

3.14 Comparison of Boron Particle Measurements to Published Data

One purpose of the present work is to study the effects of pressure and several gaseous ignition additives on boron particle ignition and combustion times to determine whether these particles may oxidize within the time constraints of high speed propulsion devices (or explosives). These applications typically operate at much higher pressures than those over which boron particle combustion has been studied previously. Due to the application, concern is restricted to particle combustion where the initial stimulus is the high temperature, high pressure ambient. Since time constraints require combustion be completed within ~10 msec, particles with diameters less than 50 μm are considered. Particles of 23.7 μm diameters are used as the baseline for the experiments in this study. In order to shed further light on the ignition and combustion characteristics of these particles at high pressure, the ambient temperature and oxygen content are also varied. Particle sizes are varied at one condition to establish diameter scaling relationships.

The applications of interest typically operate at much higher pressures than those over which boron particle combustion has been studied previously (1 atm). There are no independent data available for similarly sized particles at elevated pressure and high ambient temperature for

comparison, and it is this lack of data which provided the strong impetus for the present experiments in the first place. The measurements at high pressure are therefore compared to the existing database at low pressure where measurements were conducted in high ambient temperature oxidizing gases. This is done to draw comparisons between the new high pressure data and relationships established at lower pressures, and to draw upon similarities and highlight differences which may lead to a better understanding of boron particle dynamics over a wide range of operating conditions.

The database at low pressure includes but is not limited to determinations by Macek and Semple,[4-6] Li and Williams,[7-9] and Yeh and Kuo[10] as discussed in the Introduction, Section 1.4.1. Macek and Semple[4] investigated boron particle ignition and combustion in 1 atm flames above 2000 K with similarly sized particles to those of the present study. Their CO_2-gas-laser ignition studies[5,6] were carried out in cold ambient mixtures and were not deemed similar enough for comparison sake. Studies using smaller particle sizes have been carried out more recently by Li and Williams[7-9] and independently by Yeh and Kuo,[10] both in flat flames but at flame temperatures less than ~2000 K. Shock tube determinations of boron particle ignition between 8.5 and 35 atm carried out by Krier, et al.[30,69,70] are not included, since in these later works the short test times precluded examination of the entire ignition event. Recently Rood, et al.[11,12] investigated the ignition of smaller 7.2 and 11.8 μm diameter particles in 100% O_2 behind reflected shocks at ~8.5 atm between 2450 and 2750 K.

At elevated pressures the measured boron particle ignition delays conclusively show t_{ign} decrease with increasing pressure, as much as halving as pressure is increased from 37.5 up to 150 atm for 23.7 μm particles. This is a significant finding in that it suggests more efficient boron combustion is obtainable in high speed propulsion applications if these devices are operated at high pressures. The data of Rood, et al.[11,12] for 7.2 and 11.8 μm boron at lower pressure do not include water vapor and are somewhat confusing in that ignition times are nearly identical for the two particles sizes tested. Nevertheless, ignition delays at high pressure are a factor of ~2 shorter than those measured by Rood.

There are no other boron ignition delay measurements available for comparison at elevated pressure *and* high ambient temperatures for similarly sized small boron particles. Further testing at intermediary pressures is warranted in both the combustion chamber and in independent experiments to further corroborate the pressure dependency and to bridge the gap between the new high pressure data and atmospheric pressure data. Present particle injector design prohibits use at pressures below ~30 atm in the combustion chamber.

When comparing boron to aluminum particle characteristic times at high pressure, the boron particle ignition delays in O_2/H_2O = .20/.30 at ~2630 K are ~2.5 times longer than similarly sized aluminum particle delays over the same pressure range. Boron particle combustion times are between three and four times those for aluminum. In these comparisons, the 21.6 μm diameter Al particles have

been scaled to the 23.7 μm according to $\sim d_p^{1.8}$ for both ignition delays combustion times, based on Hermsen's[66] scaling relationships for aluminum. At high pressure, the Al particle lifetimes are significantly shorter than similarly sized boron particles.

Boron particle ignition delays at high pressure decrease with increasing ambient temperature but more interestingly t_{ign} go through a step-like transition between 2440 and 2600 K where the delay times drop considerably. Particle combustion times also decrease sharply in similar fashion. This strong temperature dependency is again an important finding for residence time-limited applications. It suggests the possibility for significantly increased boron particle combustion efficiency for operation with propellant/oxidizer formulations producing temperatures above 2600 K.

Rood[12] measured ignition delays for 7.2 and 11.8 μm boron particles at 8.5 ± 0.5 atm over a narrow temperature range which brackets the temperatures over which this sharp temperature dependency was observed in the combustion chamber experiments. Rood's data plotted in Fig. 3.21 indicate a distinct although much less pronounced decrease in ignition delays, on the order of only 15% between 2550 and 2600 K, than is measured in the hpcc and in flames. It is shown in the figure that measured times for the two particle sizes are very similar indicating a much smaller diameter scaling

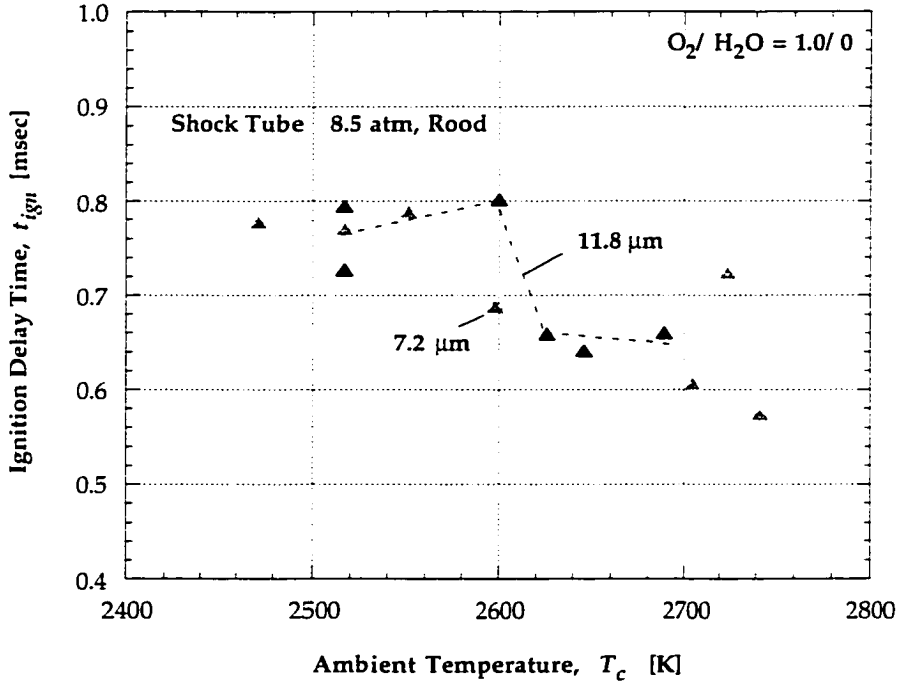

Fig. 3.21: Measured temperature effect on boron particle ignition delays near the temperature where ignition delays are observed to decrease sharply. The data is from Rood[12] obtained behind reflected shocks at 8.5 ± 0.5 atm in 100% O_2. A smaller drop is observed than was measured in the present study and in flames at 1 atm.

law than Rood reported ($t_{ign} \sim d_p^{1.5}$). No combustion times were measured due to short test times.

Macek's flat-flame data[4] at atmospheric pressure show that first stage combustion times t_1 (oxide layer removal neglecting the particle heat-up period)† are essentially independent of ambient temperature up to ~2450 K and then decrease above this temperature in both moist and dry product gases as shown in Figs. 3.22 a and 3.22 b, in similar fashion to the high pressure data. Macek's combustion times show a similar step-like drop near 2450 K, if interpreted in the same manner as the data at ~150 atm. The similarity as concerns t_1 may just be fortuitous - Macek previously interpreted t_1 to follow a linear regress and blamed the poor agreement with the resulting fit at low temperature on experimental scatter in the data. However, Macek specifically noted the sharp decrease in measured combustion times and posed the possibility that the rapid change is caused by the appearance of gas-phase radical species OH and O-atom at the higher flame temperatures. For the high pressure data, Fig. 3.23 shows there is a gradual increase in total gas-phase radical species mole-fractions from 2 to 5% as T_c increases from 2440 to 2830 K, so it is unlikely their appearance would cause such a sharp transition at high pressure.

The available experimental data between 1 and 150 atm concur that a transition occurs between 2450 and 2600 K over which sharply reduced particle lifetimes are achievable. At lower temperatures, Li measured ignition delay and combustion times of individual ~7 and ~10 μm crystalline boron particles in flat-flames at 1 atm. It was found that t_{ign} decreases gradually between 1920 and 2050 K and that t_{comb} is fairly insensitive to temperature in this range. Yeh measured ignition delay and combustion times of ~3 μm crystalline boron particles also in a flat-flame at 1 atm. Fig. 3.24 shows that both Yeh's measured ignition delay†† and combustion times decrease gradually as temperature is increased from 1780 to ~2000 K. Both sets of flat-flame data are in agreement that small-particle ignition delays are weakly temperature dependent below 2000 K, while Macek's larger particle (34.5, 44.2 μm) first stage combustion times (t_1) are independent of temperature between 2200 and ~2450 K. If the heating time contribution were added to obtain the full ignition delay time, where the heat flux by convection increases the higher the ambient temperature, and noting that this heat-up time is not negligible compared to t_1 in the flame, one would expect a decrease in t_{ign} for rising temperature from Macek's measurements as well.

---

† It is important to distinguish between ignition delay time and the time t_1 measured by Macek. The measured t_1, referred to as first-stage combustion times, only deal with the luminous portion of the particle's ignition stage, and therefore do not include particle heating to the point where active oxide-layer removal and ensuing luminosity occurs. As it turns out, particle heating from the hot surroundings is the dominant delay during the ignition stage for the conditions studied here at high pressure, and oxide layer removal is very fast once temperatures are high enough for this to occur. There is therefore a large discrepancy between these two definitions at high pressure.

†† Yeh measured two separate sequential times for the ignition stage in flames, t_i and t_1, which have been added together to compute an ignition delay time corresponding to the standard definition; thus from Yeh[10] the times quoted herein are $t_{ign} = t_i + t_1$. The measured time t_2 in that study is equated herein to the combustion time t_{comb}.

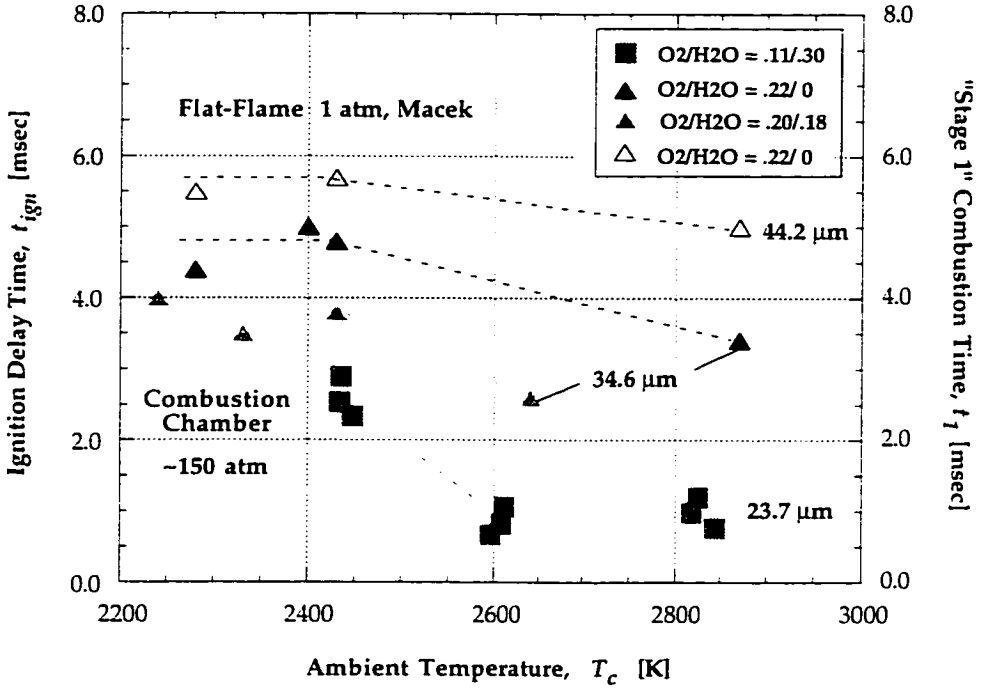

(a)

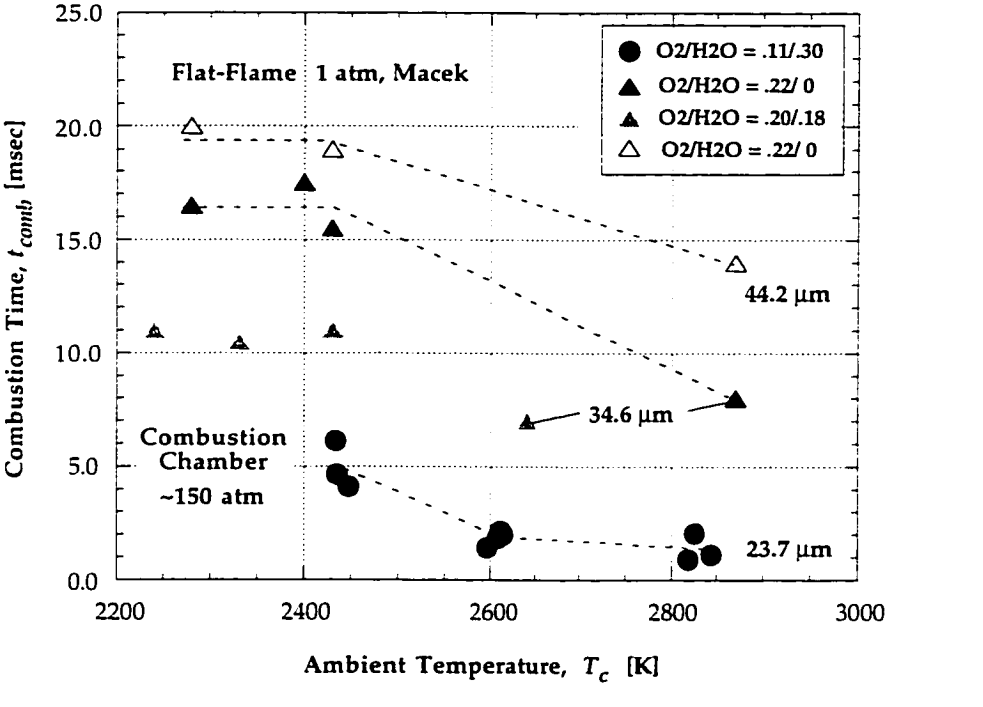

(b)

Fig. 3.22: Macek and Semple[4] measured (a) first stage combustion times (t_1) and (b) second stage combustion times (t_{comb}) for boron between 2250 and 2900 K in flat-flame at 1 atm. Both characteristic times are nearly independent of temperature below ~2450 K but decrease toward higher temperatures in similar manner to data at high pressure.

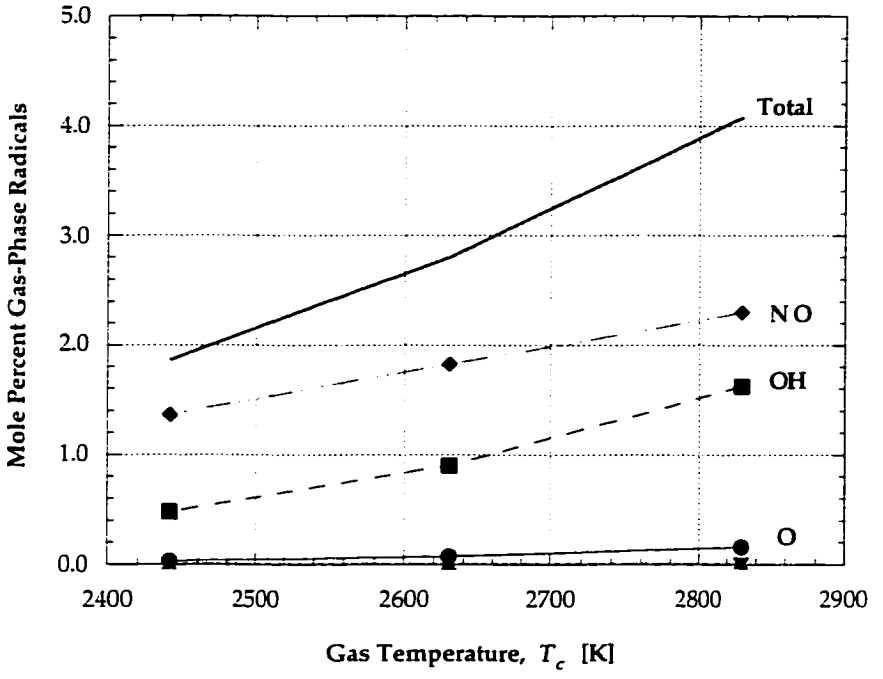

Fig. 3.23: Increase in gas-phase radical species mole fractions at high pressure (~150 atm) as temperature increases.

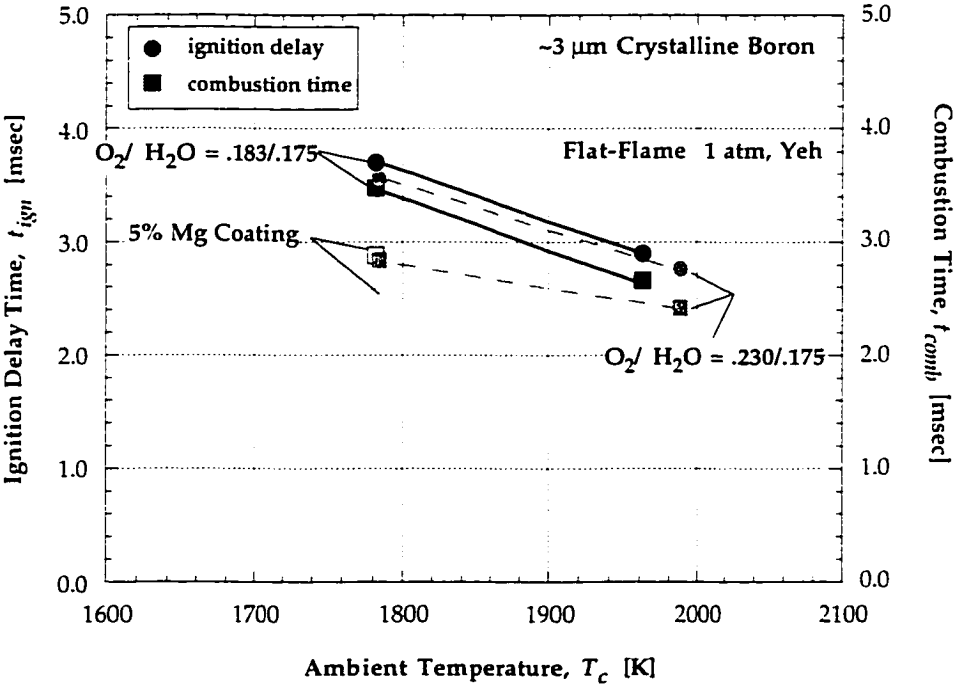

Fig. 3.24: Yeh and Kuo[10] measured ignition delay (t_{ign}) and combustion times for crystalline boron between 1780 and ~2000 K in flat-flame at 1 atm. Data show a gradual decrease in these times as temperature is increased to 2000 K.

Constructing a generalized composite picture of the just-described temperature dependency then, it appears as if boron particle ignition delay times decrease slowly with increasing ambient temperature between 1750 and ~2450 K, decrease sharply by 2600 K, and then remain essentially independent of temperature up to ~2830 K. This variation with temperature is quite different from aluminum and magnesium particles which follow the functional form $t_{ign} \sim \exp(E_0/T)$.[44] As far as combustion time is concerned, Li, Yeh, and Macek all measure t_{comb} to decrease weakly or be independent of ambient temperature between 1750 and ~2450 K (see respective figures), and both Macek's data and the high pressure data concur that a step-like transition occurs where t_{comb} drop significantly over a short temperature span between 2450 and 2600 K, similarly to the drop in ignition delay times. The high pressure data further show that combustion times decrease further, albeit weakly, up to ~2830 K.

The measurements at high pressure (~150 atm, 2620 K) exhibit behavior which is not monotonic with increasing ambient oxygen (Fig. 3.12). Ignition delays and to a larger degree combustion times decrease as X_{O_2} is raised from 0.05 to 0.11, but both times increase with a further increase in ambient oxygen up to $X_{O_2} = 0.20$. The mixtures all have $X_{H2O} = 0.30 \pm 0.01$ in addition to the oxygen.

Macek's measured t_1 in Fig. 3.25 a decrease as X_{O_2} increases between 0.20 and 0.38 at ~2440 K, and the t_1 in dry flames vary as $1/X_{O_2}^n$ where $n = 1.4$. Since particle heat-up to temperatures where oxide layer reactions assist ignition is essentially by conduction (radiative heating small), and conduction is only weakly dependent on the amount of O_2 present through the gas-phase thermal conductivity (actually X_{H2O} has a greater effect, $k_{H2O} > k_{O2} = k_{N2}$), true ignition delays ($t_{ign} = t_{heat\text{-}up} + t_1$) are expected to decrease more gradually with increasing X_{O_2} than the exponent $n = 1.4$ suggests. Combustion times likewise decrease with increasing ambient oxygen and can be described by a similar inverse power law where $n = 1.4$ also. These data are shown in Fig. 3.25 b. Li, for smaller particles (~7, ~10 μm) and at lower temperature between 1920 - 2050 K, found t_{ign} to be independent of X_{O_2} between $X_{O_2} = 0.30$ and 0.80. Yeh using ~3 μm boron measured ignition delays (see Fig. 3.26) which decrease weakly with increasing X_{O_2} between $X_{O_2} = 0.18$ and 0.28 and temperatures between 1780 and 2000 K. Combustion times from these two determinations decrease as $1/X_{O_2}^n$, where $0.9 < n < 1.0$ for Li's data in Fig. 3.27 and where $n = 1.0$ at 1780 K for the small particles measured by Yeh.

The data of Macek, Li, and Yeh indicate ignition delays (t_{ign}, not t_1) are independent of or decrease weakly as a function of X_{O_2} between $X_{O_2} = 0.18$ and 0.80. The newer findings at high pressure below $X_{O_2} = 0.11$ are in agreement with the atmospheric pressure data. However at ~150 atm there is a small but unmistakable increase in t_{ign} as X_{O_2} is raised further. In Section 4.5.3 the high oxygen partial pressures will be shown to account for this behavior, by causing the oxide layer to grow prior to removal thereby lengthening ignition delays. All data at 1 atm in flames show strong decreases in combustion times as X_{O_2} increases in direct contrast to the trend measured at high pressure where a significant 40%

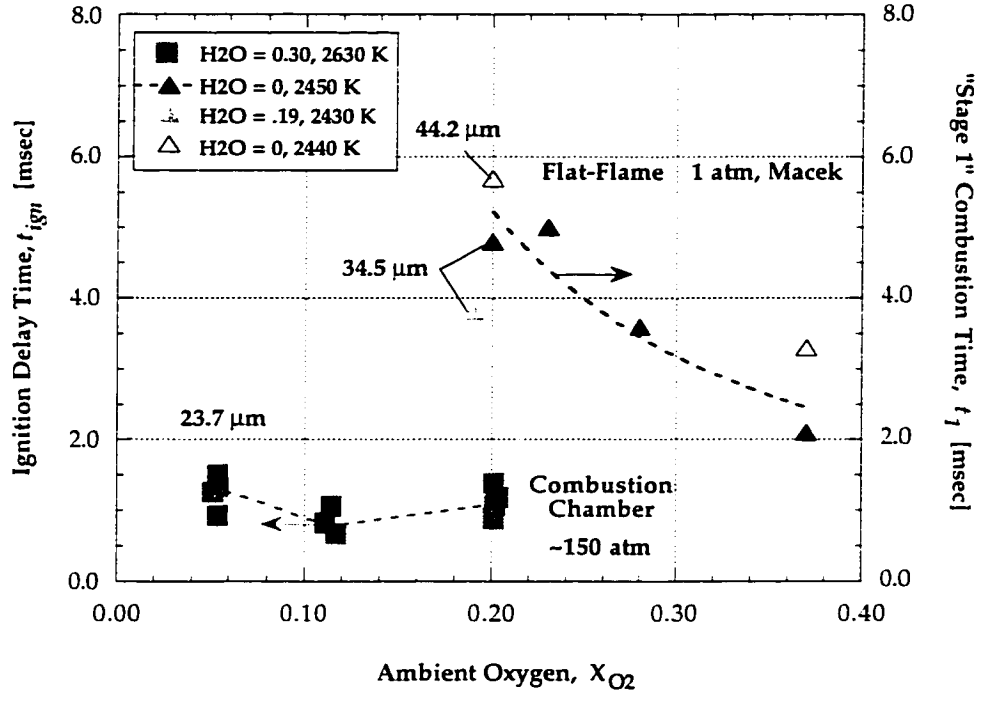

(a)

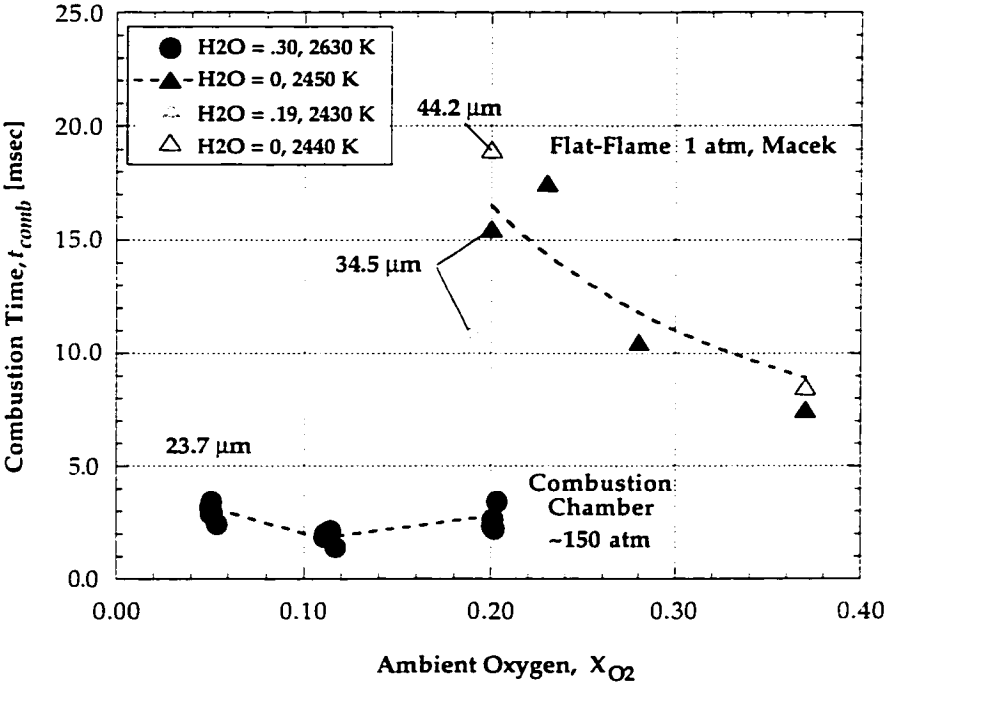

(b)

Fig. 3.25: Macek and Semple measured variation of (a) first stage combustion times t_1 and (b) second stage combustion times as a function of X_{O_2}, in flat-flame at 1 atm from Ref. (4). Both t_1 and t_{comb} decrease with increasing oxygen and are proportional to $X_{O_2}^{-1.4}$.

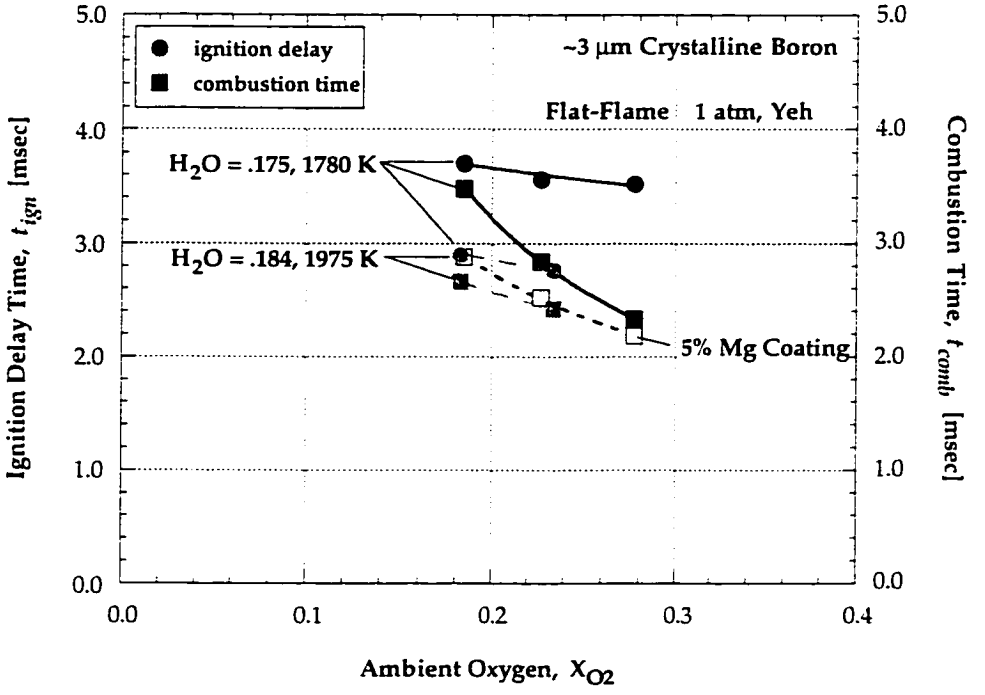

Fig. 3.26: Yeh and Kuo measured variation of ignition delay and combustion times as a function of X_{O_2}, in flat-flame at 1 atm from Ref. (10). Data show t_{ign} decrease weakly with increasing X_{O_2} whereas $t_{comb} \sim X_{O_2}^{-1}$ at 1780 K.

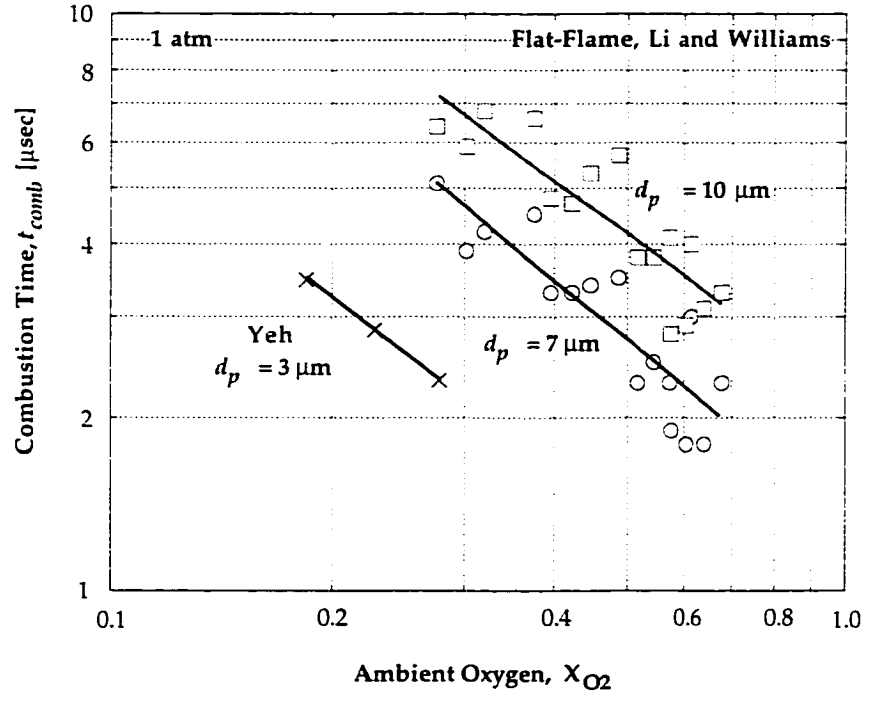

Fig. 3.27: Li and Williams measured variation of combustion times as a function of X_{O_2}, in flat-flame at 1 atm from Ref. (8). Data show $t_{comb} \sim X_{O_2}^{-n}$ where $0.9 < n < 1.0$.

increase in t_{comb} is observed between X_{O_2} = 0.11 to 0.20. The reasons for the contradicting behavior at high pressure and high temperature is unclear, although insight into possible causes is obtained from theoretical modeling work to be discussed in Chapter 4.

Measurements at high pressure in 20% O_2 indicate that particle ignition delay and combustion times increase linearly with particle diameter between 10 and 50 μm, at ~2610 K. Based on insufficient data, it appears as if ignition delays decrease more rapidly toward even smaller particle sizes. The fact that particles of all size-groups are not spherical and that many have sharp edges (see Figs. 2.49 - 2.51 in Section 2.4), raises the issue of reliability of the diameter-scaling study. Spherical particles would produce superior results for scientific purposes, although such particles would not be of the form commonly employed in industry. Once full-fledged combustion ensues, surface tension tends to form a spherical droplet in the absence of significant convective forces. Nevertheless, if ignition were purely a result of ambient heating, ignition delays would vary as $d_p^{n_i}$ where $2 \geq n_i \geq 1.45$ depending on the degree of convective heating, indicating that additional chemical reactions and/or self-heating must take place to quicken the transition to full-fledged combustion.

Because different definitions have been used in quoting times for the ignition stage, and Li does not reduce flame heights into ignition delays for the ~7 and ~10 μm particles tested (although flame heights appear to be slightly longer for the ~10 μm particles), no clear generalized particle scaling relationships for ignition delays can be drawn from that data at 1 atm. For particle combustion on the other hand, Macek's[4] measured t_{comb} in flames increase less rapidly than linearly, instead as $d_p^{0.6}$ below ~2450 K, for the 34.6 and 44.2 μm particles. Li's ~7 and ~10 μm boron particle combustion times scale as $d_p^{1.2}$ between 1920 and 2050 K. Yeh, using smaller ~3 μm crystalline boron particles, measured combustion times which when compared to Li's measurements at higher X_{O_2} scale as $d_p^{0.9}$ with the ~7 μm and d_p^1 with ~10 μm data.

Since combustion times also vary with oxygen concentration and the various particle data just described were obtained under differing oxidizer-conditions, direct comparison may be misleading. However, based on theoretical grounds, the product (t_c X_{O_2}) where t_c is short for t_{comb} should depend solely on the initial particle diameter $d_{p,0}$ at low pressure. The product (t_c X_{O_2}) is plotted in Fig. 3.28 where the data at one atmosphere all correlate with a linear variation with particle diameter, according to Eq. (3.13)

$$t_c X_{O_2} = 0 + 0.21 d_{p,0} \tag{3.13}$$

$$t_c X_{O_2} = 0.003 d_{p,0}^2 \tag{3.14}$$

until above 40 μm where ($t_c\ X_{O_2}$) increase more quickly, as d-squared by Eq. (3.14). The data for large particle sizes are from Macek[6] and were obtained in room temperature gases where the particles were laser-ignited.

The high pressure combustion chamber data also vary linearly as Eq. (3.15) indicates but it can be seen that the values are significantly less than at 1 atm.

$$t_c\ X_{O_2} = 0.02\ d_{p,0} \tag{3.15}$$

These much shorter combustion times are a result of the high pressure (~145 atm) *and high ambient gas temperature* ($T_c > 2600$ K), *not of convective effects which influence mostly the ignition delays* (see Chapter 4).

Also shown in Fig. 3.28 is that the high pressure data do not collapse to a single value for a given particle size when t_{comb} and X_{O_2} are grouped as suggested. This is because combustion times were not found to vary inversely with X_{O_2} as they do in some other studies at lower temperature. The observed linear variation of combustion times with particle size suggests combustion is kinetically

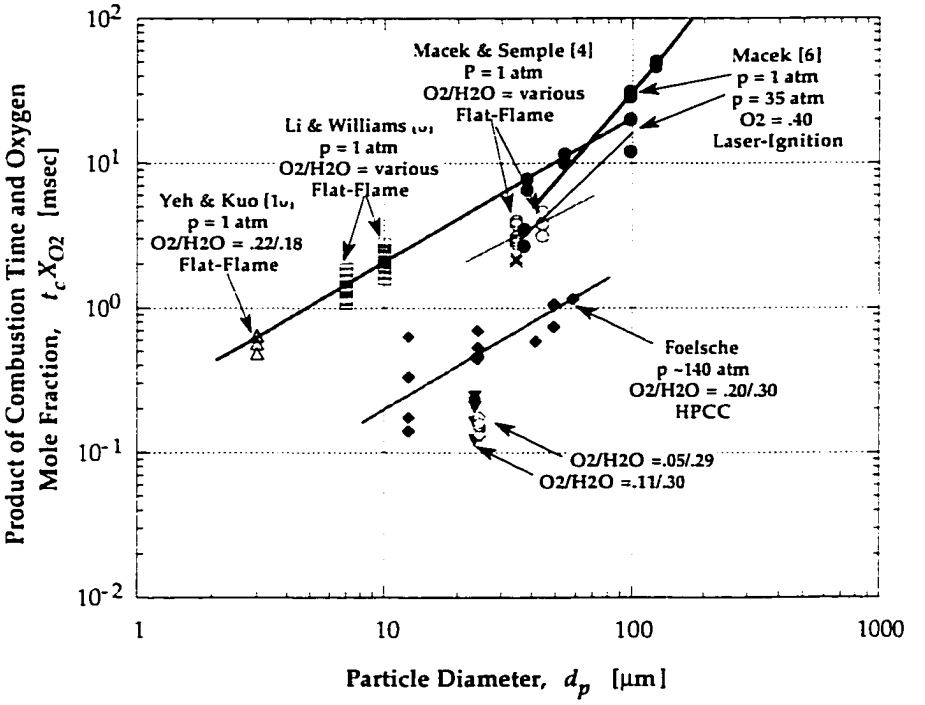

Fig. 3.28: Variation of the product ($t_c\ X_{O_2}$) with initial particle diameter from various independent experimental determinations. The data at 1 atm indicate the product varies linearly below ~50 μm; the high pressure data also vary linearly but are significantly shorter. Cold gas laser-ignition data of Macek[6] for larger particles follow a d^2-dependence.

limited, which contrasts with the findings from the pressure variation study which suggests a mix of diffusion control and kinetics-control for the 20% O_2 case. This contradiction will be discussed further in Section 4.5.4.

It is interesting that although particle sizes and especially pressures are so different between the experiments described above, that there are many similarities in the measured boron particle combustion dynamics. These similarities include the sharp temperature dependence of ignition delays and combustion times between 2450 and 2600 K, the linear variation of ignition delays and combustion times with initial particle diameters smaller than 50 μm, and the weak dependence of ignition delays on ambient oxygen over a large range of values.

3.15 Summary of Experimental Results and Comparisons

An experiment has been designed and developed which permits small particle ignition and combustion studies to be conducted in gaseous mixtures at high pressures and high temperatures produced by the combustion of nitrogen-diluted premixed hydrogen/oxygen mixtures. Once a combustible mixture is ignited and peak pressure is reached, the pressure in the chamber decays slowly permitting particle tests to be conducted at fairly constant pressure and temperature conditions. Using a novel particle injector, particles are introduced rapidly after a sufficient time delay so they may ignite in short timescales and burn to completion independently of one another. Analysis indicates that the injected particles experience increased heating rates during the ignition stage resulting from their motion through the dense gases. Particle ignition and combustion are monitored by measuring emissions with fast response photodiodes using narrow bandpass filters (546.1 ± 4 nm for boron). The experimental approach was validated by various means, and calibration against independent measurements shows good agreement for aluminum particle ignition delays and combustion times.

It has been conclusively established for the first time that boron particle ignition delays and combustion times *at high ambient gas temperatures* (2440 - 2830 K) are strong functions of pressure up to 150 atm. Ignition delays for 23.7 μm particles decrease with increasing pressure according to Eq. (3.8) of the text, $t_{ign} \sim p_c^{-0.5}$, with combustion times decreasing as well but the pressure dependency depending strongly on the amount of ambient oxygen available. It is further found that a significant change occurs between 2450 and 2600 K where both t_{ign} and t_{comb} decrease sharply toward higher temperatures; this finding agreeing with measurements obtained over 25 years ago in flames at 1 atm. It appears as if increasing ambient oxygen above 11% in 30% H_2O at ~150 atm increases t_{ign} and t_{comb}. In a mixture containing O_2/H_2O = .20/.30, both ignition delay and combustion times increase linearly with initial particle diameter as described by Eq. (3.11), $t_{ign} = 0.04\, d_{p,0}$ and Eq. (3.12), $t_{comb} = 0.095\, d_{p,0}$ for $d_{p,0}$ up to

50 μm. Both CO_2 and HF show no benefit toward reducing particle ignition delays and HF actually appears to hinder ignition at the conditions investigated.

Through comparison of the newer boron particle data at elevated pressure with lower pressure data, similarities have been noted over a range of conditions at high ambient temperatures. These include similar temperature dependencies and variation with particle size for both ignition delays and combustion times and the weak dependence of ignition delays on ambient oxygen (to as low as 5% O_2). Also noted were several differences including the measured increase of combustion times with increasing X_{O2} in direct contrast to data at 1 atm and arguments based on theoretical premises.

In the following chapter, the data at higher pressure which were presented and compared to lower pressure data in this chapter are compared to boron particle ignition and combustion model predictions. In so doing further insight into the competing processes will be gained which will explain some of the trends which were measured. The comparison will also allow these present state-of-the art models to be bench-marked at elevated pressures and temperatures.

4. COMPARISON OF MEASUREMENTS TO MODEL PREDICTIONS

Measurements at high pressure and temperature in the combustion chamber are compared to modeling predictions from two types of boron particle ignition models. In the experiments, particles are injected into a high temperature, high pressure reactive oxidizing mixture where it was shown in Section 3.5.2 that they ignite and burn independently. The particles are initially in motion and the effects of convective heating must be included.

The first model is an extension to the semi-global chemistry model developed by Li and Williams for stationary boron particles igniting in a quiescent atmosphere. The extension has been carried out as part of the present study and includes the solution of the particle kinematics equations and a coupled convective heating model. The extended model considers the particles to be introduced into a quiescent atmosphere with finite velocity after which they slow from viscous forces and are heated by the surrounding gases until they ignite and self sustained combustion occurs. Further insight into competing chemical processes is gained through execution of a second more detailed chemical reaction model. Modeling and analyses were conducted by the Princeton/Aerodyne group of researchers[13] executing their detailed finite-rate chemistry and multi-phase diffusion model. This detailed model does not include convective heating effects so direct comparison of ignition delays is not possible, but various additional insights can nevertheless be gained.

4.1 Generalized Picture of Boron Particle Ignition and Combustion

The generalized picture for boron particle oxidation under the described scenario is shown schematically in Figs. 4.1 a, b. Boron has at least two distinct combustion stages where the first stage consists of particle heating in the presence of an oxide layer leading at high ambient temperatures to removal of the oxide layer and particle ignition, and the second stage which consists of boron particle oxidation free of the oxide layer coating. Often the ignition stage is observed experimentally to further consist of two separate luminous stages. The overall processes occurring during the ignition and combustion stages are very complex if all chemical and physical processes are modeled in detail, and so only a brief description will be given here with the details postponed until Section 4.2.4 and 4.3.

Figure 4.1 a schematically depicts a typical instant during the first stage where an assumed spherical boron particle is initially coated by a thin oxide layer which melts at ~723 K (1 atm). The generalized particle ignition models found in the literature consider particle heating from the surroundings by convection and radiation. When particle temperatures are high enough, chemical reactions may contribute to particle heating and will assist with oxide layer removal. Numerous

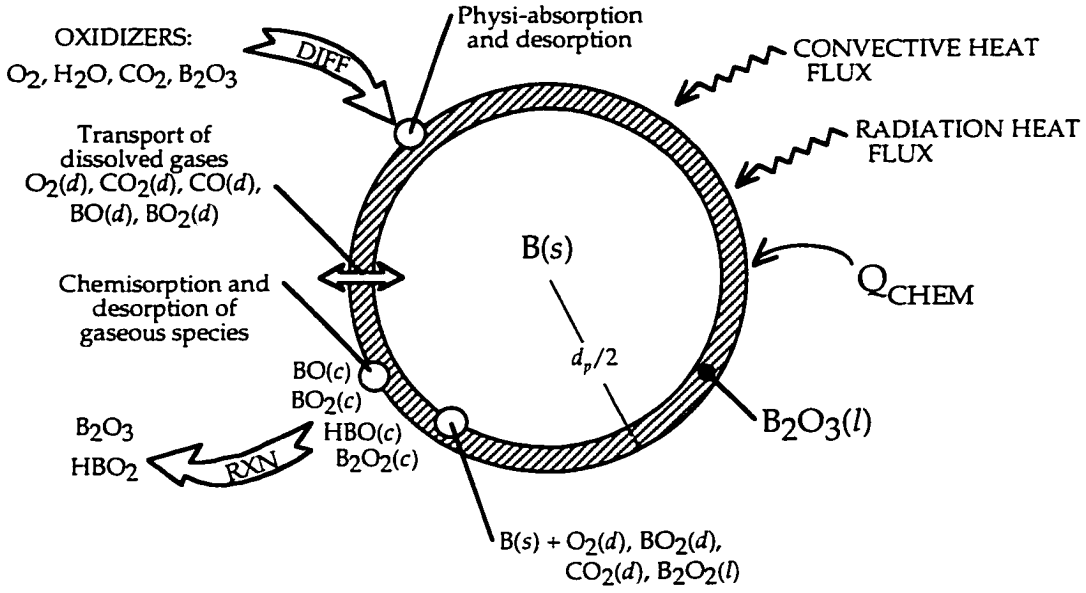

(a)

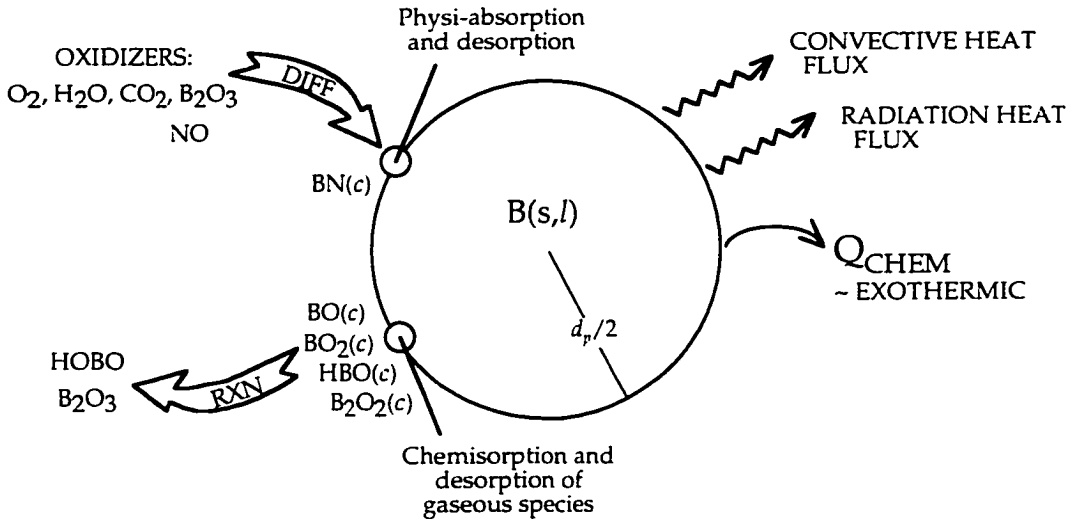

(b)

Fig. 4.1: Schematic model of boron particle (**a**) ignition stage, with a liquid oxide layer present and (**b**) combustion stage, where oxidation of the "clean" droplet occurs. The relative thickness of the oxide layer has been exaggerated for clarity.

chemical processes are considered including gas-phase, liquid-phase, and heterogeneous chemistry at the interfaces plus species transport by diffusion.

Considering the oxidation process from the point of view of gas phase reactants, these species must first diffuse inward toward the particle surface. Oxidizing species which are known to react with the oxide layer coating include O_2, H_2O, and gas-phase radical species such as OH and O-atom. Reaction with outward diffusing partially-oxidized boron intermediates also takes place. At the $B_2O_3(l)$/gas interface, gas phase reactive species are physically or chemically absorbed onto the particle surface where further chemical reactions take place. Some reactants are merely absorbed and dissolved. Boron suboxides in solution at the interface oxidize further (exothermically) and are desorbed into the gas phase forming BO_2 or B_2O_2 which diffuse outward into the ambient, and the remaining dissolved reactive oxidizing species which originated in the gas phase diffuse inward through the layer toward the boron substrate. Recent work has provided compelling evidence[7,10] that boron at the inner boron/$B_2O_3(l)$ interface dissolves into the liquid layer where a vitreous BO·BO·BO structure is formed. Reactive species also attack the boron surface and partially oxidize the boron forming dissolved sub-oxides such as BO(d) and $BO_2(d)$.[13] At relatively low particle temperatures this sublayer boron oxidation can lead to a thickening of the oxide layer. The boron sub-oxides produced at the sublayer interface diffuse outward through the liquid layer to the $B_2O_3(l)$/gas interface where they are further oxidized, liberating more boron into gas-phase products. Gasification at the gas interface also occurs by evaporation of volatile species at higher particle temperatures. These processes continue with the chemistry becoming more prominent as the particle temperature rises providing chemical self-heating and ignition-acceleration until the oxide layer is completely consumed or expelled. During ignition, detailed measurements[7] and modeling[7,10,13] indicate that the change in particle size is very small. Once the oxide layer is removed, then the process transforms to "clean" surface burning of the boron particle where oxidation of the nascent material leads to rapid particle heating. Boron ignition and early combustion generally occur while the particles are still in the solid state.

When finally the oxide layer is consumed by chemical reaction and evaporative gasification then full fledged clean surface oxidation can begin. This stage is accompanied by a rapid increase in the particle temperature and subsequent melting of the particle to form a liquid boron droplet. Simplified chemical models consider only the oxidation of boron by O_2 which is thought to be the limiting process at lower flame temperatures. However, it has been demonstrated[36,37] that H_2O and other reactive gas-phase radical species such as OH and NO also react with boron and that other boron products, such as boron nitrides, may form in addition to the oxides. A more complete picture of boron particle combustion including these processes is shown in Fig. 4.1 b. Reactive species during the combustion stage are absorbed onto the surface and react to form surface complexes followed by desorption into the gas

phase at high temperatures. Details of proposed elementary chemical-step reaction mechanisms can be found in Refs. (36), (37), and (40) for generalized H/O/C/F/N-containing combustion environments. An overview of the detailed model is be given in Section 4.3.

While particle temperatures are below ~4000 K little boron vaporization occurs and surface chemical processes such as those described will dominate combustion. The boiling temperature of boron is very high, ~4000 K[19] at 1 atm, and so oxidation is limited to slower heterogeneous processes making boron combustion much slower than would be the case for vapor phase burning. In the event that boron combustion temperatures are high enough to lead to significant boron vapor, vapor phase burn will ensue which can occur in the present experiments.

The vapor phase burn stage which only occurs at very particle temperatures has been described similarly to hydrocarbon droplet burning, where the evaporation process produces a narrow flame sheet surrounding the droplet. Early models formulated the mass evolution from the droplet in terms of transfer numbers ("*B*", see Chapter 1).[31,32] More detailed models treat evaporation, $B(l) \rightleftharpoons B(g)$, as a finite rate process similar to the formulation for other chemical reaction steps.[1,40]

Several boron particle ignition models have been developed incorporating different levels of complexity based on recent experimental determinations. Two models are considered very recent. One is the Li and Williams model,[7-9] which employs semi-global chemical reactions in competition with physical processes (diffusion, evaporation) to describe particle consumption, and the second is the more detailed chemical kinetics model developed by the Princeton/Aerodyne group.[14,36,40]

4.2 Particle Ignition Model

In the combustion experiments where particles are injected into hot and dense ambient gas mixtures the general problem is the heating of initially cold particles moving through a high temperature reactive medium. The particles are slowed by viscous forces and heated initially from the surroundings by convection and radiation. As particle temperatures increase, chemical reactions between dissolved species within the liquid oxide layer and heterogeneous reactions between the oxide layer and gas phase species lead to additional chemical self-heating. When particle temperatures increase above the ambient, generally during "clean" surface oxidation (combustion stage), convection and radiation cool the particle while chemical reactions continue to heat it further. It is generally found in these experiments that oxide layer removal for boron (and hence particle ignition) occurs while the particles are below the melting temperature of boron. Particle melting occurs at 2350 K (1 atm) and

it is found that during full-fledged combustion the particle temperatures may exceed the boiling point of boron.

4.2.1 Model for Particle Kinematics

The particle kinematics are modeled by a one dimensional analysis which considers the motion of a spherical particle in a gas medium which in the general case can be in motion also. Particle trajectories can be calculated by equating Newton's second law of motion to the external forces acting on the particles

$$\frac{d}{dt}(m_p v_p) = F_D + F_g \tag{4.1}$$

where the external forces are the decelerating viscous forces, F_D, and the force of gravity, F_g. In the equation m_p is the particle mass and v_p the particle velocity. Gravity forces can be negligibly small compared to drag forces, where $F_D / F_g \sim \rho_g(v_p-v_g)^2/(\rho_p d_p g_o)$, with g_o the acceleration due to gravity. During the particle ignition stage and a portion of combustion $F_D / F_g >> 1$. Eq. (4.1) then reduces to

$$m_p \frac{dv_p}{dt} = -\frac{1}{2}\rho_g S_p C_D (v_p-v_g)^2 \tag{4.2}$$

where the mass of the particle has been assumed constant, ρ_g is the gas density, ρ_p the particle density, S_p the particle frontal area, C_D the drag coefficient, and v_g the bulk gas velocity. In the hpcc experiments localized ignition at the spark discharge produces an advancing combustion front which traverses the chamber. A bulk gas velocity is produced locally directly behind the advancing deflagration front. Since the system is completely enclosed and particle injection occurs after gas-phase transients have subsided, the bulk gas velocity in the chamber will be negligibly small when injection occurs and is neglected in comparison to the particle velocity. Initial particle velocities at the instant of injection are between 8 and 14 m/sec.

With the assumption of spherical particles $S_p = \pi r_p^2$ and $m_p = \rho_p(\frac{4}{3}\pi r_p^3)$, Eq. (4.2) reduces to

$$\frac{dv_p}{dt} = -\frac{3}{8}\frac{\rho_g}{\rho_p}\frac{C_D}{r_p}(v_p-v_g)^2 \tag{4.3}$$

where r_p is the particle radius. The penetration distance of the particles injected into the surrounding dense gases can be calculated by solving for the particle position x_p at every instant with

$$\frac{dx_p}{dt} = v_p \tag{4.4}$$

The solution of the particle energy equation is coupled to the particle kinematics through the convective heating term (among others) where the particle motion determines the convective heat transfer. Solution of Eq. (4.3) requires C_D and accurate knowledge of mixture properties. The coefficient of drag C_D has been measured for spherical particles for $20 < Re_p < 200$ and correlated empirically as a function of particle Reynolds number and Mach number by Walsh,[72] where:

$$C_D = C_{D,C} + (C_{D,FM} - C_{D,C}) \exp(-A\, Re_p^N) \qquad M_p \geq 0.1 \qquad (4.5)$$

$$C_D = \frac{24}{Re_p}(1 + 0.15\, Re_p^{.687}) \qquad M_p < 0.1 \qquad (4.6)$$

$$C_D = \frac{24}{Re_p} \qquad Re_p \leq 1.0 \qquad (4.7)$$

In these equations, $Re_p = \rho_g\, v_p\, d_p / \mu_g$ is the particle Reynolds number, $M_p = v_p / a_g$ is the Mach number, and μ_g the gas viscosity and a_g the speed of sound. The $C_{D,C}$, $C_{D,FM}$, A and N are constants tabulated in Ref. (72) as a function of M_p for $0.1 < M_p \leq 2.0$. For the conditions in the hpcc experiments, maximum M_p ~ 0.01 and minimum $Re_p > 5$ during ignition so Eq. (4.6) is appropriate. Eq. (4.7) is recognizable as the analytical result for Stokes flow conditions.

The empirical drag coefficient given by Eq. (4.6) is plotted in Fig. 4.2 as a function of particle Reynolds number. Particle Reynolds numbers for the experiments range from a high of ~150 at high gas

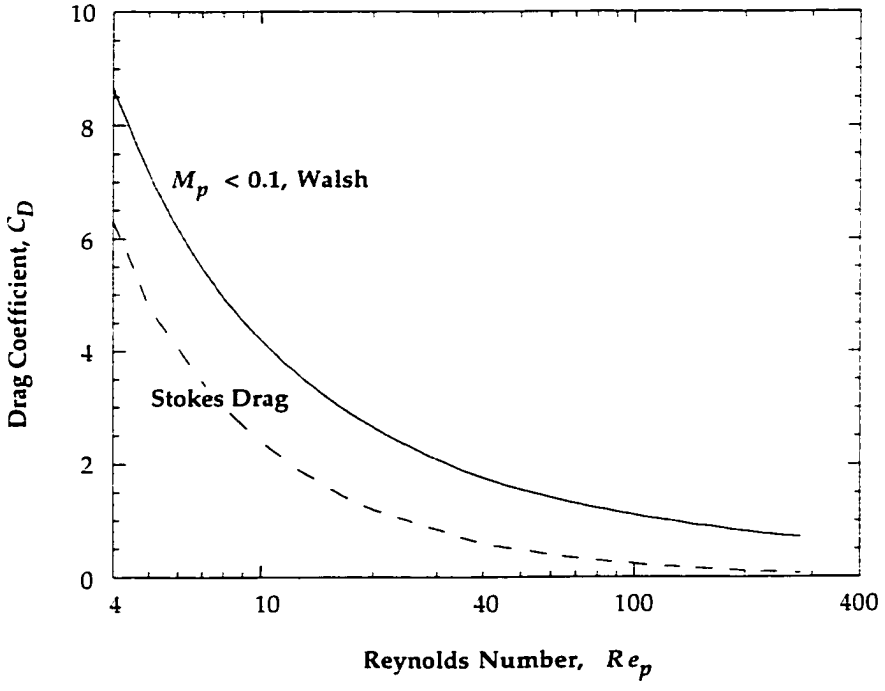

Fig. 4.2: Drag coefficient on spherical particles as a function of particle Reynolds number, Re_p for small M_p. The drag coefficient for typical experimental conditions is between 1 and 5.

pressure (density) just after injection, down to 10 at lower pressure after significant particle deceleration. Therefore the drag coefficient varies typically between 5 and 1 during ignition. The formulation here assumes steady conditions in the gas (no localized gas motions) and also no particle-particle interactions.

4.2.2 Particle Energy Balance

The generalized particle heating problem can be greatly simplified by considering the tiny irregular particles as spheres and employing a lumped capacitance form of the governing equations. This methodology assumes the internal temperature in the solid particle or liquid droplet is uniform during the transient heating process from the surrounding medium. Then the problem reduces to considering the overall or average particle energy balance since it can be assumed that there are no internal temperature gradients and heat fluxes.

The validity of the lumped capacitance assumption must be assessed by considering the rate of heat transport within the particle compared to the rate of transport from the surrounding medium. The errors associated with the lumped capacitance assumption will be small if the Biot number is small:

$$Bi \equiv \frac{\bar{h}_c L_c}{k_p} \leq 0.1 \tag{4.8}$$

In Eq. (4.8) $\bar{h}_c$ is the surface-averaged convective heat transfer coefficient, L_c is a characteristic length (ratio of volume to surface area), and k_p is the particle thermal conductivity (see Fig. 4.3). For spherical particles, $L_c = d_p/6$. The Biot number expressed in terms of the surface-averaged Nusselt number, where $Nu_p \equiv \bar{h}_c d_p/k_g$, becomes

$$Bi = \frac{Nu_p}{6}\left(\frac{k_g}{k_p}\right) \tag{4.9}$$

where k_g is the gas thermal conductivity. The Biot number is in terms of known particle and gas medium properties. For a Nusselt number of 9 which is greater than any encountered in the experiments for ~24 μm particles, Bi reduces to $Bi = 1.5\, k_g/k_p$. Maximum Biot numbers Bi_{max} taking into account the strikingly rapid drop in k_p with temperature are plotted in Fig. 4.4 as a function of temperature and particle diameter. Actual Biot numbers are calculated at every instant during integration of the particle equations and are lower than the maximum values plotted in the Fig. 4.4. The condition for the lumped capacitance assumption is satisfied for all particle sizes employed in the experiments.

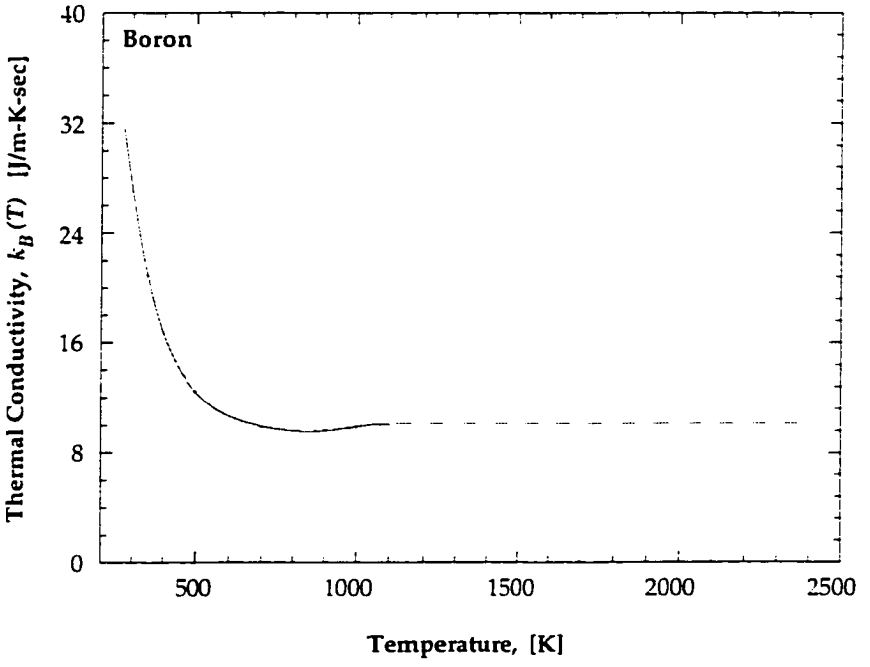

Fig. 4.3: Variation of Boron thermal conductivity k_B as a function of temperature, from Ho, et al.[21] Dashed curve represents assumed extension to high temperatures.

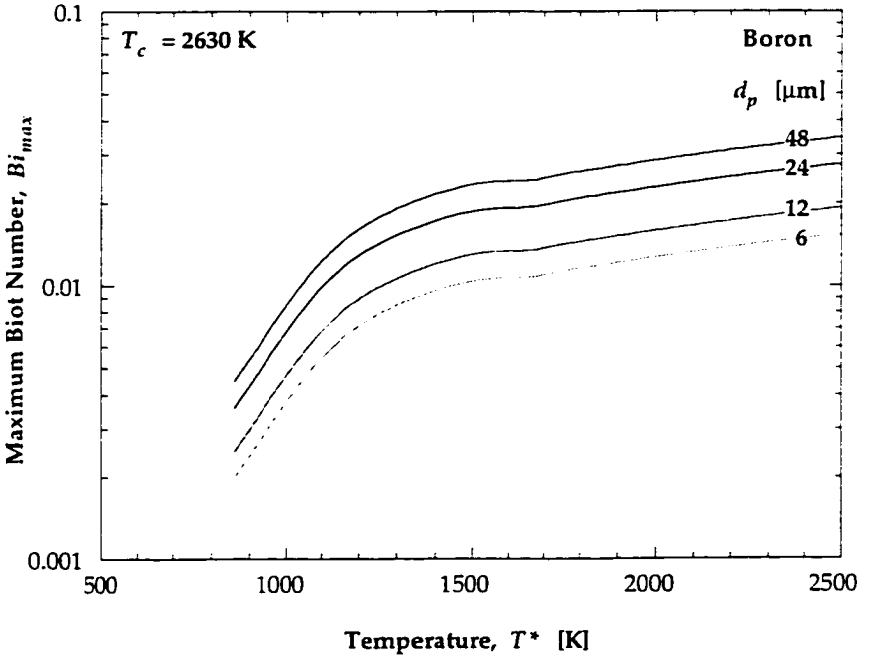

Fig. 4.4: Variation of maximum particle Biot numbers Bi as a function of temperature for various particle sizes. The values of Bi show that the lumped capacitance assumption is valid for the particles used.

With the lumped capacitance assumption the balance between the change of particle internal energy and the external energy exchange mechanisms and chemical energy production gives

$$m_p c_{p,B} \frac{dT_p}{dt} = \dot{q}_{con} + \dot{q}_{rad} + \dot{q}_{rxn} \tag{4.10}$$

where the external heat exchange mechanisms are convection ($\dot{q}_{con}$) and radiation ($\dot{q}_{rad}$), and $\dot{q}_{rxn}$ is the chemical production term. In this equation $c_{p,B}$ is the boron particle specific heat and T_p the particle temperature. The working form of Eq. (4.10) can be obtained by substituting the external energy exchange terms:

$$\dot{q}_{con} = -\bar{h}_c A_s (T_p - T_\infty) \qquad \text{and} \qquad \dot{q}_{rad} = -\varepsilon\sigma A_s (T_p^4 - T_\infty^4)$$

where A_s is the particle surface area, T_∞ the ambient temperature, ε the particle (droplet) emissivity and σ the Stefan-Boltzmann constant. Substituting for the convective heat transfer coefficient

$$\bar{h}_c = Nu_p k_g / d_p \tag{4.11}$$

the following form is obtained:

$$\left(\frac{1}{6}\rho_B c_{p,B} d_p\right)\frac{dT_p}{dt} = \left[-\frac{k_g}{d_p} Nu_p (T_p - T_\infty) - \varepsilon\sigma(T_p^4 - T_\infty^4) + \frac{\dot{q}_{rxn}}{A_s} \right] \tag{4.12}$$

For assumed spherical particles $A_s = 4\pi r_p^2$, and $d_p = 2r_p$ has been substituted.

The particle energy equation (Eq. 4.12) and the kinematic equations (Eq. 4.3 and 4.4) are coupled first order ordinary differential equations. In order to complete the specification of terms in the energy equation the Nusselt number must be known and the chemical heating term formulated. The convective heating model will be discussed in the next section followed by specification of the chemical model.

4.2.3 Model for Particle Heating by Convection

The transient particle heating problem is dictated in part by the particle's time dependent motion since particle velocities upon injection and the high gas densities result in non-negligible convective heating. Particle heating rates are substantially accelerated by convection and after sufficient temperatures are reached chemical reactions can ensue resulting in further heating and the all important stripping of the oxide layer coating. The solution of the particle's kinematics is used to determine the time dependent rate of convective heat transfer from the hot ambient gases to the moving particle. Initially for particles with an injection velocity of 12 m/sec, the particle Reynolds numbers $Re_p = \rho_g d_p v_{p,0} / \mu_g$ are between 40 and ~150 depending on gas density ρ_g (for p_c varied from 37.5 to 150 atm) for ~24 μm particles.

The formulation followed here is similar to that of Fox, et al.[73] which was also used in analyzing combusting particle experiments by Roberts, et al.[24,44] Fox, et al. have proposed an empirical expression for the surface-averaged particle Nusselt number (Nu_p) for the general compressible flow case corresponding to continuum, slip, and part of the transition flow regimes for spherical particles which agrees with experimental data for $M_p/Re_p < 0.5$:[73]

$$Nu_p = 2\left\{ \frac{\exp(-M_p)}{1+ 17\, M_p/Re_p} \right\} + 0.459\, Pr^{0.33}\, Re_p^{0.55} \left\{ \frac{2}{3}(1 + \frac{1}{2}\exp(-17\, M_p/Re_p)) \right\} \qquad (4.13\ a)$$

Here $Pr = (c_{p,g}\, \mu_g/k_g)$ is the Prandtl number which expresses the ratio molecular momentum transfer to thermal transfer of heat, with $c_{p,g}$ the gas specific heat. Eq. (4.13 a) for very small particle Mach numbers M_p reduces to

$$Nu_p = 2 + 0.459\, Pr^{0.33}\, Re_p^{0.55} \qquad (4.13\ b)$$

which is a well recognized from proposed by Drake,[74] and $Nu_p = 2$ corresponds to the analytical result for pure conduction. The resulting maximum surface-averaged particle Nusselt numbers, Nu_p, calculated with Eq. (4.13 b) are found to be between 5 and 8.5 for ~24 μm particles. This clearly shows that convective effects should be included in any analysis of particle heating.

For the gas mixtures used in the hpcc experiments the transport properties are highly temperature dependent. This can be seen in Figs. 4.5 - 4.7 where the mixture thermal conductivities, viscosities, and specific heats at constant pressure are plotted as a function of temperature. Values for the coefficients were calculated using the CHEMKIN/TRANFIT routines.[58,59,68] It is seen that not only viscosity but also the thermal conductivity and specific heat vary substantially with temperature. Since the temperature difference between the particle surface and ambient gas is significant during particle heat-up and since it is the properties in the momentum and thermal boundary layers which dictate the particle drag and heat transfer, i.e., the local properties and local gradients in v_p and T_p, then it is appropriate to evaluate the non-dimensional parameters Re_p, Pr, and Nu_p and the convective heat transfer coefficient at the geometric mean temperature $T^* = \sqrt{T_p T_g}$ between the particle surface and the ambient bulk mixture.[8,75]

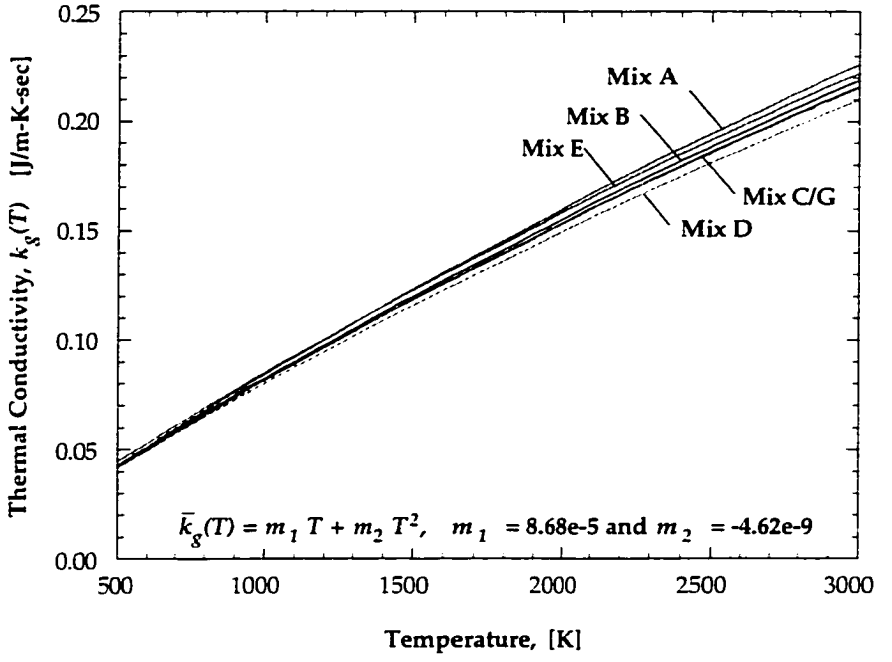

Fig. 4.5: Gas thermal conductivity k_g as a function of temperature for different gas mixtures (gas pressure has almost indistinguishable effect). The k_g are fit by a functional dependence of the form $k_g(T) = m_1 T + m_2 T^2$.

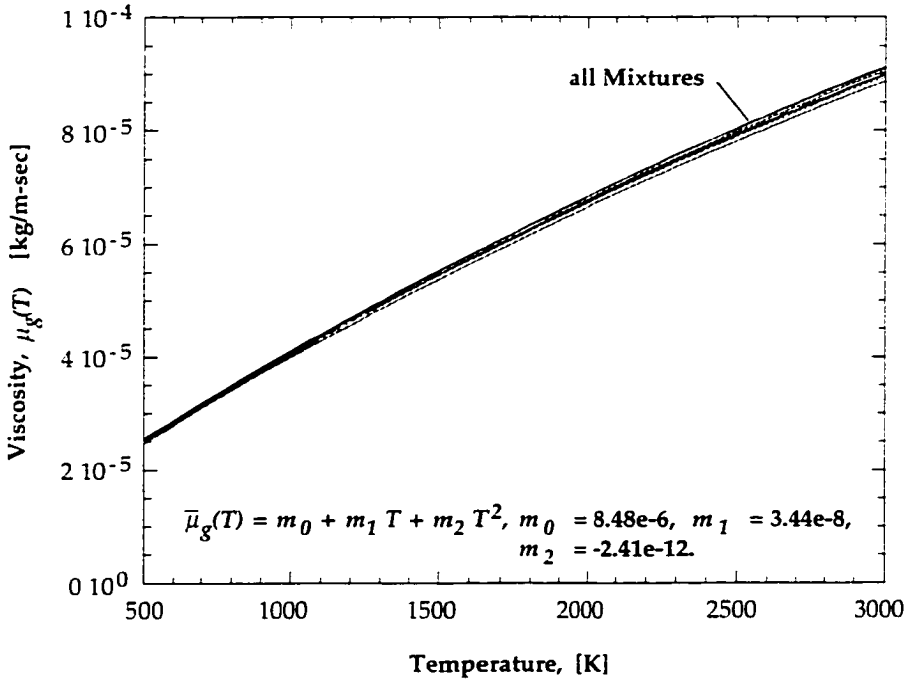

Fig. 4.6: Gas viscosity μ_g as a function of temperature for different gas mixtures (gas pressure has no noticeable effect). The μ_g can be fit by a functional dependence of the form $\mu_g(T) = m_0 + m_1 T + m_2 T^2$.

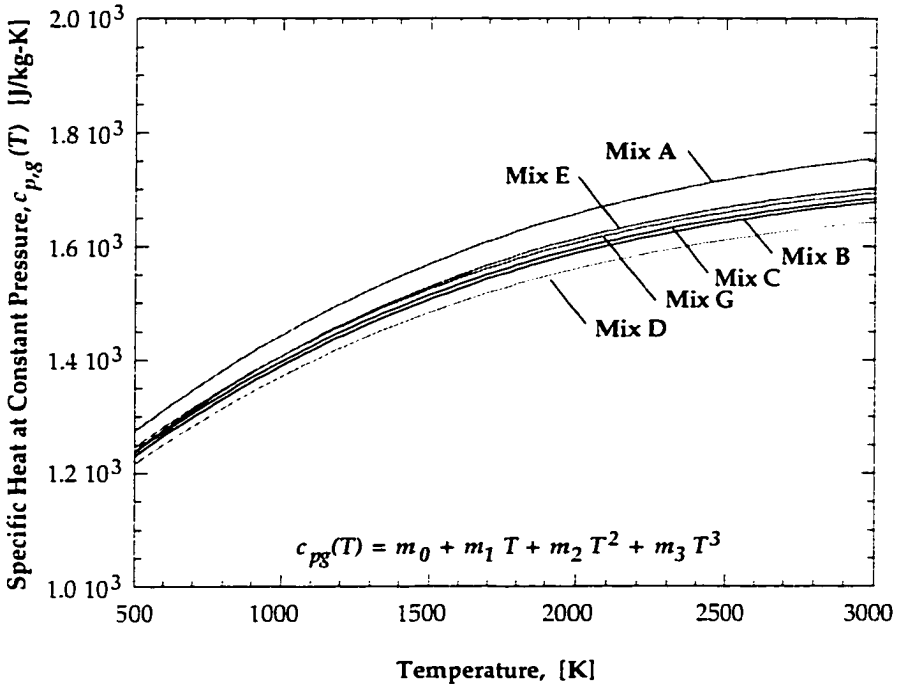

Fig. 4.7: Gas specific heat c_{pg} as a function of temperature for different gas mixtures (gas pressure has no noticeable effect). Each mixture c_{pg} is fit by a functional dependence of the form $c_{pg}(T) = m_0 + m_1 T + m_2 T^2 + m_3 T^3$, which is used during solution of the governing equations.

The Re_p, Pr, Nu_p and $\bar{h}_c$ are plotted in Figs. 4.8 and 4.9 as a function of T^* for mixture B at 145 and 37.5 atm where it is seen that Re_p is quite dependent on T^* whereas Pr is essentially independent of the choice of temperature. The surface-averaged Nusselt number varies only through the Reynolds number as $Re_p^{0.55}$ so Nu_p varies less with temperature than does Re_p. The convective heat transfer coefficient $\bar{h}_c$ increases with temperature mostly due to the increase in k_g with temperature. The sensitivity of $\bar{h}_c$ to T^* has a large effect on the calculated heating rate and subsequently on model-predicted particle ignition delay times as will be discussed further below.

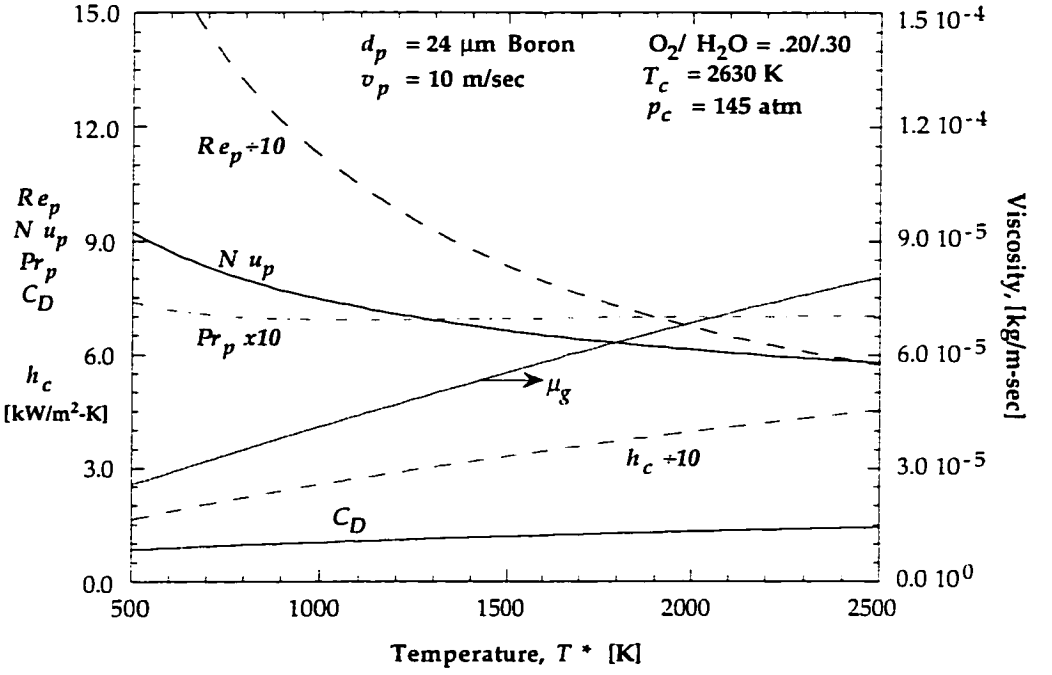

Fig. 4.8: Variation of non-dimensional parameters and $\bar{h}_c$ with temperature for mixture B; O_2/H_2O = .20/.30 at ~2630 K and 145 atm. The plot indicates the sensitivity of these parameters to the temperature T^* at which coefficients are evaluated. The Nusselt number and heat transfer coefficient are quite sensitive to the choice of temperature.

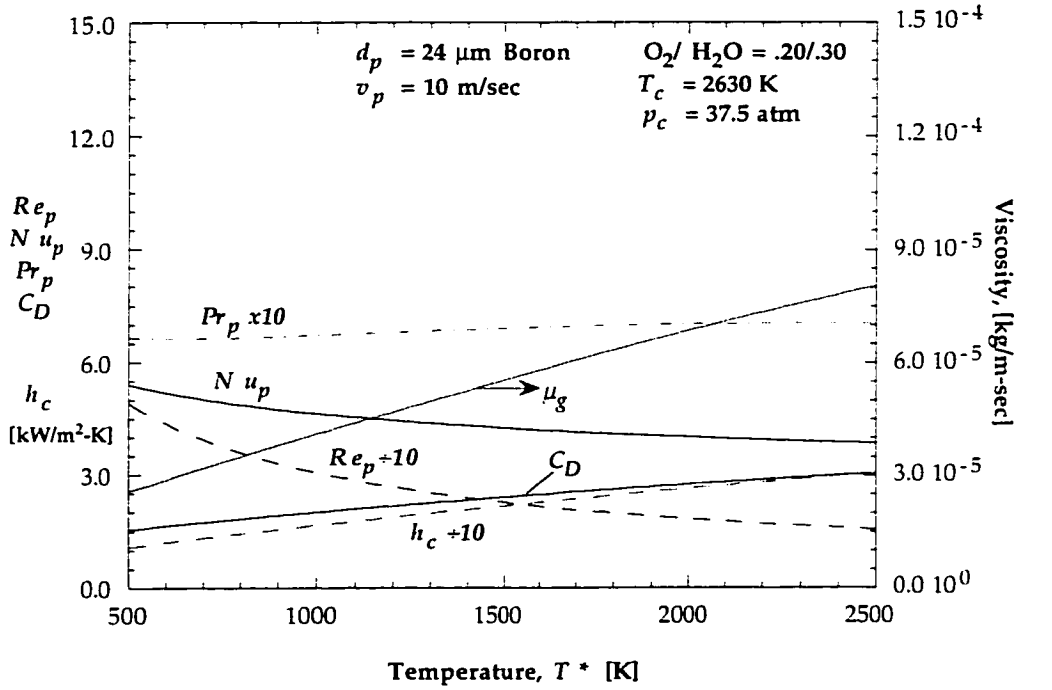

Fig. 4.9: Variation of non-dimensional parameters and $\bar{h}_c$ with temperature for mixture B; O_2/H_2O = .20/.30 at ~2630 K and 37.5 atm. The Nusselt number and heat transfer coefficient are less sensitive to the choice of temperature than at higher pressure (Fig. 4.8).

4.2.4 Model for Particle Self-Heating by Chemical Reactions

In this study the formalism developed by Li and Williams[7-9] incorporating a semi-global chemical reaction scheme to describe the oxide layer removal and ignition of boron particles has been adopted. The Li and Williams Model is presented in this section where it is shown that two additional equations, one describing the rate of change of the oxide layer thickness and the other describing the change of particle size, are added to complete the formulation of the overall problem. The details concerning rate controlling chemical reactions, competing gas-phase diffusion processes, and gasification by evaporation are introduced.

4.2.5 Description of Oxide Layer Removal Mechanism from Li and Williams Model

The Li and Williams Model[9] considers a single small spherical boron particle coated by a thin oxide layer igniting in a quiescent oxygen and water vapor atmosphere. During the ignition stage when particles are solid but coated by a liquid oxide layer, most are non-spherical and irregularly shaped but once full-fledged combustion ensues and the boron melts, surface tension will tend to form a spherical droplet. The model considers the governing equations of mass balance in the oxide layer and underlying boron substrate and the particle energy balance.

The mass balance of the oxide layer and the underlying boron is written in terms of the net mass accumulation (or depletion) balanced by chemical consumption or physical transport terms multiplied by their individual stoichiometric coefficients c_i and molecular weights W_i,

$$\frac{dm_p}{dt} = \sum_i W_i \, c_i \, \omega_i. \tag{4.14}$$

Molecular transport rates are at times also included and they appear explicitly in the formulation of the ω_i. The rate terms ω_i, in units of mol/cm^2-sec, arise from a balance between different chemical reactions which are considered and diffusion transport. Li and Williams have determined several important chemical and physical processes which dictate particle ignition and combustion.

The particle energy balance is written in terms of the energy buildup (storage) balanced by heating from the surroundings and net energy change from chemical bond rearrangement (resulting in particle self-heating). Heat transfer mechanisms between the particle and surroundings are limited to include conduction and radiation transfer, but convective heating which was developed in the previous sections will be assumed. Employing the assumptions of spherical symmetry and simplifying to one dimension (radial), for small particles which have uniform temperature based on Biot Number, $Bi < 0.1$

at all conditions, and a thin oxide layer (of negligible energy content), the energy equation rewritten in terms of the particle temperature becomes

$$\left(\frac{1}{6}\rho_B c_{p,B} d_p\right)\frac{dT_p}{dt} = \left[\sum_i Q_i\,\omega_i - \frac{k_g}{d_p}Nu_p\,(T_p - T_\infty) - \varepsilon\sigma(T_p^4 - T_\infty^4)\right], \qquad (4.15)$$

where T_p is the particle temperature, Q_i are the heats of reaction, d_p is the particle diameter, T_∞ is the ambient temperature, and the other terms have their usual meaning. In this equation the advective term for energy transport has been neglected based on Li' s determination and the specific heat and density in the thin oxide layer are taken as those of boron since the layer is of negligible thickness compared to the particle radius.

An important aspect of Li's modeling study is the proposed chemical reaction scheme and evaluated limiting physical processes which are considered to explain the oxidation process for boron. These chemical reactions are different for the ignition stage and combustion stages, where different processes dictate particle consumption.

During the ignition stage in a high temperature reactive ambient gas, the thin oxide layer coating on the particle liquefies quickly at relatively low (particle) temperature. Initially while the particle is cold, only heat absorbed from the surroundings by convection and radiation increases the particle temperature. As the particle heats and reaches a high enough temperature, evaporation proceeds at the gas surface of the oxide layer by

$$B_2O_3(l) \rightleftharpoons B_2O_3(g) \qquad + Q_1 \qquad [I]$$

which is considered to be in equilibrium, and where Q_1 = - 87.6 kcal/mol. The removal rate of $B_2O_3(l)$ by vaporization, ω_1, is determined by the balance between the process of evaporation and gas-phase diffusion of the vapor away from the surface. Li considers that process [I] may be controlled by gas-phase diffusion of the vapor in the absence of bulk gas motion, and derives expression Eq. (4.16) for ω_1,

$$\omega_1 = \frac{\alpha_1\,\nu_1\,p_{e1}}{1 + \left[\dfrac{\alpha_1\,\nu_1}{\dfrac{D_g}{R_u T_p d_p}}\right]}, \qquad (4.16)$$

where α_1 is the evaporation coefficient of $B_2O_3(l)$, ν_1 is the Hertz-Knudsen factor, T_p is the particle temperature (assumed uniform), R_u is the universal gas constant, D_g is the diffusivity of $B_2O_3(g)$, and p_{e1} is the equilibrium vapor pressure of B_2O_3. The variables are discussed fully in Ref. (7) and their values are tabulated in Table 4.1 below.

The model considers the possibility for slow oxidation[9] during the ignition stage while the particle temperature is still low. The reaction is between dissolved oxygen, which has diffused inward through the liquid layer toward the boron/$B_2O_3(l)$ interface, with the boron there;

$$B(s) + \tfrac{3}{4} O_2(g) \longrightarrow \tfrac{1}{2} B_2O_3(l) \quad + Q_{3l} \qquad [III\text{-}l]$$

where Q_{3l} = 150 kcal/mol. The rate of this reaction is ω_{3l} which is assumed to be controlled by diffusion of O_2 through the oxide layer under the assumptions that (i) O_2 reaction with boron at the substrate interface is infinitely fast and (ii) that equilibrium absorption of O_2 occurs at the $B_2O_3(l)$-gas interface. The rate expression is given by

$$\omega_{3l} = \frac{k_{3l} D_{3l} p_{O_2}}{\theta}, \qquad (4.17)$$

where k_{3l} is an effective distribution coefficient related to the amount of absorbed O_2 to that in the gas-phase, D_{3l} is the diffusion coefficient of absorbed O_2 within the liquid oxide layer, p_{O_2} is the oxygen partial pressure in the gas-phase, and θ is the instantaneous oxide layer thickness. This low temperature oxidation process is thought to be responsible for continued slow oxidation of particles in their oxide layer in the presence of a continuous external energy source, where the particle is typically in an isothermal state which can last for many hours. In high temperature reactive media, reaction [III-l] is only relevant very early during the ignition process while the particle temperature is still low. However, this mechanism allows for growth of the oxide layer thickness during particle heat-up prior to oxide layer gasification at higher temperatures. This thickening will be shown to be important for the hpcc experimental conditions where O_2 partial pressures are very high.

When the heating particles reach sufficient temperature, defined as the cutoff temperature T_{cut} by Li, fast boron oxidation and oxide layer gasification can occur. When conditions are favorable boron will readily dissolve in the oxide layer and be transported outward to the $B_2O_3(l)$/gas interface where exothermic reactions help heat the particle faster. This stage is of interest to the high temperature ignition in this study where the relevant timescales for the entire ignition process are on the order of a few milliseconds. The value of T_{cut} varies with partial pressure of O_2 between 1650 and 1820 K, and can be fit by equation (4.18),

$$T_{cut} = 1654 + 0.91\, p_{O_2} + 0.31\, p_{O_2}^2 \text{ K} \qquad 1 \le p_{O_2} \le 20 \text{ atm.} \qquad (4.18)$$

Li theorizes that the value of T_{cut} levels off at high oxygen partial pressures where excessive oxygen absorption disrupts the vitreous structure of the oxide layer. The maximum value of T_{cut} = 1850 K has been used in the calculations here.

For $T_p > T_{cut}$, oxidation in dry gas environments during the ignition stage is considered to proceed by B(s) dissolving in the liquid boron oxide layer forming a vitreous complex BO·BO·BO followed by net

diffusion of ·BO units outward to the liquid/gas interface. There the ·BO units react with dissolved oxygen to produce boron suboxides via exothermic reactions. The series of steps converting dissolved boron into products are considered to consist of oxygen absorption and the reaction $BO(d) + O_2(g) \rightarrow BO_2(a) + O(a)$, the slowest step, followed by $BO_2(a) + BO(d) \rightarrow B_2O_3(l)$ and $O(a) + BO(d) \rightarrow BO_2(g)$, where the last step liberates boron into the gas phase and is the most energetic.† Summing over the elementary reaction steps, the global step Rx. (III) results:

$$B(s) + O_2(g) \rightarrow BO_2(g) + Q_3 \qquad \text{[III]}$$

where the reaction rate is ω_3 and $Q_3 = 68 \pm 2$ kcal/mol. The entire process consists of chemical oxidation preceded by $BO(d)$ diffusion across the liquid oxide layer, and in the determination of the overall rate ω_3 the two processes are considered as series resistances, giving

$$\omega_3 = \frac{\alpha_3 \nu_3 p_{O_2} X_l}{1 + \left[\dfrac{\alpha_3 \nu_3 p_{O_2} X_l}{\dfrac{n_1 X_l D_l}{\theta}} \right]}. \qquad (4.19)$$

The limiting step is considered to be the dissolved BO-diffusion process which is much slower than gas phase diffusion of O_2 to the surface or $BO_2(g)$ diffusion away into the ambient gas. In Eq (4.19), α_3 is the reaction probability of an O_2 molecule striking a $BO(d)$ molecule at the liquid surface, ν_3 is the Hertz-Knudsen factor for O_2, p_{O_2} is the partial pressure of O_2 in the gas, n_1 the number density of $B_2O_3(l)$ approximated by $\rho_l / W_{B_2O_3}$, X_l is the equilibrium mole fraction of $BO(d)$ at the surface chosen to provide consistency with Li's observed ignition data,[7] and D_l is the diffusion coefficient of $BO(d)$ in the liquid layer. The individual expressions are given in Table 4.1.

For ignition in hot gases containing water vapor, wet-gas ignition acceleration is considered to include the exothermic water vapor reaction with dissolved BO at the $B_2O_3(l)$-gas interface, $BO(d) + H_2O(g) \rightarrow HBO(a) + OH(a)$, which is taken as the rate controlling step at the gas surface. This slow step is combined with absorbed complex reactions, $HBO(a) \rightarrow BO(d) + H(a)$, $H(a) + O_2(g) \rightarrow OH(a) + O(a)$, and $O(a) + H_2O(g) \rightarrow 2\ OH(a)$, and the desorption step $OH(a) + BO(d) \rightarrow HOBO(g)$, plus the reactive dissolution equilibrium at the boron-$B_2O_3(l)$ interface by $B(s) + B_2O_3(l) \rightleftarrows 3\ BO(d)$. The sum of the individual steps gives the global reaction

$$\tfrac{4}{3} B(s) + \tfrac{4}{3} B_2O_3(l) + 2\ H_2O(g) + O_2(g) \rightarrow 4\ HOBO(g) + Q_4 \qquad \text{[IV]}$$

where the overall rate for the global step is ω_4 and $Q_4 = 21$ kcal/mol. The two key rate limiting processes, are the reaction step $BO(d) + H_2O(g)$ and the liquid-phase diffusion of $BO(d)$, which are

† Here (a) stands for an absorbed species from the gas phase, and (d) for a dissolved species.

again considered as series resistances to the oxidation of boron atoms. The overall rate ω_4 is then given by Eq. (4.20)

$$\omega_4 = \frac{\alpha_4 \nu_4 p_{H2O} X_l}{1 + \left[\frac{\alpha_4 \nu_4 p_{H2O} X_l}{\frac{n_1 X_l D_l}{\theta}} \right]} \tag{4.20}$$

where p_{H2O} is the partial pressure of H_2O in the gas phase at the surface, ν_4 is Hertz-Knudsen factor for H_2O, α_4 is the reaction probability for $H_2O(g)$ attack on $BO(d)$, and θ is the oxide layer thickness with the other variables already mentioned.

The system of equations for the oxide layer thickness and particle temperature are integrated from the initial $d_{p,0}$, θ_0, $T_{p,0}$ for the specified gas mixtures (p_{O2}, p_{H2O}) at T_∞ and p_∞ to a final state. The Li model considers only the low temperature slow-oxidation process Rx. [III-*l*] during the heat-up period while particle temperatures are below T_{cut}, where Eq. (4.21) and (4.22) with only $\omega_{3l} \neq 0$ are:

$$\frac{d\theta}{dt} = \frac{1}{2} \frac{\omega_{3l}}{n_1} \tag{4.21}$$

$$\frac{dT_p}{dt} = \frac{[Q_{3l}\, \omega_{3l} - \frac{k_g}{d_p} Nu_p\, (T_p - T_\infty) - \varepsilon\sigma(T_p^4 - T_\infty^4)]}{\frac{1}{6} \rho_B c_{p\,B} d_p}. \tag{4.22}$$

Above the cutoff temperature, steps Rx. (I), (III), and (IV) are considered and Rx. (III-l) is neglected, with $\omega_{3l} \to 0$ and ω_1, ω_3, and $\omega_4 \neq 0$, and the change in the oxide layer thickness given by Eq. (4.14) is written explicitly as

$$\frac{d\theta}{dt} = -\frac{\omega_1 + \frac{4}{3}\omega_4}{n_1} \tag{4.23}$$

and Eq. (4.15) becomes explicitly

$$\frac{dT_p}{dt} = \frac{[Q_4\, \omega_4 + Q_3\, \omega_3 + Q_1\, \omega_1 - \frac{k_g}{d_p} Nu_p\, (T_p - T_\infty) - \varepsilon\sigma(T_p^4 - T_\infty^4)]}{\frac{1}{6} \rho_B c_{p\,B} d_p}. \tag{4.24}$$

Equations (4.21) and (4.22) for the low temperature ignition-stage and (4.23) and (4.24) for the high temperature ignition-stage are integrated numerically along with the kinetic equations (4.3) and (4.4) up to the instant of particle ignition. In this study ignition is defined as the instant when the oxide layer thickness goes to zero.

Li further considers the ignition stage for boron particles to include, beyond just the time to remove the oxide layer, the time for particles to heat up to the melting temperature of boron. After the

oxide layer is removed, "clean" surface oxidation takes place and the corresponding chemistry changes. The processes for clean surface oxidation although not included in the present formulation for calculating ignition time are included here for completeness.

During the "clean" surface oxidation stage, Li proposes the elementary step

$$B(s) + \tfrac{1}{2}\, O_2(g) \longrightarrow \tfrac{1}{2}\, B_2O_2(g) + Q_5 \qquad [V]$$

while particle temperatures limit oxidation to heterogeneous processes, for which Q_5 = 51 kcal/mol. Allowance is made for gas-phase O_2-diffusion to control the overall rate ω_5 leading to the rate expression Eq. (4.25),

$$\omega_5 = \frac{k\, p_{O_2}}{1 + \left[\dfrac{k\, R_u T_p \beta d_p}{D}\right]}. \qquad (4.25)$$

In Eq. (4.25), k is the temperature dependent surface reaction rate constant (Eq. 4.26), β = 1/2 is the stoichiometric coefficient for oxygen in Rx. [V], D is the effective diffusion coefficient of $O_2(g)$, and the other variables are already described. The surface reaction rate constant was constructed by Li from low temperature data extrapolated to fit with high temperature rate determined as part of his study[8] and is given by

$$\begin{aligned} k &= \frac{1.57\, 10^8}{\sqrt{T_p}} \exp(-32500/T_p) && 1600 < T_p \le 1750 \text{ K}, \\ &= \frac{31.5}{\sqrt{T_p}} \exp(-5630/T_p) && 1750 < T_p \le 2400 \text{ K}, \\ &= 0.0625 \pm 0.0125 \quad \text{mol/cm}^2\text{-sec-atm} && T_p > 2400 \text{ K}. \end{aligned} \qquad (4.26)$$

The equation for the decrease in the particle diameter and the rising temperature become

$$\frac{1}{2}\frac{dd_p}{dt} = -\frac{\omega_5 W_B}{\rho_B} \qquad (4.27)$$

$$\frac{dT_p}{dt} = \frac{[Q_5\, \omega_5 - \frac{k_g}{d_p} Nu_p\, (T_p - T_\infty) - \varepsilon\sigma(T_p^4 - T_\infty^4)]}{\frac{1}{6}\rho_B c_{p\,B} d_p} \qquad (4.28)$$

In the absence of convective effects $Nu_p \rightarrow 2$ and the energy equations (4.22), (4.24), and (4.28) reduce to the forms given in the references.

The Li and Williams model for combustion neglects the particle melting time and does not consider high temperature vapor phase burn. Both processes are important for the particle sizes tested in this study even though they were shown negligible for the particles which Li analyzed. Also vapor phase burn may occur under some conditions based on thermochemical calculations which are supported

by more detailed modeling.[13] Inclusion of vapor phase burn will require an additional physiochemical pathway for gasification of the liquid boron droplet. No effort has been made in the present study to extend the Li and Williams formulation to include these effects although this is warranted for complete modeling of the particle combustion stage. The Li and Williams model without account for vapor phase burn over-predicts combustion times for the present set of experiments and results are therefore not included here.

Implicit in the present formulation which uses a modified form of the Li and Williams model is the neglect of convective forces on chemical speciation near the particle, on distortion of the oxide-layer, and on distortion the diffusion envelope around the particle. The relative motion of the particles with respect to the ambient gases will distort the envelope around the particles and disturb the radial symmetry in the gas phase. The liquid oxide layer will likely also be effected. Inclusion of such effects would greatly increase the complexity of the problem as would consideration of non-spherical particles. It is not the intent of this study to develop a detailed model but rather to use simple models to help explain the observations in the experiments. It was judged based on preliminary calculations and later verified (as will be shown below) that particle heating is in general 85 to 90% of ignition delay. Under such conditions the major influence of relative motion is to increased particle heating rates.

The coupled system of equations is coded in FORTRAN[76] and integrated using the Gear-based integrator routine LSODE[77] up to the instant when the oxide layer thickness goes to zero and ignition occurs. Backward differencing is employed in the discretization and the integration routine has full control over adjusting the timestep for each iteration. Ambient gas properties were calculated as mentioned previously and curve fits for the variation with temperature are employed in the code. Gas phase species product distributions are assumed fixed at their equilibrium calculated values. The gas thermal conductivity and other transport and thermal properties are evaluated at the geometric mean of the particle and gas temperatures, given by $\sqrt{T_p T_\infty}$. The numerous physical variables required for solution of the system of equations and specification of the rate parameters are listed in Table 4.1.

Table 4.1: Variables and expressions used in the Li and Williams model for boron particle ignition calculations, from Refs. (7,9).

Parameter	Value	Units
ρ_B	2.33	gm/cm^3
$c_{p,B}$	$0.507 + 7.0\ 10^{-5}*T$	cal/gm-K
k_g	given in Fig. 4.5	cal/cm-sec-K
ε	0.8	-
σ	$1.355\ 10^{-14}$	cal/cm^2-sec-K^4
α_1	0.03	-
ν_1	$5.3/T^{0.5}$	mol/cm^2-sec-atm
p_{e1}	$\exp(\Delta S^0/R_u)\ \exp(-\Delta H^0/R_u/T)$	atm
ΔS^0	$51.61 - 1.094\ 10^{-2}*T + 2.013\ 10^{-6}*T^2$	cal/mol-K
ΔH^0	$103672 - 9.36*T + 8.36\ 10^{-4}*T^2$	cal/mol
D_g/R_uT	$2.36\ 10^{-7}\ (T*T_\infty)^{0.25}\ /p_c$	mol/cm^2-sec-atm
$k_{3l}\ D_{3l}$	$2.42\ 10^{-3}\ \exp(-34000/T_\infty)$	mol/cm-sec-atm
α_3	0.035	-
ν_3	$7.84/T^{0.5}$	mol/cm^2-sec-atm
X_l	$2.32\ 10^{-2}\ (1 - \exp(35000/T-35000/T_{cut}))$	-
D_l	$5.11\ 10^{-5}\ \exp(-7500/T)$	cm^2/sec
n_1	1.85/69.62	-
α_4	$0.40\ \exp(-5500/T)$	-
ν_4	$10.54/T^{0.5}$	mol/cm^2-sec-atm

4.3 Description of Princeton/Aerodyne Model

A more detailed boron particle chemical reaction model has been developed by the Princeton/Aerodyne Group.[13,14,36] The Princeton/Aerodyne model considers the ignition and combustion stages of an idealized spherical boron particle initially coated by a thin oxide layer. The formulation involves solving the time dependent one dimensional (radial) species conservation and energy equations, where heat exchange is by conduction, radiation, and species transport. The formulation considers detailed gas-phase chemistry, heterogeneous chemistry at the particle/liquid oxide and liquid oxide/gas interfaces, and multi-species condensed-phase and gas-phase transport during the oxide-layer gasification stage as shown schematically in Fig. 4.10, and detailed gas-phase chemistry and diffusion and heterogeneous surface reactions during the "clean" particle vigorous combustion stage. The sophisticated chemical reaction mechanism includes B/H/O/C/F/N chemistry

between 36 gas-phase species involved in 392 elementary gas-phase reactions, 75 surface reactions during the ignition stage, and 63 surface reactions during particle combustion. This model was most recently updated to include nitrogen[13] and fluorine[38-40] species reactions with boron in order to investigate boron particle combustion in hydrocarbon fuel and fluorinated propellant product gases. In a recent paper, Zhou, et al.[13] describe the latest model version and modeling analyses for the data presented here.

The numerical model solution technique involves discretizing the classical species and energy conservation equations and incorporating multi-phase diffusion, complex chemistry, and heterogeneous processes. The governing equations are time dependent, one dimensional (in radius), partial differential equations which are discretized by the Finite Element Method employing the Galerkin formulation and integrated over time via backward differentiation by an implicit Gear algorithm. The free motion of the propagating flame zone surrounding the particle is handled using a moving node technique. The separate gas and liquid phase dynamics are solved for at each timestep using a time splitting technique where the two are coupled by the $B_2O_3(l)$/gas interface boundary conditions. Further details of the mathematical formulation can be found in Ref. (78).

A subset of the chemical reaction formalism is described here. Details concerning handling of oxide layer solubilities and liquid-phase diffusion are given in Ref. (13). Gas-phase chemistry consists

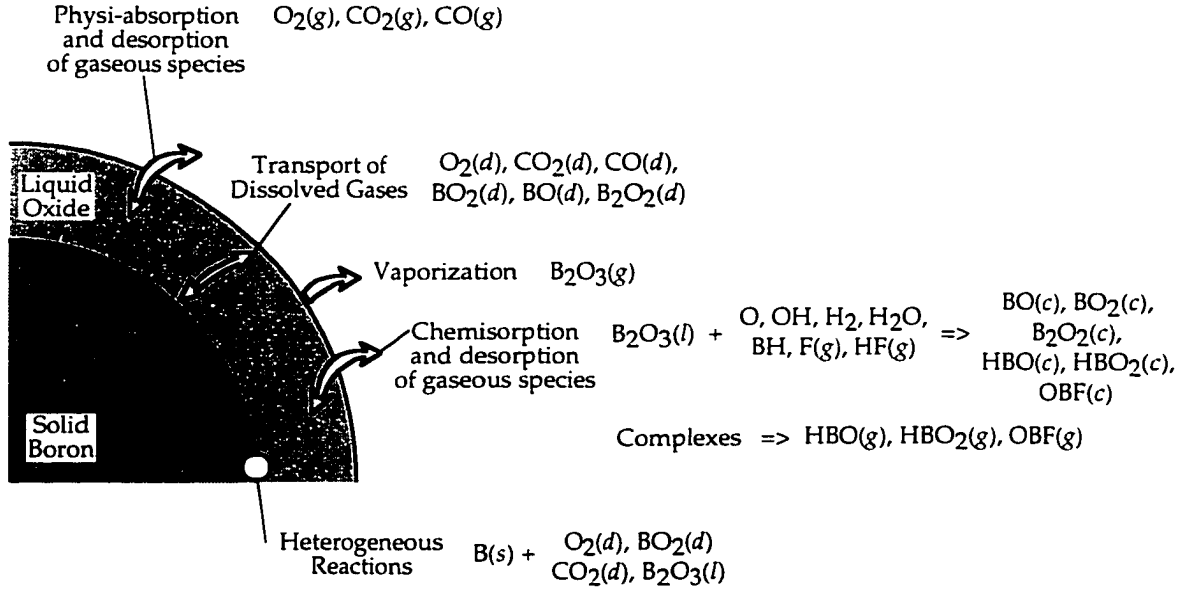

Fig. 4.10: Schematic showing detailed chemical and physical processes considered by the Princeton/Aerodyne model during boron particle ignition. The relative oxide layer thickness has been exaggerated for clarity.

of detailed elementary chemical reactions between typical hydrocarbon combustion products, nitrogen and fluorine compounds, and gasified boron oxides and oxyhydrides, boron nitrides, and boron fluorides and oxyfluorides. The gas-phase chemical reaction sub-mechanisms can be found in Refs. (33), (34), (38), and (79).

Detailed heterogeneous chemistry during the oxide layer removal stage[35,39] is formulated in terms of the gas phase species attaching to the surface, reacting, and detaching boron suboxides into the gas phase. These processes consist of physisorption and desorption, chemisorption and chemidesorption reactions, and evaporation. Viable chemical reactions which have been considered are those whose heats of reaction are comparable to the ~100 kcal/mol required for $B_2O_3(l)$ evaporation and which involve reasonable bond rearrangements. The viable overall reactions in hydrocarbon environments, for example, include $B_2O_3(l)$ -> $B_2O_3(g)$ (evaporation), $B_2O_3(l) + O(g)$ -> $BO_2(g) + BO_2(g)$, $B_2O_3(l) + OH(g)$ -> $HOBO(g) + BO_2(g)$, and $B_2O_3(l) + H_2O(g)$ -> $HOBO(g) + HOBO(g)$.

Global reactions of this form are further split into chemisorption steps and desorption steps. The general mechanism for chemisorption, the attachment of gas-phase species to the liquid oxide layer by chemical bonding, is viewed schematically as

$$\overset{O}{\bullet} > B - O - B < \overset{\bullet}{O} + XY \longrightarrow \overset{O}{\bullet} > B - O\overline{X\text{-}BY} - O, \qquad [VI]$$

where XY is a typical gas phase molecule (e.g., OH), "•" represents an unpaired electron and "-" a chemical bond, and $\overset{O}{\bullet}$>B-O$\overline{X\text{-}BY}$-O represents the surface-bound complex where the $O\overline{X\text{-}BY}$ is a loosely bound ring (X still bonded to Y). Chemisorption can be followed by a series of surface bond rearrangements and then desorption. Typically the X-Y and O-B bonds break and yield two surface-bound species:

$$\overset{O}{\bullet} > B - O - X \quad \text{and} \quad \overset{O}{\bullet} > B - Y$$

Desorption into the gas phase is considered to proceed by both first and second order processes through the breaking of a B-O bond and the formation of a double bond. First order processes are simply surface self-decomposition and are represented schematically as

$$\overset{O}{\bullet} > B - Z \longrightarrow O = B - Z \qquad [VII]$$

where O=B-Z is a gas phase species (e.g., OBH or OBF) and Z is either X or Y. Second order reactions are of the type

$$\overset{O}{\bullet} > B - X + \overset{O}{\bullet} > B - Y \longrightarrow B_2O_3(l) + XY. \qquad [VIII]$$

A subset of important surface absorption and desorption reactions is given in Table 4.2 along with proposed rate parameters. Second order surface reactions at the boron oxide/gas interface are further

detailed in Ref. (39). Chemical reaction rate constants are ascribed to each individual elementary reaction. The absorption rate $r_a(T)$ is given by the Langmuir equation

$$r_a(T) = k_a(T)\,(1-\Theta)\,[Z(g)] \tag{4.29}$$

where $[Z(g)]$ is the concentration of the gas phase reaction partner and Θ is the fraction of the surface covered by absorbate. Chemisorption rates are formulated through the rate constant $k_a(T)$, where $k_a(T)$ is given by Eq. (4.30),

$$k_a(T) = k_0 \sqrt{T}\; s_0 \exp\,(-E_a/R_u T). \tag{4.30}$$

Here $k_0 \sqrt{T}$ is the number of molecules of mass m striking the surface per unit area per second and is given by Eq. (4.31), s_0 is the sticking probability, E_a is the activation energy, and k_B is Boltzmann's constant.

$$k_0 \sqrt{T} = \left[\frac{k_B T}{2\pi m}\right]^{1/2} \tag{4.31}$$

The term on the RHS is one-fourth the average (mean) molecular speed.

The reaction rate constant for first order desorption reactions is given by Eq. (4.32)

$$k_1(T) = A_1\, T \exp\,(-E_1/R_u T) \tag{4.32}$$

in which $k_1(T)$ is the first order desorption rate constant and $(A_1\, T)$ the desorption coefficient, given approximately by $k_B T/h$, the transition state frequency factor. Second order desorption processes representing gasification are reactions between two surface complexes. These are essentially the reverse reactions of the chemisorption reactions being considered. The rate constant is expressed as

$$k_2(T) = A_2 \exp\,(-E_2/R_u T). \tag{4.33}$$

Rate constants are estimated by a variety of methods as described in the references and in a few cases are based on measurements. Calculation of reverse rate constants are by means of the equilibrium constants K_{eq} and the forward rate constants. Thermodynamic properties for the surface-bound complexes are required to perform the kinetic calculations and these are estimated based on a variety of methods and similarities to other non-boron species. The evaporation process is also expressed as a finite-rate process instead of treating the phase equilibrium balance.

Table 4.2: Elementary chemisorption and desorption reactions and rates parameters for the oxide layer removal stage.

#	Reactions	ΔH_{298} [kcal/mol]	k_0 [cm/sec]	s_0	E_a [kcal/mol]
	Chemisorption Reactions				
1	$B_2O_3(l) + O(g)$ —> $O_\bullet$>B-O + $O_\bullet$>B-O	-17.0	$920 \times T^{0.5}$	0.1	0.0
2	$B_2O_3(l) + OH(g)$ —> $O_\bullet$>B-OH + $O_\bullet$>B-O	-33.0	$892 \times T^{0.5}$	0.1	0.0
3	$B_2O_3(l) + H_2O(g)$ —> $O_\bullet$>B-OH + $O_\bullet$>B-OH	-32.0	$867 \times T^{0.5}$	0.05	10.0
4	$B_2O_3(l) + F(g)$ —> $O_\bullet$>B-F + $O_\bullet$>B-O	-50.0	$844 \times T^{0.5}$	0.1	0.0
5	$B_2O_3(l) + HF(g)$ —> $O_\bullet$>B-F + $O_\bullet$>B-OH	-32.0	$823 \times T^{0.5}$	0.05	10.0
6	$B_2O_3(l) + BF(g)$ —> $O_\bullet$>B-F + $O_\bullet$>B-BO	-59.0	$674 \times T^{0.5}$	0.01	30.0
		ΔH_{298} [kcal/mol]	A_1 [ps^{-1}]	-	E_1 [kcal/mol]
	First-Order Desorption Reactions				
7	$O_\bullet$>B-O —> $BO_2(g)$	55.6	$0.02 \times T$		55.6
8	$O_\bullet$>B-OH —> HOBO(g)	55.7	$0.02 \times T$		55.7
9	$O_\bullet$>B-OH —> OBF(g)	56.0	$0.02 \times T$		56.0
10	$O_\bullet$>B-F —> $B_2O_2(g)$	57.3	$0.02 \times T$		57.3
			A_2 [cm^2/comp lex-sec]		E_2 [kcal/mol]
	Second-Order Desorption Reactions				
11	$O_\bullet$>B-O + $O_\bullet$>B-O —> $B_2O_3(l)$ + O(g)		3.0×10^{-5}		5.0
12	$O_\bullet$>B-OH + $O_\bullet$>B-O —> $B_2O_3(l)$ + OH(g)		3.0×10^{-5}		5.0
13	$O_\bullet$>B-OH + $O_\bullet$>B-OH —> $B_2O_3(l)$ + H2O(g)		3.0×10^{-5}		10.0
14	$O_\bullet$>B-F + $O_\bullet$>B-O —> $B_2O_3(l)$ + F(g)		3.0×10^{-5}		5.0
15	$O_\bullet$>B-F + $O_\bullet$>B-OH —> $B_2O_3(l)$ + HF(g)		3.0×10^{-5}		10.0
16	$O_\bullet$>B-F + $O_\bullet$>B-BO —> $B_2O_3(l)$ + BF(g)		3.0×10^{-5}		10.0
			k_3		
	First-Order Absorption Reactions				
17	$BO_2(g)$ —> $O_\bullet$>B-O		Ref.(39)		
18	HOBO(g) —> $O_\bullet$>B-OH		Ref.(39)		
19	OBF(g) —> $O_\bullet$>B-F		Ref.(39)		
20	$B_2O_2(g)$ —> $O_\bullet$>B-BO		Ref.(39)		

During the combustion stage chemical reactions are considered to follow the general form

$$B(s,l) + Z_i(g) \rightarrow \text{boron gas-phase products.} \qquad [IX]$$

Again the overall step is broken down into absorption and desorption steps. Gas phase species are absorbed directly onto the "clean" boron surface and react to form surface complexes ("c") according to[36,40]

$$B(s) + X(g) \longrightarrow BX(c) \qquad [X]$$

where $X(g)$ is a general gas phase oxidant (e.g., OH, O_2, BO_2). Viable reactions are chosen to be energetically competitive with boron vaporization (~130 kcal/mol), be first order in the gas phase reactant, and produce viable gas phase species for the ambient conditions considered. Absorption is followed by desorption into the gas phase at high enough temperatures according to

$$BX(c) \longrightarrow BX(g) \qquad [XI]$$

where the gaseous BX can, for example, be BO_2, BF, or BN among others. In hydrocarbon combustion product environments viable gaseous boron species include BO, BO_2, HBO, HBO_2, B_2O_2 and B_2O_3.

A listing of important absorption and desorption steps and rate parameters is given in Table 4.3. The forward rate constant $k_f(T)$ is written as

$$k_f(T) = k_0 \sqrt{T}\, a(T) \qquad (4.34)$$

where $(k_0 \sqrt{T})$ is the collision frequency and $a(T)$ the surface reaction probability. This reaction probability is given by Eq. (4.35).

$$a(T) = a_0 \exp(-E_a / R_u T) \qquad (4.35)$$

All steps are considered reversible and the backward reaction rate constants $k_b(T)$ are calculated from the forward rates and the equilibrium constants, K_{eq}, as $k_b(T) = \text{fctn.}(K_{eq}, k_f)$. Desorption-step rate constants are expressed as

$$k_d(T) = A_d\, T \exp(-E_a / R_u T) \qquad (4.36)$$

in which the factor $(A_d\, T)$ is the desorption prefactor and is assumed to be equal to the transition-state frequency factor $k_B T/h$, and the activation energy E_a is set to the endothermic desorption enthalpy. The complete elementary step chemical reaction mechanism and rate constants for the reactions can be found in Refs. (36), (37), and (40) for generalized H/O/C/F/N-containing combustion environments.

Table 4.3: Elementary chemical reactions and rate parameters for the combustion stage.

#	Reactions	k_0 [cm/sec]	a_0	E_a [kcal/mol]	k_b
1	$B(s) + H(g) \rightleftarrows BH(c)$	3637	0.1	0.0	from K_{eq}
2	$B(s) + O(g) \rightleftarrows BO(c)$	909	0.8	0.0	from K_{eq}
3	$2B(s) + O_2(g) \rightleftarrows BO(c) + BO(g)$	634	0.001	1.0	from K_{eq}
4	$B(s) + O_2(g) \rightleftarrows BO_2(g)$	634	10^{-7}	0.0	from K_{eq}
5	$2B(s) + O_2(g) \rightleftarrows B_2O_2(g)$	634	0.064	1.0	from K_{eq}
6	$B(s) + OH(g) \rightleftarrows HBO(g)$	882	0.02	1.0	from K_{eq}
7	$2B(s) + OH(g) \rightleftarrows BH(c) + BO(g)$	882	0.02	1.0	from K_{eq}
8	$2B(s) + H_2O(g) \rightleftarrows BH(c) + HBO(g)$	857	0.006	8.0	from K_{eq}
9	$B(s) + BO_2(g) \rightleftarrows BO(c) + BO(g)$	556	0.001	4.5	from K_{eq}
10	$B(s) + BO_2(g) \rightleftarrows B_2O_2(g)$	556	0.005	5.0	from K_{eq}
11	$B(s) + B_2O_3(g) \rightleftarrows B_2O_2(g) + BO(g)$	436	0.87	0.0	from K_{eq}
12	$B(s) + HOBO(g) \rightleftarrows BO(c) + HBO(g)$	549	0.003	4.0	from K_{eq}
13	$2B(s) + HOBO(g) \rightleftarrows BH(c) + B_2O_2(g)$	549	0.003	4.0	from K_{eq}
14	$B(s) + CO_2(g) \rightleftarrows BO(c) + CO(g)$	548	0.001	4.5	from K_{eq}
15	$B(s) + F(g) \rightleftarrows BF(g)$	834	0.02	1.0	from K_{eq}
16	$2B(s) + HF(g) \rightleftarrows BH(c) + BF(g)$	813	0.006	10.0	from K_{eq}
17	$B(s) + BF_2(g) \rightleftarrows BF(g) + BF(g)$	521	0.004	3.0	from K_{eq}
18	$B(s) + BF_3(g) \rightleftarrows BF(g) + BF_2(g)$	442	0.004	3.0	from K_{eq}
19	$B(s) + OBF(g) \rightleftarrows BO(g) + BF(g)$	537	0.003	4.0	from K_{eq}
20	$BH(g) \rightleftarrows BH(c)$	1058	0.001	0.0	$0.2\,T \times \exp(\Delta H_{d,\#20}/R_uT)$
21	$BO(g) \rightleftarrows BO(c)$	702	0.001	0.0	$0.2\,T \times \exp(\Delta H_{d,\#21}/R_uT)$
22	$B(s) + N(g) \rightleftarrows BN(c)$	972	0.04	0.0	from K_{eq}
23	$B(s) + N_2O(g) \rightleftarrows BO(c) + N_2(g)$	548	0.2	0.0	from K_{eq}
24	$B(s) + N_2O(g) \rightleftarrows BN(c) + NO(g)$	548	0.04	0.0	from K_{eq}
25	$2B(s) + NO(g) \rightleftarrows BN(c) + BO(c)$	664	0.1	4.0	from K_{eq}
26	$B(s) + NO_2(g) \rightleftarrows BO(c) + NO(g)$	536	0.2	0.0	from K_{eq}
27	$B(s) + HNO(g) \rightleftarrows BH(c) + NO(g)$	653	0.05	0.0	from K_{eq}
28	$B(s) + HNO_2(g) \rightleftarrows BH(c) + NO_2(g)$	530	0.05	0.0	from K_{eq}
29	$B(s) + HNO_2(g) \rightleftarrows BN(c) + NO(g)$	530	0.002	4.0	from K_{eq}
30	$BN(g) \rightleftarrows BN(c)$	657	0.001	0.0	$0.2\,T \times \exp(\Delta H_{d,\#30}/R_uT)$

The dominant physical and chemical processes which dictate small-particle oxide layer gasification and combustion depend on many variables including gas pressure, temperature, particle size, and the oxidizing environment. Completely generalized statements cannot be made but certain processes have been found to dominate during small particle ignition and combustion in hot ambient

gases, which is the primary concern for the experiments described in this work. At high ambient temperature where initially cold particles are suddenly introduced into the oxidizing atmosphere, particle heating is predominantly from the ambient gases. As particle temperatures rise, heating is accompanied by oxide layer removal where initial surface chemistry and gas-phase diffusion are the rate-controlling factors. Zhou, et al.[13] have found dissolving processes and second-order surface reactions to be of secondary importance. Oxide layer removal is typically a small portion of the total ignition time, less than 20% in the high pressure and high temperature experiments. Absorption steps are found to be rate controlling for most conditions above 1600 K where HOBO(*c*) desorption is the dominant gasification step. Fluorine compounds (HF) tend to assist with particle ignition, similarly to water vapor, by lowering the temperature where oxide layer gasification occurs compared to $B_2O_3(l)$ evaporation.

During combustion of small particles such as those used in the experiments, the gasification process is generally controlled both by diffusion of oxidizers to the surface and by surface reaction kinetics. Under kinetically controlled conditions, the dominant step is $O_2(g)$ absorption and the oxidation step

$$B(s) + B(s) + O_2(g) \rightleftarrows B_2O_2(g), \qquad [5]$$

but reactions with reactive radical species are also important at high gas temperatures. In oxygen-lean environments and under diffusion controlled conditions, reactions with boron suboxides which exist in super-equilibrium concentrations in narrow flame zones very near to the particle surface also play an important role. Combustion is predominantly by heterogeneous surface reactions, i.e., the absorption and desorption steps, dictated by the very high boiling point of boron (~4000 K at 1 atm). Burn rates in general decrease with increasing ambient temperature. Unlike during ignition, HF plays less of a role during the combustion stage in gases containing both O_2/HF gases. However the presence of large amounts of fluorinated compounds can shift the product speciation from B_2O_3/HBO_2 to OBF/BF_3, increasing the overall energy release and avoiding issues related to condensation losses.

4.4 Model Predictions

Measured trends at high pressure are compared to predictions from two boron particle ignition models. Measured ignition delays are modeled with the convective heating model based on the semi-global chemistry formulation of Li and Williams[9] and excellent agreement between predicted values and trends and measurements is obtained in several cases, see Table 4.4. The model does not predict the strong pressure effect on ignition delays nor the strong temperature dependence below ~2600 K. These

differences will receive special attention. The potential for reduced ignition delays with increased pressure is a significant finding in that it suggests much higher overall combustion efficiencies may be achieved by operating combustors at higher pressures. The excellent agreement for other trends will show that convective heating effects must be included in any analysis of the particle injection measurements. The combination of particle velocities from injection and high gas densities make convective heat transfer the dominant heating process during ignition. Delays are reduced ~50% compared to the static ignition case where heat transfer is limited to conduction and radiation.

Additional insight into competing and rate controlling processes is gained through modeling which is unavailable from the measurements. To this end further calculations are performed with the convective-heating modified model under similar ambient gas conditions but for the "conduction-only" case, to distinguish between heat transfer and chemical oxide layer removal processes. Predictions under these conditions are compared to additional modeling performed with the detailed chemistry Princeton/Aerodyne model which incorporates finite-rate elementary step chemistry and multi-species and multi-phase diffusional processes, but which does not include a convective heat transfer model. The comparison in this regard further elucidates competing physiochemical processes responsible for oxide layer removal. The two models are shown to agree in most respects for the "conduction-only" case, see Table 4.5, except as concerns oxide layer growth at high oxygen partial pressures.

Particle combustion dynamics are modeled with the detailed chemical model (Table 4.4) and show good overall agreement. By the time particle combustion occurs in the experiments, convective effects are greatly reduced. Predicted combustion times are generally long but show similar trends with

Table 4.4: Comparison of measured and predicted ignition delay times and combustion times; using the convective heating-modified model based on the Li and Williams formulation,[9] and the Princeton/Aerodyne Model.[13]

			Mole Fractions			Measured	Measured	L/W Model	P/A Model
Mixture	p_c	T_c	O_2	H_2O	X_{adtv}	t_{ign}	t_{comb}	t_{ign}	t_{comb}
	[atm]	[K]				[msec]	[msec]	[msec]	[msec]
A	78	2790	0.11	0.33	0	1.56 ± 0.32	2.50 ± 0.93	0.85	-
A	150	2830	0.11	0.34	0	0.99 ± 0.22	1.37 ± 0.60	0.77	1.53
B	37.5	2640	0.19	0.31	0	2.06 ± 0.42	3.16 ± 0.74	1.10	2.12
B	76	2630	0.20	0.30	0	-	-	1.04	2.06
B	145	2630	0.20	0.30	0	1.13 ± 0.21	2.66 ± 0.54	1.05	2.03
C	150	2610	0.11	0.30	0	0.85 ± 0.20	1.86 ± 0.32	0.94	1.91
D	150	2440	0.11	0.26	0	2.59 ± 0.28	4.95 ± 1.05	1.18	2.58
E	145	2620	0.16	0.31	0.048	0.95 ± 0.40	2.17 ± 0.60	1.02	-
F	34	2570	0.20	0.28	0.047	3.74 ± 0.49	2.99 ± 0.65	-	-
G	150	2630	0.05	0.29	0	1.25 ± 0.24	2.98 ± 0.38	0.82	2.05

varying pressure and temperature at high temperature. It will be shown that differences in magnitudes between measurements and predictions, which are at most a factor of two, may be linked to specification of the combustion time. A major difference is realized between model-predicted combustion times and measurements below ~2600 K. A tentative mechanism responsible for the marked increase in measured combustion times resulting from a drop in temperature from 2600 and 2400 K which is linked to boron nitride formation is identified. This mechanism is undergoing further study.

In all calculations discussed in detail below, ignition delay time is considered to include the time to heat the particles from the instant of injection and to remove the oxide layer ($\theta \rightarrow 0$) after which the onset of combustion leads to a rapid increase in particle luminosity. Zhou, et al.[13] prescribe ignition to occur when the initial oxide layer shrinks to 5% of its initial thickness. The initial oxide layer thickness θ_0 is assumed to be 0.15 μm for all calculations based on recommendations from Ref. (13), and it is found here that calculated times are insensitive to this choice of $\theta_0 \pm 50\%$. Combustion times from model predictions are defined differently from the definition used in practice; modeled t_{comb} include the time to completely consume the particles, posing a possible source of discrepancy. Only ignition delays are predicted with the convective heating model based on the Li and Williams formulation. Both ignition and combustion stages are modeled with Princeton/Aerodyne Model keeping in mind that absolute magnitudes should not be compared for ignition delays because convective heating effects are not included in that model. The corresponding measured and calculated times are compared in Table 4.4 and in subsequent figures, and are discussed below.

In the upcoming sections the comparisons between model predictions and measured trends are treated individually where first the effect of pressure on ignition delays and combustion times is examined. This is followed by the effects of ambient temperature, ambient oxygen concentrations, and initial particle size. No modeling of ignition-enhancement effects has been conducted but this chapter is concluded by indicating certain criteria which would be useful for proposed ignition-enhancers.

4.5 Comparison of Measured Trends to Model Predictions

4.5.1 Pressure Effect

Measured ignition delays decrease as $t_{ign} \sim p_c^{-0.5}$ between 37 and 156 atm. Numerous theoretical analyses[1,9,10] based on semi-global chemistry with empirical ignition parameters have historically been predicting ignition delays which are independent of pressure above 10 to 35 atm.

Figure 4.11 a shows calculated predictions of boron particle ignition delays at various pressures using several boron particle ignition models. The ambient gases are mixture B containing O_2/H_2O =

.20/.30 at 2630 K, for particles with $d_{p,0}$ = 23.7 μm. The Li and Williams model including convective heating ("conv" in the plots) and M. King's approach[1] both predict ignition delays to be essentially independent of pressure. Ignition delays predicted by the convective heating model are very close to measurements at 145 atm but are under-predicted at both 76 and 37.5 atm. The calculations of Zhou[13] using the more detailed Princeton/Aerodyne model, with the most recent proposed kinetics but neglecting convective heating ("cond" in the plots), match measured times at 37.5 atm but also predict no pressure effect. Inclusion of convective heat transfer in the detailed model would result in shorter calculated times and shift the curve downward.

Modeled combustion times obtained with the Princeton/Aerodyne Model[13] agree well with the measurements (see Fig. 4.11 b) within experimental uncertainties and both show t_{comb} decreasing as pressure is increased. Convective heating has less effect on combustion time predictions than on ignition delay predictions because the particles have slowed significantly by the time combustion occurs. However finite particle motion will distort the envelope of counter-diffusing product and ambient gas species surrounding the burning particles and this effect has not been included in the detailed analysis. Under moderately convective conditions for example, products are swept away from the particle surface and fresh oxidizers are continually brought to it.

Useful insight into the underlying processes is obtained by examining calculated time resolved particle histories. Time dependent profiles for the oxide layer thickness, particle velocity, non-dimensional flow parameters, and the convective heat transfer coefficient are shown in Fig. 4.12 a and b for mixture B at 145 atm. Initially upon injection at t = 0 in the plots the particles decelerate rapidly ($v_p/v_{p,0}$ curve) and are heated by convection (T_p and Nu_p curves). The oxide layer is predicted to melt after ~150 μsec while the particles are in motion. After ~500 μsec the oxide layer is seen to thicken rapidly as absorbed O_2 reacts with subsurface boron in the liquid layer before oxide removal ensues ($T_p < T_{cut}$). The growth of the layer at high oxygen partial pressures (p_{O_2} ≈ 29 atm) is nearly 40% of the original thickness. At ~870 μsec and 1850 K, oxide layer removal begins ($T_p > T_{cut}$) and is very fast, lasting only ~180 μsec. This removal time $t_{ox\text{-}rem.}$ is typically only 15% of the total ignition delay time defined by $t_{ign} \equiv t_{heat\text{-}up} + t_{ox\text{-}rem}$. The temperature of the particle at ignition is 2015 K which is below the melting temperature of boron. At this point clean surface oxidation begins and it is seen that the particle temperature increases rapidly up to the melting temperature of boron, where the calculations are stopped.

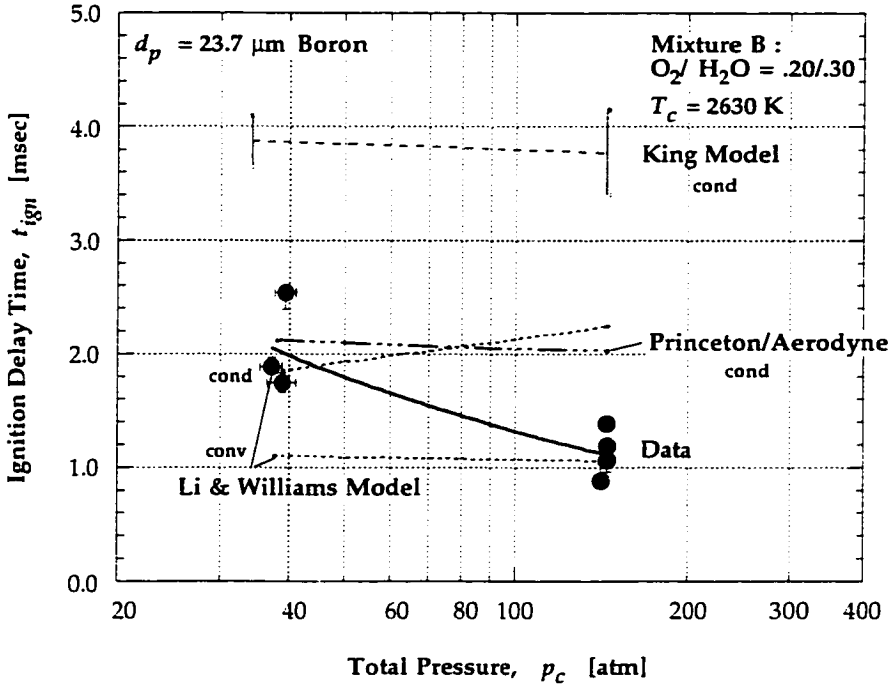

(a)

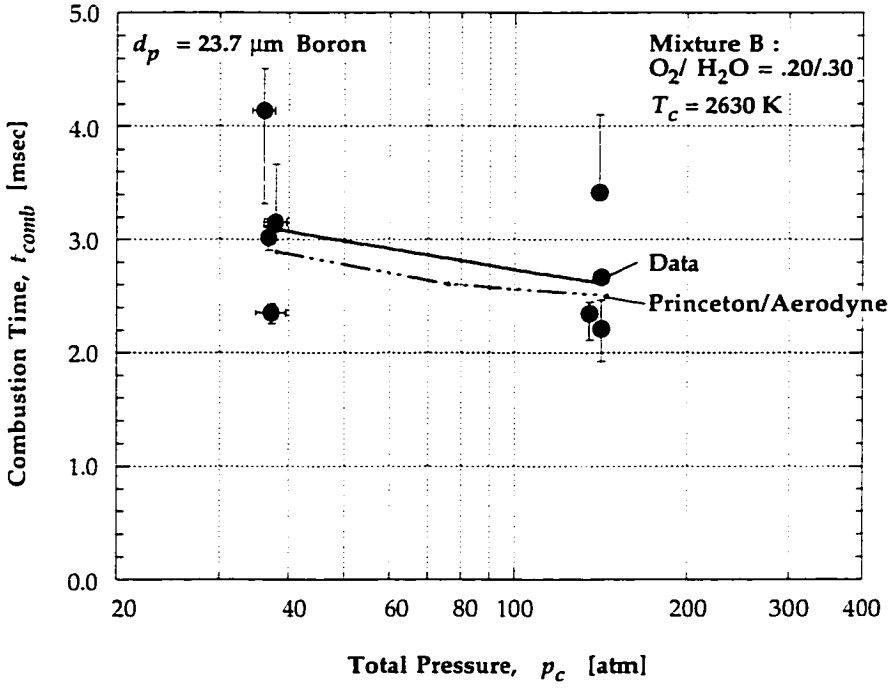

(b)

Fig. 4.11: Comparison of measured and various model-predicted ignition delays and combustion times as a function of pressure in O_2/H_2O = .20/.30, 2630 K. (a) For ignition delays, data show strong dependence on pressure which none of the models substantiates. (b) For combustion times, agreement is excellent within scatter of the data.

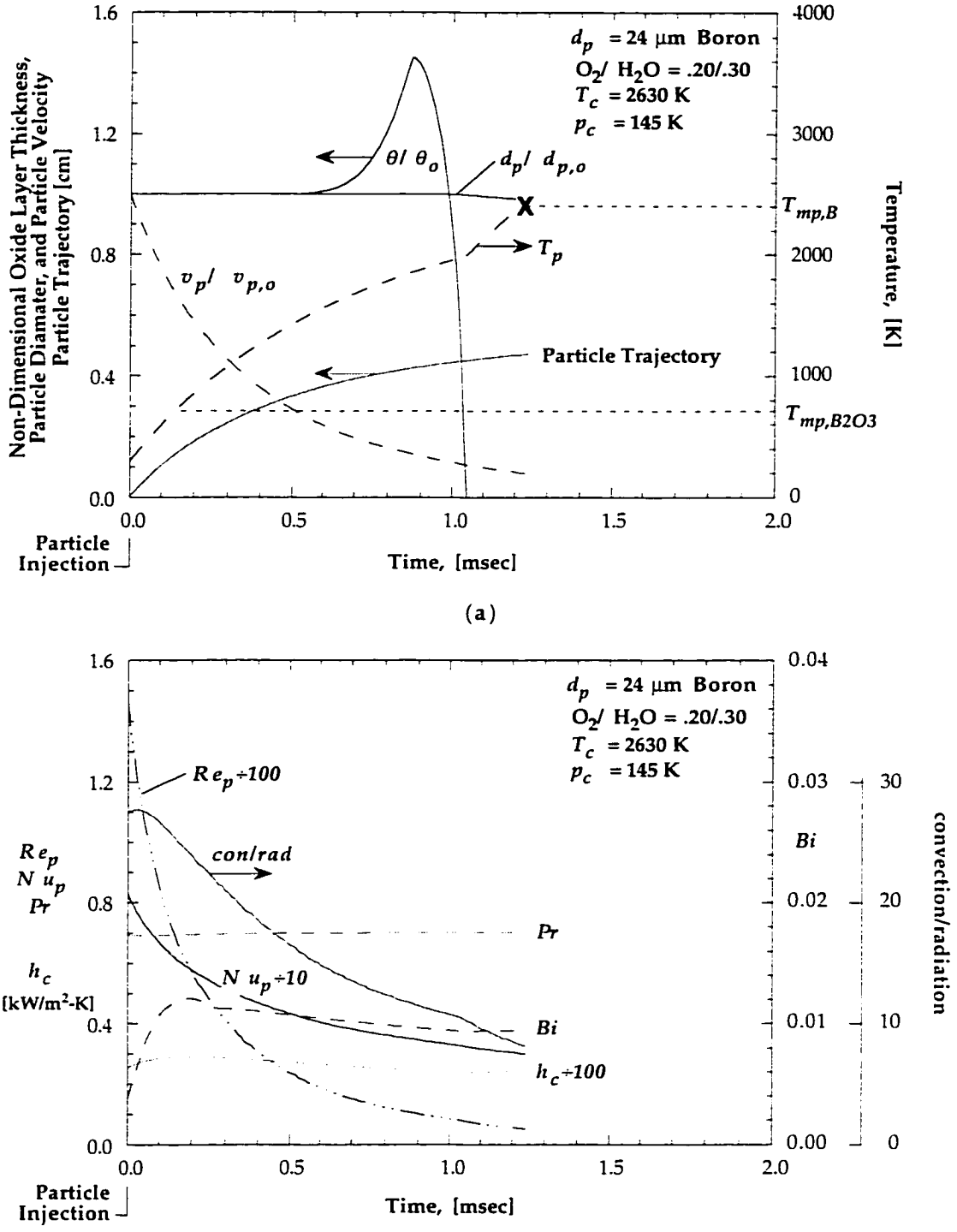

Fig. 4.12: Calculated time dependent profiles for particle ignition and early combustion stage up to particle melting, at 145 atm (high pressure) in O_2/H_2O = .20/.30 and 2630 K. (**a**) Shown are profiles of oxide layer thickness, particle diameter, particle velocity and trajectory into the dense ambient gases. In (**b**) are shown curves for the various non-dimensional flow properties, convective heat transfer coefficient, and ratio of convective heating to radiation.

During this entire sequence the particle travels through the dense ambient gases and penetrates ~5 to 6 mm into the ambient. Although not a great distance, this penetration depth places the particles far outside growing thermal layers above the injector as was shown in Section 3.5.1. The penetration depth depends heavily on ambient gas density through the particle drag and particles penetrate further into the gas at lower total pressures.

Figure 4.12 b shows that convective heating is significantly greater than heating by radiation from the surrounding gases. The condition that particle $Bi \leq 0.1$ is satisfied throughout the calculation supporting the use of lumped capacitance assumption. Although Re_p and Nu_p vary significantly with time (and temperature), the convective heat transfer coefficient $\bar{h}_c$ is fairly constant throughout the ignition stage, ~30 kW/m^2-K.

The picture at low pressure (37.5 atm) is displayed in Figs. 4.13 a and b and is similar in several respects to the high pressure condition. The most significant difference however is that the oxide layer does not grow appreciably for this low pressure case where the partial pressure of oxygen (p_{O_2}) is only ~7.5 atm. The smaller accumulation of the oxide layer is a result of quicker transition to oxide layer removal, due to the lower T_{cut} at lower p_{O_2} (see Eq. 4.18). Particle Nu_p and Re_p are significantly lower than at the high pressure condition.

A direct comparison of time resolved profiles of θ/θ_0, T_p, x_p and $\bar{h}_c$ for the two pressures is shown in Fig. 4.14. Particle heat-up is faster at high pressure but a higher temperature is required to begin oxide layer removal. As a result the calculations show that particle temperature at ignition is higher at higher pressure. Convective heating rates are higher at higher pressure and are always greater than particle heating by radiative means; recall that $\bar{h}_c \sim Nu_p \sim 2 + \text{const.} x Re_p^{0.55}$ where $Re_p \sim \rho_g$, the gas density. A significant finding then is that although convective heating rates increase as total pressure increases, this effect is counterbalanced to some extent by the significant thickening of the oxide layer increased p_{O_2}, which does not occur at lower pressure.

In Fig. 4.15 calculated time resolved profiles under typical experimental conditions are compared to the case considering only pure conduction, namely stagnant particles for which $Nu_p = 2$. For the stagnant particle case predicted heating times are longer than when convective effects are included, as is to be expected. The predicted ignition delay time would be more than twice as long as measured at high pressure if the particles were not in motion. More notable however is that *for the pure conduction case the model predicts that ignition delays increase with increased pressure*, as shown in Fig. 4.11 a by the curve labeled "cond", Li and Williams Model. Under stagnant particle heating conditions, the heat transfer is independent of pressure whereas T_{cut} increases as p_{O_2} increases.

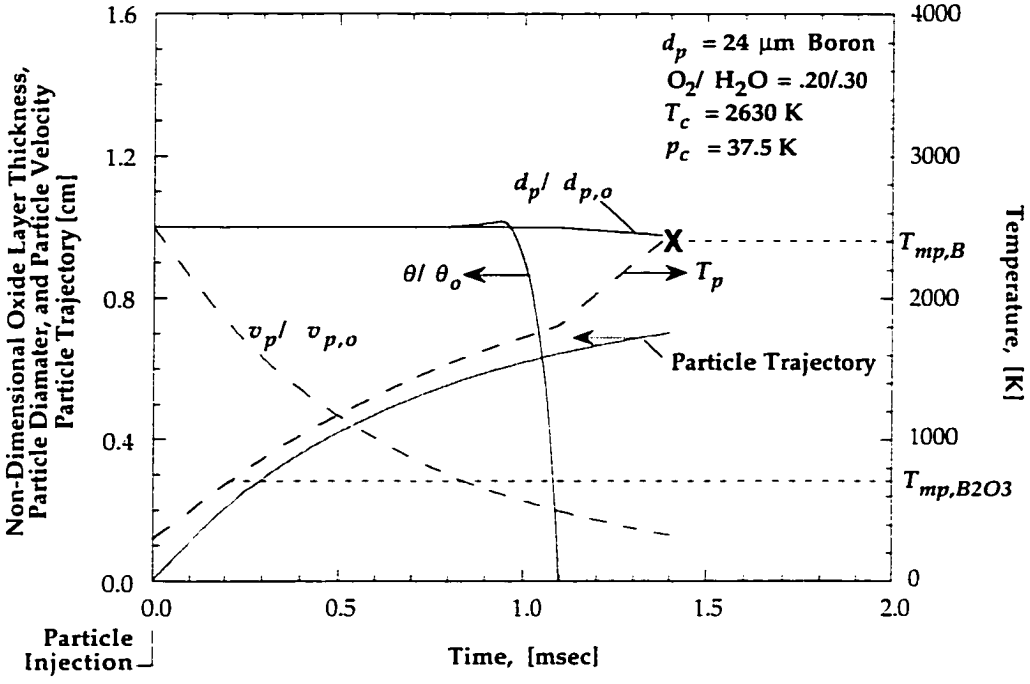

(a)

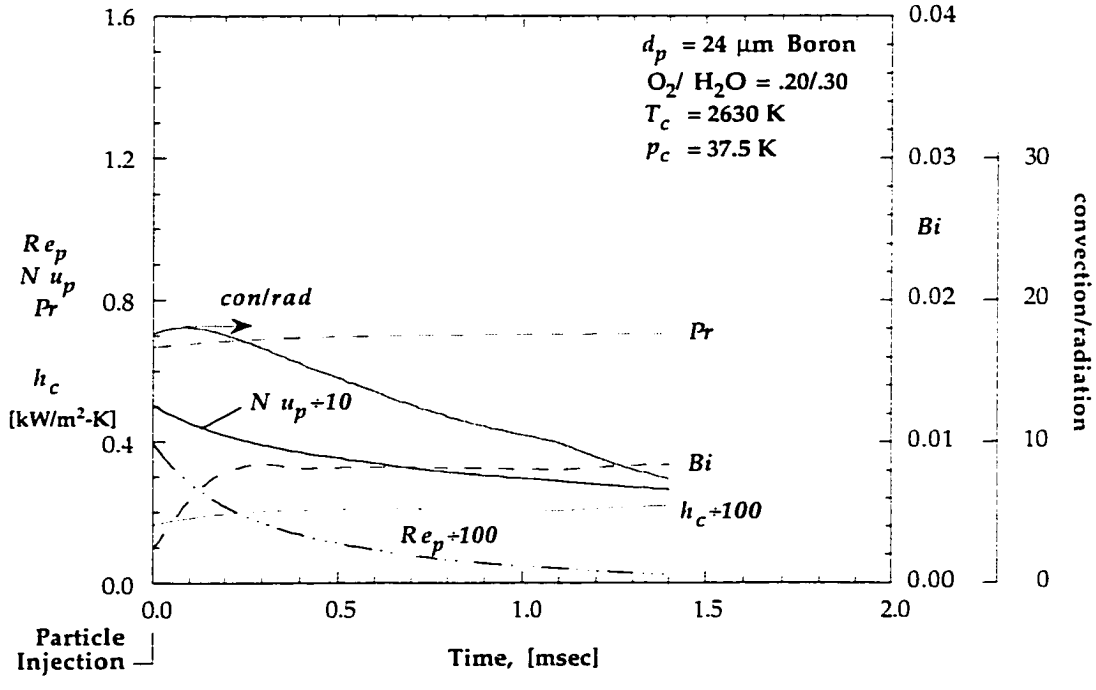

(b)

Fig. 4.13: Calculated time dependent profiles (**a**,**b**) for particle ignition and early combustion stage up to particle melting, at 37.5 atm (low pressure) in O_2/H_2O = .20/.30 and 2630 K.

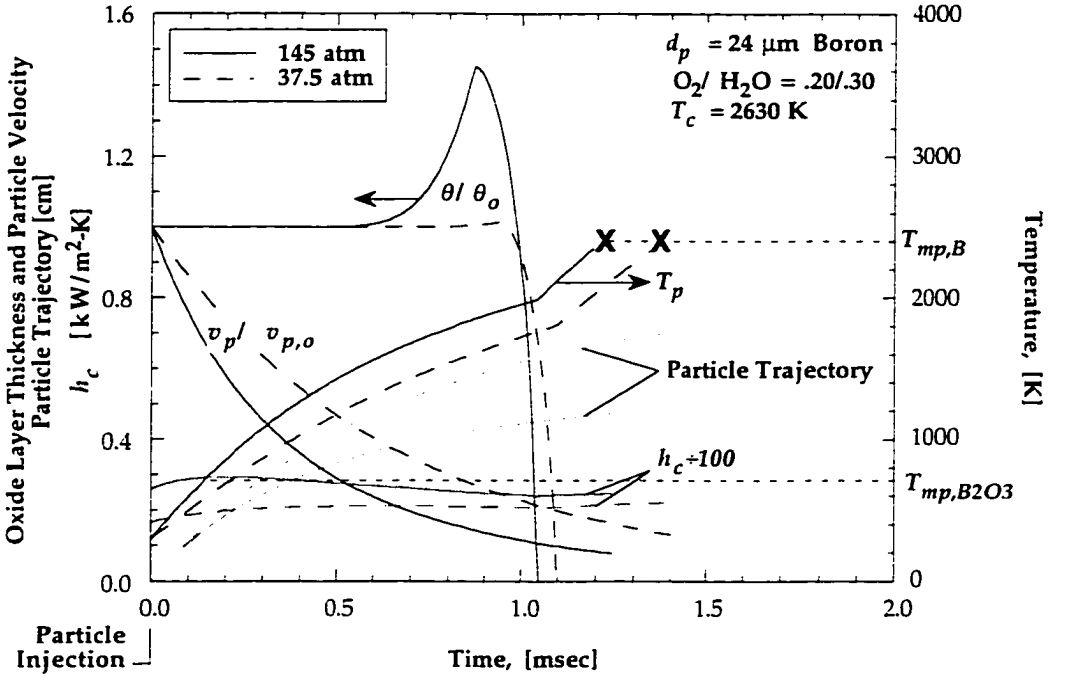

Figs. 4.14: Direct comparison of profiles for 37.5 and 145 atm cases. Convective heating is higher at higher pressure but this is counterbalanced by the buildup in the oxide layer which is negligible at low pressure.

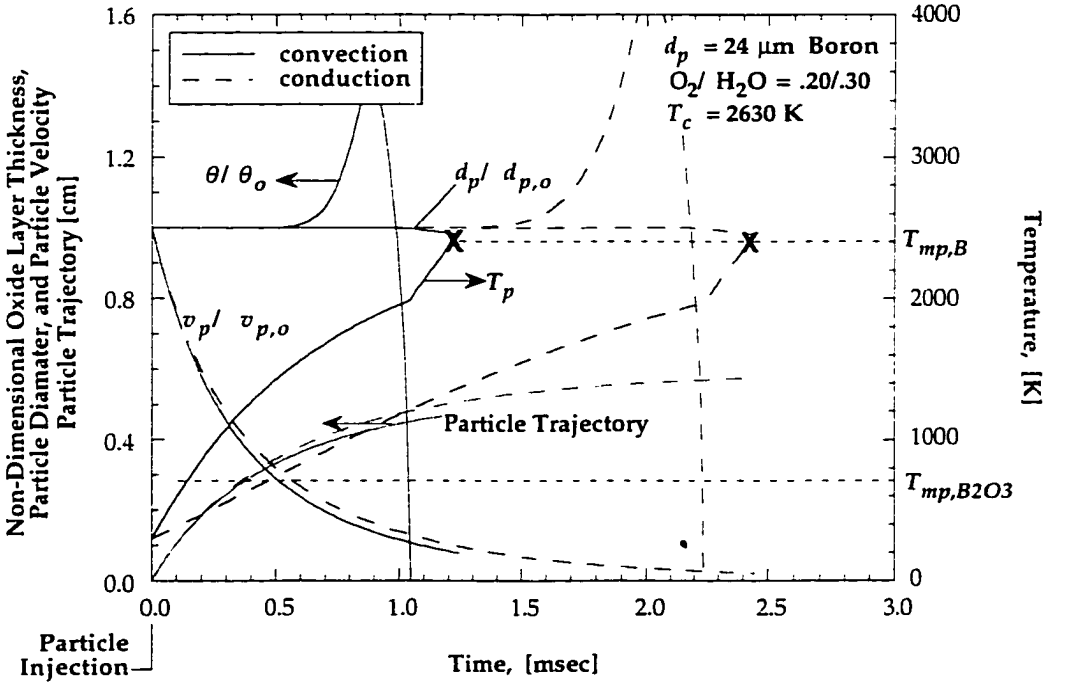

Figs. 4.15: Comparison of predicted ignition delay times including and excluding convective particle heating at 145 atm. Particle heating is greatly enhanced and thus ignition delays reduced by convective heat transfer from the surrounding gases.

Predictions for the "conduction-limited" case are further compared between each of the models in Fig. 4.11 a and values are tabulated in Table 4.5. Other than the slight predicted increase in ignition delays with pressure, the Li model predictions for the conduction-limited case agree remarkably well in magnitude with predictions using the detailed chemistry model. This is believed to be a result of very similar heating models employed in the two cases and the fact that ignition delays are predominantly particle heat-up times, during much of which time oxide layer removal chemistry is not important. The two models do disagree however as to the growth of the oxide layer. The mechanism for oxide layer thickening is not included in the detailed chemical model although further analysis[13] of competing processes has indicated that there is no tendency for this growth to occur under present conditions.

The preceding analysis indicates that although convective heating greatly enhances particle heating and that heating rates increase with pressure, that this effect alone is not responsible for the measured decrease in ignition delays with increased pressure. Further possibilities beyond purely particle heating effects which could account for the measured pressure dependence are particle surface chemistry and gas-phase diffusion during the oxide layer removal stage. According to the detailed model, for the case where surface chemistry controls oxide layer removal, the gasification rate is directly proportional to surface reaction rates which are linear functions of pressure through the gaseous absorbate concentrations. So for kinetically controlled gasification both particle heat-up and oxide gasification times are reduced as pressure is increased. For diffusive controlled systems the gasification rate is only weakly dependent on pressure through the term $\overline{\rho_g D_g}$. Predictions with the detailed model show that pressure effects ignition delays only negligibly through chemical reaction rates. The combined effects still cannot account for the measured results however, since none of the

Table 4.5: Comparison of various model-predicted ignition delay times for the case of stagnant particles, where convective heating reduces to pure conduction.

			Mole Fractions			L/W Model	P/A Model	King Model
Mixture	p_c	T_c	O_2	H_2O	X_{adtv}	t_{ign}	t_{ign}	t_{ign}
	[atm]	[K]				[msec]	[msec]	[msec]
A	78	2790	0.11	0.33	0	1.56	-	-
A	150	2830	0.11	0.34	0	1.65	1.53	-
B	37.5	2640	0.19	0.31	0	1.85	2.12	3.88
B	76	2630	0.20	0.30	0	1.98	2.06	-
B	145	2630	0.20	0.30	0	2.24	2.03	3.78
C	150	2610	0.11	0.30	0	2.02	1.91	-
D	150	2440	0.11	0.26	0	2.53	2.58	-
E	145	2620	0.16	0.31	0.048	2.16	-	-
G	150	2630	0.05	0.29	0	1.88	2.05	-

model variations predict as strong a pressure effect as is measured. All of the models were developed mainly for atmospheric pressure modeling.

During combustion competition occurs between oxidizer diffusion to the particle surface and consumption of the oxidizer by chemical reactions at the surface. Using the non-dimensional Damköhler number analysis of Li and Williams,[9] where *Da* is defined as the ratio of the O_2-diffusion timescale to the O_2-surface reaction timescale (only reaction with O_2 is considered), the ratio of competing rates is found to be proportional to the product of total pressure and initial particle diameter, $p_c\, d_{p,0}$. For the conditions in the pressure study *Da* are ~15, 30, and 60 for 24 μm particles at p_c = 37.5, 75, and 150 atm, suggesting that combustion times are controlled by oxidizer diffusion to the particle surface and should therefore be independent of pressure (and vary inversely with X_{O_2} and be proportional to $d_{p,0}^2$). This agrees with combustion times in 20% O_2 at ~2630 K, which vary weakly with pressure, but not with measurements in 11% O_2 at ~2830 K, where measured times vary as p_c^{-N}. When surface oxidation kinetics are rate controlling, $Da \ll 1$, then combustion times are expected to vary inversely with pressure.

Detailed-model analyses indicate that combustion is controlled by both gas-phase transport and surface chemistry so the pressure effect on combustion times is expected to be non-negligible. Analyses for kinetically controlled combustion indicates that the combustion time can be expressed analytically as[13]

$$t_{comb} = \frac{d_{p,0}}{Y_{g,ox,\infty}\, T_p^n \exp\left(-E/R_u T_p\right)} C_0' \, p_c^{-C_1(d_{p,0},T_\infty)} \tag{4.37}$$

showing that combustion times are inversely proportional to pressure. Diffusive-controlled combustion conversely is only weakly dependent on pressure through the gas diffusivities. Combustion times in mixture B with X_{O_2} = 0.20 at 2630 K show a definite pressure dependence which is weaker than that measured in mixture A at X_{O_2} = 0.11 and 2820 K. The non-negligible measured decrease in combustion times with increasing pressure is indicative of a combination of kinetics and diffusion-controlled combustion.

The condition of kinetically limited combustion suggests that convective distortion of the envelope of counter-diffusing reactants and products is of secondary importance since gas-phase diffusion is already fast enough to supply fresh reactants to the surface as needed. The fact that distortion of this envelope has been neglected in the modeling may then actually not be of so great a concern.

4.5.2 Temperature Effect

Boron particle ignition delays at high pressure are measured to decrease with increasing ambient temperature between 2440 K and 2830 K. The variation does not follow a smooth functional form, but rather the curve for t_{ign} as a function of temperature has a definite kink (goes through a step-like transition) between 2440 and 2600 K where the delay times drop 3-fold. Measured particle combustion times also decrease sharply in a similar manner.

The convective heating model of Sections 4.2 and 4.3 leads to the predictions shown in Fig. 4.16 a where ignition delay times decrease linearly with increasing ambient temperature (O_2/H_2O = .11/.30±.04 at ~150 atm). The agreement with data at high temperature is very good. Analysis of calculated profiles as a function of time (Fig. 4.17) indicates some oxide layer growth (~10% in the three cases) and rapid heating from convection. As the ambient temperature increases by 400 K above 2440 K, the temperature difference (T_c - T_p) increases as does $\bar{h}_c$ by a small amount, with the overall result being higher heat fluxes at higher temperature. This increased heat flux causes the particles to heat faster and oxide layer removal to occur earlier. Since ignition delay times are predominantly particle heating, it is to be expected that predictions show only a small effect on ignition delay times.

The Li and Williams model and Princeton/Aerodyne model lead to similar predictions in the case where only conduction heat transfer is considered (radiation is shown to be small in comparison). Convection is again seen to reduce particle heat-up times by ~50%. The Princeton/Aerodyne model, which considers more detailed chemistry including gas-phase radical chemistry with the oxide layer and the clean boron surface, leads to a similar predicted trend that ignition delays vary approximately linearly with ambient temperature. This model predicts that oxide layer gasification is rate-controlled at these high ambient temperatures by surface chemisorption and desorption reactions and not processes internal to the oxide layer.[13]

The data show a sharp decrease in ignition delays as temperature increases above 2440 K which is not predicted by either model, nor is the experimentally observed temperature independence above 2600 K predicted. The sharp transition above 2440 K, which was observed as well by Macek[4] in flame studies at 1 atm and to a lesser extent by Rood in shock tube experiments at 8.5 atm (see Section 3.14), cannot be accounted for by convective heating effects. This suggests that both models lack a description of some aspect of boron particle ignition which is still not fully understood but which is highly temperature dependent between 2440 and 2600 K.

Figure 4.16 b compares the Princeton/Aerodyne model predicted combustion times to data and although the model is a factor of two high at higher temperature, the slope of the temperature dependence above 2600 K is matched most closely. Again it is stressed that convective heating is less

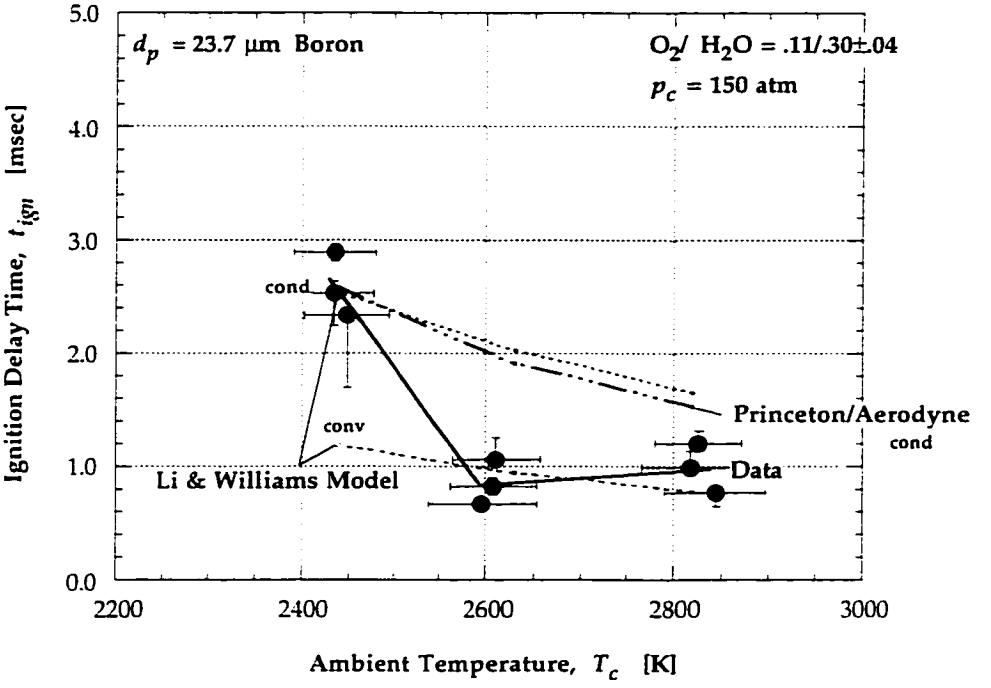

(a)

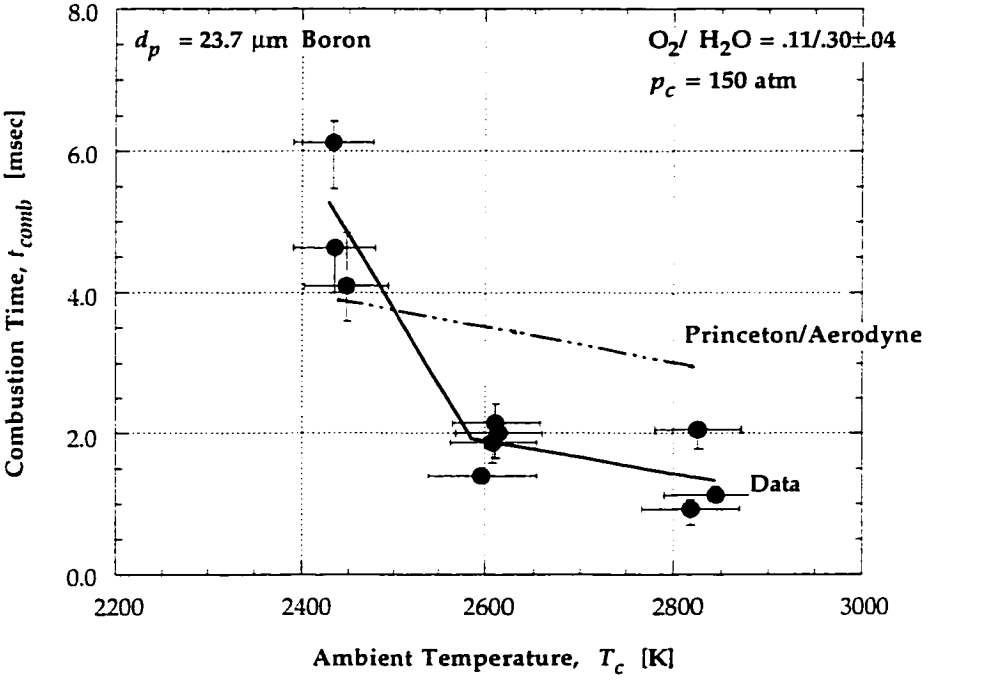

(b)

Fig. 4.16: Comparison of measured and model-predicted ignition delays and combustion times as a function of ambient temperature, in O_2/H_2O = .11/.30 at ~150 atm. (a) For ignition delays, agreement at higher temperatures is good; however the data show a sharp decrease between 2440 and 2600 K which the models fail to predict. (b) Model-predicted combustion times are a factor of ~2 long but show similar temperature dependency above 2600 K.

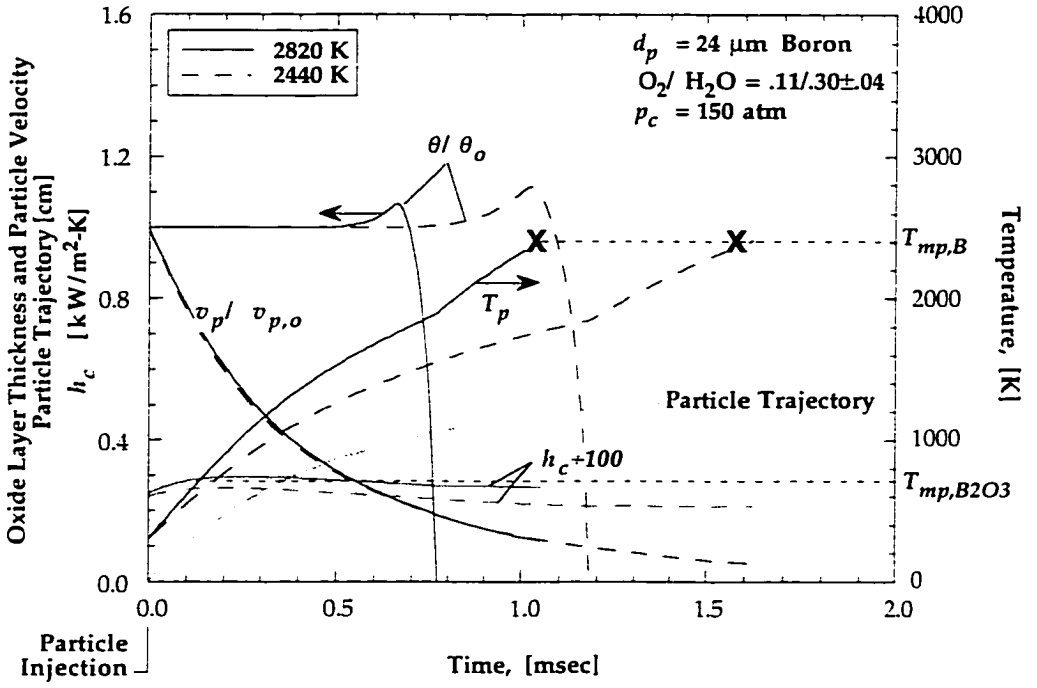

Fig. 4.17: Direct comparison of transient particle profiles for 2820 K and 2440 K up to particle melting, at 150 atm (high pressure) in O_2/H_2O = .11/.30±.04. Increased particle heating and quicker onset of oxide layer removal couple to produce decreased ignition delays as temperature is increased.

important during the combustion stage where particles have decelerated substantially and have nearly attained the temperature of the ambient gases. The model predicts a linear decrease in combustion times with increasing temperature but fails to predict the sharp decrease between 2440 and 2600 K. It is pointed out that measured combustion times are consistently shorter than predicted times, and this difference may be a result of differing interpretations of when particle combustion is completed.

Zhou, et al.[13] have tentatively identified a mechanism responsible for the sharp temperature effect on combustion times and this mechanism is undergoing further scrutiny. They find that gaseous NO (nitric oxide) is absorbed onto the surface during particle combustion and forms the surface complex BN(*c*), which eventually desorbes at high temperature. Due to a high desorption enthalpy required for this step however, ~170 kcal/mol, at lower temperatures BN(*c*) has a tendency to coat the surface and passivate active surface sites available for chemical reactions. For the present conditions, the ambient temperature where surface-coating becomes a problem appears to be below ~2600 K, close to the boron nitride boiling point near 2600 K (at 1 atm). An narrow zone of ~10^{-4} mole fraction BN(*g*) forms very close to the particle surface[13] where the condensation of boron nitride at low ambient temperatures could further delay combustion.

At a certain point at even lower ambient temperatures, depending on other gas parameters, less NO forms in the gas phase and the mechanism which coats the particle surface with BN(*c*) ceases. Thus the chemical mechanism is only important over a limited ambient temperature range. This is even more important in propellant applications where measurements by Hsieh, et al.[15] tend to indicate that gaseous nitrogen compounds and not fuel-bound nitrogen are responsible for the formation of boron nitrides. Presently the detailed model accounts for surface passivation by BN(*c*) but does not consider condensation from the gas phase back onto the particle. Further investigations are underway and perhaps additional modeling analyses will uncover a related mechanism which accounts for the similar observations during boron particle ignition.

4.5.3 Ambient O_2 Effect

Measured ignition delays and combustion times at high pressure (~150 atm, ~2620 K) exhibit behavior which is not monotonic with increasing ambient oxygen mole fractions, see Fig. 4.18 a. Ignition delays, and to a larger degree combustion times shown in Fig. 4.18 b, first decrease as X_{O2} is raised from 0.05 to 0.11, and then increase with increasing ambient oxygen from X_{O2} = 0.11 to 0.20 plus X_{H2O} = 0.30 ± 0.01.

The convective heating-modified Li and Williams model predicts ignition delays to increase slightly as ambient oxygen mole fraction is increased from 0.11 to 0.20, similar to what the data show. As shown in Fig. 4.18 a the agreement between data and predicted values is excellent when convective heating is treated appropriately. Analysis of temporal profiles shown in Fig. 4.19 indicates that particle heating and the oxide layer removal rate given by the slope of θ/θ_0 are essentially identical for the X_{O2} = 0.11 and X_{O2} = 0.20 mixtures. Water vapor reactions are dominant during the removal process and the amount of water vapor is the same for the four mixtures compared (B, E, C, and G: X_{H2O} = 0.30). For mixture E it has been assumed based on observations that the CO_2 does not enhance ignition but acts merely as a diluent.

It is the increased growth of the oxide layer with increasing X_{O2} and the higher T_{cut} which causes the longer ignition delays at high X_{O2}. At higher p_{O2} the solubility of O_2 in the liquid oxide layer increases and subsequent reaction with dissolved boron can result in temporary growth of the oxide layer thickness, while the particle is being heated but its temperature is still too low for oxide layer gasification by chemical reactions ($T_p < T_{cut}$). The lack of ambient oxygen at X_{O2} = 0.05 likely accounts for the measured increase in delays for low oxygen concentrations, whereas the Li and

Williams model is ambivalent to conditions of starved O_2. Particle ignition delays are predominantly particle heating over the entire range of ambient O_2 mole fractions.

Predictions assuming $Nu_p = 2$ are again shown to compare model predictions to the detailed Princeton/Aerodyne model which considers only the stagnant heating case. Convective heating is again shown to account for ~50% decrease in ignition delay times. The Princeton/Aerodyne model predicted values although too high show some evidence for the non-monotonic behavior evident in the measurements. The cause for this was not investigated closely. At the high ambient temperatures, Zhou, et al.[13] predict that oxide layer removal is enhanced by O-atom and OH-radical chemistry on the particle surface.

Combustion times in Fig. 4.18 b are over-predicted by the Princeton/Aerodyne model for $X_{O_2} < 0.16$ but decrease with increasing X_{O_2} as might be expected, in contrast to the data. Convective effects are much smaller during combustion than ignition but if included in the analysis, better agreement could be anticipated. Revisiting the *Da* analysis of Li and Williams, for O_2-diffusion controlled combustion ($Da >> 1$) the combustion times should decrease as $1/X_{O_2}$, slightly more rapidly than the calculations predict, and contradicting the measured result. One would expect that oxygen plays a significant role during "clean" surface combustion because the reaction with oxygen is the only one considered in the simplified model, and the more oxygen available the faster the oxidation rate. For very low ambient oxygen mole fractions, other processes in addition to boron oxidation by molecular oxygen may require consideration during combustion and as mentioned previously, the detailed model indicates that at high ambient temperatures combustion is controlled by surface reactions involving O-atoms, OH radicals, and H_2O in addition to O_2-chemistry.

The four mixtures in which the effect of variable X_{O_2} are studied contain different amounts of nitrogen diluent to keep the combustion temperatures roughly equal. It was pointed out in the previous section that in addition to radical species, that nitrogen oxides and predominantly NO may have a dramatic effect on particle combustion times through the formation of boron nitride which can coat the particle surface at lower temperatures. Fig. 4.20 shows equilibrium predicted mole fractions of the reactive radicals over the range of ambient O_2 mole fractions studied. The highest concentrations of NO appear in the high-X_{O_2} mixtures where there is also the least N_2. The perceived increase in combustion times at high X_{O_2} may be linked to higher NO levels but further modeling is required. Test temperatures and pressures (within ± 7 atm) are the same for the four mixtures studied.

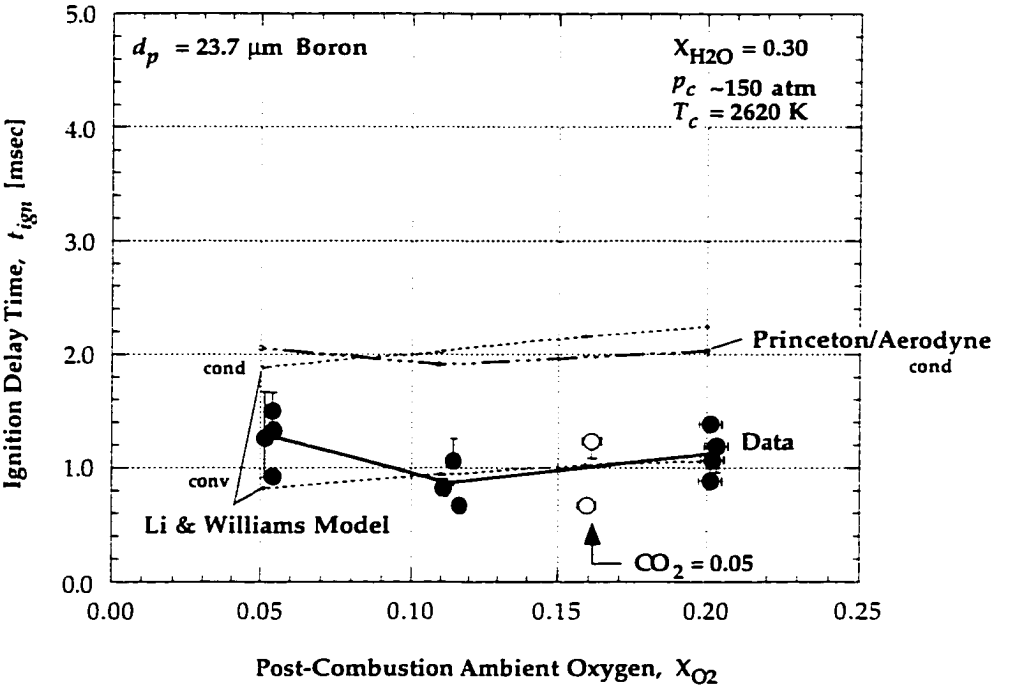

(a)

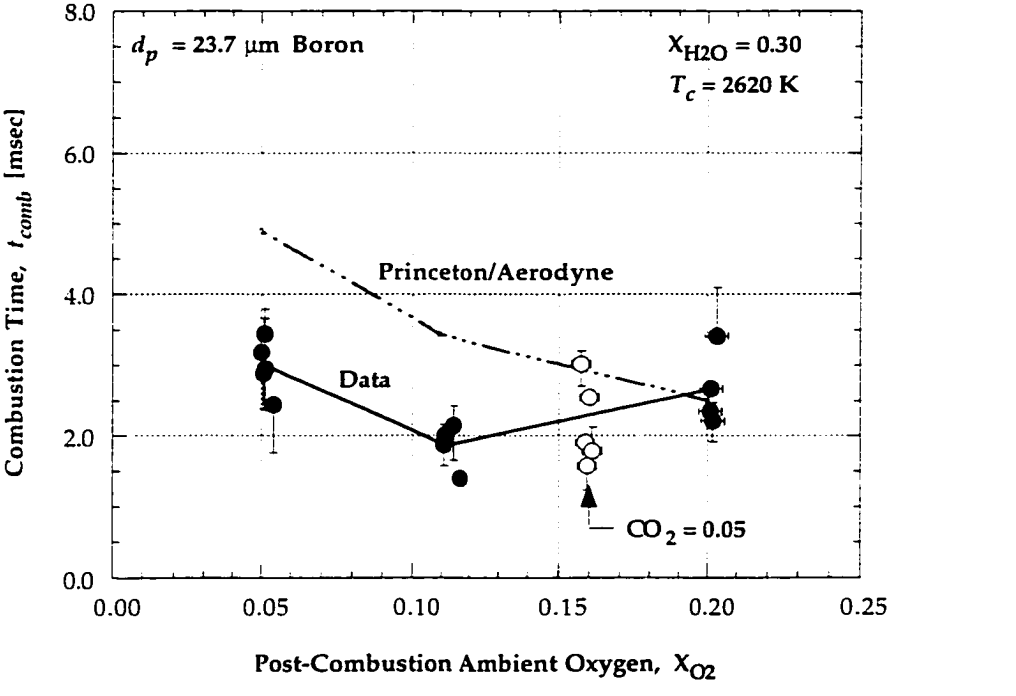

(b)

Fig. 4.18: Comparison of measured to model-predicted (a) ignition delays and (b) combustion times as a function of ambient oxygen, with X_{H2O} = 0.30 at ~2620 K and ~150 atm. Model predictions including convective heating show excellent agreement with the data and also predict increasing delays with increased X_{O2}. Modeled combustion times do not corroborate the increase in combustion times above X_{O2} = 0.11.

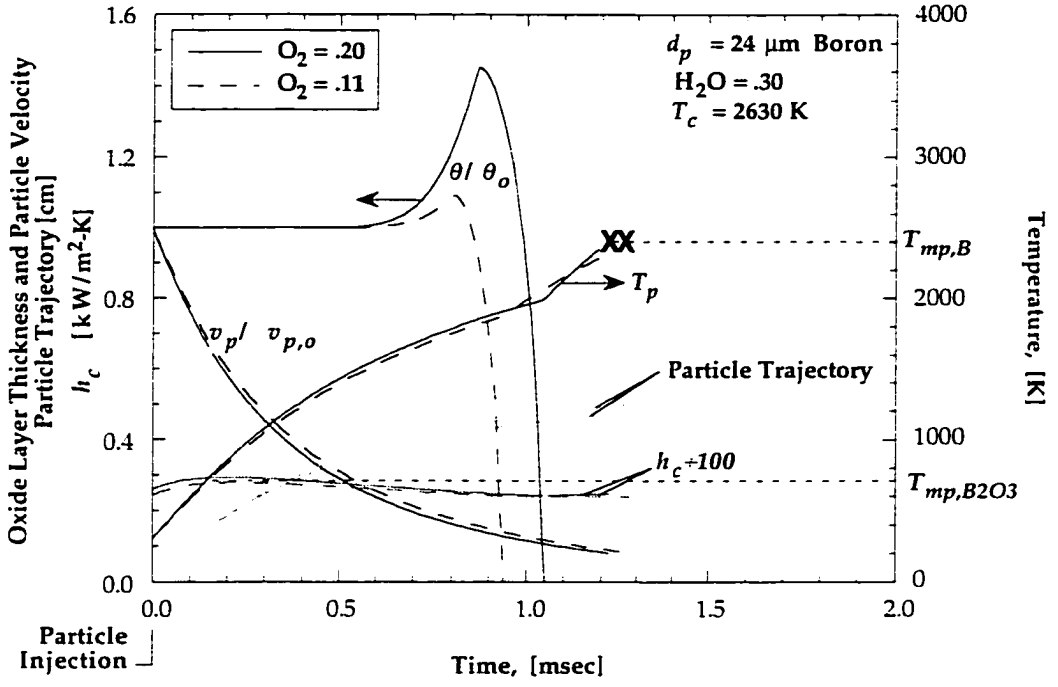

Fig. 4.19: Direct comparison of transient particle profiles for X_{O2} = 0.11 and 0.20 at 150 atm (high pressure) with X_{H2O} = 0.30. The growth of the oxide layer accounts for the increase in delays at higher ambient O_2 levels. Oxide layer removal is predominantly by H_2O reactions and by O and OH in the detailed model.

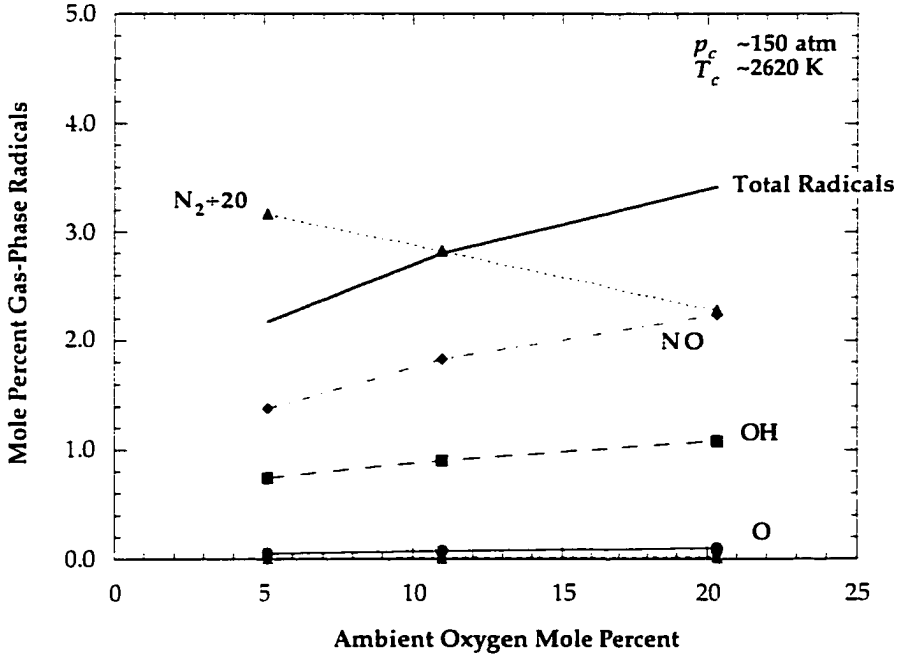

Fig. 4.20: Variation of important radical species mole-fractions with ambient oxygen in the product mixtures where particle combustion is studied. Reactive radical species become more abundant as X_{O2} increases.

4.5.4 Particle Size Effect

Particle scaling relationships are crucial for propellant and explosives designers since particle lifetimes will dictate which particles will be most effective for the given application. These types of scaling relationships are fairly widely accepted for aluminum particles. The scaling exponent n_c for Al has been found to decrease as pressure increases from 1 atm to high pressure.[80]

Measurements at ~140 atm in gases containing O_2/H_2O = .20/.30 at ~2615 K indicate that boron ignition delay and combustion times vary linearly with initial particle diameter, so that measured n_i = n_c = 1. The predicted variation of ignition delays with particle size at experimental conditions is shown in Fig. 4.21 along with the measurements. Predicted times for small particles (d_p < 30 μm) agree very well with the measured fit, t_{ign} = 0.04 $d_{p,0}$ (Eq. 3.11, with $d_{p,0}$ in μm and time in msec), but diverge for larger particle sizes where there is also significantly higher scatter in the data. A curve fit of calculated times gives

$$t_{ign} = 0.0081\, d_{p,0}^{1.54} \tag{4.38}$$

where for the "condensation-only" case the predicted delays are proportional to $d_p^{1.8}$. It is seen that increased heat transfer from particle motion (convective heating) reduces the scaling exponent n_i, which is indirectly a function of pressure through the particle Reynolds number which affects the convective heat transfer coefficient $\bar{h}_c$. Convective heating in the experiments reduces ignition delays for ~24 μm particles by about ~50% compared to stationary particles.

A linear variation of ignition delays with particle size suggests a combination of accelerated particle heating by external means or chemical self-heating and kinetically controlled oxide layer removal. This can be seen by a quick comparison of particle heating terms in Eq. 4.12. If heating from the bulk gases is predominantly by convection up to the point where chemical gasification begins and oxide removal is assumed to be very fast, then Eq. (4.12) reduces to $dT_p/dt \approx 6Nu_p k_g/(\rho_B c_{p,B} d_p^2)*(T_p-T_\infty)$. Recall that radiative heating is found to be small compared to convection. Integrating between $T_p = T_{p,0}$ at t = 0 and $T_p = T_{cut}$ at $t = t_{heat\text{-}up}$ and (i) noting that the particle size changes insignificantly during ignition and (ii) considering average and constant values for the thermodynamic properties (for arguments sake only), one finds $t_{ign} \approx t_{heat\text{-}up}$ = fctn.$_1(T_p)\, d_p^2/Nu_p$. Since Nu_p is a function of the Reynolds number through $Re_p^{0.55}$ then $t_{ign} \sim d_p^{n_i}$ where 1.45 < n_i < 2. If particle chemical reactions produce significant heating or reactions are kinetically controlled then $dT_p/dt \approx 6 \sum_i Q_i\omega_i/(\rho_B c_{p,B} d_p)$, and performing the integration for fixed properties gives t_{ign} = fctn.$_2(T)\, d_p$. If during ignition both processes are important then t_{ign} = term$_1$*$d_p^{n_i}$ + term$_2$*d_p, showing the above-mentioned processes introduce linearity. Based on this analysis, the data suggest that not only is convective heating important but that ignition is likely kinetically controlled as well. However reference to profiles in previous sections

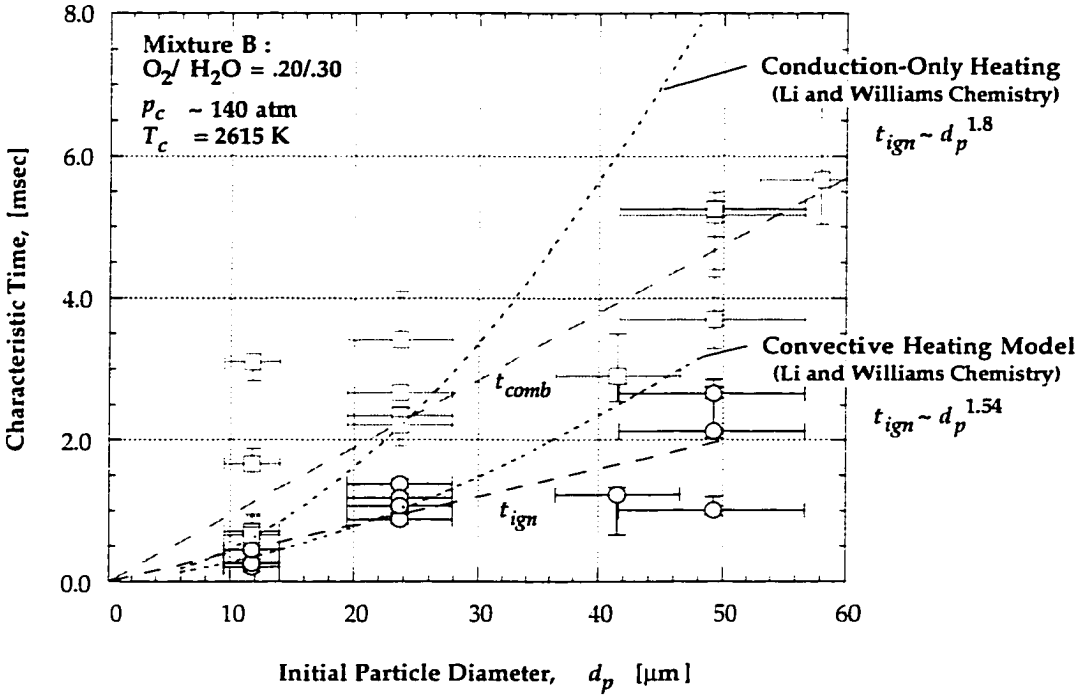

Fig. 4.21: Comparison of measured and model-predicted variation of ignition delays with initial particle diameter, in O_2/H_2O = .20/.30 mixture at ~2615 K and ~140 atm. Agreement for small particle sizes is very good with divergence for larger sizes.

indicates that the chemical reaction stage (oxide removal) is much shorter than particle heat-up and therefore tign ≈ $term_1 * d_p^{n_i}$ where the minimum n_i is 1.45. The measured n_i of 1 is thus rather unexpected.

Measured combustion times are also found to vary linearly with initial particle size, t_{comb} = 0.095 $d_{p,0}$ (Eq. 3.12), suggesting combustion is also kinetically controlled. Numerous other small particle measurements at 1 atm were compared in Fig. 3.28 of Section 3.14 where the product $t_c X_{O2}$ was shown to vary approximately linearly with $d_{p,0}$. A noteworthy exception is Macek's high temperature flame data at 1 atm where measured combustion times varied as $d_{p,0}^{0.6}$, and Li found a slightly higher exponent, $t_{comb} \sim d_{p,0}^{1.2}$. The functional dependence depends on whether combustion is kinetically ($\sim d_{p,0}^1$) or diffusion-limited ($\sim d_{p,0}^2$), and for a given particle size the distinction between the different regimes depends on pressure as well. The transition from kinetics to diffusion control at fixed pressure is evidenced in the laser-experiments of Macek and Semple[5,6] in room temperature ambient gases. Most of the data in Fig. 3.28 are for small particles under kinetically limited conditions.

For conditions in the hpcc experiments, Li's Damköhler analysis gives Da = {30, 60, 120} for {12, 24, 48 μm} particles at 150 atm, for which diffusion control is expected and then combustion times should scale as $d_{p,0}^2$, which is contrary to the measurements. This analysis however assumes that only O_2-diffusion and O_2-surface reaction are the dominant processes during combustion. Calculations with

the detailed-chemistry Princeton/Aerodyne model indicate that radicals such as O and OH are also efficient oxidizers. Zhou, et al.[13] express the dependence of combustion times on gas and particle properties analytically as

$$t_{comb} = C_0(d_{p,0}, Y_{g,ox,i}, T_p)\, p_c^{-C1(dp,0,T_\infty)} \tag{4.39}$$

where $0 < C_1 < 1$ and C_1 is a function of the initial particle diameter and ambient temperature, and C_0 depends on particle size, boron-oxidizing gas-phase species mass fractions $Y_{g,ox,i}$, and particle temperature. For kinetically controlled systems (i.e., where surface chemical reactions are the rate limiting steps and hence C_0 depends on T_p and not T_∞),

$$C_0 = \frac{d_{p,0}}{Y_{g,ox,i}\, T_p^n\, \exp(-E/R_u T_p)}\, C_0' \tag{4.40}$$

where the denominator is an Arrhenius-type rate constant for a series of limiting surface reactions and C_0' further depends weakly on gas and particle parameters. For diffusive controlled systems

$$C_0 = \frac{d_{p,0}^2}{\overline{\rho_g D_g(T_p)}\ \ln(1 + \xi\, Y_{g,ox,i})}\, C_0' \tag{4.41}$$

where $\overline{\rho_g D_g(T_p)}$ is the mixture average temperature-dependent diffusivity and ξ is a constant. For small particles combustion is kinetically controlled as is observed in the experiments, where temperature and ambient oxidizer concentration have the strongest impact on combustion times. For very large particle sizes, combustion is diffusion controlled and t_{comb} should then vary as $d_{p,0}^2$.

To summarize, there is experimental evidence and analytical analysis which suggests combustion should be a mix of kinetically controlled and diffusion-controlled processes for the small particle sizes employed here, and then $1 < n_c < 2$. Therefore the measured n_c so close to unity appears to be an additional unexpected result.

It is desired to extract scaling exponents from the data which are free of convective heating effects since it has been shown that convection tends to reduce n_i and perhaps n_c as well. To this end the data are scaled by the ratio of heat transfer coefficients to extract the enhanced heating influence inherent in the measurements during the ignition stage. Assuming ignition delays are predominantly heat-up times, which holds within 15% maximum error for $d_{p,0} < 30$ μm, then ignition delays under stagnant conditions (conduction only) differ from those in the hpcc convective environment only by the ratio of the heat transfer coefficients. This ratio reduces to $Nu_p/2$, where 2 is for pure conduction. The ratio of surface averaged Nusselt numbers is not constant however and varies with time as the particles decelerate and heat up. A time averaged Nusselt number $\overline{Nu}_p$ during ignition is therefore used which is typically $Nu_p \pm 30\%$ for mixture B in which the particle-size study was performed.

The plot of convective heating-corrected measured ignition delay times, $t^*_{ign} = t_{ign}\,(\overline{Nu}_p/2)$, is shown in Fig. 4.22. A curve fit of t^*_{ign} gives a particle size scaling exponent of $n_i^* = 1.5$ which is greater than the measured value, as is to be expected. For the combustion stage convective heating (cooling) is less important since particles have slowed significantly. so $n_c^* = n_c$ is suggested for use. The proposed scaling laws in the absence of convective heating at high pressure are

$$t^*_{ign} = 0.020\, d_{p,0}^{1.5} \qquad (4.42) \qquad \text{and} \qquad t^*_{comb} = 0.095\, d_{p,0}^{1} \qquad (4.43)$$

The measured and corrected scaling laws may still be somewhat specious since the particles employed are not spherical and will remain irregular throughout ignition, since the particles will not melt as is the case for the oxide layer and aluminum particles. Macek's critical review[6] of early data tended to discredit use of irregularly shaped particles for use in determining scaling relationships. For such particles, surface irregularities including ridges and sharp edges increase the effective surface area over which particle heating and surface reactions can occur.

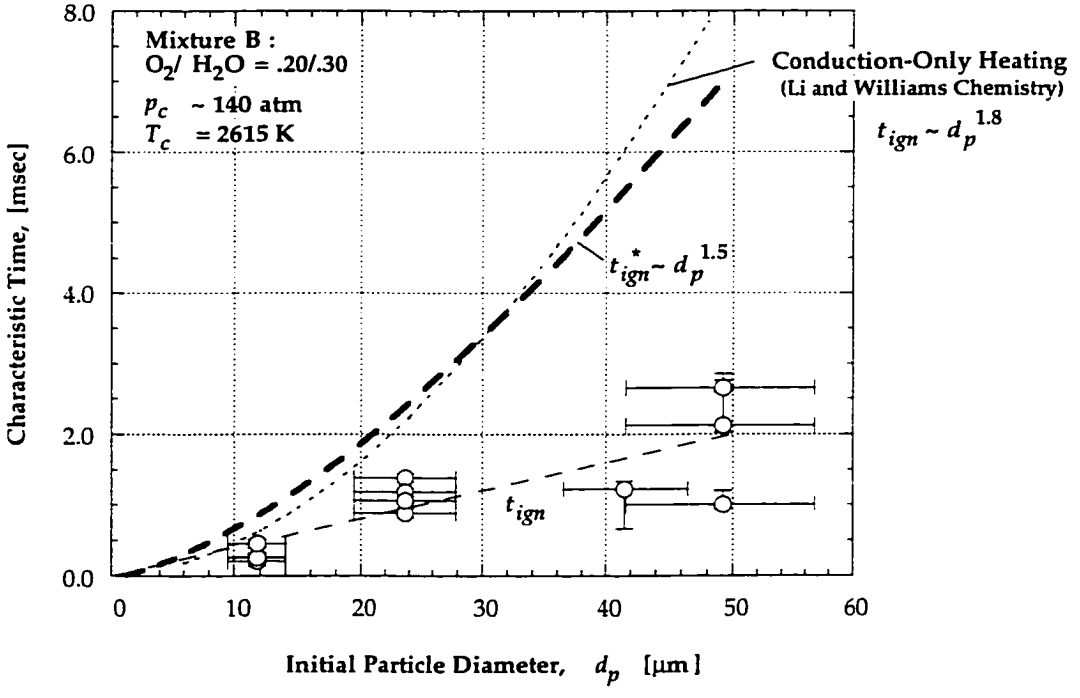

Fig. 4.22: Plot of convective heating-corrected measured ignition delays, t^*_{ign} indicating that particles igniting under stagnant conditions follow a $d_{p,0}^{1.5}$ power-law rather than $d_{p,0}^{1}$.

4.5.5 Ignition-Enhancement by H_2O and HF

No systematic investigation of the effects of water vapor on boron particle ignition-enhancement was conducted in this study. However insight can be gained with the convective heating particle ignition model (Li and Williams formulation) at conditions which cannot be produced experimentally. This has been done to investigate the role which water vapor plays during ignition. The results are shown in Fig. 2.23 where predicted ignition behavior in mixture B (O_2/H_2O = .20/.30) is compared to a mixture free of water vapor (O_2/H_2O = .20/0), at 145 atm and 2630 K.

Referring to the figure, up to ~1850 K particle temperature the particle heating for the two cases is similar and subsurface boron oxidation causes the oxide layer to thicken in an identical manner. Above ~1850 K oxide layer removal can occur by evaporation and water vapor reaction:

$$B_2O_3(l) \rightleftharpoons B_2O_3(g) \qquad [I]$$

$$\tfrac{4}{3}B(s) + \tfrac{4}{3}B_2O_3(l) + 2\,H_2O(g) + O_2(g) \longrightarrow 4\,HOBO(g). \qquad [IV]$$

Note that in moist gases Rx. [IV] converts liquid oxide to gaseous product by chemical means. In the absence of water vapor, oxide layer removal is limited to vaporization and is delayed until higher particle temperatures (T_p ~ 2200 K) and is not completed until the boiling temperature of the oxide layer is exceeded, $T_p > T_{bp,B2O3}$ (2316 K at 1 atm). Thus *water vapor reduces the effective oxide layer removal temperature*. At high pressure water vapor is seen to essentially cut the boron ignition delay time in half, which is a significant reduction.

Hydrogen fluoride produces a similar effect to water vapor under certain conditions. The Li and Williams model has not been extended in the present study to include HF chemistry and the Princeton/Aerodyne model which includes this HF chemistry has not been executed at experimental conditions (mixture F) as of this writing. However, Zhou, et al.[13,40] have performed calculations in fluorinated gases at 1 atm pressure and certain generalized statements can be made from their findings.

Fluorine compounds such as HF reduce the minimum ignition temperature of boron particles in a similar manner to water vapor by chemically reacting with the liquid oxide and producing volatile species, such as OBF. Hydrogen fluoride greatly increases the oxide layer gasification rate for small particles at low pressure (e.g., ~3 μm) but has an almost negligible effect on larger particles (~35 μm). An important conclusion drawn from the modeling is that HF has a greater impact under kinetically-controlled conditions than under diffusive-controlled ones. The burn rate of "clean" boron is suppressed in gases with low F/O-atom ratios but can be increased at high HF concentrations. At 1 atm and 2300 K for 10 μm diameter particles, mixtures with F/O ratios between 0 and 1 are predicted to cause a decrease

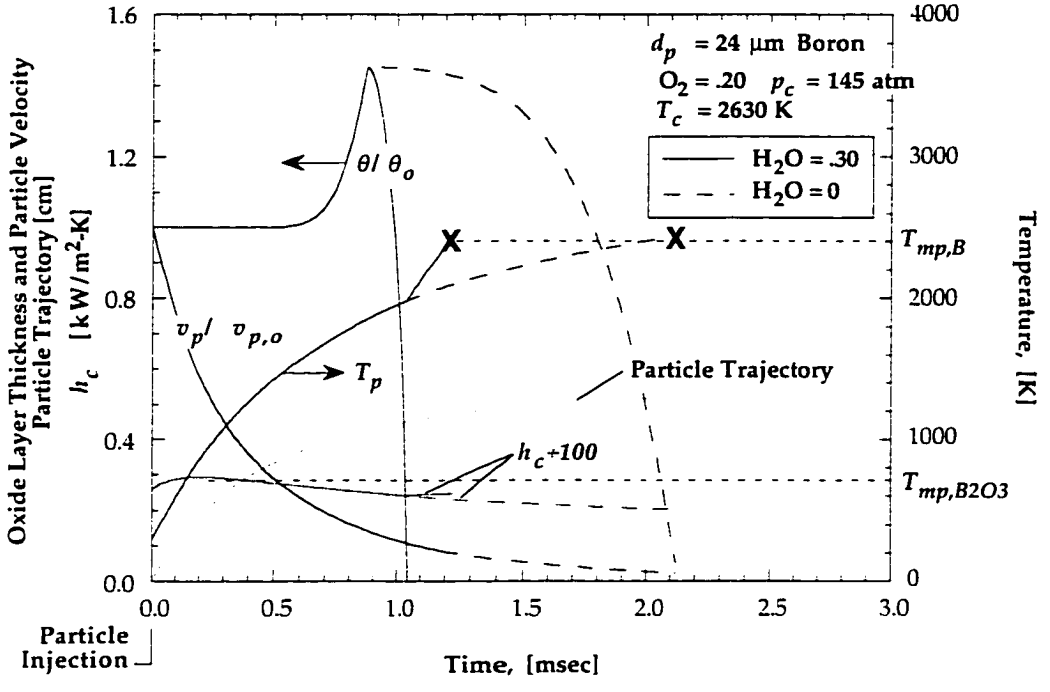

Fig. 4.23: Comparison of predicted oxide layer removal in moist and dry gases at the conditions of mixture B at 145 atm and 2630 K. Water vapor reduces the temperature where rapid oxide layer removal ensues and effectively halves the resulting ignition delay time for ~24 μm particles.

in the boron burning rate whereas mixtures with F/O > 1 cause the burn rate to increase.[40] No modeling has been conducted at higher pressure, but the F/O ratios in mixture F at ~34 atm are very low, ~0.07.

4.6 Remarks Concerning Model Predictions

The published Li and Williams model[9] for boron particle ignition has been extended in this study to include convective heating effects which are important for the present tests where particles are injected into hot, dense, stagnant gases. Particle kinematic equations are developed which make use of a drag coefficient formulation to calculate particle deceleration and a surface-averaged Nusselt number formulation for particle convective heat transfer. The empirical drag coefficient and Nusselt number correlations are obtained from the literature and are applicable over a wide range of conditions for spherical particles. The detailed chemistry model developed by Princeton/Aerodyne researchers[13] has been used to model the combustion stage and provide further insight into competing chemical processes. Good agreement is obtained between model predictions and various trends measured in the experiments.

Due to the high ambient temperatures and gas densities, particle heat transfer with the surroundings is the major factor influencing ignition for the small particles tested and not oxide layer removal which is typically only 15% of the total ignition delay time. In fact the moderate injection velocities used to provide good particle dispersion lead to approximately 50% reduction in ignition delay times compared to stagnant particle heating. During ignition time-averaged particle Reynolds numbers in the experiments are typically 10 to 30 based on an average slip velocity of ~5 m/sec, resulting in time-averaged convective heat transfer coefficients between 20 to 30 kW/m-K. In typical rocket motor chambers burning metal-particle laden HTPB/AP (12/88%) propellants at 1000 psia (68 atm), average particle slip velocities are on the order of 5-10 m/sec, and using temperature-averaged transport coefficients $\mu_g \approx 8.8 \times 10^{-5}$ kg/m-sec and $k_g \approx 0.2$ J/m-K-sec, time-averaged convective heat transfer coefficients are calculated to be 30 to 35 kW/m-K. Thus convective heating rates in typical rocket motor chambers are comparable to those in the hpcc experiments. Radiative heating in rocket propellant systems would tend to increase the particle heating rates even further.

Beyond particle heating, the growth of the oxide layer is predicted by one model to be important for high ambient oxygen partial pressures. This growth is predicted to be as large as 40% of the initial thickness by the Li and Williams model, whereas the detailed chemistry Princeton/Aerodyne model does not indicate a tendency for growth. Further investigation is suggested to resolve this issue and perhaps the growth is overstated by the semi-global reaction model; however, the measured ignition delays at high pressure tend to corroborate the proposed growth mechanism.

The Li and Williams model for boron oxide layer gasification was developed for particle ignition below ambient temperatures of ~2400 K. Both (1) a re-evaluation of the competition between evaporating B_2O_3 and diffusion away from the surface and (2) inclusion of gas-phase radical chemistry with the liquid boron oxide layer may be required for predictions at high temperatures and pressures. Equilibrium calculations predict significant dissociation of B_2O_3 vapor into BO_2 and conversion to HBO_2 in the gas phase for the conditions covered here. For the combustion phase, more detailed chemical modeling has shown that high temperature surface chemistry with gas-phase radicals (OH, O, NO), H_2O, and boron sub-oxides BO_x are important. Both models predict that particle temperatures approach the boiling point of the boron droplet during the combustion stage. Boron vaporization is considered in the Princeton/Aerodyne model, although the pressure dependence of the vaporization parameters is poorly known.

Prevention of oxide layer growth during particle heat-up would generally assist boron particle ignition. Oxide layer growth occurs at lower temperatures whereas oxide removal is delayed until relatively high temperatures, 1650 to 1850 K. Gasification is very fast once high enough temperatures are reached. Increased heating rates locally near the particle surface provided by the burn-off of

specialized coatings which oxidize at low temperature, for example, would be advantageous. So would gas-phase ignition-enhancers which are capable of reacting with the oxide layer at temperatures below which the onset of oxide layer removal normally occurs in water vapor and HF-containing environments. Based on modeling analysis, it would appear that high oxygen concentrations hinder ignition but greatly assist combustion while nitrogen can cause problems at low ambient temperatures (via boron nitride formation and condensation on the particle). In addition to chemical agents, highly convective environments are also beneficial to ignition because they greatly increase particle heating rates.

To summarize the modeling at high pressures, several measured trends are corroborated very closely by the models. Agreement includes ignition delays at high pressure and temperatures above ~2600 K, which are closely matched by the calculations, as well as the small measured increase in ignition delays with increased oxygen partial pressure. Combustion times at low and high temperature are also modeled well with the detailed chemistry model as is the measured pressure effect on combustion times. Model predictions are of the correct order of magnitude for all conditions tested even though both models were developed primarily for conditions of 1 atm pressure. Instances where several key measurements are not corroborated by modeling include under-prediction of the strong measured pressure dependency of boron ignition delays, the failure to predict the sharp decrease in ignition delays and combustion times between 2440 and 2600 K, and the lack of corroboration of the measured increase in combustion times at high X_{O2}.

Future research to reconcile these differences would do much to elucidate our understanding of the complex processes involved in boron particle ignition and combustion.

5. CONCLUSIONS AND RECOMMENDATIONS FOR FUTURE WORK

5.1 Conclusions

The ignition and combustion of small crystalline boron particles have been investigated experimentally at high pressure and high temperatures in oxygen/water vapor/nitrogen mixtures produced by the combustion of nitrogen-diluted hydrogen/oxygen mixtures. The measurements were performed in a constant volume combustion bomb where the particles were injected into the dense ambient mixtures after sufficient delay for gas phase ignition transients to subside, in such a way that they ignited and burned individually at nearly constant pressure and temperature conditions. Particle ignition and combustion were monitored optically where emissions from the combusting particles could be differentiated from the highly luminous hot-gas background by optically bandpass filtering collected emissions and judiciously restricting the measurement field-of-view. Using this approach, the ignition and combustion times of ~24 μm particles were measured over a range of pressures (30-150 atm), at high temperatures (2440, 2630, 2830 K), for various excess O_2 concentrations (5, 11, 20%), and with two proposed ignition enhancers (CO_2, HF). Several particle sizes were also investigated at one high pressure condition (~12, ~24, ~48 μm) to determine particle scaling laws.

Investigations performed in this study have shown that boron particle ignition delays and combustion times continue to decrease with pressure up to 150 atm and decrease strongly with temperature over a narrow range between 2450 and 2600 K, as has been observed previously at low pressures. These findings suggest more efficient boron combustion is obtainable in high speed propulsion applications if these devices are operated at high chamber pressures and temperatures. At high pressures ambient oxygen hinders ignition by causing the oxide layer to thicken while the particles are being heated from the surrounding gases, while water vapor greatly enhances ignition by chemically reacting with the oxide layer thereby lowering the temperature where effective oxide layer gasification occurs. Particle lifetimes for ~24 μm boron particles vary between ~8 msec at 2440 K and 2.3 msec at 2830 K, including mixtures containing a little as 5% excess O_2, indicating that these particles are suitable for additives in either slurried fuels or solid propellants. Based on measurements with smaller particles it is believed that 1-10 μm sized particles, which have still shorter lifetimes, may be appropriate for addition to explosives where they can be used to tailor the expansion work of the detonation front. This is shown in Fig. 5.1 where the measured reduction in ignition delays and combustion times with particle size is superposed on the reduction with increased pressure and the trends are extrapolated to much higher pressures.

Several aspects of the ignition behavior of small boron particles have been successfully modeled at high pressure using a convective heating-modified ignition model based on the semi-global

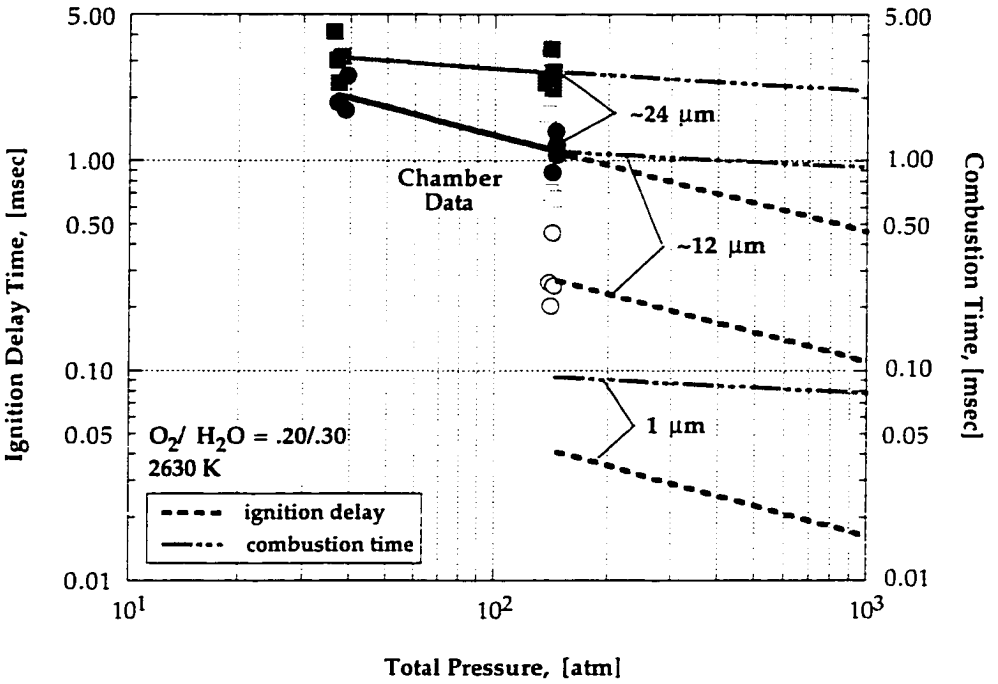

Fig. 5.1: Extrapolation of measured pressure trend to higher pressures and measured diameter scaling law to smaller particle sizes than tested showing the potential for very short particle lifetimes if 1-10 μm diameter particles are employed at high pressures. This suggests such small particles may be appropriate for use in explosives.

chemistry formulation of Li and Williams.[9] The combustion stage of these particles has been modeled using the detailed-chemistry Princeton/Aerodyne model.[13] Based on experimental measurements and modeling analyses several specific conclusions can be drawn concerning the behavior of igniting and combusting particles at high pressures and temperatures.

1.) Due to the small particle diameters and relatively high particle thermal conductivity, the particle temperature may be treated as uniform and a lumped capacitance energy equation used. Convective heating, which arises from particle motion through the dense gases, decreases particle heat-up times by approximately 50% compared to stationary particles heated predominantly by conduction.

2.) At high pressures and temperatures, particle ignition delay is primarily a heating delay. Oxide layer removal is typically only ~15% of the total ignition time for the conditions covered, but this time *would be significantly longer in the absence of water vapor.* To shorten ignition delays even further, prospective techniques should inhibit oxide layer growth during particle heat-up and lower further the effective gasification temperature of the oxide coating. Neither CO_2 nor HF additives in small quantities were found to provide

chemically assisted ignition-enhancement. Hydrogen fluoride (5% HF in O_2/H_2O = .20/.30) seems to lengthen the ignition process, and produces only a minimal decrease in combustion times at ~2570 K and 34 atm. These data with HF are below 2600 K where ignition delays tend to increase rapidly as temperatures decreases (see 4).

3.) Ignition delays and combustion times of ~24 μm boron particles decrease with increasing pressure up to 150 atm. Ignition delays for these particles are between 1-2 msec at high pressure in mixtures with O_2/H_2O = .11-.20/.30-.34 and temperature above 2600 K. Measurements indicate a four-fold increase in pressure between 37.5 and 150 atm roughly halves particle ignition delays, where the data can be approximated by $t_{ign} = 13\ p^{-0.5}$, with t_{ign} in msec and p in atm. Modeled ignition delays are of the correct magnitude but times are predicted to be essentially independent of pressure. Although convective heating rates increase with pressure, this alone cannot account for the measured pressure dependency.

4.) Ignition delay and combustion times at high pressure decrease sharply between 2450 and 2600 K in similar fashion to low pressure data. In mixtures containing O_2/H_2O = .11/.30±.04 diluted with N_2 at 150 atm, the drop in both times is about 50%. Above 2600 K (up to 2830 K) both ignition and combustion times decrease only weakly with temperature. Current models fail to predict this phenomenon but predictions agree quite well with the measurements at the low and high temperatures studied.

5.) Excess oxygen can delay particle ignition at high pressures by causing the oxide layer to thicken during particle heating. Measured ignition delays were found to increase ~30% between X_{O_2} = 0.11 and 0.20, at ~2620 K and 150 atm. Likewise measured combustion times increased ~40% over this range in contrast to model predictions and other measurements at lower pressure; the reason for the discrepancy requires further investigation. Particles were found to ignite and burn readily (less than 10 msec) in only 5% excess O_2 concentrations suggesting potentially efficient use of boron even in O_2-lean systems.

6.) Both ignition delays and combustion times increase linearly with particle diameter ($\sim d_{p,0}^{1}$) between 12 and 48 μm, in O_2/H_2O = .20/.30 at ~2610 K and 140 atm. Convective effects are responsible in part for the low measured scaling-exponent for ignition times - diameter scaling laws corrected for particle motion scale approximately as $d_{p,0}^{1.5}$. *Additional ignition acceleration is provided by water vapor reaction with the oxide layer.*

7.) The measured boron particle ignition delays are a factor ~2.5 longer than aluminum particle delays for similar sized particles. Combustion times are also significantly less for

aluminum particles. Aluminum particle (21.6 μm) lifetimes are ~0.9 msec at 140 atm, in O_2/H_2O = .20/.30 at 2630 K.

Based on the preceding discussions and by tying in the observations at high pressure with those at lower pressures, the following general comments can be made about the ignition and combustion behavior of boron particles in high temperature oxidizing environments.

Boron particle ignition delays decrease strongly as a function of pressure between 1 and ~10 atm and *continue to decrease with increased pressure up to 150 atm.* Theoretical arguments and measurements indicate that combustion times for these sized particles decrease with increased pressure - combustion is controlled to a large degree by heterogeneous surface chemistry, which includes reactions with water vapor and reactive gas-phase radicals, and the reaction rates depend upon pressure.

Ignition times are weakly dependent on temperature up to ~2440 K and decrease sharply over a narrow temperature range between 2440 and 2600 K, after which they continue to decrease weakly to higher temperatures. The weak temperature dependence is basically a thermal heating effect, whereas the sharp decrease between 2440 and 2600 K requires further theoretical investigation. Combustion times are weak functions of ambient temperature up to ~2450 K above which they drop similarly to ignition delays. Modeling indicates that in general particle temperatures increase dramatically during "clean" surface oxidation and it is the particle temperature and not the ambient temperature which dictates combustion rates. The sharp observed increase in times as temperatures are lowered below 2600 K may be linked to the formation of boron nitride (BN) produced by the surface reaction between absorbed NO and boron, where BN has the potential to coat the particle surface during the combustion stage below 2600 K. The requirements for both sufficient NO in the gas phase and BN passivation of the surface in this scenario confines the mechanism to a narrow temperature range, similar to the range over which the behavior was observed.

Oxygen hinders ignition at high O_2 partial pressures by causing the oxide layer to thicken during particle heating. The proposed mechanism (Li and Williams model) which is responsible involves O_2 dissolving in the liquid oxide layer and reacting with dissolved boron at relatively low temperatures before oxide removal occurs. Oxygen on the other hand is required for the combustion stage where at lower pressure combustion times decrease with increasing O_2 mole fractions. Excess oxygen appears to hinder combustion as well at high partial pressures, for reasons which remain unclear. Water vapor assists greatly with oxide removal by chemically reacting with the oxide and producing volatile species such as HBO and HBO_2, which gasify much more readily than $B_2O_3(l)$. Small quantities of hydrogen fluoride did not produce any benefit under the limited conditions tested, but can at larger concentrations assist with oxide layer removal and combustion under conditions when the process is surface kinetics-controlled.

5.2 Recommendations for Future Work

Important information concerning the ignition and combustion characteristics of small boron particles at elevated pressures has been revealed. The results indicate that significantly shorter particle lifetimes can be achieved by operating at higher pressure and temperatures above 2600 K. The ~24 μm boron particle lifetimes even in ambient oxygen concentrations as low as 5% excess O_2 are less than 10 msec indicating that these particles may be suitable in high speed propulsion applications. Even smaller particles between 1-10 μm (see Fig. 5.1), which have still shorter lifetimes, may be appropriate for addition to explosives.

Based on the observations at high pressure further research efforts are suggested in several areas which encompass both experimental and theoretical issues.

As concerns the present optical detection technique, there remains the issue whether monitoring particle emissions about a narrow band of wavelengths corresponding to molecular emission bands from excited state intermediates (e.g., BO_2, AlO) is a good indication of particle ignition and combustion, without directly viewing the disappearance of representative particles. Narrow bandpass filtering was employed as discussed in Section 2.2.3 to reject as much of the hot-gas emissions as possible while simultaneously emphasizing the particle emission contribution, and this technique is similar to that used to investigate aluminum particle combustion in relatively opaque propellant product gases. It was shown in Fig. 2.45 that BO_2 emission bands are of moderate magnitude compared to the particle "black body" continuum and therefore a large contribution to the measured signal originates from the hot particle glow. Thus interpretation of ignition delays from the measured optical signal is influenced by rapid particle heating which accompanies the transition to full-fledged combustion. This is in line with associating particle ignition with removal of the oxide layer *and* subsequent transition to rapid oxidation.

Towards the fading stages of particle combustion, lingering emissions from excited state BO_2 or condensed-phase products (a problem with aluminum) could interfere with the interpretation of combustion times based on luminosity measurements. To further resolve these issues, additional experiments are suggested which monitor particle emissions at wavelengths other than those corresponding to molecular bands and to investigate broadband emissions more closely. For several experiments in this study emissions were monitored at 514.5 nm and 486.1 nm and these signals could be further analyzed to determine if our choice of bandpass filtering effects the determined times - preliminary investigations at one condition only (20% O_2, mixture B) have found only minor differences which are within experimental uncertainties. Further uncertainties regarding this technique might be resolved with a direct measurement of decreasing particle sizes, by Mie scattering for example.

Application of such a technique would first require careful examination of optical properties of oxide-coated boron particles at high pressures and temperatures.

The issue of irregularly shaped particles versus spherical particles should also receive further critical attention to assess the effect of irregular shape on measured diameter-scaling laws. If spherical particles become available additional experiments would be fruitful to investigate any differences caused by particle shape. A review by Macek[6] of his own early data tended to discredit use of irregularly shaped particles for determining scaling relationships. For such particles, surface irregularities including ridges and sharp edges increase the effective surface area over which particle heating and surface reactions can occur. The ratio of surface area to volume is important to particle heating and to surface chemistry, and the effects of shape irregularities on particle drag, motion, and heat transfer would be useful to have incorporated into the theoretical formulation.

Based on the extrapolation of measured pressure and particle size dependencies shown in Fig. 5.1, crystalline boron particles less than 10 μm in diameter would ignite sufficiently quickly to allow efficient application to explosives. Interests in using even smaller particles which are ca. 1 μm in diameter to obtain very short particle ignition delays may require consideration of boron of the amorphous form and not only crystalline form. Certain thermophysical properties for amorphous boron are different than for crystalline boron, such as density and melting point.[18] Yeh and Kuo[10] have shown that ~3 μm amorphous boron particles ignite and combust more readily than ~3 μm crystalline boron particles at 1 atm and temperatures below 2000 K. No tests were conducted in the present study with amorphous particles however these differences warrant that present measurements at high pressure and high ambient temperatures be replicated using amorphous boron particles to investigate what effect the nature of the boron has on ignition and combustion times.

As concerns theoretical modeling, current particle ignition and combustion models fail to predict the pressure effect on particle ignition times. Re-evaluation of competing chemical and diffusional processes and the pressure dependence of reaction rates during the ignition stage is suggested. At high gas temperatures for example, gas-phase radical species become very important and effective reactants. Most models have been developed for 1 atm or low pressure conditions in general.

Observations at low and high pressure indicate that important processes are occurring which result in a sharp decrease in ignition and combustion times between 2440 and 2600 K, processes which current state-of-the-art models do not currently resolve correctly. Important chemical processes involving boron nitride formation and surface coating may be responsible for the observed behavior during the combustion stage. Further investigation into boron-NO_x chemistry is required. Currently very little information is available about specific boron-NO_x kinetic rate constants and the mechanisms of boron nitride condensation and/or crystallization in high pressure combustion

environments. Further fundamental rate measurements and continued mechanistic modeling studies in this regard are suggested. Additionally, boron particle experiments in a shock tube, for example, where concentrations of NO and other gaseous nitrogen compounds can be varied easily and independently of other gas parameters, would provide greatly needed macroscopic-scale information.

Limited tests with HF and CO_2 show little beneficial effect on reducing boron particle ignition delay times. In fact HF is shown to increase delays and produce only limited benefit to combustion for the condition tested where the gas temperatures were within the range of 2440 to 2600 K where ignition delays and combustion times are very sensitive to temperature. In fluorinated propellant product gases however, where very little free oxygen is available for combustion and where temperatures are generally higher than tested, the processes involving HF, CO_2, H_2O, and NO_x reactions with boron and its oxide coating will play the critical roles during ignition and combustion. Additional laboratory and computational modeling experiments over a range of *elevated* pressures at high temperatures should be conducted to further elucidate the mechanisms involved.

It is believed that the current tests can be used as a baseline for studying further the effects of other gas-phase ignition enhancing techniques as well as various particle surface coatings. Modeling suggests that potential methods for ignition-enhancement must function at temperatures lower than ~1650 K to be most effective, must inhibit oxide layer thickening, and must simultaneously reduce temperatures required for oxide layer gasification.

An experimental facility and methodology has been developed to study small particle ignition and combustion at high pressure. Tests have been performed up to 150 atm in gas-phase combustion products which can be extended to even higher pressures. The capability also exists for solid propellant combustion to be used to establish ambient mixtures for particle study. Further experimental investigations are suggested in this facility at higher pressures to gain additional crucial information at pressures more representative of explosives applications where boron may find increased utilization.

Appendix A: Derivation of Particle Injector Kinematic Equations

In this appendix the kinematic equations describing the particle injector plunger motion are derived. These equations were used during injector design to tailor its motion to the pressure rise in the chamber. The resulting system of equations is incorporated into a computer code and solved numerically to study injector performance and the effect of changing different design variables on subsequent injector operation.

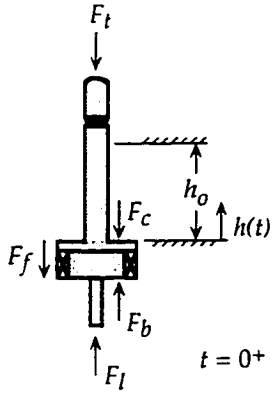

Fig. A.1: Force diagram for particle injector plunger.

The particle injector governing equations are derived by equating Newton's Second Law of motion to the sum of the forces acting on the piston/plunger. Forces on the piston arise from various pressures acting on the plunger base, from seal friction, and from the resistance from the gases being compressed above the plunger as it moves upward in Fig. A.1. The forces are indicated in the figure and the resulting force balance is given by:

$$F_p(t) = m_p\, dV_p/dt = F_b(t) + F_l(t) - F_t(t) - F_f(t) - F_c(t) \ , \qquad \text{(A.1)}$$

where $F_p(t)$ is the net force on the plunger, m_p the plunger mass and V_p the plunger velocity; $F_b(t)$ is the pressure force acting on the base of the plunger, $F_l(t)$ the force on the tiny pintle, $F_t(t)$ the pressure force acting on the top of the injector; $F_f(t)$ is the seal friction force; and $F_c(t)$ is the resistance from the gases being compressed above the injector. The plunger velocity and position $h(t)$ are then obtained by integration of

$$dV_p/dt = \frac{F_b(t) + F_l(t) - F_t(t) - F_f(t) - F_c(t)}{m_p} \ , \qquad \text{(A.2)}$$

$$dh/dt = V_p \qquad \text{(A.3)}$$

The pressure in the combustion chamber $p_\infty(t)$ is a result of gas-phase combustion and is time dependent and known from measurements. Gases from the chamber flow through the annulus formed between the tiny pintle and the sharp edged orifice. A pressure drop occurs as a result of flow through the orifice and the resulting pressure which acts over the base of the injector is $p_b(t)$. The gas which flows through the orifice is assumed to be of frozen composition and (stagnation) temperature corresponding to the chamber conditions. The mass flow is given by the sharp edged orifice relations measured by Perry[81] for air at room temperature;

$$\dot{m}_g = \rho_g V_g A_e = \text{fctn}_1.(p_\infty, p_b) = 0.465 \frac{p_\infty A_e}{\sqrt{T_g}} \sqrt{1\text{-}r^2} \ , \qquad \text{unchoked} \qquad \text{(A.4a)}$$

$$\dot{m}_g = \rho_g V_g A_e = \text{fctn}_2(p_\infty, p_b) = \frac{p_\infty A_e}{\sqrt{T_g}} (0.449 + 0.241\, r) \sqrt{1\text{-}r}\ , \quad \text{choked} \qquad \text{(A.4b)}$$

where $r = p_b/p_\infty$ is the ratio of pressure "downstream" to "upstream" of the orifice. The constants in Eqs. (A.4) require that p_∞ and p_b have units of psia, T_g be in °R, and A_e in in^2 giving $\dot{m}_g$ in lbs/sec. Since the pressure ratio p_b/p_∞ will drop below 0.528 as the chamber pressure $p_\infty(t)$ continues to rise, the flow will choke (become sonic) after which $\dot{m}_g$ for a real orifice is not constant but given by Eq. (A.4b). These empirical flow relations are assumed to hold even though the pintle protrudes into the orifice and the gases are not air at room temperature.

The effective orifice flow area A_e depends on whether the pintle is in the orifice or has been retracted by the rising plunger just prior to injection,

$$A_e = \pi/4\,(d_o^2\text{-}d_p^2) \qquad \text{if pintle in orifice,} \qquad \text{(A.5a)}$$

or

$$A_e = \pi/4\,(d_o^2) = A_o \qquad \text{if pintle retracted.} \qquad \text{(A.5b)}$$

In Eqs. (A.5) $(d_o^2) \sim 25(d_o^2\text{-}d_p^2)$ where d_o and d_p are orifice and pintle diameters, respectively. The increasing pressure $p_b(t)$ is affected by the mass flow through the orifice *and* by the moving plunger which expands the volume below the plunger. The pressure is obtained from the ideal gas equation of state

$$p_b(t) = \rho_g(t) R T_g = \frac{m_g(t)}{h(t) A_b} R T_g \qquad \text{(A.6)}$$

where $\rho_g(t)$ is the gas density in the piston bore and T_g the temperature (= T_∞), the product $h(t)A_b$ is the volume of gas beneath the injector, $m_g(t) = \int \dot{m}(t')\, dt'$ is the mass of gas accumulating beneath the rising injector with $\dot{m}_g$ given by either Eq. (A.4a) or (A.4b), and $R = R_u/\bar{W}_g$ is the specific gas constant. The force pushing the piston upward is then $F_b(t) = p_b(t)\, A_b$. The base area depends on whether the pintle is protruding through the orifice or is retracted inside the injector housing. If the pintle is protruding through the orifice then the area is the annular base area and the force acting on the pintle, $F_l(t)$, is from the external gas pressure $p_\infty(t)$.

The force acting on the top of the plunger $F_t(t)$ is from the chamber pressure and this force is given by $p_\infty(t)$ times the cross-sectional area of the top of the plunger.

As the injector rises it compresses the gases which initially filled the plunger bore above it. These gases have the same composition as the initial chamber gases ($H_2/O_2/N_2$) at initial p_1 and T_1 before gas-phase combustion occurred. The gases are assumed to be compressed adiabatically and retain their initial composition, so that $p_g/\rho_g{}^\gamma = const.$, and it is assumed there are no seal leaks so that the mass is fixed (no seal leaks). The volume above the rising injector shrinks and the resulting pressure

rise can be related to the change in height giving

$$\frac{p_\infty(t)}{p_1} = \left[\frac{h_0}{h_0 - h(t)}\right]^\gamma \qquad \text{(A.7)}$$

where the ratio of heights is equivalent to the ratio of initial volume to reduced volume at time t and γ is the ratio of specific heats. The retarding force from the compressed gas is then $F_c = p_c A_c$ where A_c is the annular area over which the force acts and $h(t)$ is solved for during the numerical integration.

The frictional forces are between the Teflon base seals and piston bore and the Teflon guide collar seal and plunger shaft. Note there is no metal-to-metal contact anywhere between the plunger and the injector housing. The maximum force due to friction occurs when the plunger is initially at rest and this has been measured to vary between 25 and 35 lbs (a very tight fit indeed!). This initial static frictional force is less than 1:20 of the upward forces acting on the plunger within only a few microseconds of pressure buildup from inrushing chamber gases and so friction has been neglected in the calculations, $F_f \rightarrow 0$. Friction definitely effects injector operation at low chamber pressures (37.5 atm).

The resulting three coupled ordinary differential equations which must be integrated are Eq. (A.2), (A.3), and (A.4) for V_p, h, and m_g. These equations must be solved simultaneously. They are discretized using backward differencing in time and integrated numerically using the LSODE[77] routine once the input parameters are specified. The integration routine has full control over timestep adjustment. The initial conditions for $\{h, V_p, m_g\}$ are {0.1 cm, 0, ~0} at $t = 0$. The injector must be offset from the base by ~1 mm so that the full base area A_b, not just A_o, can be acted upon by pressures. Otherwise the injector will never move because $F_t(t) >> F_l(t)$ with the same pressure acting on the respective surfaces.

B. Emission Transitions of Various Boron Gas Phase Species

This appendix consists of a tabulation of selected emission bands for various metal-oxides and oxyhydrides and other reactive gas phase species of interest to combustion. Many of the interesting molecules such as HBO, HBO_2, and OBF have detectable transitions which are in the infrared. The wavelengths are in micrometer (μm) or nanometer (nm) units as indicated. Transitions were obtained from the references indicated at the end of the table. The interested reader should refer to the original references about details as to detection in combustion systems or exhaust plumes where appropriate.

Table B.1: Emission bands for several boron species, metal oxides, and other gas phase species of interest.

Species	Bands λ [μm]	Lines λ [μm]	Comments	Refs.
B_2O_3	4.9	-	very strong	b
B_2O_3	5.1	-	weak	b
B_2O_3	8.1	-	medium	b
B_2O_3	19.3	-	strong	b
B_2O_2	4.7	-	strong	b
B_2O_2	4.9	-	very strong	b
B_2O_2	8.1	-	very strong	b
B_2O_2	20.4	-	strong	b
B_2O_2	21.0	-	strong	b
HBO_2	2.7	-	-	c,d
HBO_2	4.9	-	-	c,d
HBO_2	7.0	-	-	c
HBO_2	8.0	-	-	c
HBO	5.5	5.4-5.5	v3 band of (11)B	e
OBF	4.8	4.79-4.82	v1 band of (11)B	f
	λ [nm]	λ [nm]		
BN	360	-	triplet	a
BN	380	-	triplet	a
AlO	465	464.8, 467.1	easily observed	a
AlO	485	484.2, 486.6	easily observed	a
AlO	512	507.9, 510.2, 512.3, 514.3	easily observed	a
MgO	~500	497.5, 498.6, 499.7, 500.7	easily observed	a

Table B.1: cont.

Species	Bands λ [nm]	Lines λ [nm]	Comments	Refs.
OH	496	-	weak	a
OH	512	-	relatively strong	a
OH	548	-	relatively strong	a
OH	553	-	weak	a
N_2	580	575.5, 580.4, 581.5	weak	a
N_2	590	585.4, 590.6, 595.9	medium	a
N_2	635	632.3, 639.5	weak	a
N_2	~650	646.9, 654.5	relatively strong	a
NO	404	402.7, 404.2	weak	a
NO	533	533.4	weak	a
NO	600	600.1	weak	a
NO	638	637.8	weak	a
NO_2	439	-	-	a
NO_2	446	444.8, 448	-	a
NO_2	463	-	-	a
NO_2	609	-	-	a
NO_2	631	-	-	a

a: Ref. (54)
b: Ref. (83)
c: Ref. (85)
d: Ref.(82)
e: Ref. (84)
f: Ref. (86)

Appendix C: Selection of Typical Combusting Particle Measurements

This Appendix contains figures with typical boron (and aluminum) particle combustion signals. Each plot includes the pressure measurement, bandpass filtered photodiode signal, and injection timing measurement for the respective particle experiment superposed on the respective average background pressure and hot gas emission measurements, which are discussed in Section 2.3.6 of the thesis text. In most cases the particle signals are seen to increase above hot-gas background levels after particle injection, to peak , and return to the background as the particles burn to completion. The photodiode and injection timing signals have been scaled to fit on the same axis, and can be considered to have arbitrary units. Conditions for the respective particle tests are given in the plot legends and therefore no figure captions are included.

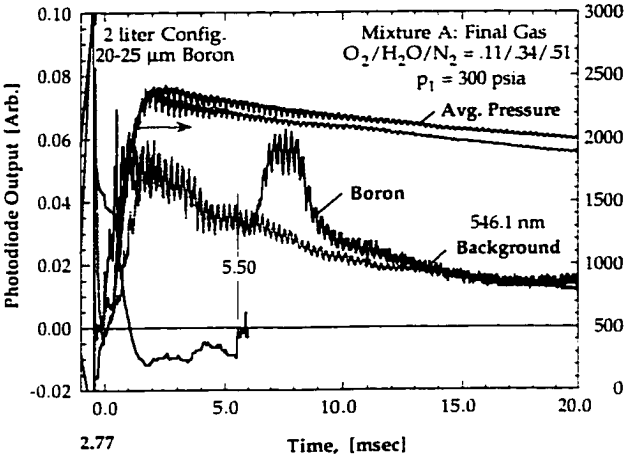

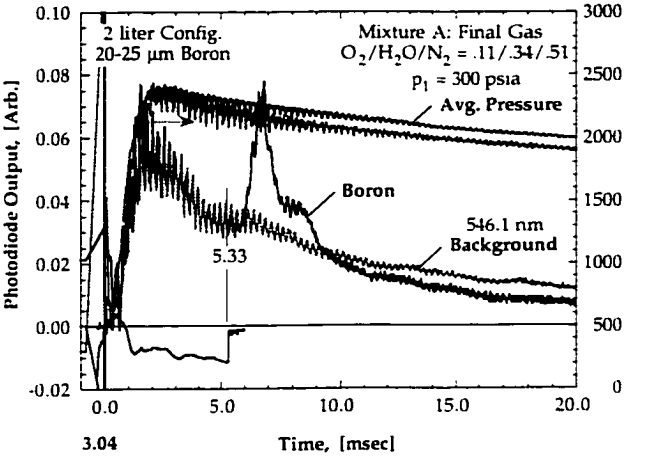

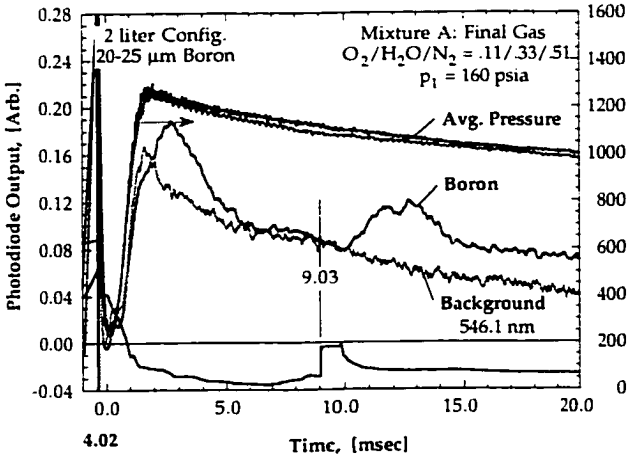

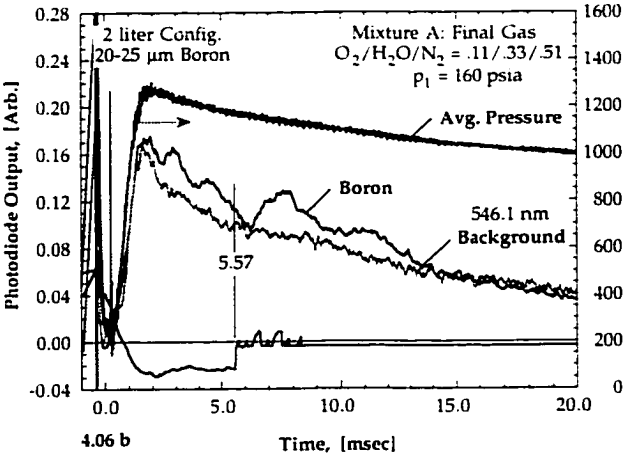

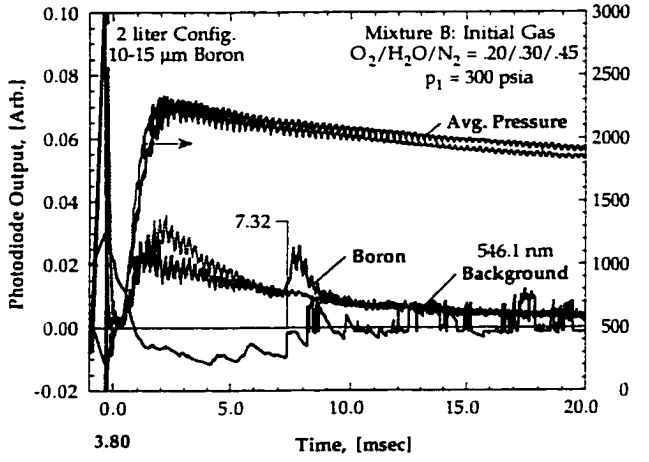

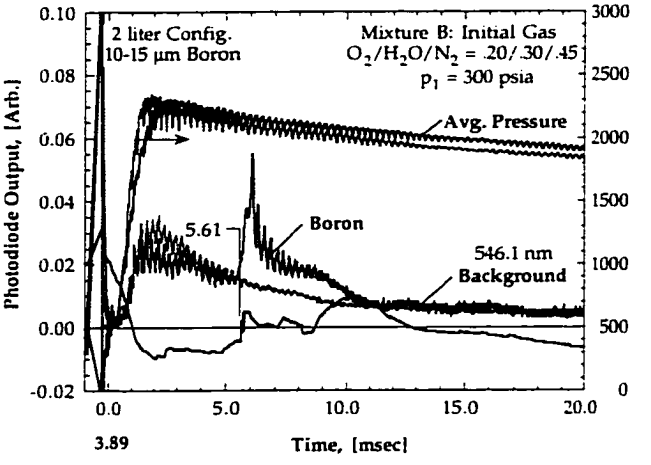

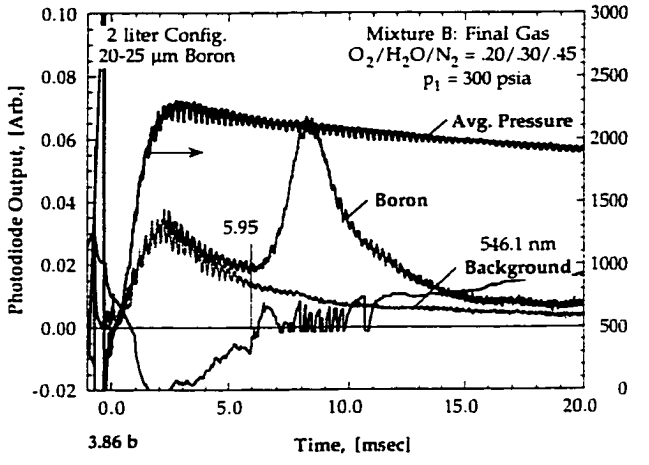

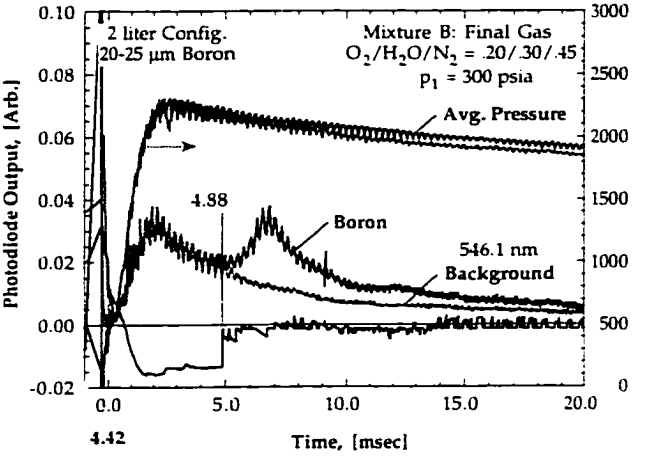

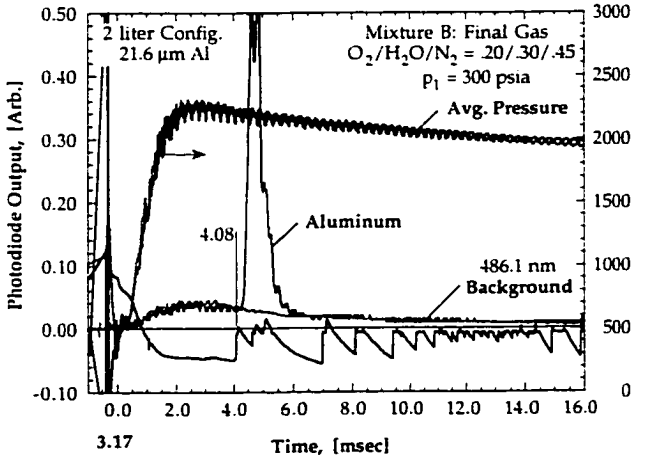

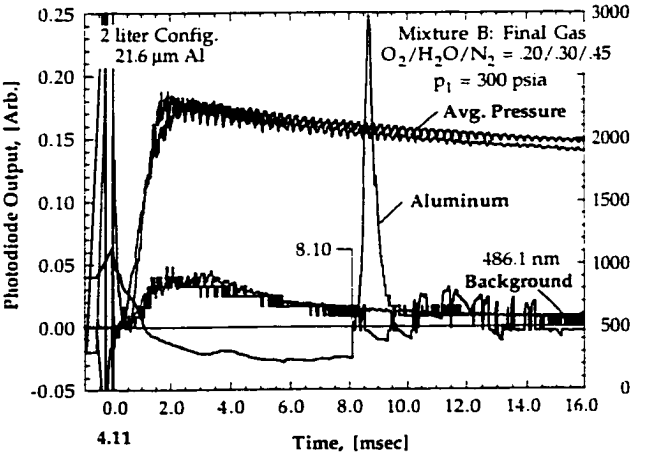

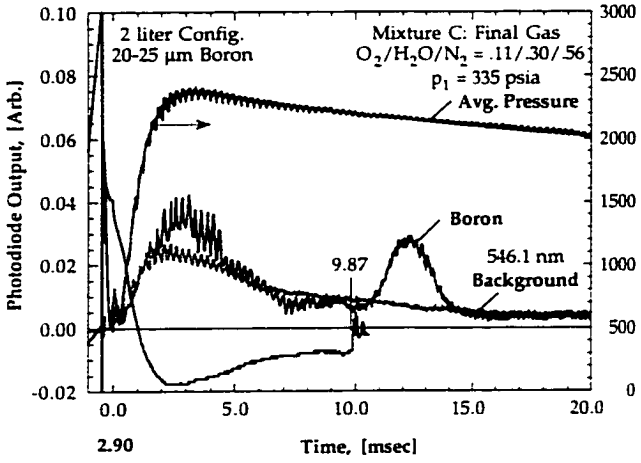

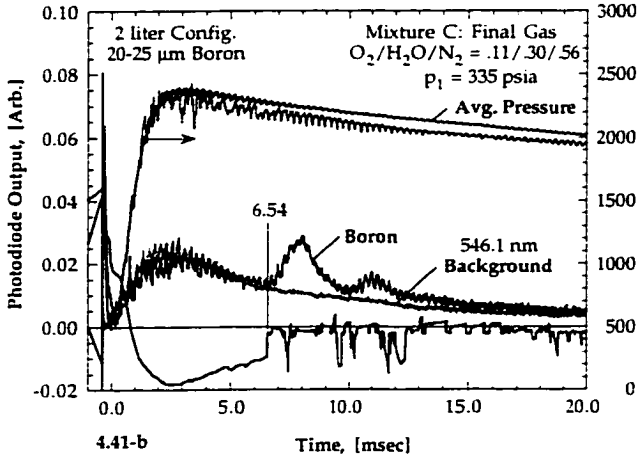

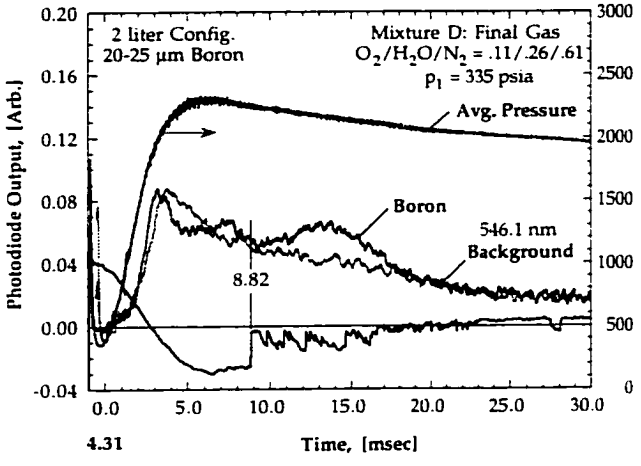

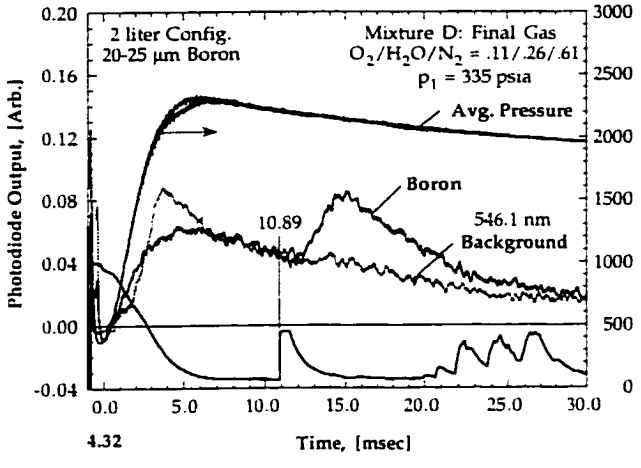

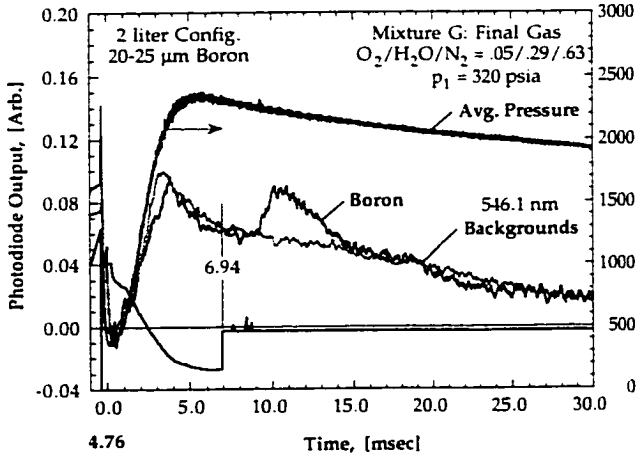

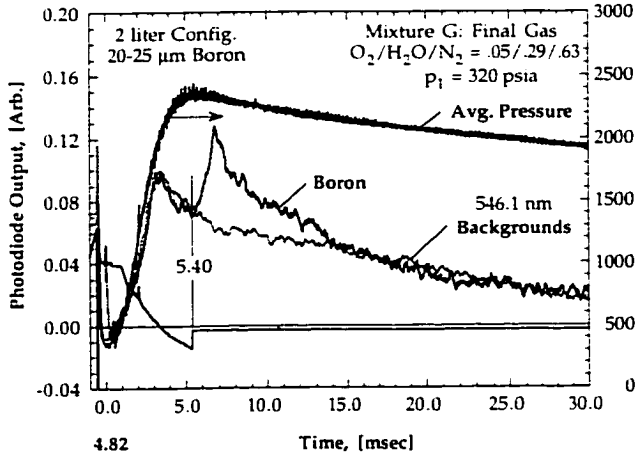

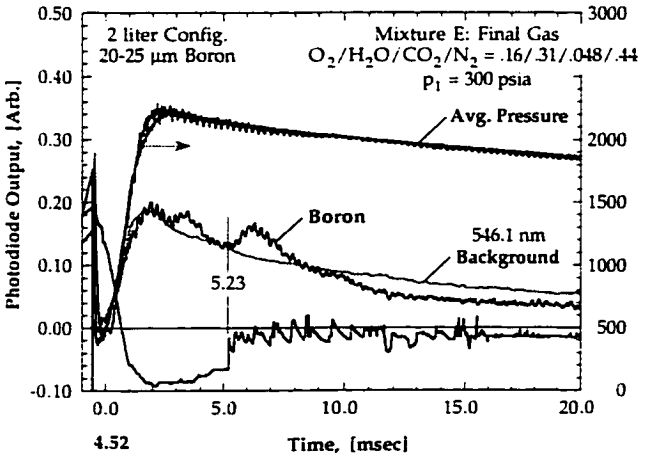

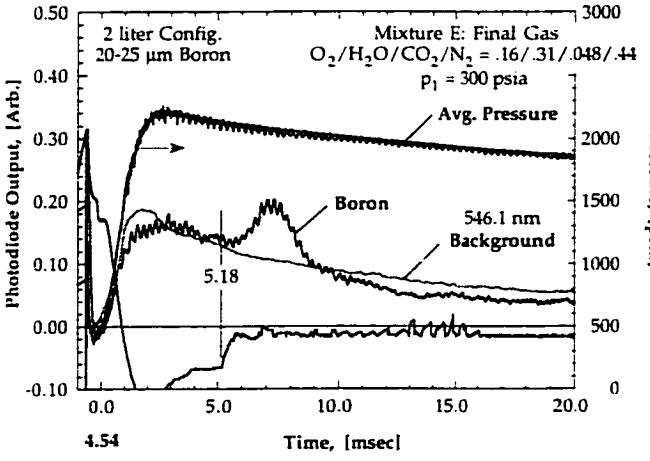

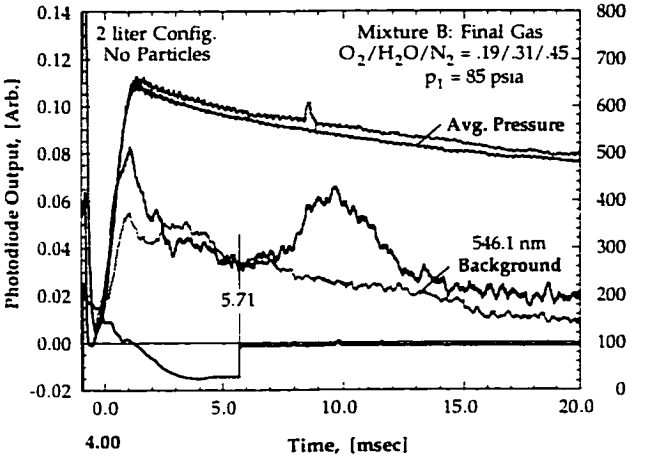

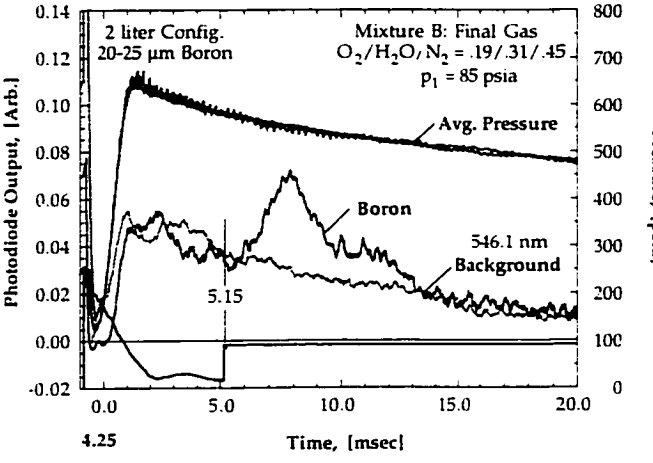

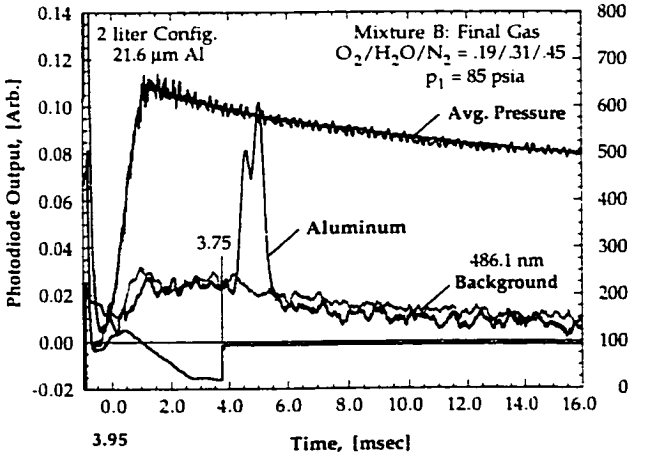

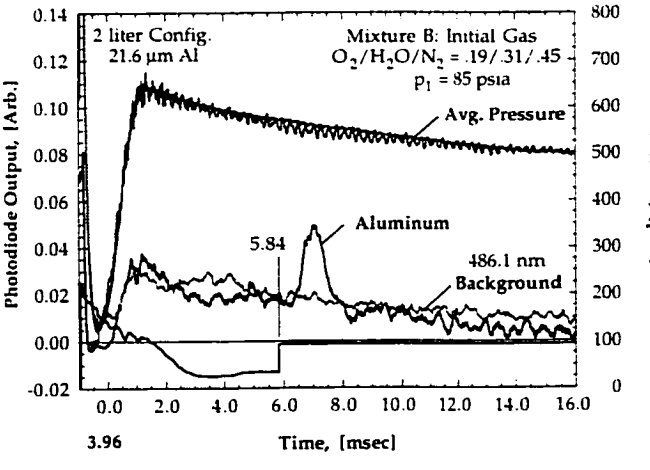

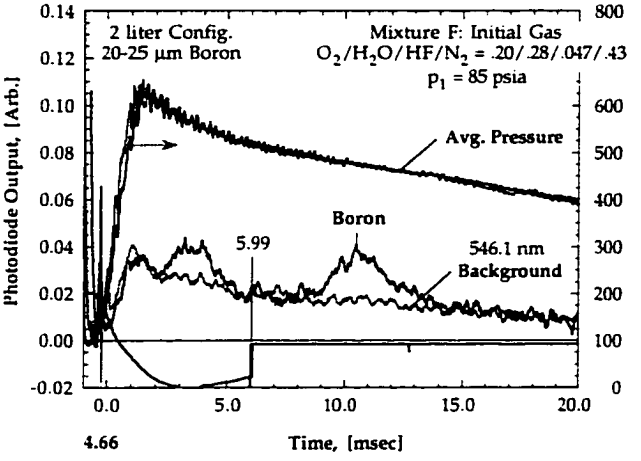

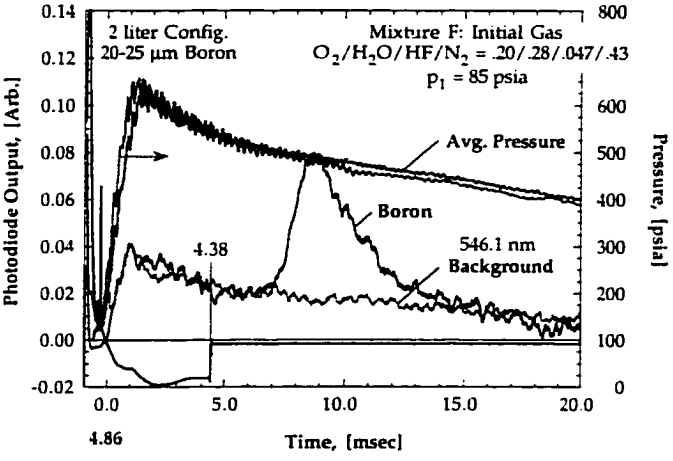

List of References

1. King, M. K., A Review of Studies of Boron Ignition and Combustion Phenomena at Atlantic Research Corporation over the Past Decade, in *Combustion of Boron-Based Solid Propellants and Solid Fuels*, K. K. Kuo and R. Pein, Eds., Begell House Publishing Co. and CRC Press, Inc., Boca Raton, 1993, pp. 1-80.

2. Price, E. W., Combustion of Metalized Propellants, in *Fundamentals of Solid-Propellant Combustion*, Progress in Aeronautics and Astronautics Series vol. 90, K. K. Kuo and M. Summerfield, Eds., AIAA Publishers, New York, 1984, pp. 479-514.

3. Besser, H. L., Strecker, R., Overview of Boron Ducted Rocket Development During the Last Two Decades, in *Combustion of Boron-Based Solid Propellants and Solid Fuels*, K. K. Kuo and R. Pein, Eds., Begell House Publishing Co. and CRC Press, Inc., Boca Raton, 1993, pp. 133-178.

4. Macek, A., Semple, J. M., Combustion of Boron Particles at Atmospheric Pressure, *Combustion Science and Technology*, vol. 1, pp. 181-191 (1969).

5. Macek, A., Semple, J. M., Combustion of Boron Particles at Elevated Pressures, *Thirteenth Symposium (International) on Combustion*, The Combustion Institute, Pittsburgh, 1970, pp. 859-868.

6. Macek, A., Combustion of Boron Particles: Experiment and Theory, *Fourteenth Symposium (International) on Combustion*, The Combustion Institute, Pittsburgh, 1972, pp. 1401-1411.

7. Li, S. C., Williams, F. A., Ignition and Combustion of Boron in Wet and Dry Atmospheres, *Twenty-Third Symposium (International) on Combustion*, The Combustion Institute, Pittsburgh, 1990, pp. 1147-1154.

8. Li, S. C., *Experimental and Theoretical Studies of Ignition and Combustion of Boron Particles in Wet and Dry Atmospheres*, Ph.D. Thesis, Department of Mechanical and Aerospace Engineering, Princeton University, 1990.

9. Li, S. C., Williams, F. A., Ignition and Combustion of Boron Particles, in *Combustion of Boron-Based Solid Propellants and Solid Fuels*, K. K. Kuo and R. Pein, Eds., Begell House Publishing Co. and CRC Press, Inc., Boca Raton, 1993, pp. 248-271.

10. Yeh, C. L., Kuo, K. K., Ignition and Combustion of Boron Particles, *Progress in Energy and Combustion Science*, vol. 22, pp. 511-541 (1996).

11. Rood, T. J., Spalding, M. J., Krier, H., Burton, R. L., Ignition Dynamics of Boron Particles in a Shock Tube, *AIAA Paper No. 97-3234*, Presented at the 33rd AIAA/SAE/ASME/ASEE Joint Propulsion

Conference, Seattle, WA July 1997.

12. Rood, T. J., *Shock Tube Ignition of Boron Particles in Oxygen with Infrared Detection of Boron-Oxide Removal*, Masters Thesis, Department of Mechanical and Industrial Engineering, University of Illinois at Urbana/ Champaign, 1997.

13. Zhou, W., Yetter, R. A., Dryer, F. L., Rabitz, H., Brown, R. C., Kolb, C. E., Multi-Phase Model for Ignition and Combustion of Boron Particles, *Combustion and Flame*, submitted for review Aug. 1997.

14. Zhou, W., Yetter, R. A., Dryer, F. L., Rabitz, H., Brown, R. C., Kolb, C. E., A Comprehensive Physical and Numerical Model of Boron Particle Ignition, *Twenty-Sixth Symposium (International) on Combustion*, The Combustion Institute, Pittsburgh, 1996, pp. 1909-1917.

15. Hsieh, W.-H., Peretz, A., Huang, I.-T., Kuo, K. K., Combustion Behavior of Boron-Based BAMO/NMMO Fuel-Rich Solid Propellants, *Journal of Propulsion and Power* , vol. 7, pp. 497-504 (1991).

16. Bucher, P., Yetter, R. A., Dryer, F. L., Parr, T. P., Hanson-Parr, D. M., Vicenzi, E. P., Flame Structure Measurement of Single, Isolated Aluminum Particles Burning in Air, *Twenty-Sixth Symposium (International) on Combustion*, The Combustion Institute, Pittsburgh, pp. 1899-1908 (1996).

17. Bucher, P., Yetter, R. A., Dryer, F. L., Vicenzi, E. P., Parr, T. P., Hanson-Parr, D. M., Observations on Aluminum Particles Burning in Various Oxidizers, *33rd JANNAF Combustion Subcommittee Meeting*, Monterey, CA (1996).

18. Greenwood, N. N., Boron, in *Comprehensive Inorganic Chemistry*, J. C. Bailar, et al., Eds., Pergamon Press, Oxford, 1969, pp. 684-689.

19. Chase, M. W. J., Davies, C. A., Downey, J. R. J., Frurip, D. J., McDonald, R. A., Syverud, A. N., JANAF Thermochemical Tables, 3rd Edition, *Journal of Physical and Chemical Reference Data*, vol. 14 (Suppl 1), (1985).

20. Incropera, F. P., DeWitt, D. P., *Fundamentals of Heat and Mass Transfer, 3rd Edition*, John Wiley & Sons, New York, 1990, pp. 48.

21. Ho, C. Y., Powell, R. W., Liley, P. E., Thermal Conductivity of the Elements, *Journal of Physical and Chemical Reference Data*, vol. 1 no. 2, pp. 279-420, (1972).

22. Turns, S. R., Holl, J. T., Solomon, A. S. P., Faeth, G. M., Gasification of Boron Oxide Drops in Combustion Gases, *Combustion Science and Technology*, vol. 43, pp. 287-300 (1985).

23. Hammond, C. R., Properties of the Elements and Inorganic Compounds, in *CRC Handbook of*

Chemistry and Physics, 73rd Edition, D. R. Lide, Ed., CRC Press, Inc., Boca Raton, 1992, pp. S4-36 to S4-45.

24. Roberts, T. A., *The Shock Tube Ignition and Combustion of Aluminum/ Magnesium Alloy Particles in Oxygen at High Pressure*, Ph.D. Thesis, Department of Aeronautical and Astronautical Engineering, University of Illinois at Urbana/ Champaign, 1993.

25. Reader, J., Corliss, C. H., Atomic, Molecular, and Optical Physics, in *CRC Handbook of Chemistry and Physics, 73rd Edition*, D. R. Lide, Ed., CRC Press, Inc., Boca Raton, 1992, pp. S10-305.

26. Anon., *Thermophysical Properties of High Temperature Solid Materials; Volume 4: Oxides and Their Solutions and Mixtures*, Y. S. Touloukian, Ed., vol. 4 pt. 1, MacMillen Co., New York, 1967, pp. 22-25.

27. Brandes, E.A., *Smithells Metals Reference Book, 6th Ed.*, Butterworth, London, 1983.

28. Gurevich, M. A., Kir'yanov, I. M., Ozerov, E. S., Combustion of Individual Boron Particles, *Combustion, Explosions, and Shock Waves*, vol. 5, pp. 150-153 (1969).

29. Yuasa, S., Isoda, H., Ignition and Combustion of Small Boron Lumps in an Oxygen Stream, *Combustion and Flame*, vol. 86, pp. 216-222 (1991).

30. Krier, H., Burton, R. L., Pirman, S. R., Spalding, M. J., Shock Initiation of Crystalline Boron in Oxygen and Fluorine Compounds, *Journal of Propulsion and Power*, vol. 12, no. 4, pp. 672-679 (1996).

31. King, M. K., Ignition and Combustion of Boron Particles and Clouds, *Journal of Spacecraft and Rockets*, vol. 19 no. 4, pp. 294-306 (1982).

32. Mohan, G., Williams, F. A., Ignition and Combustion of Boron in O_2/Inert Atmospheres, *AIAA Journal*, vol. 10 no. 6, pp. 776-783 (1972).

33. Yetter, R. A., Cho, S. Y., Rabitz, H., Dryer, F. L., Brown, R. C., Kolb, C. E., Chemical Kinetic Modeling and Sensitivity Analysis for Boron Assisted Hydrocarbon Combustion, *Twenty-Second Symposium (International) on Combustion*, The Combustion Institute, Pittsburgh, 1988, pp. 919-929.

34. Yetter, R. A., Rabitz, H., Dryer, F. L., Brown, R. C., Kolb, C. E., Kinetics of High-Temperature B/O/H/C Chemistry, *Combustion and Flame*, vol. 83, pp. 43-62 (1991).

35. Brown, R. C., Kolb, C. E., Rabitz, H., Cho, S. Y., Yetter, R. A., Dryer, F. L., Kinetic Model of Liquid B_2O_3 Gasification in a Hydrocarbon Combustion Environment: I. Heterogeneous Surface Reactions, *International Journal of Chemical Kinetics*, vol. 23, pp. 957-970 (1991).

36. Brown, R. C., Kolb, C. E., Cho, S. Y., Yetter, R. A., Dryer, F. L., Rabitz, H. R., Kinetic Model of

Hydrocarbon-Assisted Particulate Boron Combustion, *International Journal of Chemical Kinetics*, vol. 26, pp. 319-332 (1994).

37. Brown, R. C., Kolb, C. E., Cho, S. Y., Yetter, R. A., Rabitz, H., Dryer, F. L., Kinetics of High Temperature, Hydrocarbon Assisted Boron Combustion, in *Gas-Phase Metal Reactions*, A. Fontijn, Ed., Elsevier Science Publishers B.V., 1992, pp. 643-660.

38. Brown, R. C., Kolb, C. E., Yetter, R. A., Dryer, F. L., Rabitz, H., Kinetic Modeling and Sensitivity Analysis for B/H/O/C/F Combination Systems, *Combustion and Flame*, vol. 101, pp. 221-238 (1995).

39. Yetter, R. A., Dryer, F. L., Rabitz, H., Brown, R. C., Kolb, C. E., Effect of Fluorine on the Gasification Rate of Liquid Boron Oxide Droplets, *Combustion and Flame*, accepted for publication, (1997).

40. Zhou, W., Yetter, R. A., Dryer, F. L., Rabitz, H., Brown, R. C., Kolb, C. E., Effect of Fluorine on the Combustion of "Clean" Surface Boron Particles, *Combustion and Flame*, accepted for publication, (1997).

41. Foelsche, R. O., Burton, R. L., Krier, H., High Pressure Ignition and Combustion of Boron Particles at 30 - 150 Atmospheres, *Combustion and Flame*, submitted for review June 1997, no. CF97-085.

42. Rosenbland, V., Natan, B., Gany, A., Ignition of Boron Particles Coated by a Thin Titanium Film, *AIAA Paper No. 93-2201*, Presented at the 29th AIAA/SAE/ASME/ASEE Joint Propulsion Conference, Monterey, CA June 1993.

43. Smolanoff, J., Sowa-Resat, M., Lapicki, M., Hanley, L., Ruatta, S., Hintz, P., Anderson, S. A., Kinetic Parameters for Heterogeneous Boron Combustion Reactions via the Cluster Beam Approach, *Combustion and Flame*, vol. 105, pp. 68-79 (1996).

44. Roberts, T. A., Burton, R. L., Krier, H., Ignition and Combustion of Aluminum/Magnesium Alloy Particles in O_2 at High Pressures, *Combustion and Flame*, vol. 92, pp. 125-143 (1993).

45. Megli, T. W., *Aluminum-Magnesium Particle Ignition in Shocked Mixtures of Water Vapor and Argon*, Masters Thesis, Department of Mechanical and Industrial Engineering, University of Illinois at Urbana/ Champaign, 1993.

46. Megli, T. W., Krier, H., Burton, R. L., Shock Tube Ignition of Aluminum/Magnesium Alloys in Water Vapor and Argon, *Proceedings of the 3rd International Conference on Experimental Heat Transfer, Fluid Mechanics, and Thermodynamics, Vol. 2*, M. D. Kelleher, et al., (Eds.), Elsevier Science Publishers B.V., 1993, pp. 1097-1105.

47. Pirman, S.R., *Shock Initiation of Crystalline Boron in Oxygen and Flourine Compounds*, Masters

Thesis, Department of Mechanical and Industrial Engineering, University of Illinois at Urbana/ Champaign, 1994.

48. Raizer, Y. P., *Gas Discharge Physics*, Springer-Verlag, NY, 1991, pp. 130-135.

49. Naber, J. D., Siebers, D. L., Effects of Gas Density and Vaporization on Penetration and Dispersion of Diesel Sprays, *SAE Technical Paper Series No. 960034*, Reprinted from: Investigations into Diesel Engine Combustion Processes (SP-1159).

50. Siebers, D. L., personal communication, (1996).

51. Lord, M. E., *Performance of A 40-MM Combustion-Heated Light Gas Gun Launcher*, VKF, ARO, Inc. Report No. AEDC-TN-60-176, (1960).

52. Luikov, A. V., *Analytical Heat Diffusion Theory*, Academic Press, New York, 1968, pp. 119-131 and pp. 401-405.

53. Nettleton, M. A., *Gaseous Detonations: Their Nature, Effects and Control*, Chapman and Hall, New York, 1987, pp. 255.

54. Pearse, R. W. B., Gaydon, A. G., *The Identification of Molecular Spectra*, 4th Ed., Chapman and Hall, London, 1976, pp. 59.

55. Spalding, M. J., *Ignition of Boron Particles in a Shock Tube Using Emission Spectroscopy*, Masters Thesis, Department of Mechanical and Industrial Engineering, University of Illinois at Urbana/ Champaign, 1996.

56. Spalding, M. J., Krier, H., Burton, R. L., Emission Spectroscopy During Ignition of Boron Particles at High Pressure, *AIAA Paper No. 97-0119*, presented at the 35th AIAA Aerospace Sciences Meeting, Reno, NV Jan. 1997.

57. Robinson, J. W., *CRC Handbook of Spectroscopy, vol. 1*, CRC Press, Cleveland, OH, 1974, pp. 779-780.

58. Kee, R. J., Rupley, F. M., Miller, J. A., *CHEMKIN - II: A FORTRAN Chemical Kinetics Package for the Analysis of Gas-Phase Chemical Kinetics*, Sandia National Laboratories Report SAND89-8009, Livermore, CA (1989).

59. Kee, R. J., Rupley, F. M., Miller, J. A., *The Chemkin Thermodynamic Data Base*, Sandia National Laboratories Report SAND87-8215B, Livermore, CA (1990).

60. Reynolds, W. C., STANJAN-III Equilibrium Program, v. 3.95, Stanford University, September 1993.

61. Olsen, S. E., Beckstead, M. W., Burn Time Measurements of Single Aluminum Particles in Steam and Carbon Dioxide Mixtures, *AIAA Paper No. 95-2715*, presented at the 31st AIAA/ASME/SAE/ASEE Joint Propulsion Conference, San Diego, CA June 1995.

62. Macek, A., Fundamentals of Combustion of Single Aluminum and Beryllium Particles, *Eleventh Symposium (International) on Combustion*, The Combustion Institute, Pittsburgh, 1966, pp. 203-217.

63. Schneider, D. S., *Aluminum Particle Combustion in a Windowed Solid Propellant Flow Reactor*, M.S. Thesis, Department of Aeronautical and Astronautical Engineering, University of Illinois at Urbana/ Champaign, 1997.

64. Davis, A., Solid Propellants: The Combustion of Particles of Metal Ingredients, *Combustion and Flame*, vol. 7, pp. 359-367 (1963).

65. Belyaev, A. F., Frolov, Y. V., Korotkov, A. I., Combustion and Ignition of Finely Dispersed Aluminum, *Combustion, Explosions, and Shock Waves*, vol. 6, no. 3, pp. 182-185 (1968).

66. Nickerson, G. R., Coats, D. E., Dang, A. L., Dunn, S. S., Berker, D. R., Hermsen, R. L., Lamberty, J. T., *The Solid Propellant Rocket Motor Performance Prediction Computer Program (SPP), Version 6.0, Volume I: Engineering Manual*, Air Force Astronautics Laboratory Report No. AFAL-TR-87-078, (1987).

67. Golovko, V. V., Kondratyev, E. N., Polishchuk, D. I., Ignition and Combustion of Boron Particles in Chlorine, in *Combustion of Boron-Based Solid Propellants and Solid Fuels*, K. K. Kuo and R. Pein, Eds., Begell House Publishing Co. and CRC Press, Inc., Boca Raton, 1993, pp. 272-284.

68. Kee, R. J., Dixon-Lewis, G., Warnatz, J., Coltrin, M. E., Miller, J. A., *A FORTRAN Computer Code Package for Evaluation of Gas-Phase Multicomponent Transport Properties*, Sandia National Laboratories Report SAND86-8246, 1990 Reprint, (1990).

69. Krier, H., Burton, R. L., Pirman, S. R., *Shock Initiation of Crystalline Boron in Oxygen and Fluorine Compounds*, University of Illinois at Urbana/ Champaign Report UILU-ENG 94-4010, (1994).

70. Foelsche, R. O., Spalding, M. J., Burton, R. L., Krier, H., High Pressure Ignition of Boron in Reduced Oxygen Atmospheres, in *Decomposition, Combustion, and Detonation Chemistry of Energetic Materials* (Materials Research Society Symposium Proceedings), T. B. Brill, et al., Eds., vol. 418, 1995, pp. 187-193.

71. Foelsche, R. O., Burton, R. L., Krier, H., Ignition and Combustion of Boron Particles in Hydrogen/Oxygen Explosion Products, *AIAA Paper No. 97-0127*, presented at the 35th AIAA Aerospace Sciences Meeting, Reno, NV Jan. 1997.

72. Walsh, J. M., Drag Coefficient Equations for Small Particles in High Speed Flows, *AIAA Journal*, vol. 13, no. 11, pp. 1526 - 1528 (1975).

73. Fox, T. W., Rackett, C. W., Nichols, J. A., Shock Wave Ignition of Magnesium Powders, in *Shock Tube and Shock Wave Research, Proceedings of the Eleventh International Symposium on Shock Tubes and Waves*, B. Ahlborn, A. Hertzberg, and D. Russell, Eds., University of Washington Press, Seattle, vol. 11, 1977, pp. 262-268.

74. Drake, R. M., Discussion in Connection with Forced Convection Heat Transfer From an Isothermal Sphere to Water, *Journal of Heat Transfer*, vol. 83, pp. 170 - 172 (1961).

75. Hirschfelder, J. O., Curtiss, C. F., Bird, R. B., *Molecular Theory of Gases and Liquids*, John Wiley & Sons, Inc., New York, 1954, pp. 528-604.

76. Foelsche, R. O., *Computer Program for Predicting Ignition of Boron Particles Injected into High Pressure Combustion Chamber*, University of Illinois at Urbana/ Champaign Report UILU-ENG 97-0512, Urbana, IL (1997).

77. Hindmarsh, A. C., LSODE Software: Livermore Solver for Ordinary Differential Equations, Lawrence Livermore National Laboratories, Livermore Ca, March 30, 1987 version.

78. Cho, S. Y., Yetter, R. A., Dryer, F. L., Brown, R. C., Kolb, C. E., Rabitz, H. R., Kinetic Model for Liquid B_2O_3 Gasification in a Hydrocarbon Combustion Environment: II. Mathematical Modeling and Sensitivity Analysis, *Journal of Computational Physics*, vol. 102, pp. 160-179 (1992).

79. Yetter, R. A., Dryer, F. L., Allen, M. T., Gatto, J. L., Development of Gas-Phase Reaction Mechanisms for Nitramine Combustion, *Journal of Propulsion and Power*, vol. 11, pp. 683-697 (1995).

80. Pokhil, P. F., Belyaev A. F., Frolov, Y. V., Logachev, V. S., Korotkov, A. I., *Combustion of Powdered Metals in Active Media*, Defense Technical Information Center Report AD-769 576, (1972).

81. Perry, J. A., Critical Flow Through Sharp-Edged Orifices, *Transactions of the ASME*, vol. 71, pp. 757-764 (1949).

82. Eisenreich, N., Liehmann, W., Emissionspectroscopy of Boron Ignition and Combustion in the Range of 0.2 μm to 5.5 μm, *Propellants, Explosives, and Pyrotechnics*, vol. 12, pp. 88-91 (1987).

83. Sommer, A., White, D., Linevesky, M. J., Mann, D. E., Infrared Absorption Spectra of B_2O_3, B_2O_2, and BO_2 in Solid Argon Matrices, *Journal of Chemical Physics*, vol. 38, pp. 87-98 (1963).

84. Kawashima, Y., Kawaguchi, K., Hirota, E., Detection of HBO By Discharge Modulated Infrared

Diode Laser Spectroscopy, *Chemical Physics Letters*, vol. 131, pp. 205-208 (1986).

85. Nelson, H. F., Tucker, E. O., Boron Slurry-Fueled Jet Engine Exhaust Plume Infrared Signatures, *Journal of Spacecraft and Rockets*, vol. 23, pp. 527-533 (1986).

86. Kawashima, Y., Kawaguchi, K., Endo, Y., Hirota, E., Infrared Diode Laser and Microwave Spectra and Molecular Structure of an Unstable Molecule, FBO, *Journal of Chemical Physics*, vol. 87, pp. 2006-2009 (1987).

VITA

Robert Oliver Foelsche was born on July 24, 1968 in Bayshore, New York. He resided in Bellport, New York for eighteen years and was educated in the public school system. He received his B.S. Degree in Mechanical Engineering from Cornell University, Ithaca, New York and entered the University of Illinois at Urbana-Champaign in the Fall of 1990. In 1993 he received his M.S. Degree at the University of Illinois at Urbana-Champaign.

Education:

Ph.D., 1996, Dept. of Aeronautical and Astronautical Engineering, University of Illinois, Urbana, IL. Advisor : Prof. Rodney L. Burton.

M.S., 1993, Dept. of Aeronautical and Astronautical Engineering, University of Illinois, Urbana, IL. Advisor : Prof. Wayne C. Solomon.

B.S., 1990, Dept. of Mechanical and Aerospace Engineering, Cornell University, Ithaca, NY. Advisor : Prof. Franklin C. Gouldin.

Experience:

05/93-11/97 : Ph.D. Student, University of Illinois, Shock Tube and High Pressure Combustion Laboratory, Urbana IL

As a graduate research assistant, designed and instrumented a high pressure combustion chamber and developed a high frequency-response diagnostics technique for metal particle combustion. Performed experimental and theoretical investigation of boron particle ignition and combustion at elevated pressures in a constant volume combustion bomb in oxygen/water vapor/nitrogen oxidizing mixtures.

07/95-08/95 : Technical Consultant to Combustion Sciences, Inc., Urbana IL

Computationally simulated the pressurization history and rupture of a tar melting chamber and feed system. Prepared technical documentation of predictions for use in court case proceedings.

07/90-05/93 : M.S. Student, University of Illinois, Urbana IL

Compiled and evaluated a large elementary chemical kinetic reaction mechanism for the combustion of complex hydrocarbon fuel mixtures and developed computer model to simulate the high temperature, non-equilibrium combustion performance of a liquid-fueled ramrocket preburner simulator.

01/92-05/92 : Teaching Assistant, University of Illinois, Urbana IL

Supervised and taught lab sessions in undergraduate aerodynamics lab.

1988-1989 : Coop Engineer, General Dynamics, Electric Boat Division, Groton CT

Provided shipyard engineering construction support including on board component and systems inspection and testing. Provided structural and mechanical analysis of flawed or partially defective parts, processed vendor nonconformances.

Academic Honors:

NASA Fellowship, 8/91 - 5/92, 8/92 - 5/93
Graduated with Honors, M.S., 1993, with Distinction, B.S., 1990
Dean's List, all semesters, 8/86 - 5/90

Publications and Papers:

Foelsche, R. O., Burton, R. L., Krier, H., High Pressure Ignition and Combustion of Boron Particles at 30 - 150 Atmospheres, *Combustion and Flame*, submitted for review June 1997, no. CF97-085.

Foelsche, R. O., *Computer Program for Predicting Ignition of Boron Particles Injected into High Pressure Combustion Chamber*, University of Illinois at Urbana/ Champaign Report UILU-ENG 97-0512, Urbana, IL (1997).

Foelsche, R. O., Burton, R. L., Krier, H., Ignition and Combustion of Boron Particles in Hydrogen/Oxygen Explosion Products, *AIAA Paper No. 97-0127*, presented at the 35th AIAA Aerospace Sciences Meeting, Reno, NV Jan. 1997.

Foelsche, R. O., Spalding, M. J., Burton, R. L., Krier, H., High Pressure Ignition of Boron in Reduced Oxygen Atmospheres, in *Decomposition, Combustion, and Detonation Chemistry of Energetic Materials* (Materials Research Society Symposium Proceedings), T. B. Brill, et al., Eds., vol. 418, 1995, pp. 187-193.

Foelsche, R. O., Keen, J. M., Solomon, W. C., Buckley, P.F., Corporan, E., Non-Equilibrium Combustion Model for Fuel Rich Gas Generators, Journal of Propulsion and Power, vol. 10 no. 4, pp. 461-472 1994, *also*, AIAA Paper #93-2041, presented at 29th Joint Propulsion Conference, Monterey CA June 1993.

Foelsche, R. O., Keen, J. M., Solomon, W. C., A Chemical Kinetic Reaction Mechanism and Thermodynamic Database for Fuel Rich Hydrocarbon Combustion Modeling, Internal Report No. AAE 93-13 (UILU 93-0513), Dept. of Aeronautical and Astronautical Engineering, University of Illinois at Urbana-Champaign, August 1993.

Foelsche, R. O., Keen, J. M., Solomon, W. C., A Non-Equilibrium Computational Method for Predicting Fuel Rich Gas Generator Performance and Exhaust Properties, Volume II: Reaction Kinetics and Computational Results, Final Report for Contract No. F33615-89-C-2912, Dept. of Aeronautical and Astronautical Engineering, University of Illinois at Urbana-Champaign, March 1993.

Foelsche, R. O., A Non-Equilibrium Systems Approach to Modeling Fuel Rich Gas Generator Exhaust Properties, Masters Thesis, Dept. of Aeronautical and Astronautical Engineering, University of Illinois at Urbana-Champaign, March 1993.